The Identification of Structural Modal Parameters, as an Alternative *in-vivo* Diagnosis for Osteoporosis.

by

Victor Balden.

Dissertation submitted as partial fulfilment of the requirements for the degree of

Master of Science in Engineering
at the
University of Cape Town,
Faculty of Mechanical Engineering.

Declaration.

This is to certify that the results, calculations and other work presented in this thesis are essentially my own work, and that no part of it has been submitted for a degree at any other University. Appendix I lists the additional coursework completed in fulfilment of the requirements for this degree.

.....
V. H. Balden
September 1996

Dedication.

I dedicate this dissertation to my parents, especially my father.

Acknowledgements.

This project was funded by a postgraduate bursary from the Medical Research Council (MRC) and a University of Cape Town Research Associateship. Additional funding was supplied by the FRD and Mechanical Engineering Department. The author would like to express his gratitude to these organisations for their financial support.

The author is indebted to the following companies and researchers

- Professor Gerald Nurick, under whose supervision this thesis was conducted.

- Dr. Lee Peterson, of the Centre for Aerospace Structures, at the University of Colorado, Boulder USA. Also Mr Ken Alvin, of the Sandia National Laboratory, USA.
  Both Dr. Lee Peterson and Mr. Ken Alvin graciously assisted with aspects concerning the Eigensystem-Realization Algorithm and Impulse Response Technique.

- Dr. Nico Theron, of the Mechanical Department, University of Stellenbosch, who provided inspiration and encouragement in the latter part of the dissertation. Special thanks also to the Mechanical Department, of the University of Stellenbosch, for allowing the use of their vibration equipment.

- Dr. Norman Morrison, of the Electrical Engineering Department at UCT, for his guidance with various topics concerning Fourier Analysis.

- Aerodyne, who donated the carbon fibre tube which was used in the construction of the impact hammer.

Special thanks to my family, Debbie, Lulu and Garth for their support. Finally, thanks to my wife, Vasiliki, who supported, encouraged and makes all things worthwhile.

Abstract.

An alternative non-invasive diagnostic technique was sought for the diagnosis of osteoporosis in human subjects. The tibia vibration technique was proposed after reviewing the literature on detection techniques for osteoporosis. The basis of diagnosis of the tibia vibration technique is the measured resonant frequency of the patient's tibia. The patient's tibia is excited, generally by means of an impact hammer, while the response is captured and resonant frequencies extracted.

This dissertation does not attempt to measure the resonant frequencies of a human tibia, but rather develop and validate the required experimental protocol and system identification procedures, on a simple test structure. A theoretical finite element model of the test structure was developed to ensure that both the experimental protocol and system identification procedures provided accurate results.

The impulse response technique was adopted to excite the test structure. An impact hammer was built to apply the measured impact force to the structure. Two accelerometers were strategically placed on the test structure to capture the resultant vibration response. A third accelerometer was placed opposite the impact location. A four-channel low-pass filter, including anti-aliasing filtering, was also built to provide appropriate signal conditioning. The vibration responses were digitally sampled, before the ensemble averaged frequency and impulse response functions were calculated, for each accelerometer location.

The quality of both the frequency and impulse response functions were generally satisfactory. However, some of the anti-resonant peaks were ill-defined and unrealistic, which suggests that the captured vibration results were inconsistent. Also, significant high frequency modes were excited in many of the responses, these modes were outside the bandwidth of the filter and resulted in poor correlation of the identified impulse response functions.

A time-domain system identification procedure was instituted, namely the 'Eigensystem Realization Algorithm'. This system identification algorithm performs a least-squares fit of the captured vibration response data yielding a least order discrete state-space representation. In addition to identifying the modal parameters, this system identification algorithm identifies minimal order mass, damping and stiffness matrices which represent the excited system.
In general the correlation of the identified modal parameters, frequency and impulse response functions to the experimentally measured responses was excellent. Discrepancies only existed at those ill-defined anti-resonant peaks where the identified frequency response functions provided a more realistic representation. Correlation of the impulse response function for those responses containing significant high frequency modes was also degraded.

The finite element method was used to theoretically model the structure and provide predictions of the modal parameters, frequency and impulse response functions. A 3-node Timoshenko beam element was formulated and a finite element source code developed to solve the required modal parameters.

The predicted resonant frequencies agreed within ≈1% of the experimentally measured and identified resonant frequencies. Both the frequency and impulse response functions did not correlate well with their experimentally measured counterparts. Reasonable agreement for the location and magnitude of the resonant peaks could only be obtained for the case of zero damping. Even so, the finite element predictions with zero damping did not correlate well at the anti-resonant peaks. The proportional damping model which was instituted in the finite element model did not predict the modal damping accurately, as the resulting predicted damped frequency response functions deviated substantially from the measured responses.

The finite element predictions could not validate either the measured or the identified frequency and impulse response functions. However, the measured and identified resonant frequencies were correctly predicted by the finite element model. Both the experimental protocol and system identification procedures were successfully instituted and the dissertation goals met.

Table of Contents.

Chapter C. Finite Element Modelling of the Test Structure.

Chapter D. Time Domain Identification.

Chapter E. Experimental Details.

Nomenclature.

Notation	Description
γ	modal damping ratio
ν	Poisson's ratio
ζ	isoparametric co-ordinate
κ	Timoshenko shear coefficient
ω	circular frequency
ρ	material density
δ_{ij}	kronecker delta
θ_x , θ_y , θ_z	local rotational element co-ordinates
[ε]	strain tensor
[σ]	stress tensor
A	area or element area
A_d , A_c	discrete and continuous State Transition Matrix
B_d , B_c	discrete and continuous Input Influence Matrix
C	damping matrix
C_d , C_c	discrete and continuous Output Influence Matrix
C_{disp} , C_{vel} and C_{accel}	Output Influence Matrix, (displacement, velocity & acceleration)
D	dissipation energy function
E	Young's Modulus
$freq$	frequency
G	Shear Modulus
I	identity matrix
I_x , I_y , I_z	second moment of area, about respective axes
J	Jacobian matrix
K	stiffness matrix
L	length or element length
M	mass matrix
$q(t)$	displacement vector
t	time
$u_f(t)$	externally applied excitation force

List of Figures.

List of Tables.

Chapter A.

Introduction.

A. Introduction.

A.1 Background of Dissertation.

The accurate *in-vivo* diagnosis of osteoporosis in human subjects requires specialist equipment and hence is an expensive test. A cost-effective alternative procedure was proposed after discussions with the Head of the Osteoporosis and Arthritis Group, Dr. Kalla, at Groote Schuur Hospital.
The tibia vibration method was proposed after reviewing the literature on the non-invasive detection techniques for osteoporosis. The tibia vibration method requires that the tibia of the patient be impacted with a measured force, while the vibration response of the tibia is measured. The diagnosis is based on the comparison of the measured natural frequencies of the patient's tibia, to a database of natural frequencies from previously measured and diagnosed subjects.

This dissertation does not attempt to measure the natural frequencies of the human tibia, but rather, develop and validate the required experimental protocol and system identification procedures on a simple test structure.

A.2 Goals and Strategy of Dissertation.

The first goal of this dissertation is to experimentally capture the vibration response of the test structure. The second goal is then to process this captured data and identify the modal parameters. In order to ensure that both of these procedures are providing realistic results, a third goal is introduced. The third goal is to theoretically model the test structure, thus providing results for comparison. The goals and strategy that were followed in the dissertation are best indicated by inspection of figure A.1.

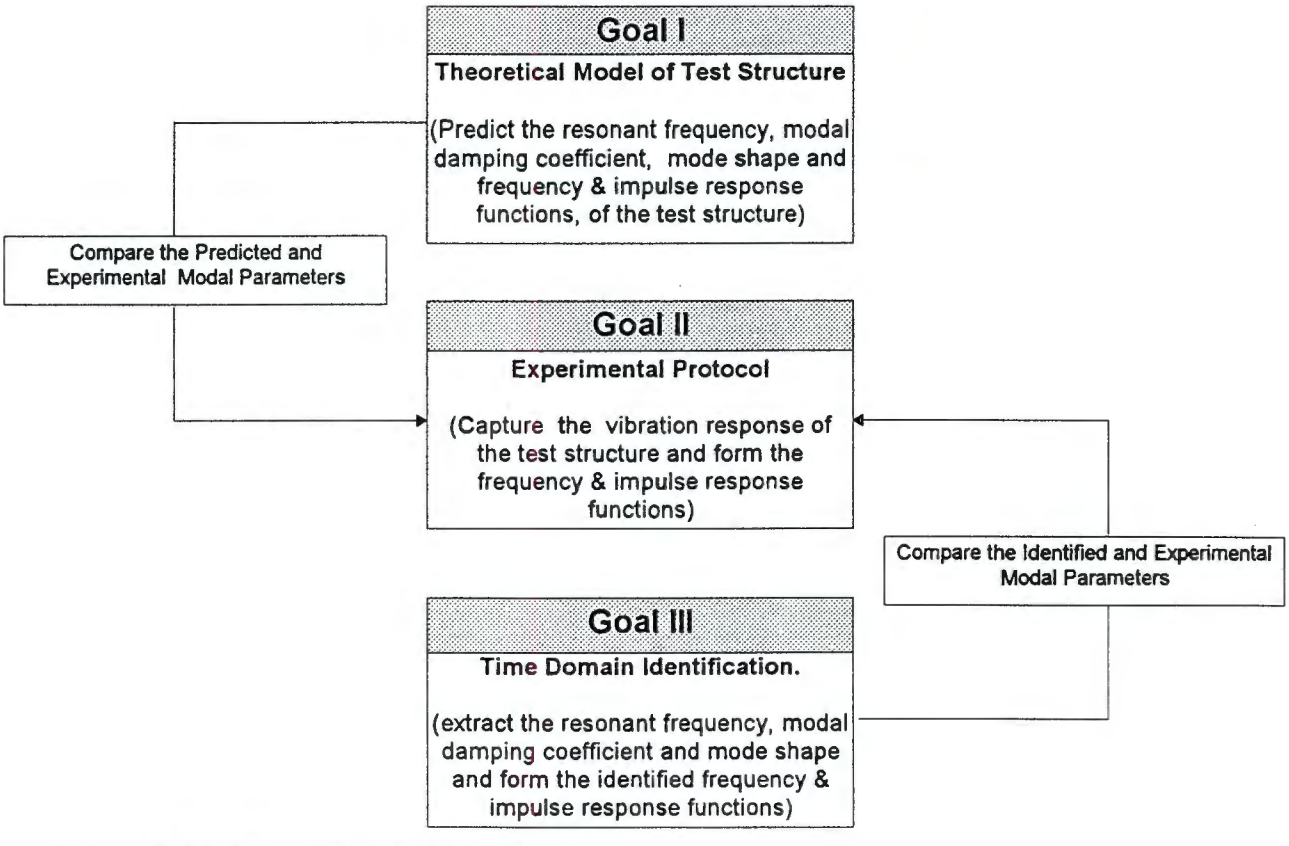

Figure A-1 Dissertation Goals and Strategy

A.3 Organisation of Dissertation Document.

The basic organisation of this dissertation document follows the goals depicted in figure A-1. In addition, a discussion of the non-invasive detection methods for the diagnosis of osteoporosis is included.

Chapter B, Non-Invasive Detection Methods for the Diagnosis of Osteoporosis.
The relation between bone density and bone stiffness is initially presented. Next, the mechanism of osteoporosis is described as the deduction in bone density, and hence loss of bone strength.

A number of different detection techniques, some of which detect bone density changes rather that deduction in bone stiffness, are discussed. The tibia vibration technique is one of these techniques.

Chapter C, Finite Element Modelling of the Test Structure.
Chapter C begins with a literature review of the various techniques for theoretically modelling the dynamic behaviour of the human tibia. Motivated by the reviewed literature, the tibia is modelled as a beam-like structure. A 3-node Timoshenko beam element is derived and a finite element source code written to implement the finite element model of a generic test structure. The finite element code predicts the modal parameters of the test structure.

Chapter D, Time Domain Identification.
The eigensystem realization algorithm, used to identify the modal parameters of the captured impulse response functions, was chosen as the time-domain system identification algorithm. The eigensystem realization algorithm provides a least order state-space representation of the test structure. In addition, least order mass, stiffness and damping matrices may be formulated which represent the dynamic behaviour of the test structure. The theoretical development of the eigensystem realization algorithm is presented in this chapter. The chapter concludes by describing the software implementation of this algorithm.

Chapter E, Experimental Details.
The impulse response technique was chosen as the method to excite the test structure. Features such as: the choice of location of the impact and response accelerometers on the test structure, sampling frequency, and mounting of the accelerometers are discussed in this chapter. The design and construction of both an impact hammer and low-pass filter are also described. The chapter concludes by discussing the ensemble averaging technique for calculating both the frequency and impulse response functions.

Chapter F, Discussion of Results.
The final chapter presents the comparison of the modal parameters and response functions; for the theoretical finite element model, the experimental results and the identified results. The correlation of the data is then presented and discussed.

Chapter B.

Non-Invasive Detection Methods for the Diagnosis of Osteoporosis.

B. Non-Invasive Detection Methods for the Diagnosis of Osteoporosis.

The purpose of this chapter is to provide the reader with information concerning osteoporosis, discussing various detection and diagnostic techniques. An attempt has been made to present the information in a logical sequence throughout this chapter. Figure B-1 is included to aid in this respect.

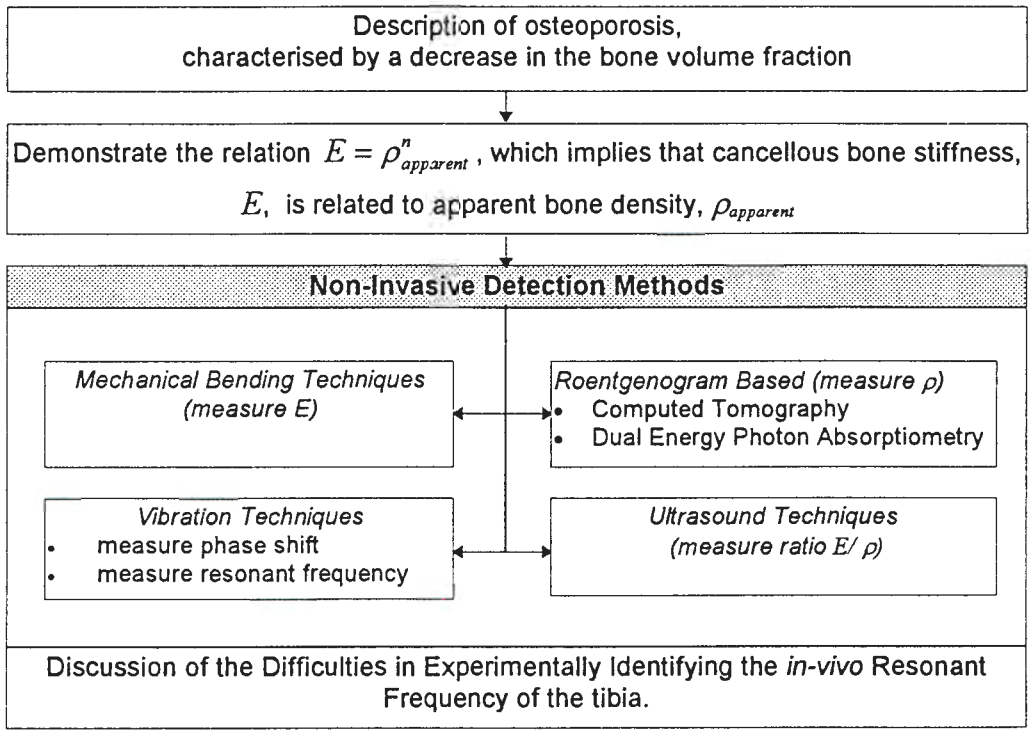

Figure B-1 Organisation of Chapter B.

B.1 Clinical Description of Osteoporosis.

Osteoporosis is clinically characterised by a decrease in bone mass caused by either decreased bone formation or an increase in bone resorption, or both. In osteoporosis the volume fraction of bone present in an unit volume specimen decreases.

B.2 Dependence of the Mechanical Properties of Cancellous Bone on Bone Density.

There are opposing opinions in the literature on whether the stiffness of cancellous bone, E, varies linearly, $n=1$, or according to a power relationship, $n>1$, with apparent bone density, $\rho_{apparent}$.

$$E \propto \rho_{apparent}^{n} \qquad \textbf{(B-1)}$$

Apparent bone density is the product of the material density that makes up the individual trabeculae ,ρ_{tissue} , and the volume fraction, $V_{fraction}$,of the bone present in the bulk specimen

$$\rho_{apparent} = \rho_{tissue} V_{fraction} \qquad \textbf{(B-2)}$$

The volume fraction ranges typically from 0.05 for porous cancellous bone to 0.60 for dense cancellous bone. The wet tissue density of human trabeculae bone is fairly constant in the approximate range of 1.6 $\rightarrow$ 2.0 g/cm^3 . Hence from equation B-2 the wet apparent bone density is in the range 0.08 $\rightarrow$ 1.2 g/cm^3 . *Galante (1970), Kuhn et al (1990)* and *Schoenfeld et al. (1974) Linde et al. (1989)*

Galante et al (1970) reported a linear relationship, i.e. $n=1$, between the stiffness of cancellous bone and the apparent bone density. More recent studies by *Ashman et al (1988) & (1989)* confirmed this linear relationship.

However, *Carter and Hayes (1977), Turner et al. (1990)* and *Rice et al.(1988)* reported that the stiffness of cancellous bone was proportional to the square of the apparent bone density, i.e. $n=2$ in equation (B-1). Other research groups obtained similar power relationships between the stiffness of cancellous bone and the apparent bone density. For example: *Currey (1986)* found an optimum fit using a power coefficient of $n= 1.62$. As summarised by *Turner,* power relationships fit the data better throughout the physiological range, while the linear relationship better describes the data over limited ranges within the physiological range.

While the exact formulation of the relationship between the stiffness of cancellous bone and the apparent bone density is disputed, there is undoubtedly a relationship. The discrepancy in the relationship may be due to the large potential range of apparent bone density, which is influenced by the choice of harvest site within the bone from which the bone samples were extracted. Many non-invasive detection methods for the diagnosis of osteoporosis measure the stiffness of bone and hence infer the apparent bone density from the equation (B-1). From this discussion it should be appreciated that these diagnosis methods are valid.

B.3 Non-Invasive Bone Density Measurement Techniques.

Four, non-invasive detection techniques are discussed. Roentgenogram-based techniques measure the apparent bone density directly, while the other three techniques rely on the relationship that exists between apparent bone density and the stiffness of cancellous bone.

B.3.1 Roentgenogram based Measurement Techniques.

The most characteristic feature of osteoporosis is a decreased radiographic density in the standard roentgenogram. The radiographic density, however, may vary by up to 30% because of variations in several factors associated with film development, patient mass or the amount of x-ray exposure. Also the resolution of a standard roentgenogram is insufficient to yield precise measurements of bone density. For these reasons the standard roentgenogram is not used to measure apparent bone density. *Peck (1987)*

More sophisticated roentgenogram methods for assessing skeletal density are available and include:

- *computed tomography*, (CT), is applicable to the vertebrae;
- *single energy photon absorptiometry*, is applicable to the appendicular skeleton and
- *dual energy photon absorptiometry,* applicable to the spine and hip.

- *Computed tomography* is a visual diagnostic tool. Both anatomical geometry and density can be simultaneously recorded. This feature allows three-dimensional, spatial models of the human anatomy to be studied, as reported by *Marom & Linden (1990).* Two research groups, *Bentzen et al (1987) and Hvid et al (1989)* , investigated the relationship between radiographic density, as measured by the CT, and the tested mechanical properties of tibia trabecular bone. Both research groups reported correlation factors in excess of 0.8, and concluded that the CT could accurately assess the apparent bone density.

- *Dual energy photon absorptiometry*, allows measurement of bone density in the lumbar spine, hip, or total body with reasonable precision (2 to 4% for local areas and 1 to 2% for skeleton). Radiation exposure of the patient is extremely low, (5 to 10 mrem), as compared to a standard chest roentgenogram (60 to 100 mrem). The total bone mineral in the scan path is measured, including all components of the vertebrae or hip, and any vascular calcification or degenerative changes in the bone that may be present. Results are therefore less reliable in individuals 75 years of age or older, where vascular calcification would be anticipated. *Peck (1987)*

The *dual energy photon absorptiometry* technique is currently the accepted method for the measurement of apparent bone density and hence the diagnosis of osteoporosis.

B.3.2 Ultrasound Techniques.

The longitudinal velocity of an ultrasonic wave in a material is proportional to the mechanical properties E and ρ. Any changes in these structural parameters will directly affect the ultrasound velocity, υ, as given by equation (B-3).

$$\upsilon = \sqrt{\frac{E}{\rho}} \qquad \textbf{(B-3)}$$

This relationship was used by *Ashman et al (1988) & (1989)* to determine the elastic modulus of cancellous bone from the proximal tibia. As cylindrical cancellous bone samples were required, this technique could only be conducted on bone samples from cadavers. Thus, the ultrasound technique has not being utilised for the *in-vivo* determination of the apparent bone density.

B.3.3 Mechanical Bending Techniques.

Bone stiffness may be determined by measuring the deflection or displacement of the bone resulting from a known applied load.

The mechanical bending technique is widely used to assess the stiffness of a healing fracture. As reported by *Cunningham et al (1990)* and *Richards (1987)* the stiffness of the fracture and hence bone increases as the fracture heals. The technique is feasible as the deflection monitoring equipment may be mounted on the external fixators. Although attachment to internal fixators is possible, there is a risk of infection entering via the percutaneous leads.

Thus the mechanical bending technique is rather impractical for generalised measurement of bone stiffness.

B.3.4 Vibration Techniques.

Vibration techniques have been used to determine the mechanical properties of bone both *in-vitro Doherty et al (1974)* and *in-vivo Thompson et al (1976).* It has also been proposed that this method is sensitive enough to detect changes in apparent bone density and stiffness evidenced with osteoporosis. *Jurist. (1970), Steele et al (1988) & Stussi et al (1988).*

In general two categories of vibration techniques are reported in the literature.

- The first category measures the stress-wave velocity or associated phase shift of an imposed shock load to the tibia. The stress-wave velocity or associated phase shift may then be used as the criteria for the diagnosis of osteoporosis.

- The second category performs modal analysis on the vibration response of the tibia. The extracted resonant frequencies or modal damping coefficients may then be used as the criteria for the diagnosis of osteoporosis.

Category One: Measurement of stress-wave velocity or associated phase shift.

1. *Pelker and Saha (1983)* considered the travelling wave characteristics of a single compressive pulse in both embalmed and fresh tibia cadaver specimens. For each of the two specimens the compressive pulse was generated by the impact of a steel ball bearing on the proximal end. The resultant stress wave was monitored by two semiconductor strain gauges, mechanically bonded to the bone.

   Characteristics such as the stress-wave velocity, attenuation coefficient and the dispersion coefficient of the stress wave were correlated to the bone density, volume fraction and cross-sectional area of the respective specimens. The results indicated a strong correlation between the volume fraction and the attenuation coefficient. Thus it could be feasible to deduce the volume fraction of the bone from the measured attenuation coefficient.

   However the *in vivo* application of this technique seems impractical. The use of strain gauges bonded to the bone is unacceptable and the delivery of a compressive pulse to the proximal tibia is also difficult.

2. In a theoretical paper presented by *Chen and Saha (1987),* the human femur was modelled as a axisymmetric fluid filled shell, as studied by *Love (1927).* The propagation characteristics of a stress wave were then analysed using this model.

   Chen and Saha utilised data samples from a study by *Martin and Atkinson (1977)* of human femurs of varying age and sex. Applying this data to their theoretical model, they made the following observations.
   - Both the phase velocity[1] and group velocity[1] were different for the age groups above and below 55 years, which could reflect the onset of senile osteoporosis.
   - For the same age groups, these velocities were also different for males and females, which correctly reflects their differing skeletal status.

   These results are reproduced in figure B-2

[1]The transfer of information requires a wave pulse, which can be thought of a superposition of sinusoidal waves. If the individual waves all have the same wave speed, the pulse is transmitted without change at a common **phase velocity**. The wave is dispersionless. However, if the individual waves have different wave speeds, then dispersion occurs and the pulse changes shape as it travels. The pulse then travels at the **group velocity**.

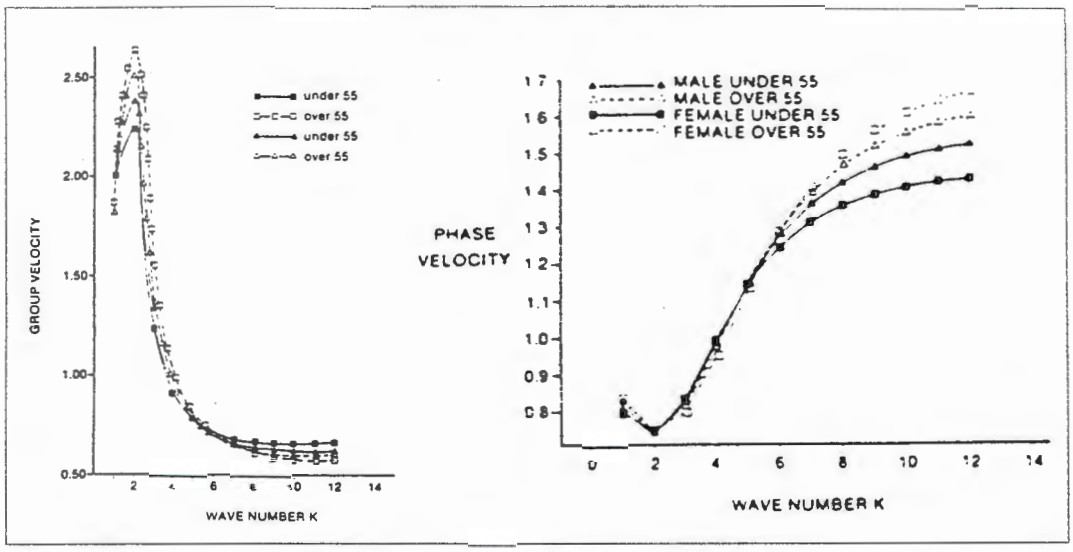

Figure B-2. Theoretical predictions for the phase velocity of the human femoral shaft. Notice especially the differing velocity between the respective sex and age groups

A limitation of the mathematical model is that it assumes the bone to be of constant cross-section and uniform thickness, which is not the case. A further limitation of the model is the omission of shear deformation in the analysis. Notwithstanding the theoretical limitations of the model, the observations made by *Chen and Saha* demonstrate how the stress-wave velocity may be used to diagnose osteoporosis.

3. *Fah and Stussi (1988)* proposed a technique to measure the phase velocity of the fundamental flexural mode in the human tibia. An *in-vivo* study was performed with 43 subjects. An impulse was applied to the tibia at the height of the medial condyle, by means of an electromechanical hammer. The vibration response of the tibia was determined by two accelerometers mounted in an adapter to hold the distance between the accelerometers constant. This configuration enabled the phase difference of the propagating stress wave between the two accelerometers to be measured.

   Good correlation between the phase velocity and the bone density, was reported. In addition the reduction in bone density was predicted by a decrease in the phase velocity.

Category Two: Measurement of Resonant Frequency.

The frequency at which a simple structure will vibrate is proportional to the stiffness, length, density and support conditions. Changes in any of these parameters will affect the resonant frequencies of the structure. These relationships are stated in Table B-1

Table B-1 The series of natural frequencies of longitudinal and lateral vibration. The support conditions in both cases are free-free.

$$freq_n = \frac{n}{2L}\sqrt{\frac{E}{\rho}} \quad \text{Hz} \quad \text{(longitudinal vibration of a bar)}$$

$$freq_n = \frac{(B_n)^2}{2\pi}\sqrt{\frac{EI}{\rho AL^4}} \quad \text{Hz} \quad \text{(lateral vibration of beams)}$$

where $B_n = [4.730041 \quad 7.853205 \quad 10.995608 \quad 14.137165 \quad \ldots\ldots \quad B_N]$

and $n = 1$ to N

Generalising the statements of Table B-1, it is possible to rewrite these expressions as

$$freq_n L = \varphi_n \upsilon = \varphi_n \sqrt{\frac{E}{\rho}} \qquad \textbf{(B-4)}$$

where: φ_n is a vector function of the boundary conditions, geometry and mode of vibration.

Jurist (1970) measured the resonant frequency of the human ulna. A sinusoidal force was applied at the olecranon process of the ulna, while the response of the ulna was measured at the distal end, by means of an accelerometer. The frequency response function was obtained by scanning the frequency range and recording the response as a function of frequency, i.e. the steady-state frequency scan method.

Jurist experimentally determined the product of ulna resonant frequency and length as measured for 172 normal men and 222 women. Of the 222 women, 28 were previously diagnosed to be suffering from osteoporosis and 15 were previously diagnosed to be diabetic. Diabetic subjects were included as diabetes has been reported to be associated with a relatively high incidence of osteoporosis. Jurist reported that the reproducibility of determining the ratio $freq_n L$ was of the order $2 \rightarrow 3\%$.

The results of Jurist's study show that previously diagnosed women with osteoporosis exhibited $freq_n L$ values averaging $\approx 44\%$ less than those of age-matched controls, while diabetic women had $freq_n L$ values averaging $\approx 20\%$ less than those of age-matched controls. Jurist claims to have achieved a confidence level of 82% in the discrimination of women with osteoporosis from their age-matched normal controls, by measurement of their ulna $freq_n L$ ratio.

This study does not attempt to physically identify the values of Young's Modulus or density, but rather diagnose osteoporosis on the basis of a collected measurement database of the ulna $freq_n L$ ratio. Since the classic work of *Jurist (1970),* there has been further research on establishing the resonant frequency of human long bones. The research effort has concentrated on the tibia, rather than the ulna. The tibia offers advantages over the ulna, as the medial condylae and tibia tuberosity are subcutaneous. Also much of the medial surface of the tibia is subcutaneous which facilitates the placement of transducers along the length of the tibia.

Currently, the *in-vivo* studies utilise the impulse response method rather than the steady-state frequency scan method, to determine the resonant frequency. The impulse response method is less invasive to the patient, as the patient is not 'connected' to a mechanical shaker. Further, the impulse response technique has the advantage that the impact can be delivered along the length of the tibia. The impulse is typically applied to the bone by using an impact hammer.

B.4 Complexity in Experimentally Measuring the Tibia Natural Frequencies.

Whichever *in-vivo* vibration technique is chosen there are complexities outside the control of the investigator, which make the correct interpretation of the response signals difficult. Three of the major complicating factors will be discussed namely;

- the effect of the subcutaneous tissue,
- attached muscle and
- the effect of the fibula, on the vibration response of the tibia.

Other factors such as: the effect of the assumed modelling boundary conditions and effect of both the ankle and knee joints, on the resonant frequencies are reported to be insignificant. *Cornelissen et al. (1986)* , *Van der Perre et al. (1983)* and *Fah & Stussi (1988)*

B.4.1 The effect of the subcutaneous tissue.

Both the input force and response signal must travel through the subcutaneous tissue layer overlaying the tibia, graphically depicted in *figure B-3*. Various researchers have reported on the effect of the subcutaneous tissue on the vibration response of the tibia.

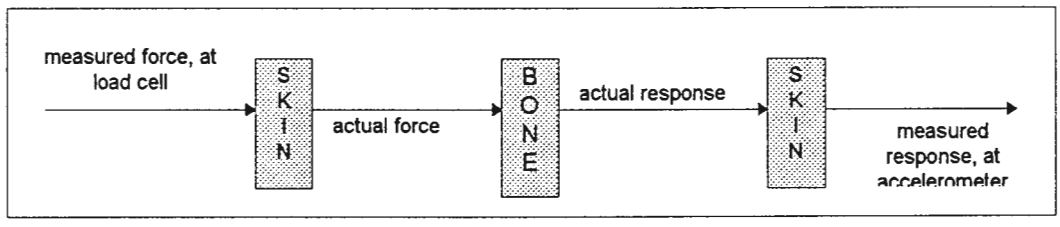

Figure B-3 Influence of the skin at the bone-transducer interface.

Saha and Lakes (1977) pointed out that the quantity of subcutaneous tissue overlaying the tibia influences the results of stress-wave propagation experiments. To overcome this *Sonstegard and Mattews (1976)* measured the vibration response directly on the bone using hypodermic needles. This procedure does eliminate the filtering effect of the subcutaneous tissue between the bone and transducer, but is invasive and thus undesirable

Cornelissen et al. (1986) considered the influence of the subcutaneous tissue and concluded that the effect was to shift the natural frequency up to 5%. Less noticeable effects were reported by *Van der Perre et al. (1983)*, as given in Table B-2, where the effect of removing the subcutaneous tissue shifted the natural frequency by ≈2%.

Table B-2 Damped natural frequency of a partially dissected tibia. Reproduced form *Van der Perre et al. (1983)*

	Specimen State					
Bending Mode	1	2	3	4	5	6
Single Bending I	264 Hz	267 Hz	314 Hz	-	320 Hz	318 Hz
Single Bending II	336 Hz	341 Hz	-	420 Hz	-	435 Hz
		≈2% change from specimen state #1	≈10% change from specimen state #1		≈15% change from specimen state #1	

	Explanation of the Specimen State
1	intact specimen, accelerometer held by hand
2	skin removed from the medial face of the tibia, accelerometer fixed using strain gauge glue
3	all muscles removed, but joint capsules of knee and ankle intact,
4	foot and ankle joint removed
5	knee joint removed, tibia and fibula with tibiofibular membrane
6	free tibia

Considering the impulse force, *Cornelissen et al.* concluded that the force measured by the load cell was not significantly different from the force that is actually applied to the bone through the subcutaneous tissue. This is in agreement with the theoretical models of the skin proposed by *Thompson et al (1976),* where the skin is modelled as a spring, and *Orne (1974),* where the skin is modelled as a spring-spring damper system.

However, the skin does influence the waveform of the impulse force. The duration of the impulse force is longer if subcutaneous tissue is present between the load cell and the tibia. This implies that the subcutaneous tissue limits the practical frequency range. (The reader is referred to a more complete discussion on this topic in section E.3)

Similarly the subcutaneous tissue alters the vibration response of the tibia. Applying a pre-load on the accelerometer reduces this effect, but causes a shift in the measured resonant frequencies.

B.4.2 The effect of attached muscle.

The effect of the attached muscle is to increase the damping ratio and mass effect of the dynamic system, as the muscles can be thought of as a viscous fluid dissipating energy. In fact, *Cornelissen et al. (1986)* demonstrated that if the tibia vibrates in the medio-lateral plane it would cause more muscle to vibrate, than if it were vibrating in the anterior-posterior plane.

In a study by *Van der Perre et al. (1983)* they demonstrated the effect of muscle was to reduce the resonant frequency by ≈10%, as shown in Table B-2.

B.4.3 Influence of the Fibula.

Cornelissen et al. (1986) reported that the effect of the fibula was to stiffen the tibia. When the fibula was removed the tibia's resonant frequencies decreased by 5 → 11%. *Van der Perre et al. (1983)* demonstrated similar effects measuring a ≈15% decrease in the resonant frequency, as shown in Table B-2.

Consider the cross-sectional properties for the tibia and fibula together and the tibia alone. The second moment of area in the medio-lateral direction increases by a factor of 10 for the case when the tibia and fibula are together. In the anterior-posterior direction the second moment of area almost remains the same for both configuations. Thus, it should be expected that the fibula would influence the medio-lateral vibrations more than the anterior-posterior vibration modes.

Chapter C.

Finite Element Modelling of the Test Structure.

C. Finite Element Modelling of the Test Structure.

This chapter is divided into four main sub-sections, as depicted in Figure C.1. The background information and insights gained in each of the sub-sections are presented in the proceeding sub-sections. In this way it is hoped that the reader will appreciate the motivation for the modelling choices taken.

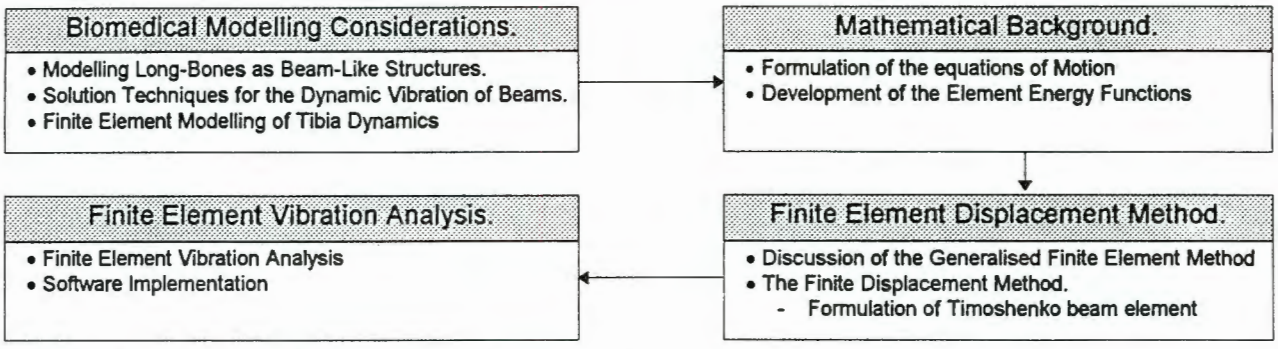

Figure C-1 Outline of the organisation of Chapter C

C.1 Biomedical Modelling Considerations.

C.1.1 Modelling Long-Bones as Beam-Like Structures.

Scientific interest in bone mechanics has a long tradition, *Galileo (1638)* and *Bourgery (1832)*. *Wolff (1870)* noticed the similarity between the orientation of cancellous bone in a human femur and the lines of principle stress predicted from simple beam theory. Later *Koch (1917)* published a comprehensive study of the femur in which the femur was modelled as a two-dimensional curved beam. In more recent studies by *Cowin et al (1985)* and *Huiskes (1982)* human long bones were modelled as three dimensional curved beam structures. Excellent correlation was demonstrated between the static experimental results and the three dimensional beam theory.

As general beam theory is applicable to the static loading of human long-bones. It is reasonable to assume that the dynamic behaviour of human long-bones would be successfully modelled as dynamic beam-like structures.

C.1.2 Solution Techniques for the Dynamic Vibration of Beams.

There are two distinct techniques for the solution of dynamic beam theory:

1. *closed-form* solutions, and
2. *numerical techniques*.

The choice of solution technique is generally prescribed by the complexity of the problem at hand. A brief description of each of the solution techniques are given below.

1. The *closed-form* solution of the set of coupled partial differential equations is generally only possible for simple support conditions and uniform material and geometric properties. The fundamental difficulty is the computational effort required to account for the varying geometric and material properties.
2. In general the *numerical techniques* satisfy the static constraints but do not explicitly satisfy all the dynamic restraints. Examples of numerical techniques are the Rayleigh-Ritz method and the finite element method, which is a generalisation of the Rayleigh-Ritz method.

Human long-bones, in particular the tibia, possess varying geometrical properties along their length. As an example the varying geometrical properties of the tibia are depicted in figure C-2.

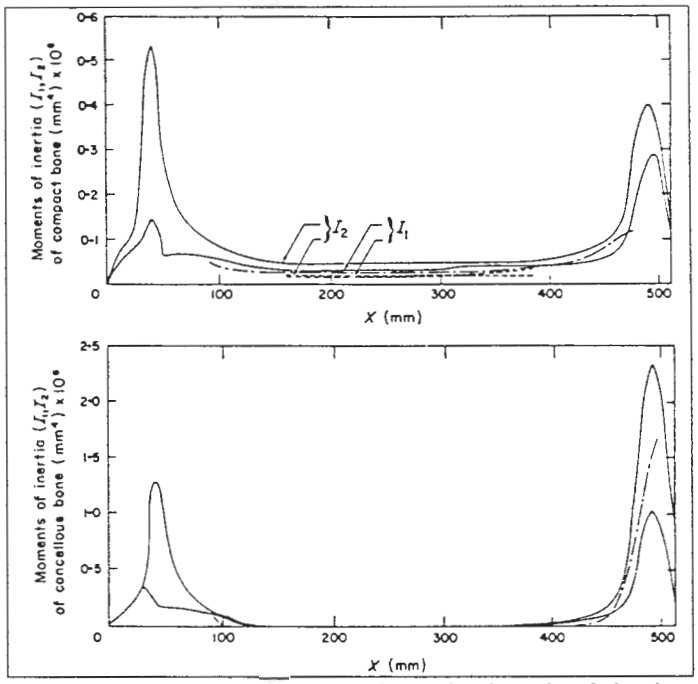

Figure C-2 Variation of the geometrical properties along the length of the human tibia. Reproduced from *Khalil et. al. (1981).*

It was considered that these geometrical variations could not be analytically described, which precluded the closed-form solution technique. Thus a numerical technique was adopted, in particular the finite element method was favoured.

C.1.3 Review of Literature: Dynamic Finite Element Modelling of the Tibia.

The published literature on the dynamic finite element modelling of the tibia may be separated into two categories, on the basis of which type of element is utilised. The first category of published literature utilises three-dimensional continuum elements, while the second category utilises two-dimensional beam elements.

To evaluate the accuracy of the respective categories is difficult as all reviewed researchers modified the bone material properties to optimise the correlation between the theoretical and experimental natural frequencies of the tibia. This obscures the performance of the finite element method.

Dynamic Finite Element Modelling of the Tibia, utilising *Continuum Elements.*

Hobatho et al (1991) performed modal analysis on a *dry* tibia. A commercially available finite element software package was used to model the tibia. The isotropic material properties initially used in the finite element model were extracted from the literature, but were subsequently optimised to ensure that the resonant frequencies predicted by the undamped finite element model were within 3% of the experimentally measured results.

Dynamic Finite Element Modelling of the Tibia, utilising *Beam Elements.*

This category may be sub-divided on the basis of the type of beam theory used, namely Euler-Bernoulli or Timoshenko beam theory. To make definitive decisions regarding the suitability of the type of beam theory, is once again difficult. As mentioned the difficulty is due to the optimisation of material properties implemented by the researchers. Thus any shortcoming of the chosen type of beam theory and / or geometry is compensated for by the material optimisation procedure.

This is well illustrated by *Collier et al(1982),* who modelling the tibia as a hollow Euler-Bernoulli beam, of constant triangular cross-section. Model / experimental correlation, within 5%, was obtained for flexural vibrations by allowing the value of Young's Modulus to vary with the direction of excitation. This demonstrates that although the beam theory and geometry were unrealistic, by optimising the material properties acceptable results may be achieved.

In general researchers utilised the Timoshenko beam theory in preference to the Euler-Bernoulli beam theory, while still implementing the material property optimisation. For slender beam-like structures the Euler-Bernoulli beam theory is acceptable. However for non-slender structures or structures where the shear effects or rotary inertia cannot be ignored, the Timoshenko beam theory should be used in preference. *Timoshenko (1955).* A selection of this published work is now presented:-

1. *Viano et al (1976)* proposed a non-uniform Timoshenko beam model of a human femoral shaft. The ratio for κ/J , the Timoshenko shear coefficient divided by the polar moment of area, and torsion rigidity were assumed constant. Both these parameters are a function of cross-section properties and hence are not uniform. *Viano et al* also do not include the effect of cancellous bone or bone marrow in their model formulation.

   Unknown material parameters were determined by matching the lowest undamped natural frequencies predicted by the model to the damped natural frequencies observed experimentally. Thus optimising the material parameters good correlation of the resonant frequencies was achieved.

2. *Hight et al (1980)* examined the significance of various modelling aspects in a Timoshenko beam element model of the tibia. The importance of modelling the tibia twist, axis of curvature and physical boundary conditions was considered. The analysis indicated that the assumed boundary conditions were most influential. The first natural frequency was reported to change by a factor of five from a fixed-fixed boundary condition to a free-fixed boundary condition. In contrast, the tibia twist and curvature were less significant, introducing errors of less than 5%. However the model predictions were not experimentally verified.

3. *Thomsen (1990)* modelled the tibia mathematically as a straight non-uniform Timoshenko beam structure. Each beam element, of constant cross-section, consisted of three materials: compact bone, cancellous bone and bone marrow. Both compact and cancellous bone were modelled as linearly elastic and transversely isotropic materials, while bone marrow was modelled as a perfectly flexible material.

   Thomsen considered the variation of both Timoshenko shear coefficient and the torsion rigidity. This approach is in contrast to other studies, notably *Viano et al (1976)* and *Khalil et al (1981)* where the Timoshenko shear coefficient, κ, was computed by assuming a constant value for κ/J along the bone axis.

The eigenvalue problem was solved and the material parameters in the model were determined by a Bayesian parameter estimation approach, thus optimising the correlation of the model to the experimentally determined undamped resonant frequencies.

Thomsen also considered the effect of modelling the tibia twist and curvature of the axis. The conclusion was that the effect of omitting the tibia shaft twist would alter the resonant frequencies by 0.5 → 1.5%. The omission in modelling the curvature of the axis was also considered insignificant, as the tibia centroid trajectory deviated from the straight neutral axis by less than 2% of the midshaft diameter.

From the reviewed literature the following requirements for the development of a finite element model of the tibia were conceived:

- Acceptable correlation may be achieved using two dimensional beam elements.
- The Timoshenko beam theory should be used in preference to the Euler-Bernoulli beam theory.
- The effect of tibia shaft twist and curvature may be neglected with minimum effect on the theoretically predicted frequencies.
- In general it is not possible to exactly define the material properties of cortical, cancellous bone or bone marrow, other than gross global values.

C.2 Mathematical Background.

C.2.1 Formulation of the Equations of Motion.

The analysis of all structural vibration problems rely on the correct formulation and satisfaction of the equations of motion. The equations of motion of any dynamic system may be derived using Newton's second law of motion, which states that *'the rate of change of momentum of a body is equal to the force acting upon it'*

For complex structures the vector addition of all of the forces acting at each mass point, is difficult. Vector addition may be overcome by first applying d'Alembert's Principle[#1] and then the Principle of Virtual Displacements[#2]. Although the Principle of Virtual Displacements overcomes the problem of vector addition of forces, virtual work is calculated from the dot product of two vectors, one representing a force and one a virtual displacement. This disadvantage may be overcome by using Hamilton's principle to determine the equations of motion.

Hamilton's principle, equation (C-1), is stated without proof or derivation, *Timoshenko (1955).*

$$\int_{t_1}^{t_2}\left[\delta(T-V)+\delta W_{NC}\right]dt=0 \qquad \textbf{(C-1)}$$

where δ is the virtual operator,
T is kinetic energy, V is potential energy, and
W_{NC} is the non-conservative work done

Hamilton's principle may be applied to both discrete multi-degree of freedom systems or continuous systems. The advantage of this principle is that only scalar energy quantities are required, although vector quantities may be required for the calculation of the work done by the non-conservative forces. The only type of potential energy, V, which is considered in this dissertation, is elastic potential energy or strain energy, U. Thus Hamilton's principle may be re-stated as

$$\int_{t_1}^{t_2}\left[\delta(T-U)+\delta W_{NC}\right]dt=0 \qquad \textbf{(C-2)}$$

When Hamilton's principle is applied to discrete systems it can be expressed in a more convenient form, the Lagrange equations.

$$\frac{d}{dt}\left(\frac{\partial T}{\partial \dot{q}_i}\right)+\frac{\partial D}{\partial \dot{q}_i}+\frac{\partial U}{\partial q_i}=u_{f_i}\ , \qquad i=1 \text{ to } m \qquad \textbf{(C-3)}$$

where q = displacement vector
u_f = externally applied excitation force

Expressions for the kinetic and strain energy are derived in **Appendix II-1**. The form of the dissipation energy, D, is derived and discussed in section C.4. Given overleaf is a summary of the derivation given in the Appendix.

[#1] d'Alembert's Principle. In essence it is the introduction of a fictitious force, referred to as an inertia force, of magnitude mq_{accel}, acting in the opposite direction to the direction of acceleration, q_{accel}. This allows an equation of dynamic equilibrium to be reformulated using concepts of static equilibrium.

[#2] Principle of Virtual Displacements. This principle states that *'if a system, which is in equilibrium under the action of a set of forces, is subjected to a virtual displacement, then the total work done by the forces will be zero'*

- **Strain energy** can be stated

$$U = \tfrac{1}{2} q^T K q \qquad \textbf{(C-4)}$$

Strain energy, U, is always positive or in the exceptional case of zero stiffness it is zero. The stiffness matrix, K, is thus a *real, symmetric* and *positive semi-definite matrix.*

- The **kinetic energy** may be formulated as

$$T = \tfrac{1}{2} \dot{q}^T M \dot{q} \qquad \textbf{(C-5)}$$

Since kinetic energy, T, cannot be negative the product $\dot{q}^T M \dot{q}$ can never be negative. Provided that there is not a degree of freedom possessing zero mass, or $\dot{q}$ is not a null vector, this implies that the kinetic energy will always be positive. Also implied is that M must be a *real positive definite symmetric* matrix.

The general equation of motion of a linear elastic system with fixed supports can now be stated, using Lagrange's equations of motion. If there are m degrees of freedom, M & K have order [m x m] and they are both real and symmetric matrices. To apply Lagrange's equations, it is convenient to express (C-4) and (C-5) in double summation format

$$T = \tfrac{1}{2} \sum_{j=1}^{m} \sum_{k=1}^{m} M_{jk} \dot{q}_j \dot{q}_k \qquad \textbf{(C-6)}$$

$$U = \tfrac{1}{2} \sum_{j=1}^{m} \sum_{k=1}^{m} K_{jk} q_j q_k \qquad \textbf{(C-7)}$$

then the equations of motion can be stated in terms of the mass, stiffness matrices and the vector of displacement responses, $\{ q \}$

$$\sum_{j=1}^{m} M_{ij} \ddot{q}_j + \sum_{j=1}^{m} K_{ir} q_j = Q_i \,, \qquad i = 1 \text{ to } m \qquad \textbf{(C-8)}$$

where the elements of the vector Q include all the non-conservative forces which cannot be represented by the potential energy U, and include both damping terms, $C\dot{q}$, and externally applied excitation forces, u_f. In matrix form, the well known formulation is

$$M\ddot{q} + Kq = Q = \left(u_f - C\dot{q}\right)$$
and
$$M\ddot{q} + C\dot{q} + Kq = u_f \qquad \textbf{(C-9)}$$

The form of the damping matrix, C, will be shown in section C-4.

C.2.2 Development of the Element Energy Functions.

In the previous chapter it was shown that the equations of motion of any structural system could be obtained from the kinetic ,potential and dissipation energy functions of the system. In this section, the specific element energy functions are derived for a Timoshenko beam element.

The details of the derivations are given in **Appendix II-2**. The completed derivations are presented below

Timoshenko Beam Element, for vibration in the plane *xy*	
$U_{bend.xy} = \frac{1}{2}\int_{x_1}^{x_2} EI_z\left(\frac{\partial\theta_z}{\partial x}\right)^2 dx + \frac{1}{2}\int_{x_1}^{x_2}\kappa AG\left(\frac{\partial v}{\partial x}-\theta_z\right)^2 dx$	**(C-10)**
$T_{bend.xy} = \frac{1}{2}\int_{x_1}^{x_2}\rho\, I_z\left(\dot{\theta}_z\right)^2 dx + \frac{1}{2}\int_{x_1}^{x_2}\rho A\dot{v}^2 dx$	**(C-11)**
$\delta W_{bend.xy} = \int_{x_1}^{x_2} p_y \delta v\, dx$	**(C-12)**
Timoshenko Beam Element, for vibration in the plane *xz*	
$U_{bend.xz} = \frac{1}{2}\int_{x_1}^{x_2} EI_y\left(\frac{\partial\theta_y}{\partial x}\right)^2 dx + \frac{1}{2}\int_{x_1}^{x_2}\kappa AG\left(\frac{\partial w}{\partial x}-\theta_y\right)^2 dx$	**(C-13)**
$T_{bend.xz} = \frac{1}{2}\int_{x_1}^{x_2}\rho\, I_y\left(\dot{\theta}_y\right)^2 dx + \frac{1}{2}\int_{x_1}^{x_2}\rho A\dot{w}^2 dx$	**(C-14)**
$\delta W_{bend.xz} = \int_{x_1}^{x_2} p_z \delta w\, dx$	**(C-15)**

C.3 *The Finite Element Displacement Method .*

C.3.1 Discussion of the Generalised Finite Element Method.

There are a number of numerical techniques for determining approximate solution to Hamilton's Principle. The Rayleigh-Ritz method is one such method. A generalisation of the Rayleigh-Ritz method, known as the finite element displacement method is utilised in this dissertation. As an introduction to the finite displacement method the Rayleigh-Ritz method is initially discussed.

C.3.1.1 The Rayleigh-Ritz method.

Hamilton's principle requires that equation (C-2) is satisfied, where the energy functions are represented by the equations (C-4) & (C-5). Since Hamilton's principle is derived using the principle of virtual displacements, then the solution $q(x,t)$ must satisfy both the geometric boundary conditions as well as Hamilton's principle. Conversely satisfaction of Hamilton's principle will ensure that both the equation of motion and the natural boundary conditions are satisfied.

Rayliegh-Ritz approximates the solution with a finite expansion of the form

$$q^n(x,t) = \sum_{i=1}^{n} \phi_i(x)\chi_i^n(t) \qquad \textbf{(C-16)}$$

where the $\chi_i^n(t)$ are unknown functions of time, t, and the $\phi_i(x)$ are prescribed functions of x, which are linearly independent. A set of functions are said to be linearly independent if

$$\sum_{i=1}^{n} \phi_i(x)\alpha_i = 0 \qquad \text{for all } x \qquad \textbf{(C-17)}$$

which implies that $\alpha_i = 0 \qquad \text{for } i = 1,2.....n \qquad \textbf{(C-18)}$

Each of the functions $\phi_i(x)$ must satisfy the geometric boundary conditions in order to ensure that the solution, as given by equation (C-2) satisfies this condition. A continuous deformable body, such as a beam , consists of an infinite number of material points, and therefore, it has infinitely many degrees of freedom. By assuming that the motion is given by equation (C-16), the continuous system has been reduced to a system with a finite number of degrees of freedom. This has been achieved by applying the constraints

$$\chi_{n+1}^n = \chi_{n+2}^n = ...0 \qquad \textbf{(C-19)}$$

Then expression equation (C-19) is substituted into equation (C-2) and the parameters $\chi_i^n(t)$ solved. Since the system has been reduced to one with finite degrees of freedom, then the application of Hamilton's Principle leads to the Lagrange's equations. In matrix form may be written as

$$M\left\{\frac{\partial^2 \chi^n}{\partial t^2}\right\} + C\left\{\frac{\partial \chi^n}{\partial t}\right\} + K\{\chi^n\} = \{Q^n\} \qquad \textbf{(C-20)}$$

Equation (C-20) can be solved for $\{\chi^n\}$, which when substituted into equation (C-16) will yield the approximate solution for $q(x,t)$.

If the integrals in Hamilton's equation, equation (C-2), involve derivatives up to order p, then the functions $\phi_i(x)$ must satisfy the following criteria in order to ensure convergence of the solution:

1. Be linearly independent.
2. Be continuous and have continuous derivatives up to order $(p\text{-}1)$.
3. Satisfy the geometric boundary , which involve derivatives up to order $(p\text{-}1)$
4. Form a complete series.

A series of functions is said to be complete if the 'mean square error' vanishes in the limit, that is

$$\lim_{n\to\infty}\int_0^L\left(q-\sum_{i=1}^{n}\phi_i(x)\chi_i^n(t)\right)^2 dx=0 \qquad \textbf{(C-27)}$$

Examples of complete series functions are: polynomials, Legendre polynomials, Tchebycheff polynomials, Jacobi polynomials or hypergeometric polynomials as well as trigonometric functions. Polynomials are the preferred prescribed functions utilised in the finite displacement method, as will be shown in the following section

C.3.1.2 Finite Displacement Method

When analysing either structures of complex shape or built-up structures, difficulties arise in constructing a set of prescribed functions which satisfy the geometric boundary conditions. The finite element displacement method provides an automatic procedure for constructing the approximate functions in the Rayleigh-Ritz method.

The prescribed shape functions are constructed in the following manner:

1. Select a set of reference or 'node' points on the structure
2. Associate with each node a given number of degrees of freedom (displacement, slope, etc.)
3. Construct a set of functions such that each one gives a unit value for one degree of freedom and zero for all others.

In order to satisfy the convergence criteria of the Rayleigh-Ritz method, the shape functions should satisfy the following criteria:

1. Be linearly independent.
2. Be continuous and have continuous derivatives up to order $(p\text{-}1)$ both within the element and across element boundaries.
3. Polynomial shape functions must be complete polynomials of at least degree p. If any terms of greater degree than p are used, they need not be complete.
4. Satisfy the geometric boundary conditions.

In the Rayleigh-Ritz method, convergence is obtained as the number of prescribed functions is increased. To increase the number of prescribed functions in the finite element method, the number of node points and therefore the number of elements, is increased. An alternative strategy, which is utilised in this dissertation, is to increase the number of nodes and hence the number of prescribed functions of each element.

C.3.2 Finite Element Model of the Timoshenko Beam Element.

C.3.2.1 Literature Review: Methods of Modelling Timoshenko Beam elements.

A number of Timoshenko beam elements have been proposed in the literature. The various elements can be divided into two classes, namely simple and complex.

- A *simple* element formulation, for unidirectional bending in the principle plane, has a total of four degrees of freedom, two at each of the two boundary nodes.
- The *complex* element formulation is an element with more than two degrees of freedom at a node or more than two nodes in the element.

A summary of the different published elements are listed in Table C.1

Table C.1 Examples of both the simple and complex Timoshenko beam element formulations
(v, is the transverse displacement and Θ, rotation of the cross-section and ψ is the shear deformation)

	Reference	Number of Nodes	dofs	Order of Shape Function	Description of Degree of Freedom
simple	*Davis et al (1972)*	2 ends	4	cubic function for v quadratic function for Θ	v, Θ
	Nickell & Secor (1972) *Severn (1970)*	2 ends	4	cubic function for v quadratic function for dv/dx	v, dv/dx
complex	*Dawe (1978)*	3 end & centre	6	quintic function for v quartic function for Θ	v, Θ
	Thomas et al (1973)	2 ends	6	cubic function for v cubic function for Θ linear variation ψ	v, Θ & ψ
	Nickell & Secor (1972)	3 end & centre	7	cubic function for v quartic for Θ	v, dv/dx, Θ at end nodes and Θ at middle node
	Kapur (1966)	2 ends	8	cubic function for v_b cubic function for v_s	v_b , dv_b/dx v_s , dv_s/dx
	Carnegie et al (1969)	4 end & thirds	8	cubic function for v cubic function for Θ	v, Θ

The correct nodal degrees of freedom are the transverse displacement, v, and the cross-section rotation, Θ. Some authors have used dv/dx in place of Θ; however this does not allow the correct representation of the clamped boundary condition or provide the correct coupling of adjacent elements in general cases. These element formulations were discounted.

Table C.2 provides a comparison of the relative accuracy of the remaining element formulations.

Table C.2 Comparison of the relative accuracy of various element formulations.(slenderness ratio = 0.08)

Element Formulation	Error in the Prediction of 1st Resonant Mode	Error in the Prediction of 2nd Resonant Mode
Davis et al (1972)	1.16 %	71.54%
Carnegie et al (1969)	< 0.2 %	18.2 %
Dawe (1978)	< 1 %	< 2 %

From the table, the element formulation proposed by *Dawe (1978)* clearly is the most accurate. Although the accuracy of the *Carnegie et al (1969)* element is not as accurate in predicting the 2^{nd} resonant mode, the convergence is very rapid. However, a disadvantage with the element proposed by *Carnegie et al* is that the magnitude of the element stiffness matrix increases as $\kappa \rightarrow 0$ and a slender beam element formulation is not obtained when $\kappa = 0$.

The element formulation proposed by *Dawe (1978)* was adopted, as it processes the correct nodal degrees of freedom and is highly accurate compared to the reviewed element formulations.

C.3.2.2 Shape Function Formulation.

Consider an infinitesimal length, δx, of a uniform beam element vibration with circular frequency, ω, in dynamic equilibrium under the action of the shear force, bending moment, inertia force and inertial couple, as depicted in *figure C-3*

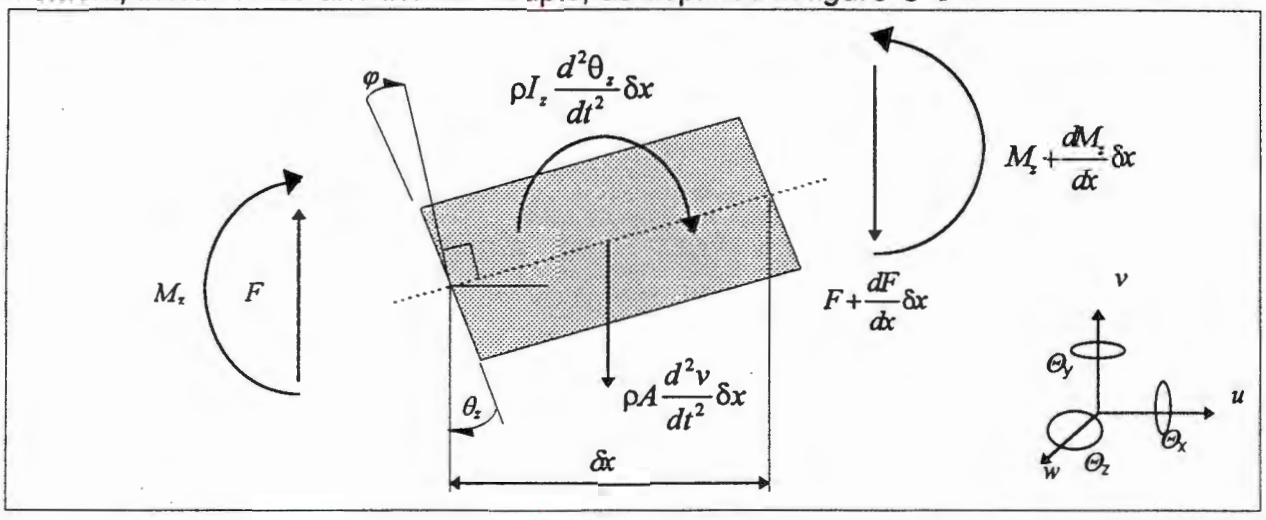

figure C-3 Equilibrium of an Infinitesimal length of beam.

Then from Timoshenko beam theory, the element is governed by the following set of equations. *Timoshenko (1955)*

Dynamic Equilibrium Equations

$$\frac{dF}{dx} = \rho A v \omega^2 \qquad \textbf{(C-23)}$$

$$\frac{dM_z}{dx} - F = -\rho I_z \theta_z \omega^2 \qquad \textbf{(C-24)}$$

Moment-Curvature Relations

$$\frac{d\theta_z}{dx} = \frac{M_z}{EI_z} \qquad \textbf{(C-25)}$$

Shear Force-Shear Deformation Relations

$$F = \kappa AG\varphi \qquad \textbf{(C-26)}$$

Compatibility relation linking the geometric deformations

$$\theta_z = \frac{dv}{dx} + \varphi \qquad \textbf{(C-27)}$$

Normally in applying the finite element displacement method only the elasticity and compatibility relations are explicitly satisfied within an element. Equations (C-25) to (C-27) are explicitly satisfied, while both equations (C-23) and (C-24) are modified. The form of the modified equations are given below

$$\frac{dF}{dx} = 0 \qquad \textbf{(C-28)}$$

$$\frac{dM_z}{dx} - F = 0 \qquad \textbf{(C-29)}$$

This results in an element with constant shear force along its length, linear variation of bending moment, quadratic variation of cross-sectional rotation and cubic variation of transverse displacement. The element model derivation is thus based on explicit satisfaction of equation (C-28) and an approximation to equation (C-29). Combining equations (C-25) to (C-27) and equation (C-28) leads to equation (C-30)

$$EI_z \frac{d^2\theta_z}{dx^2} = \kappa AG\left(\theta_z - \frac{dv}{dx}\right) \qquad \textbf{(C-30)}$$

This procedure implies that the rotary inertia term is ignored in the moment equilibrium equation within the element, but the effect of rotary inertia will be included in "lumped" form at the nodes.

Assume that the deflection, v, and beam slope, θ_z, vary along the length of the beam, as described by *Dawe (1978)*

$$v = a_1 + a_2\zeta + a_3\zeta^2 + a_4\zeta^3 + a_5\zeta^4 + a_6\zeta^5 \qquad \textbf{(C-31)}$$

$$\theta_z = b_1 + b_2\zeta + b_3\zeta^2 + b_4\zeta^3 + b_5\zeta^4 \qquad \textbf{(C-32)}$$

It may be shown that of the eleven coefficients only six are independent, when the assumed functions are substituted into the equilibrium equation (C-30). The complete derivation of the shape functions are presented in **Appendix II-3**.

The relationship of the displacement and slope of the beam to the shape functions are given as equations (C-33) & (C-34) respectively.[#3]

$$\theta_z = \begin{bmatrix}\Gamma_1 & \Gamma_2 & \Gamma_3 & \Gamma_4 & \Gamma_5 & \Gamma_6\end{bmatrix} \begin{bmatrix} v_1 \\ \theta_{z_1} \\ v_2 \\ \theta_{z_2} \\ v_3 \\ \theta_{z_3} \end{bmatrix} \quad \text{or more generally as } \theta_z = \Gamma \eta_{elmt} \qquad \textbf{(C-33)}$$

The corresponding shape functions are plotted in figure C-4a .

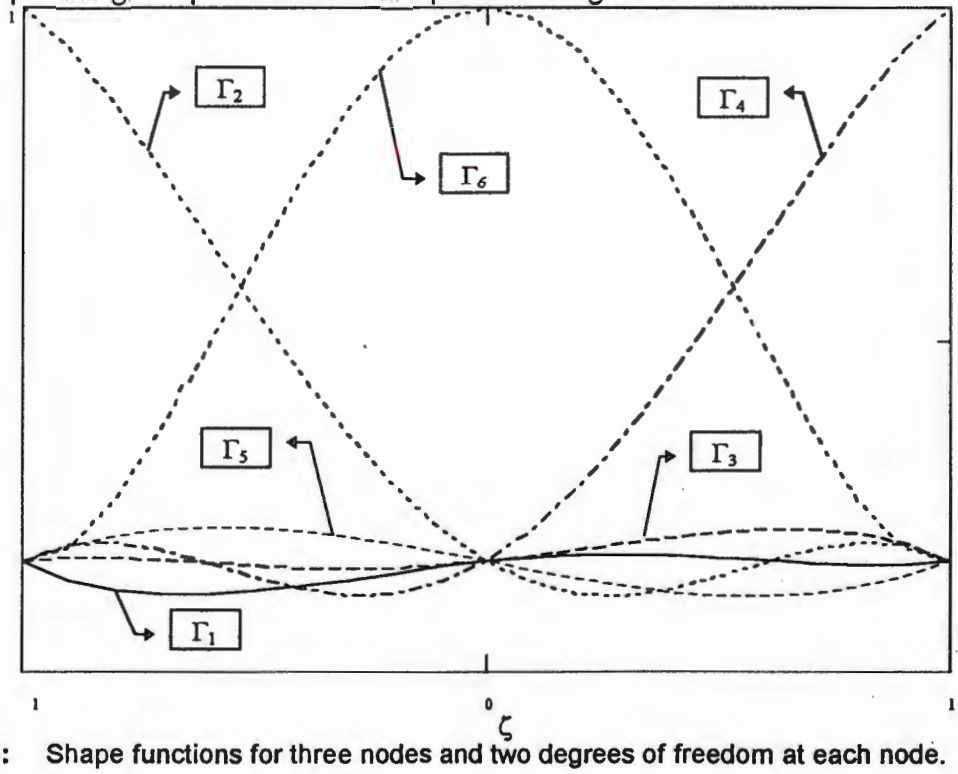

Figure C-4a: Shape functions for three nodes and two degrees of freedom at each node.

[#3] Note that only the bending in the xy plane is considered here, but the equations for vibration in the xz plane may be written if w is substituted for v and θ_y is substituted for θ_z. This substitution is possible as the shape functions for both planes of vibration are identical.

$$v = \begin{bmatrix} \Lambda_1 & \Lambda_2 & \Lambda_3 & \Lambda_4 & \Lambda_5 & \Lambda_6 \end{bmatrix} \begin{bmatrix} v_1 \\ \theta_{z1} \\ v_2 \\ \theta_{z2} \\ v_3 \\ \theta_{z3} \end{bmatrix} \quad \text{or more generally} \quad v = \Lambda \eta_{elnt} \qquad \textbf{(C-34)}$$

The corresponding shape functions are plotted in figure C-4b.

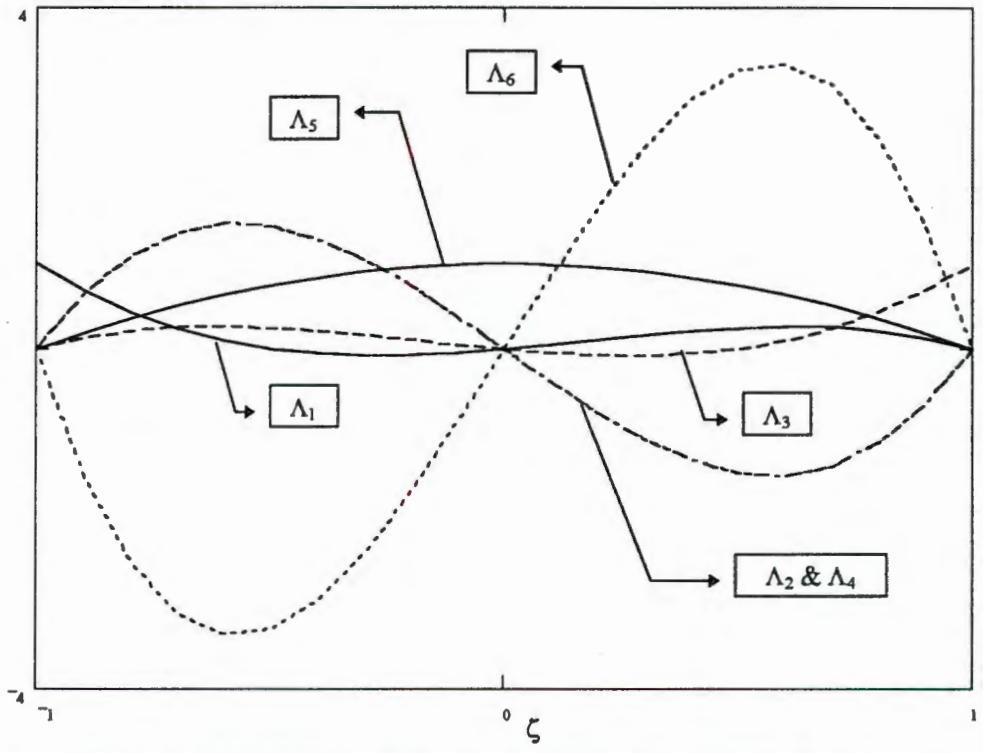

Figure C-4b: Shape functions for three nodes and two degrees of freedom at each node.

C.3.2.3 Formulation of the Stiffness and Mass matrices.

The appropriate form of the strain and kinetic energy, for vibration in the *xy* plane, were developed in **Appendix II-2** and restated as equations (C-10) and (C-11) respectively. It was also shown in **Appendix II-1** how the strain energy is related to the stiffness matrix and also how the kinetic energy relates to the mass matrix, see equations (C-4) and (C-5). It is this dual definition that will now be exploited to derive the expression for stiffness and mass matrices. A typical element is depicted in figure C-5

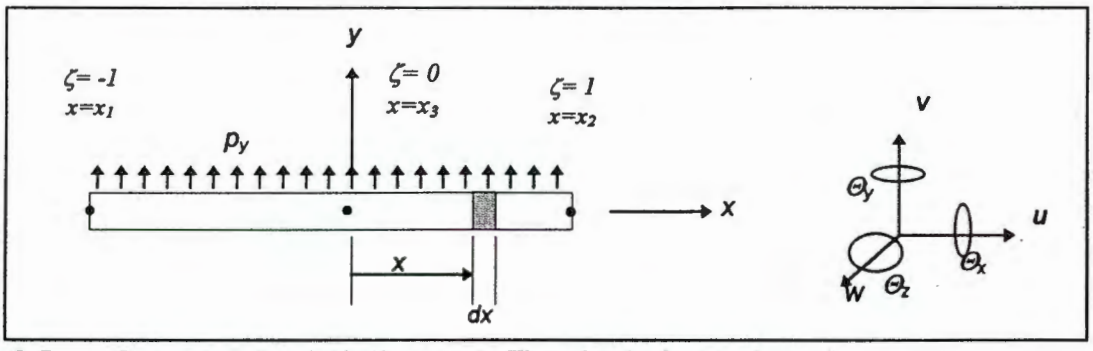

Figure C-5 Geometry of a single three node Timoshenko beam element

It should be appreciated that both strain and kinetic energy are expressed in the global "length" variable x, where as the finite element operates on single local element axis, as shown in figure C-5. Thus a transformation of co-ordinates must be implemented. The transform is given by

$$x = \frac{(1-\zeta)}{2}x_1 + \frac{(1+\zeta)}{2}x_3 \qquad \textbf{(C-35)}$$

and hence the derivative by

$$\frac{dx}{d\zeta} = \frac{L_{elmt}}{2} = J \qquad \textbf{(C-36)}$$

where J is the Jacobian

- The **stiffness element matrix** can be derived from the strain energy expression, equation (C-10). Restating in terms of the local co-ordinate frame

$$U_{bend.xy} = \tfrac{1}{2}\int_{-1}^{1} EI_z\left(\frac{\partial\theta_z}{\partial\zeta}\frac{\partial\zeta}{\partial x}\right)^2 J d\zeta + \tfrac{1}{2}\int_{-1}^{1}\kappa AG\left(\frac{\partial v}{\partial\zeta}\frac{\partial\zeta}{\partial x} - \theta_z\right)^2 J d\zeta \qquad \textbf{(C-37)}$$

and then substituting the shape function representation for the displacement and slope respectively

$$\begin{aligned} U_{bend.xy} = \tfrac{1}{2}\int_{-1}^{1} EI_z\left(\frac{\partial\Gamma}{\partial\zeta}\eta_{elmt}\right)^T\left(\frac{\partial\Gamma}{\partial\zeta}\eta_{elmt}\right)\frac{J}{J^2}d\zeta + \\ \tfrac{1}{2}\int_{-1}^{1}\kappa AG\left(\frac{\partial\Lambda}{\partial\zeta}\frac{1}{J}\eta_{elmt} - \Gamma\eta_{elmt}\right)^T\left(\frac{\partial\Lambda}{\partial\zeta}\frac{1}{J}\eta_{elmt} - \Gamma\eta_{elmt}\right)Jd\zeta \end{aligned} \qquad \textbf{(C-38)}$$

Collecting terms

$$U_{bend.xy} = \tfrac{1}{2}(\eta_{elmt})^T\left[\int_{-1}^{1} EI_z\left(\frac{\partial\Gamma}{\partial\zeta}\right)^T\left(\frac{\partial\Gamma}{\partial\zeta}\right)\frac{J}{J^2}d\zeta + \int_{-1}^{1}\kappa AG\left(\frac{\partial\Lambda}{\partial\zeta}\frac{1}{J} - \Gamma\right)^T\left(\frac{\partial\Lambda}{\partial\zeta}\frac{1}{J} - \Gamma\right)Jd\zeta\right]\eta_{elmt} \qquad \textbf{(C-39)}$$

the stiffness matrix can extracted, on comparison of equations (C-4) and (C-39)

$$\boxed{K_{bend.xy_{elmt}} = \int_{-1}^{1} EI_z\left(\frac{\partial\Gamma}{\partial\zeta}\right)^T\left(\frac{\partial\Gamma}{\partial\zeta}\right)\frac{J}{J^2}d\zeta + \int_{-1}^{1}\kappa AG\left(\frac{\partial\Lambda}{\partial\zeta}\frac{1}{J} - \Gamma\right)^T\left(\frac{\partial\Lambda}{\partial\zeta}\frac{1}{J} - \Gamma\right)Jd\zeta} \qquad \textbf{(C-40)}$$

The formulation of the bending in the xz plane follows an identical formulation and thus is not repeated, but merely stated without derivation as

$$\boxed{K_{bend.xz_{elmt}} = \int_{-1}^{1} EI_y\left(\frac{\partial\Gamma}{\partial\zeta}\right)^T\left(\frac{\partial\Gamma}{\partial\zeta}\right)\frac{J}{J^2}d\zeta + \int_{-1}^{1}\kappa AG\left(\frac{\partial\Lambda}{\partial\zeta}\frac{1}{J} - \Gamma\right)^T\left(\frac{\partial\Lambda}{\partial\zeta}\frac{1}{J} - \Gamma\right)Jd\zeta} \qquad \textbf{(C-41)}$$

- Similarly the **mass element matrix** can be derived from the kinetic energy expression. Restating equation (C-11) in terms of the local co-ordinate frame and shape function formulations

$$T_{bend\,xy} = \tfrac{1}{2}(\dot{\eta}_{elmt})^{T}\left[\int_{-1}^{1}\rho\, I_z(\Lambda^T\Lambda)J d\zeta + \int_{-1}^{1}\rho\, A(\Gamma^T\Gamma)J d\zeta\right](\dot{\eta}_{elmt}) \qquad \textbf{(C-42)}$$

The mass matrix can be extracted, on comparison of equations (C-5) and (C-42)

$$\boxed{M_{bend\,xy_{elmt}} = \int_{x_1}^{x_2}\rho\, I_z(\Gamma^T\Gamma)\, J\, d\zeta + \int_{x_1}^{x_2}\rho\, A(\Lambda^T\Lambda)\, J\, d\zeta} \qquad \textbf{(C-43)}$$

The formulation of the bending in the *xz* plane follows an identical formulation and thus is not repeated, but merely stated without derivation as

$$\boxed{M_{bend\,xz_{elmt}} = \int_{-1}^{1}\rho\, I_x(\Gamma^T\Gamma)\, J\, d\zeta + \int_{-1}^{1}\rho\, A(\Lambda^T\Lambda)\, J\, d\zeta} \qquad \textbf{(C-44)}$$

The Gauss-Legendre numerical integration technique was employed to compute the respective stiffness and mass matrices, i.e. the numerical evaluation of equations (C-40), (C-41), (C-42) and (C-43). A description of the Gauss-Legendre numerical integration technique and the subsequent software implementation are discussed in **Appendix II-4.**

The assembly procedure of respective stiffness and mass matrices into the global stiffness and mass matrices, which describe the finite element model of the entire structure, is described in **Appendix II-5.** The global stiffness and mass matrices are assembled from the individual contribution of each element within the finite element model of the structure being analysed.

C.4 Finite Element Vibration Analysis.

The purpose of this section is to develop expressions for both the frequency and impulse response functions. These response functions may be solved by two possible theoretical techniques, namely the *modal analysis* or the *state-space solution* technique. The modal analysis technique was implemented in preference to the state-space technique, due to the computational simplicity. The modal analysis technique, unlike the state-space technique, takes advantage of the characteristics of both the mass and stiffness matrices i.e. symmetric and either semi-positive or positive definite.

C.4.1 Modal Analysis Solution Technique.

The modal analysis technique commences by solving the complementary portion of the solution to the classical second-order differential equation. The complementary solution predicts the undamped natural frequencies and mode shapes. The variable basis of the differential equation is then transformed, using the eigenvectors of the complementary solution. This permits the second order differential equation to be de-coupled into a system of first-order differential equations. Due to the symmetry of the resulting first-order differential equations the solution is trivial. The inverse of the variable basis is then applied to the modal solution thereby transforming the modal solution back into the physical domain.

The modal analysis technique is limited to applications where the matrices describing the second-order differential equation are symmetric and either semi-positive or positive definite. This limitation is of significance as this limits the type of damping which may be modelled using this solution technique. The implementation of the modal analysis solution technique is described in the following section.

- Consider the coupled second-order linear differential equation, of the form derived in section C.1

$$M\ddot{q} + C\dot{q} + Kq = u_f(t) \qquad \textbf{(C-45)}$$

where $q(t)$ is the displacement vector, of dimension [m] , and
$u_f(t)$ is the input force vector

- Consider now the undamped natural frequencies of the conservative system

$$M\ddot{q} + Kq = 0 \qquad \textbf{(C-46)}$$

where M and K are both real, symmetric matrices.

Let the free-vibration solution be

$$q(t) = \Phi e^{j\omega_{nat}t} \qquad \textbf{(C-47)}$$

where Φ are the eigenvectors, and
ω_{nat} are the eigenvalues and undamped natural frequencies

then, on substituting $q(t)$ into equation (C-46),

$$\left[-\omega_{nat}^2 M + K\right]\Phi = 0 \qquad \textbf{(C-48)}$$

pre-multiplying by M^{-1}, results in

$$\boxed{\left(M^{-1}K\right)\Phi = \Phi\omega_{nat_i}^2} \qquad \textbf{(C-49)}$$

This is the standard eigenvalue problem.

It can be shown that if M is positive definite, then $M^{-1}K$ has only real eigenvalues, either positive or zero, and an independent set of eigenvectors. Also, the eigenvectors form an orthogonal basis.

As the scaling of the eigenvectors is arbitrary i.e. a scalar multiple of the original eigenvector basis is also a solution of equation (C-48). It is convenient to choose this multiplier in such a way that Φ has some desirable property. For example,

$$\Phi^{\mathrm{T}} M \Phi = I \qquad \textbf{(C-50)}$$

The eigenvectors are then *mass normalised*. Manipulating equation (C-49) into the form

$$\Phi^{\mathrm{T}} K \Phi = \left(\Phi^{\mathrm{T}} M \Phi\right) \omega_{nat_i}^2 \qquad \textbf{(C-51)}$$

and substituting the *mass normalised* eigenvectors, equation (C-50), results in

$$\boxed{\Phi^{\mathrm{T}} K \Phi = \left[\operatorname{diag} \omega_{nat_i}^2\right] = \Omega} \qquad \textbf{(C-52)}$$

- Now consider the substitution into the coupled equations of motion. A co-ordinate transformation is performed using the mass normalised eigenvectors of equation (C-50),

$$q = \Phi z \qquad \textbf{(C-53)}$$

On substituting for u in equation (C-45) and pre-multiplying by Φ^{T}, results in

$$\left(\Phi^{\mathrm{T}} M \Phi\right)\ddot{z} + \left(\Phi^{\mathrm{T}} C \Phi\right)\dot{z} + \left(\Phi^{\mathrm{T}} K \Phi\right) z = \Phi^{\mathrm{T}} u_f(t) \qquad \textbf{(C-54)}$$

and finally using equations (C-50) and (C-52), this reduces to

$$\boxed{\ddot{z} + \left(\Phi^{\mathrm{T}} C \Phi\right)\dot{z} + \Omega z = \Phi^{\mathrm{T}} u_f(t)} \qquad \textbf{(C-55)}$$

This equation may only be successfully decoupled if

$$\Phi^{\mathrm{T}} C \Phi = \text{diagonal matrix} \qquad \textbf{(C-56)}$$

is a **diagonal** matrix. The appropriate form of the damping matrix is considered next.

C.4.1.1 Representation of Damping.

The dissipation function has not been derived since damping is not necessarily an inherent property of the vibrating beam structure. Damping forces depend not only on the structure itself, but also on the surrounding medium. For example structural damping is caused by the internal friction within the material and at joints between components, while viscous damping occurs when a structure is moving in liquid or a fluid.

Generally the formulation of mathematical expressions for the damping forces in a structure are complicated. For this reason simplified models exist. Viscous damping is one of these simplified models and is the only model considered. The motivation for this choice being that viscous damping is able to satisfy equation (C-56).

Viscous damping can be used whatever the form of excitation, whereas structural or hysteric damping can only be used when the excitation of the structure is harmonic. The most common form of viscous damping is Rayleigh or proportional damping given by equation (C-57), which is the only form of viscous damping considered in this thesis.

$$C = \alpha M + \beta K \qquad \textbf{(C-57)}$$

The advantage of representing the damping matrix, C, in this form is that it satisfies the diagonal requirement of the modal analysis solution technique. i.e. equation (C-56) is satisfied.

After pre-multiplying equation (C-57) by Φ^T and post-multiplying by Φ, the equation may be restated after substituting both equation (C-50) and (C-52) as

$$\Phi^T C \Phi = \alpha I + \beta \Omega = \Xi \qquad \textbf{(C-58)}$$

where

I is an identify matrix,

$\Xi = \left[\text{diag } 2\omega_{nat_i}\gamma_i\right]$, and **(C-59)**

γ_i is the modal damping ratio.

On inspection of (C-58) it should be appreciated that there are three possible permutations for the value of the damping matrix.

1. If α=0, then the mass matrix has no contribution to the damping, then the damping is referred to as *stiffness-proportional damping.*

2. If β=0, then the stiffness matrix has no contribution to the damping, then the damping is referred to as *mass-proportional damping.*

3. The final permutation, is when neither α or β are zero valued, the so-called *proportional damping* case.

Each of the three possible damping permutations is indicated in figure C-6

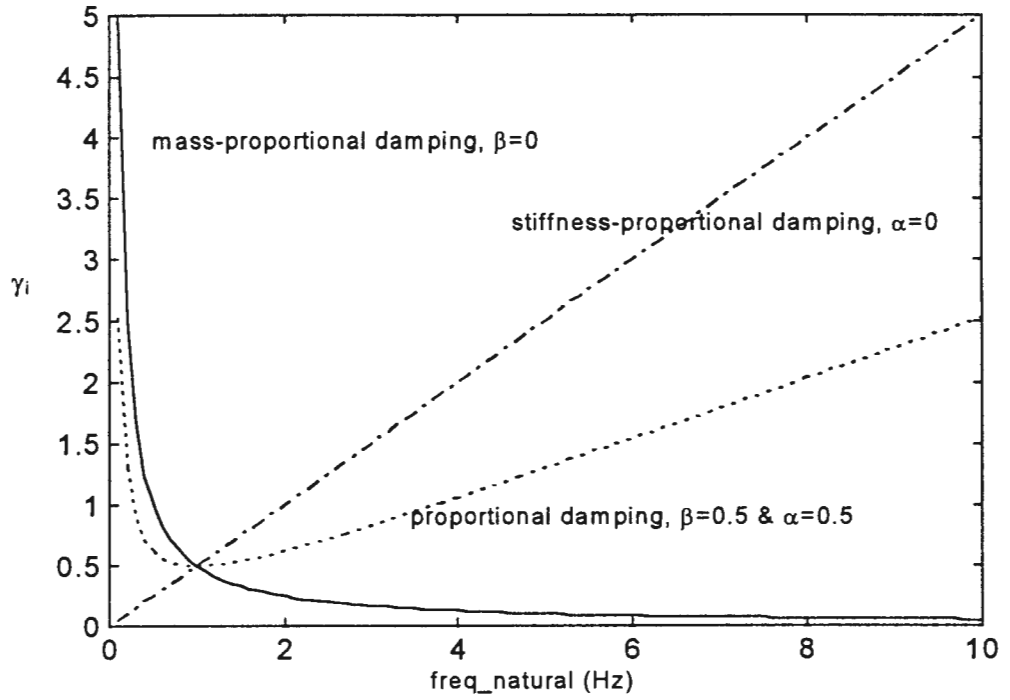

Figure C-6 Typical plot of the modal damping ratio versus natural frequency. Each of the three possible damping permutations are indicated.

C.4.1.2 Development of the Impulse Response Function.

The form of the damping matrix may be substituted into equation (C-55), yielding

$$\ddot{z} + \Xi\dot{z} + \Omega z = \Phi^{\mathrm{T}} u_f(t) \qquad \textbf{(C-60)}$$

Thus the second-order equation of motion has successfully been decoupled and may be re-written as

$$\ddot{z}_i + \left(2\omega_{nat_i}\gamma_i\right)\dot{z}_i + \left(\omega^2_{nat_i}\right)z = \left[\Phi^{\mathrm{T}} u_f(t)\right]_i \qquad \textbf{(C-61)}$$

for i=1 to m

Let $h_i(t)$ be the unit *impulse response function* for $z_i(t)$ when the excitation vector is replaced by a delta function at $t=0$. Then the solution is given by the convolution integral as

$$z_i(t) = \int_{-\infty}^{t} h_i(t-\tau)\left[\Phi^{\mathrm{T}} u_f(\tau)\right]_i \mathrm{d}\tau \qquad \textbf{(C-62)}$$

There is a similar equation to (C-62) for each of the rows defined in equation (C-61), combining all these into a single matrix equation results in

$$z(t) = \int_{-\infty}^{t} \left[\mathrm{diag}\, h_i(t-\tau)\right]\Phi^{\mathrm{T}} u_f(\tau)\mathrm{d}\tau \qquad \textbf{(C-63)}$$

Or reverting to the vector of physical-response co-ordinates, using (C-53)

$$q(t) = \int_{-\infty}^{t} \Phi\left[\mathrm{diag}\, h_i(t-\tau)\right]\Phi^{\mathrm{T}} u_f(\tau)\mathrm{d}\tau \qquad \textbf{(C-64)}$$

The impulse response functions, which are solutions of equation (C-61) may be restated as

$$\ddot{h}_i + \left(2\omega_{nat_i}\gamma_i\right)\dot{h}_i + \left(\omega_{nat_i}^2\right)h = \delta(t-\tau) \qquad \textbf{(C-65)}$$

and hence the modal *impulse response function* is given by (C-66), for a unit impulse input to mode *i*.

$$h_i(t-\tau) = \frac{e^{-\omega_{nat_i}\gamma_i(t-\tau)}}{\omega_{nat_i}\sqrt{1-\gamma_i^2}}\sin(\omega_{nat_i}\sqrt{1-\gamma_i^2}(t-\tau)) \qquad \textbf{(C-66)}$$

$$for\ i=1\ to\ m$$

The elements of the [*mxm*] matrix of the physical response functions *h(t)* may be found as follows.

If $u_f(\tau)$ in (C-64) is given by

$$u_f(\tau) = [\ \delta(\tau)\ \ 0\ \ 0\ \ .....\ 0\ ]^T \qquad \textbf{(C-67)}$$

then the response vector *q(t)* will be

$$q(t) = [\ h_{11}(t)\ \ h_{21}(t)\ \ h_{31}(t)\ \ .....\ \ h_{m1}(t)\ ]^T \qquad \textbf{(C-68)}$$

and on substituting equations (C-66) and (C-67) into equation (C-64) and completing the integral

$$\begin{bmatrix} h_{11}(t) \\ h_{12}(t) \\ \\ h_{M1}(t) \end{bmatrix} = \int_{-\infty}^{t} \Phi\left[\text{diag}\, h_i(t-\tau)\right]\left[\Phi^T\right]_1 \delta(\tau)\mathrm{d}\tau$$
$$= \Phi\left[\text{diag}\, h_i(t)\right]\left[\Phi^T\right]_1 \qquad \textbf{(C-69)}$$

where $\left[\Phi^T\right]_1$ is the first column of Φ^T

If instead $u_f(\tau)$ in equation (C-67) is given by

$$u_f(\tau) = [\ 0\ \ \delta(\tau)\ \ 0\ \ 0\ \ .....\ 0\ ]^T \qquad \textbf{(C-70)}$$

then the response vector *q(t)* will be

$$q(t) = [\ h_{21}(t)\ \ h_{22}(t)\ \ h_{32}(t)\ \ .....\ \ h_{m2}(t)\ ]^T \qquad \textbf{(C-71)}$$

and a similar result to equation (C-69) is obtained, except that $[\Phi^T]_1$ will be replaced by $[\Phi^T]_2$ the second column of Φ^T. Thus combining the results for the impulsive input in all *m* positions in the vector $u_f(\tau)$, the matrix of impulse response functions is given by

$$h(t) = \Phi\ [\ \text{diag}\ h_i(t)\ ]\ \Phi^T \tag{C-72}$$

or substituting equation (C-66)

$$\boxed{h_{rs}(t) = \sum_{i=1}^{m} \Phi_{ri}\Phi_{si} \frac{e^{-\omega_{nat_i}\gamma_i(t)}}{\omega_{nat_i}\sqrt{1-\gamma_i^2}} \sin(\omega_{nat_i}\sqrt{1-\gamma_i^2}(t))} \tag{C-73}$$

C.4.1.3 Development of the Frequency Response Function.

Let $H_i(j\omega)$ be the frequency response function for the i^{th} normal co-ordinate $z_i(t)$, as given in equation (C-61). Then the steady state solution to equation (C-61) is

$$z_i(t) = H_i(j\omega)\left[\Phi^T u_f(t)\right]_i \tag{C-74}$$

where the i^{th} element of the excitation vector equals $\left[\Phi^T u_f(t)\right]_i = e^{j\omega t}$

Then if equation (C-74) is substituted into equation (C-61),

$$H_i(j\omega) = \frac{1}{(j\omega)^2 + 2\omega_{nat_i}\gamma_i(j\omega) + \omega_{nat_i}^2} \tag{C-75}$$

The time-domain variables are transformed to their equivalent frequency-domain expressions, via the Fourier Transform

$$\begin{aligned} z_i(t) &\overset{FFT}{\Leftrightarrow} Z_i(j\omega) \\ y_i(t) &\overset{FFT}{\Leftrightarrow} Y_i(j\omega) \\ \left[\Phi^T u_f(t)\right]_i &\overset{FFT}{\Leftrightarrow} \left[\Phi^T U_f(j\omega)\right]_i \end{aligned} \tag{C-76}$$

Equation (C-61) may be re-stated in the frequency domain as

$$Z_i(j\omega) = H_i(j\omega)\left[\Phi^T U_f(j\omega)\right]_i \tag{C-77}$$

for i=1 to m

and a single matrix equation can be written for the system of m equations

$$Z(j\omega) = [\text{diag}\, H_i(j\omega)]\ \Phi^T U_f(j\omega) \tag{C-78}$$

or from (C-53)

$$\boxed{H(j\omega) = \Phi\ [\text{diag}\, H_i(j\omega)]\ \Phi^T} \tag{C-79}$$

which is the frequency domain equivalent to the convolution integral, of equation (C-64)

Similarly, the [m x m] matrix of frequency response functions for the vector of displacements $q(t)$ may be obtained from equation (C-79). The strategy that is followed is similar to that used to derive the impulse response function matrix, thus the frequency response function matrix is merely stated

$$H(j\omega) = \Phi \left[\text{diag}\, H_i(j\omega)\right] \Phi^{\mathrm{T}} \qquad \textbf{(C-80)}$$

or

$$\boxed{H_{rs}(j\omega) = \sum_{i=1}^{m} \Phi_{ri}\Phi_{si} \frac{1}{(j\omega)^2 + 2\omega_{nat_i}\gamma_i(j\omega) + \omega^2_{nat_i}}} \qquad \textbf{(C-81)}$$

C.5 Software Implementation of the Finite Element Method.

To implement the finite element method it was necessary to develop a computer software program. The Watcom™ FORTRAN compiler was chosen as the development language, in preference to C++ due to the availability of a dos-extender included in the compiler.

The implementation of the finite element method may be conveniently subdivided into four subsections.

1. The numerical integration of the local mass and stiffness matrices using the Gauss-Legendre numerical integration scheme i.e. the evaluation of equations (C-40), (C-41), (C-43) and (C-44). This is described in **Appendix II-4.**

2. The assembly procedure of the local mass and stiffness matrices into the respective global mass and stiffness matrices for the entire structure. This is described in **Appendix II-5.**

3. The eigen-decomposition of the eigen-problem given by equation (C-49). The eigen-problem requires the solution of the matrix product $M^{-1} K$, prior to the extraction of the eigenvalues and eigenvectors.

   Rather than performing the obvious matrix calculation, the matrix product was re-written as $M(M^{-1} K) = K$ or $M(x) = K$. The matrix, x, may now be solved using the LU decomposition technique. Further details are presented in **Appendix II-6.1.**

   The eigenvalues are solved using the QR Method. **Appendix II-6.2** discusses the reduction to a Hessenberg form and the subsequent implementation of the QR method. The calculation and scaling of the eigenvectors is also discussed in **Appendix II-6.2**.

4. A selection of FORTRAN listings are given in **Appendix II-7.**

Chapter D.

Time-Domain Identification.

D. Time Domain Identification.

The time domain system identification procedure is graphically depicted in figure D-1. The organisation of this chapter mimics this structure. There are essentially three major sub-divisions of the time domain identification procedure, namely:

1. *Modal Parameter Identification*,
2. the formation of the *Mass, Damping and Stiffness Matrices*, and finally the
3. software implementation of the identification procedures.

Detailed descriptions of the various sub-sections follow.

The eigen-realization algorithm (ERA) performs a least squares 'fit' to the impulse response data, resulting in a least order discrete state-space representation of the system. The next essential step is the McMillian transformation, which transforms the state-space realization of the system into a form which may be physically identified. The modal parameters, i.e. undamped natural frequencies, modal damping and mass normalised mode shapes, may then be extracted.

These modal parameters are then used to define the mass, stiffness and damping matrices. These matrices are of minimum order and their definition is based on the Craig Bampton component mode syntheses (CMS) method. The CMS method is related to the statically condensed Guyan Reduction method.
The tactic which is followed is to describe the statically reduced Guyan matrices in terms of the identified modal parameters, (i.e. undamped natural frequencies, modal damping and mass normalised modes shapes) and then substitute these expressions into the definitions for the Craig Bampton CMS matrices. The result is minimum order mass, damping and stiffness matrices which describe the system.

The final section is concerned with the software implementation of the Time Domain Identification procedure. The mathematical visualisation software, Matlab™ , was used as the principle development tool. Once the development was complete the code was transformed into C++ code and compiled into executable form using the Borland™ C++ V4.52 compiler.

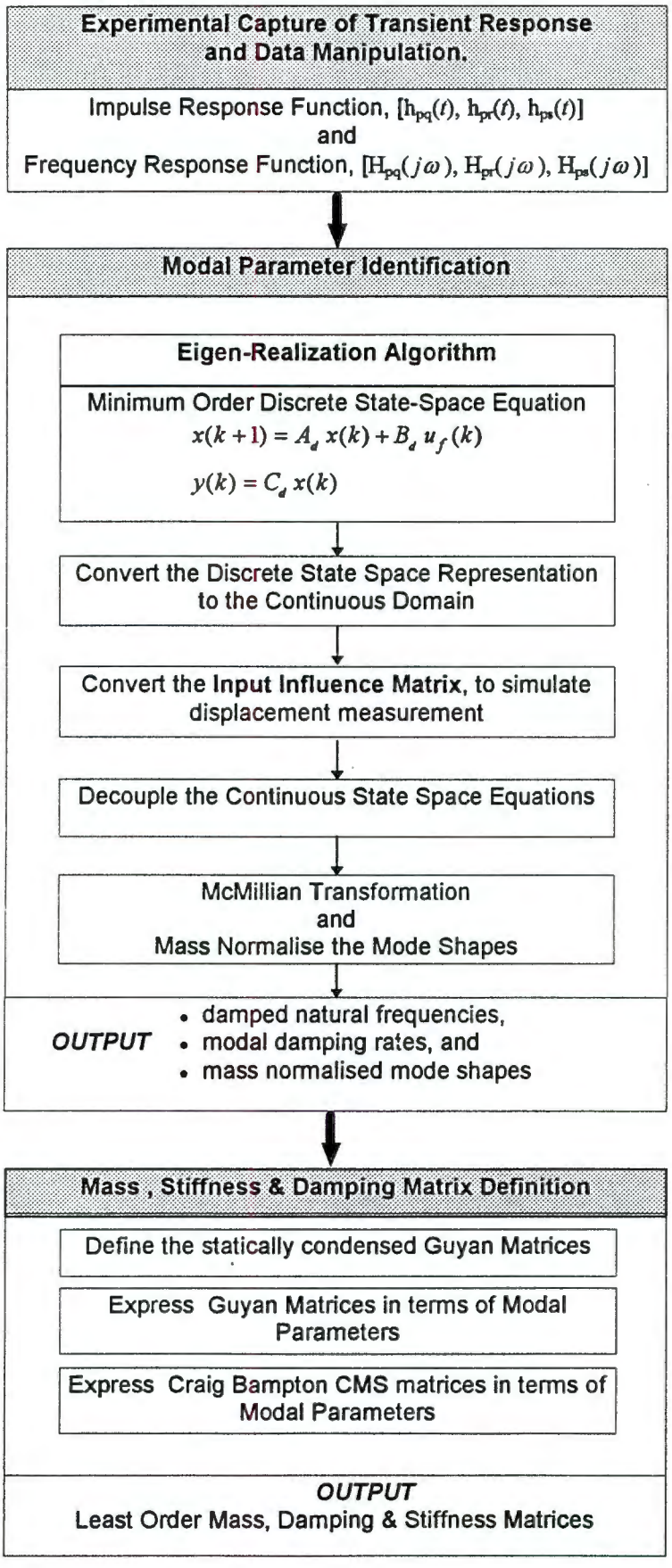

Figure D-1. Flow Chart of the Identification Procedure.

D.1 Background Information.

This section discusses background information which is relevant to the remainder of this chapter. The motivation for the choice of the ERA identification technique is presented, in the brief literature review of time domain identification procedures. No attempt has been made to discuss all identification procedures and the reader is referred to references such as *Ewins (1974)* and *Franklin et. al. (1990),* for a more encompassing discussion.
In the following section the concept of the state-space form of the classic second order differential equation of motion is presented. The distinction is also made between the continuous and discrete form of the state-space equations, and their relationship to one another is shown. Finally, the concepts of system realization and minimum realization are discussed.

D.1.1 Literature Review of Time Domain Identification Methods.

There are advanced data analysis techniques, although not fully accepted, which use both the frequency and impulse response functions for direct identification of modal parameters. *Vold & Russell (1983).* However, generally time domain methods utilise the impulse response function of the structure under test, while frequency domain methods utilise the frequency response functions to identify the modal parameters.

Most of the existing time domain methods can be reformulated in an unified way under the framework of 'system realization theory'. *Ewins (1984)* and *Juang (1987)*
The various methods are:

- eigensystem realization algorithm (ERA) *Juang & Pappa (1983),* which is a special form of realization, the so-called internal balanced realization
- Q-Markov COVER (QMC), *Wagie and Skelton (1986)*
- Prony's algorithm, *Van Blaricum & Mittra (1978)*
- Ibrahim time-domain method, *Ibrahim & Mikulcik (1973)* and the
- polyreference technique *Vold et al (1982)*

all of these methods are related to the canonical-form realization technique. *Juang (1987)*

System Realization Theory, in particular the ERA

Gilbert (1963) and *Kalman (1963)* introduced the concepts of realization theory in terms of the concepts of controllability and observability. Later *Kalman & Ho (1965)* showed that the minimum realization problem is equivalent to a representation problem involving a sequence of real matrices known as Markov parameters (impulse response functions) assembled into a large matrix, so-called Hankel matrix. A weakness of the preceding schemes was that the effect of noise on the data analysis was not evaluated. *Zeiger & McEwen (1974)* proposed a combination of the Ho-Kalman algorithm with singular value decomposition (SVD) for the treatment of noisy data.

A major advantage of the ERA over other system realization methods is that theoretically it finds the smallest order model that fits the data for a given accuracy. This is accomplished through the SVD of the Hankel matrix. By discarding all but the largest singular values of the Hankel matrix, the ERA user can separate measurement components that are due to true modal dynamics from components that are due to measurement noise or weakly excited modes. *Pappa & Juang (1988).*

A further advantage of the ERA is that the numerical technique of SVD is robust in the presence of repeated roots and measurement noise. *Golub & Reinsch (1970)*

Finally, the ERA technique has been successfully utilised to verify the modal parameters of complex structures, with repeated or closely spaced eigenvalues. Both *Pappa & Juang (1988)* and *Chen (1984)* report on the successful use of the ERA on vibration test data from the Galileo spacecraft.

Minimal-Order Mass, Damping and Stiffness Matrices.

Due to practical considerations there are only a finite number of locations on the structure from which data can be collected. These measured points form a subset of the total degrees of freedom (dof) of the structure. In fact, generally the number of measurement points may be less than the total number of resonant modes identified in the test. Therefore, if p sensors are used to identify modal data for m modes, where $m > p$, there is not a unique model of the classical mass/stiffness form with physical dof which possesses m order dynamics given only p spatial measurement points. Conversely, if $m = p$ *or* $m < p$, then it is possible to uniquely solve for the mass and stiffness, this is the so-called inverse dynamics problem. *Ewins (1984)*

In the paper by *Yang & Yeh (1990)* mass and stiffness matrices are determined directly from the continuously time system realizations. A major drawback of this approach, is that it requires the dimension of the physical model to be equivalent to the number of second-order states, implying that the number of independent sensors measured are equal to the number of identified modes. As discussed, this is generally not the case and thus it is reasoned rather to compute the mass and stiffness matrices with the complete set of measured modes, independent of the number of sensors.

An alternative approach, proposed by *Alvin et. al. (1995)*[1] *and Alvin et. al. (1995)*[2] , is to solve the inverse vibration problem directly, when $m > p$. The authors begin by solving for the Guyan reduced matrices in terms of the m identified modes. These matrices condense the m modal dof into p physical dof. Guyan reduced matrices preserve the low-frequency modes more accurately than the higher modes of the modal spectrum. *Guyan (1965)* A further shortcoming of the Guyan Reduction method is that as the identified test dynamics are condensed into a smaller dimensional space, the measured eigenvectors and eigenvalues are not accurately preserved by the Guyan reduced mass and stiffness matrices. Hence the model defined by these reduced order matrices is not equivalent to the test structure in terms of measured transfer functions.

To overcome these difficulties the Craig Bampton component mode synthesis (CMS) method is utilised. *Craig & Bampton (1968)* The Craig Bampton method is related to the Guyan reduction technique, in that for the derivation of minimal order mass and stiffness matrices, the measured physical dof are augmented by a set of generalised dof which are the modal co-ordinates of the residual dynamics.
The *essential fact* is that the residual dynamic matrix is the difference between the identified eigenvalues and the projection of the reduced stiffness through the measured mode shapes. (*see equation (D-77)).* A singular value decomposition of the residual dynamic matrix is performed, to determine the rank deficiency of the reduced stiffness matrix. A minimum augmentation of the mode shapes using the orthonormal vectors of the retained singular values is performed, to solve for the new minimal order stiffness and mass matrices.

D.1.2 Continuous & Discrete State Space Equations.

The equations of motion for a finite-dimensional linear dynamic system are a set of m second-order differential equations, where m is the number of independent co-ordinates. The form of the equation, equation (D-1), was developed in section C.2.1. Unlike the modal analysis technique discussed in section C.4.1, the state-space analysis technique is invariant to the form of the mass, damping and stiffness matrices, other than they are real valued matrices.

In the following section the equations of motion will be reduced to both a continuous and discrete state-space representation. The state-space representation is used throughout the system identification.

Consider a second order linear differential equation, of the form derived in section C.2.1

$$\boxed{\begin{aligned} M\ddot{q}+C\dot{q}+Kq &= B_{force}u_f(t) \\ y(t) &= \begin{cases} C_{displ}\ q(t), & \text{or} \\ C_{vel}\ \dot{q}(t), & \text{or} \\ C_{accel}\ \ddot{q}(t) \end{cases} \end{aligned}} \qquad \textbf{(D-1)}$$

where $q(t)$ is a displacement vector , dimension [m] and,
$y(t)$ dimension [p], is the *appropriate* measured output variable of the system, using sensors such as strain gauges, accelerometers, etc., i.e. the measured quantity may be displacement, velocity or acceleration.

If we define a new m^{th} order vector $w(t)$, as the derivative of $q(t)$ so that

$$\dot{q} = w \quad \text{and hence} \quad \ddot{q} = \dot{w} \qquad \textbf{(D-2)}$$

then re-writing (D-1) and combining with (D-2) as

$$\begin{bmatrix} \dot{q} = w \\ M\dot{w}+Cw+Kq = B_{force}u_f \end{bmatrix} \qquad \textbf{(D-3)}$$

if we now define a new variable $x[2m=n]$, such that

$$x = \begin{bmatrix} q \\ w \end{bmatrix} \quad \text{and hence} \quad \dot{x} = \begin{bmatrix} \dot{q} \\ \dot{w} \end{bmatrix} \qquad \textbf{(D-4)}$$

then (D-1) can be rewritten as

$$\dot{x}(t) = \begin{bmatrix} 0 & I \\ -M^{-1}K & -M^{-1}C \end{bmatrix} x(t) + \begin{bmatrix} 0 \\ M^{-1}B_{force} \end{bmatrix} u_f(t) \qquad \textbf{(D-5)}$$

or more conveniently in the form

$$\dot{x}(t) = A_c x(t) + B_c u_f(t)$$
$$y(t) = C_c x(t)$$
where
$$A_c = \begin{bmatrix} 0 & I \\ -M^{-1}K & -M^{-1}C \end{bmatrix} \text{ dimension } [n \text{ x } n], \quad B_c = \begin{bmatrix} 0 \\ M^{-1}B_{force} \end{bmatrix} \text{ dimension } [n \text{ x } m]$$
$$C_c = \begin{cases} [C_{displ} \quad 0], & or \\ [C_{vel} \quad 0]A_c, & or \\ [C_{accel} \quad 0]A_c^2 \end{cases} \quad \text{dimension } [p \text{ x } n]$$

(D-6)

The matrices by convention are named:-

- $x(t)$ is the continuous **state vector matrix,**
- A_c is the continuous **state transition matrix**,
- B_c is the continuous **input influence matrix**, and
- C_c is the continuous **output influence matrix.**

Using initial conditions $x(t_0)$ equation (D-7) gives the solution to the continuous time state-space equation with an input $u_f(t)$, *see Franklin et. al. (1990)*

$$x(t) = \left[e^{A_c(t-\tau)}x(t_0)\right] + \int_{t_0}^{t} e^{A_c(t-\tau)}B_c u_f(\tau)\, d\tau \qquad \textbf{(D-7)}$$

for $t \geq t_0$.

It will be shown that the evaluation of $x(t)$ at equally spaced intervals of time t can be obtained by a discrete time representation of equation (D-7). Let the equally spaced times be given by $\{0, \Delta t, 2\Delta t, \ldots\ldots k\Delta t\}$, where Δt is a constant time interval. Substitution of $t=(k+1)\Delta t$ and $t_0=k\Delta t$ into equation (D-7) yields

$$x((k+1)\Delta t) = \left[e^{A_c\Delta t}x(k\Delta t)\right] + \int_{k\Delta t}^{(k+1)\Delta t} e^{A_c((k+1)\Delta t-\tau)}B_c u_f(\tau)\, d\tau \qquad \textbf{(D-8)}$$

If $u_f(\tau)$ is assumed to be constant over the interval $k\Delta t \leq \tau \geq (k+1)\Delta t$ and has the value $u_f(k\Delta t)$, then equation (D-8) with a constant B_c becomes

$$x((k+1)\Delta t) = \left[e^{A_c\Delta t}x(k\Delta t)\right] + u_f(k\Delta t)\int_0^{\Delta t} e^{A_c(\tau')}d\tau'\, B_c \qquad \textbf{(D-9)}$$

where the variable τ in equation (D-9) has been changed by letting $\tau'=(k+1)\Delta t-\tau$.
Now define

$$A_d = e^{A_c\Delta t}$$
$$B_d = \int_0^{\Delta t} e^{A_c(\tau')}d\tau'\, B_c \qquad \textbf{(D-10)}$$
$$x(k+1) = x((k+1)\Delta t) \text{ and } u_f(k) = u_f(k\Delta t)$$

Therefore the discrete state-space form may be written as

$$x(k+1) = A_d x(k) + B_d u_f(k)$$
$$y(k) = C_d x(k)$$
$$\text{where} \quad C_d = \left\{ [C_{displ} \quad 0], \text{ or } [C_{vel} \quad 0]A_d, \text{ or } [C_{accel} \quad 0]A_d^2 \right. \qquad \textbf{(D-11)}$$

D.1.2.1 Continuous & Discrete Impulse Response Functions.

Consider the case when starting from zero initial conditions, *i.e.* $x(0)=0$, a unit impulse excitation is applied at the i^{th} input location at $t=0$. Then equation (D-7) would reduce to

$$x(t) = e^{A_c t} B_c \qquad \text{and hence}$$

$$h(t) = C_c e^{A_c t} B_c = y(t) \tag{D-12}$$

with sampled data, this solution can be expressed as

$$h(k) = \begin{cases} C_d B_d & \text{for } k = 0 \\ C_d A_d^{k-1} B_d & \text{for } k > 0 \end{cases} \tag{D-13}$$

where $h(t)$ & $h(k)$ are the respective continuous and discrete **impulse response functions** or **Markov parameters**. The response of this model to any vector of inputs $u_f(k)$ is then a discrete convolution sum,

$$y(k) = \sum_{i=1}^{k} h(k-i) u_f(i) \tag{D-14}$$

D.1.3 System Realization.

Given the sequence of sampled impulse response functions $\{ h(k),\ 0 \le k < \infty \}$ solving for the state-space matrices, $[A_d, B_d, C_d]$, that accurately model the system, is termed ***realization.*** *Franklin et. al. (1990)*

Any system has an ***infinite number of realizations*** which could predict the identical response for a particular input.
Consider

$$x = T z \tag{D-15}$$

where T is any non-singular square matrix. Substituting (D-15) into equation (D-11) yields

$$\begin{aligned} z(k+1) &= [T^{-1} A_d T]\, z(k) + [T^{-1} B_d]\, u_f(k) \\ y(k) &= [C_{displ} T]\, z(k) \end{aligned} \tag{D-16}$$
$$k=0,1,2, \ldots..$$

The effect of input $u_f(k)$ on $y(k)$ will be the same for the new system of equation (D-16) as equation (D-11). Thus, the triple $[\ [T^{-1} A_d T],\ [T^{-1} B_d\ ],\ [C_{displ} T\ ]\ ]$ will also be a realization for the same system. Also, the predicted responses using the realization $[\ [T^{-1} A_d T],\ [T^{-1} B_d\ ],\ [C_{displ} T\ ]\ ]$ will be identical to those predicted using $[A_d, B_d, C_d]$, as there exists an infinite number of non-singular matrices, T.

Minimum realization implies a model with the smallest state-space dimension among the systems that have the same input-output relations. *All minimum realizations have the same set of eigenvalues which are the parameters of the system itself.* It is therefore convenient to transform the realization using the eigenvectors of the state matrix, A_d, as the eigenvalues of the system are the modal parameters required. This is more fully described and executed in section E.2.4

D.2 Modal Parameter Identification Procedure.

The procedure is graphically depicted in figure D-1, each of the sub-sections will be individually addressed.

D.2.1 The Eigensystem Realization Algorithm. (ERA)

The Eigenrealization Algorithm (ERA) begins by forming the [r x s] block generalised Hankel matrix, as described by *Juang (1987)*

$$H_{rs}(k-1)=\begin{bmatrix} h(k) & h(k+t_1) & \cdots & h(k+t_{s-1}) \\ h(k+j_1) & h(k+j_1+t_1) & \cdots & h(k+j_1+t_{s-1}) \\ \vdots & \vdots & & \vdots \\ h(k+j_{r-1}) & h(k+j_{r-1}+t_1) & \cdots & h(k+j_{r-1}+t_{s-1}) \end{bmatrix} \qquad \textbf{(D-17)}$$

where j_i *(i=1, ... , r-1)* and t_i *(i=1, ... , s-1)* are arbitrary integers. The significance of the Hankel matrix is that in the limit of r and s becoming very large the numerical rank is the smallest order that can reproduce the impulse response functions. Now observe from equation (D-13), that the generalised Hankel matrix can be restated as

$$H_{rs}(k)=V_r A_d^k W_s \qquad \textbf{(D-18)}$$

where

$$V_r=\begin{bmatrix} C_d \\ C_d A_d^{j_1} \\ \vdots \\ C_d A_d^{j_{r-1}} \end{bmatrix} \text{ and } W_s=\begin{bmatrix} B_d & A_d^{t_1}B_d & \cdots & A_d^{t_{s-1}}B_d \end{bmatrix}$$

Matrices V_r and W_s are the observability and controllability matrices, respectively. If the order of the system is n, then the minimum order will also be n. Further, if the system is controllable and observable, the block matrices V_r and W_s are of rank n. Hence the Hankel matrix will also be of rank n, by equation (D-18), if $r+1 \geq n$ & $s+1 \geq n$.

In the ERA the shift of the Hankel matrix from time discrete $k=1$ to $k=2$ is utilised, together with the fact that the observability, V_r , and controllability matrices, W_s ,may be computed from $H_{rs}(0)$. The time-shifted Hankel matrices at discrete time $k=1$ and $k=2$, may be defined by substitution into both equations (D-17) & (D-18).

$$H_{rs}(0)=\begin{bmatrix} h(1) & h(2) & \cdots & h(s) \\ h(2) & h(3) & \cdots & h(s+1) \\ \vdots & \vdots & & \vdots \\ h(r) & h(r+1) & \cdots & h(r+s-1) \end{bmatrix}=V_r W_s \qquad \textbf{(D-19)}$$

and

$$H_{rs}(1)=\begin{bmatrix} h(2) & h(3) & \cdots & h(s+1) \\ h(3) & h(4) & \cdots & h(s+2) \\ \vdots & \vdots & & \vdots \\ h(r+1) & h(r+2) & \cdots & h(r+s) \end{bmatrix}=V_r A_d W_s \qquad \textbf{(D-20)}$$

The **state transition matrix**, A_d, may be solved by a least squares solution of equation (D-20)

$$\boxed{A_d = V_r^+ \, H_{rs}(1) \, W_s^+} \qquad \textbf{(D-21)}$$

where

V_r^+ is the pseudoinverse of V_r , and similary

W_s^+ the pseudoinverse of W_s

To solve equation (D-21), $H_{rs}(0)$ is decomposed by means of the *singular value decomposition* technique,

$$H_{rs}(0) = P \, D \, Q^{\mathsf{T}} \qquad \textbf{(D-22)}$$

where P and Q the columns of matrices are orthonormal and D is a rectangular matrix. Truncating following the N largest singular values,

$$H_{rs}(0) \approx P_N \, D_N \, Q_N^{\mathsf{T}} \qquad \textbf{(D-23)}$$

where $P_N = P(1{:}rp, 1{:}N)$,
$D_N = D(1{:}N, 1{:}N)$, *and*
$Q_N = Q(1{:}ms, 1{:}N)$

Therefore from equation (D-19) and (D-21), the following relations can be stated

$$\begin{aligned} &H_{rs}(0) = V_r W_s \approx \left[P_N \, D_N^{1/2}\right]\left[D_N^{1/2} Q_N^T\right] \\ &\textit{hence} \\ &V_r \approx \left[P_N D_N^{1/2}\right] \text{ and the pseudoinverse } V_r^+ \approx \left[D_N^{-1/2} P_N^T\right] \\ &W_s \approx \left[D_N^{1/2} Q_N^T\right] \text{ and the pseudoinverse } W_s^+ \approx \left[Q_N D_N^{-1/2}\right] \end{aligned} \qquad \textbf{(D-24)}$$

and the transition matrix solved for

$$A_d \approx \left[D_N^{-1/2} P_N^T\right] H_{rs}(1) \left[Q_N D_N^{-1/2}\right] \qquad \textbf{(D-25)}$$

It follows immediately from equation (D-20), of the definition of the controllable and observable matrices that

$$B_d \approx D_N^{1/2} Q_N^T \begin{bmatrix} I_{m \times m} \\ O_{(s-m) \times m} \end{bmatrix} \text{ and } \; C_d \approx P_N \begin{bmatrix} I_{p \times p} \\ O_{p \times (r-p)} \end{bmatrix}^T D_N^{-1/2} \qquad \textbf{(D-26)}$$

The Eigensystem Realization Algorithm is complete. The ERA took as input the impulse response functions of each accelerometer and produced the triple matrices $[A_d, B_d, C_d]$, which define the discrete state-space equation.

D.2.1.1 ERA Performance Check.

A systematic approach to the checking of the ERA has been followed. Five checks are performed during the software analysis:-

Check #1.

By definition equation (D-22) is correct, due to the singular value decomposition theorem. However equation (D-23) is an approximation of $H_{rs}(0)$, depending on the number of singular values retained. The reader is deferred to the results section (F.2.1.1), where the rapid decrease in the normalised singular values are observed.

Check #2 & #3.

By definition $P^{\mathrm{T}}P = Q^{\mathrm{T}}Q = I$, as the matrices are orthonormal. Hence the truncated matrices should satisfy $P_N^{\mathrm{T}}P = Q_N^{\mathrm{T}}Q = I_{N\times N}$

Check #4 & #5.

The equality given by equation (D-24) ,defines the controllability and observability Grammians as

$$W_s W_s^{\mathrm{T}} = V_r^{\mathrm{T}} V_r = D_N \qquad \textbf{(D-27)}$$

The significance that both the controllability and observability Grammians are equal and diagonal implies that the realization $[A_d, B_d, C_d]$, is as controllable as it is observable. This property is called an ***internally balanced realization.*** This means that the signal transfer from the input to the state and then from the state to the output are similar and balanced.

D.2.2 Conversion of Discrete to Continuous State Space.

Due to the continuous form of the physical parameters that are to be solved, it is necessary to convert the discrete state-space form of the system realization to the equivalent continuous form. Thus the system matrices $[A_d, B_d, C_d]$, where the subscript d refers to the discrete form, are to be transformed to the equivalent system matrices $[A_c, B_c, C_c]$, where the subscript c refers to the continuous form.

Franklin et. al. (1990) discuss suitable numerical techniques to transform the system matrices, without incurring numerical inaccuracies. The numerical technique is a series evaluation of the 'inverse' of equation (D-11). The Matlab™ routine, d2c.m, was used. (*personal correspondence Peterson L* and *Alvin K.)*

D.2.3 Manipulation of the Input Influence Matrix.

If the measured variable, $y(t)$, is acceleration, as in this dissertation, then it is not possible to solve for a unique mass normalising scaling factor at each degree of freedom, as the solution results in an over-defined system of equations. (This will be demonstrated in section E.2.5.) Hence, the input influence matrix, C_c, must be manipulated into a format as if displacement or velocity were the measured variable.

Consider the case when acceleration is measured, i.e. $y(t)$ is an acceleration time history. Integration will result in velocity and double integration of $y(t)$ in displacement. Recalling from equation (D-6), this has the effect on the input influence matrix of

$$C_{c\_displ} = C_{c\_accel} A_c^{-1} A_c^{-1} \qquad \textbf{(D-28)}$$

The parameter identification can now continue as if displacement was measured.

D.2.4 Decoupling of the Continuous-Time State Space Equations.

Assume that the state transition matrix, A_c, of order n has a complete set of linearly independent eigenvectors $\Psi = [\ \psi_1, \psi_2, \ldots\ldots, \psi_n\ ]$, with corresponding eigenvalues $[\ \lambda_1, \lambda_2, \ldots\ldots, \lambda_n\ ]$. Defining the diagonal matrix of eigenvalues Λ=diag($\lambda_1, \lambda_2, \ldots, \lambda_n$), such that the standard eigen-decomposition of A_c, may be expressed as

$$\Lambda = \Psi^{-1} A_c \Psi \tag{D-29}$$

Implementing the transformation as stated in equation (D-15), but T=Ψ,

$$\begin{aligned} &\dot{z}(t) = \left[\Psi^{-1} A_c \Psi\right] z(t) + \left[\Psi^{-1} B_c\right] u_f(t), \\ &\text{or} \\ &\dot{z}(t) = \Lambda z(t) + B_{c\_z} u_f(t) \\ &y(t) = C_{c\_z} z(t) \end{aligned} \tag{D-30}$$

where

$B_{c\_z} = \left[\Psi^{-1} B_c\right]$, initial modal amplitudes

$C_{c\_z} = \left[\Psi C_{c\_displ}\right]$, mode shapes (*not* mass normalized)

The diagonal matrix, Λ, contains the information of modal-damping rates and damped natural frequencies, ω, of the system. Such that

$$\lambda_i = \begin{bmatrix} \sigma_i + j\omega_i & 0 \\ 0 & \sigma_i - j\omega_i \end{bmatrix} \tag{D-31}$$

where the eigenvalues of A_c can be expressed in terms of natural frequencies and damping ratios of the modes of the physical system

$$\begin{aligned} \omega_{nat_i}^2 &= \sigma_i^2 + \omega_i^2 \\ -\xi_i \omega_{nat_i} &= \sigma_i \end{aligned} \tag{D-32}$$

As an observation, the discrete state transition matrix, A_d, may be similarly decoupled. The eigenvalues of A_d, may be converted to the time-domain by the inverse of the transform given by equation (D-10), namely $\Lambda = \ln(\Lambda_{discrete}) / \Delta t$

D.2.5 McMillian Transformation & Mass Normalisation of Mode Shapes.

Consider the modal analysis solution technique discussed in section C.4.1. Recall that the second-order differential equation, of order m, could be manipulated to a decoupled system of differential equations, also of order m. Repeating for clarity, the equations are

$$M\ddot{q}+C\dot{q}+Kq = B_{force}u_f(t)$$
$$y(t) = \begin{cases} C_{displ}\ q(t), & or \\ C_{vel}\ \dot{q}(t), & or \\ C_{accel}\ \ddot{q}(t) \end{cases} \qquad \textbf{(D-33)}$$

and decoupling by means of the homogeneous solution $M\ddot{q}+Kq=0$, yields the following relations

$$(M^{-1}K)\Phi = \Phi\Omega$$

such that

$$\Phi^T M\Phi = I_{mxm} \quad \text{(definition of mass normalized eigenvectors)} \qquad \textbf{(D-34)}$$
$$\Phi^T K\Phi = \Omega = diag(\omega^2_{nat\,i} \quad i=1,\ldots..,m)$$
$$\Phi^T C\Phi = \Xi = diag(2\xi_i\omega_{nat_i} \quad i=1,\ldots..,m)$$

Hence equation (D-33) may be restated as a system of m decoupled second order differential equations, via the transformation $q=\Phi\vartheta$

$$\ddot{\vartheta} + \Xi\dot{\vartheta} + \Omega\vartheta = \Phi^T B_{force}u_f(t)$$
$$y(t) = \begin{cases} C_{displ}\ \Phi\vartheta(t), & or \\ C_{vel}\ \Phi\dot{\vartheta}(t), & or \\ C_{accel}\ \Phi\ddot{\vartheta}(t) \end{cases} \qquad \textbf{(D-35)}$$

the system of m decoupled second order differential equations are converted to a system of first order differential equations, i.e. state-space format, by the substitution of

$$x(t) = \begin{bmatrix} \vartheta \\ \dot{\vartheta} \end{bmatrix} \quad \text{then}$$

$$\boxed{\begin{aligned} \dot{x}(t) &= A_{MDV}x(t) + B_{MDV}u_f(t) \\ y(t) &= C_{MDV}x(t) \end{aligned}} \qquad \textbf{(D-36)}$$

where

$$A_{MDV} = \begin{bmatrix} 0 & I \\ -\Omega & -\Xi \end{bmatrix},\quad B_{MDV} = \begin{bmatrix} 0 \\ \Phi^T B_{force} \end{bmatrix},\quad \text{and}\quad C_{MDV} = \begin{cases} [\Phi C_{displ} \quad 0], & or \\ [\Phi C_{vel} \quad 0]A_{MDV}, & or \\ [\Phi C_{accel} \quad 0]A^2_{MDV} \end{cases}$$

The form of equation (D-36) is frequently referred to as *the 'modal displacement velocity' (MDV)*, model. { notice the sirnilarity to equation (D-6) }

The McMillian transformation, *Longman & Juang (1987),* is a rotational transformation implemented on each of the identified modes of the system matrices [Λ, B_{c_z}, C_{c_z}], to realize the physical system given by the system matrices [A_{MDV}, B_{MDV}, C_{MDV}]. The columns of the output influence matrix C_{MDV} are then typically interpreted as the physical mass normalised mode shapes. However, the state basis resulting from application of the McMillian transformation, is not successful in mass normalising the eigenvectors as the final form of input influence matrix is not of the form given in equation (D-36). *Alvin & Park (1994)* describe a scaling factor which can be used to achieve mass normalised mode shapes, provided that the transfer function of a co-located actuator and sensor is available.

For clarity equation (D-36) is restated in terms of each of the identified modes, and considers ***only*** the case of displacement measurement

$$\begin{bmatrix}\dot{\vartheta}_i\\ \ddot{\vartheta}_i\end{bmatrix}=\begin{bmatrix}0 & 1\\ -\omega_{nat_i}^2 & -2\xi_i\omega_{nat_i}\end{bmatrix}\begin{bmatrix}\vartheta_i\\ \dot{\vartheta}_i\end{bmatrix}+\begin{bmatrix}0\\ \Phi_i^T B_{force}\end{bmatrix}u_f(t), \quad for\ i=1,\ .....\ ,m \tag{D-37}$$

$$y(t)=\sum_{i=1}^{m}\Phi_i C_{displ}\vartheta_i$$

The McMillian transformation, as applied to equation (D-30), is of the form

$$z_i = \mathrm{T}_i x_i \tag{D-38}$$

<u>resulting in :-</u>

$$A_{c\_norm}=\mathrm{T}_i^{-1}\Lambda_i\mathrm{T}_i=\begin{bmatrix}0 & 1\\ -\omega_{nat_i}^2 & -2\xi_i\omega_{nat_i}\end{bmatrix}, \tag{D-39}$$

$$B_{c\_norm}=\mathrm{T}_i^{-1}\left(B_{c\_z}\right)=\begin{bmatrix}0\\ \Phi_i^T B_{force}\end{bmatrix}, \text{ and} \tag{D-40}$$

$$C_{c\_norm}=C_{c\_z_i}\mathrm{T}_i=\begin{bmatrix}\Phi_i C_{displ} & 0\end{bmatrix} \tag{D-41}$$

The transformation, T_i, can be determined as a product of two transformations and an appropriately chosen scaling factor.

$$\mathrm{T}_i = d_i\,\mathrm{T}_{1i}\,\mathrm{T}_{2i} \qquad for\ i=1,\ ....\ ,\ m \tag{D-42}$$

The first transformation, T_{1i}, rotates the state transition matrix from the diagonal form in equation (D-30) to the physical form of equations (D-36) & (D-37). The second transformation, T_{2i} , must then not alter the elements of the transition matrix, while enforcing the definition of the physical input influence matrix. Finally, the scaling factor, d_i, enforces the definition of the output influence matrix, which also mass normalise the mode shapes.

The ***first transformation*** , T_{1i} , may be defined as

$$T_{1i} = \begin{bmatrix} \tau_{11} & \tau_{12} \\ \tau_{13} & \tau_{14} \end{bmatrix} \tag{D-43}$$

Then substituting this transformation to equation (D-39)

$$\begin{aligned} &\tau_{11}\tau_{14}\lambda_i = \tau_{12}\tau_{13}\lambda_i^* \\ &\tau_{12}\tau_{14}(\lambda_i - \lambda_i^*) = \tau_{11}\tau_{14} - \tau_{12}\tau_{13} \\ &-\tau_{11}\tau_{13}(\lambda_i - \lambda_i^*) = -(\sigma_i^2 + \omega_i^2)(\tau_{11}\tau_{14} - \tau_{12}\tau_{13}) \\ &\tau_{11}\tau_{14}\lambda_i^* - \tau_{12}\tau_{13}\lambda_i = 2\sigma_i(\tau_{11}\tau_{14} - \tau_{12}\tau_{13}) \\ &\textit{where} \\ &\lambda_i = (\sigma_i + j\omega_i) \end{aligned} \tag{D-44}$$

Hence a solution, not necessarily unique, is given by

$$\boxed{T_{1i} = \frac{j}{2\omega_i}\begin{bmatrix} (\sigma_i - j\omega_i) & -1 \\ (-\sigma_i - j\omega_i) & 1 \end{bmatrix}} \tag{D-45}$$

The ***second transformation*** , T_{2i} , may be defined as

$$T_{2i} = \begin{bmatrix} \tau_{21} & \tau_{22} \\ \tau_{23} & \tau_{24} \end{bmatrix} \tag{D-46}$$

As described, the second transformation must retain the form of the state transition matrix, that is

$$T_{2i} A_{MDVi} = A_{MDVi} T_{2i} \tag{D-47}$$

Then substituting the transformation, (D-46), into equation (D-47)

$$\begin{aligned} &\tau_{23} = -\tau_{22}(\sigma_i^2 + \omega_i^2) \\ &\tau_{24} = \tau_{21} + 2\sigma_i\tau_{22} \\ &-\tau_{24}(\sigma_i^2 + \omega_i^2) = -2\sigma_i\tau_{23} - \tau_{21}(\sigma_i^2 + \omega_i^2) \\ &\tau_{23} + 2\sigma_i\tau_{24} = -2\sigma_i\tau_{24} - \tau_{22}(\sigma_i^2 + \omega_i^2) \end{aligned} \tag{D-48}$$

There are only two independent equations in equations (D-48) and thus there is no unique solution for the elements of the rotation matrix without imposing additional constraints to the problem. The additional imposed constraint is the satisfaction of equation D-40. Applying both the transforms T_i and setting $\tau_{22}=d_i$ and $\tau_{21}= d_i e_i$, equation (D-40) may be restated as

$$T_i^{-1}(B_{c\_s}) = \begin{bmatrix} \Re(b_i) + j\Im(b_i) \\ \Re(b_i) - j\Im(b_i) \end{bmatrix} \xrightarrow{T_i} 2\begin{bmatrix} \left(\dfrac{(e_i + \sigma_i)\Re(b_i) + \omega_i\Im(b_i)}{d_i(e_i^2 + 2\sigma_i e_i + \sigma_i^2 + \omega_i^2)}\right) \\ \left(\dfrac{(\sigma_i^2 + \omega_i^2 + \sigma_i e_i)\Re(b_i) - \omega_i e_i\Im(b_i))}{d_i(e_i^2 + 2\sigma_i e_i + \sigma_i^2 + \omega_i^2)}\right) \end{bmatrix} = \begin{bmatrix} 0 \\ \Phi_i^T B_{force_i} \end{bmatrix} \tag{D-49}$$

in order to satisfy equation (D-49)

$$(e_i+\sigma_i)\Re(b_i)+\omega_i\Im(b_i)=0$$

therefore **(D-50)**

$$e_i=-\sigma_i-\frac{\Im(b_i)}{\Re(b_i)}\omega_i$$

Combining the constraints from equations (D-48) and (D-50), the second transformation may be expressed as

$$\mathrm{T}_{2i}=\begin{bmatrix}\left(-\sigma_i-\dfrac{\Im(b_i)}{\Re(b_i)}\omega_i\right) & 1\\ \left(-\sigma_i^2-\omega_i^2\right) & \left(\sigma_i-\dfrac{\Im(b_i)}{\Re(b_i)}\omega_i\right)\end{bmatrix} \quad \textbf{(D-51)}$$

The ***mass normalisation scaling factor***, d_i, may be determined by co-located sensor/actuator information at physical degree of freedom q_k. Evaluating equations (D-39), (D-40) and (D-41) with the current transformation, we get the following matrices

$$A_{c\_norm}=\begin{bmatrix}0 & 1\\ -\omega_{nat_i}^2 & -2\xi_i\omega_{nat_i}\end{bmatrix}, \quad \textbf{(D-52)}$$

$$B_{c\_norm}=\begin{bmatrix}0\\ \dfrac{2\Re(b_i)}{d_i}\end{bmatrix}=\begin{bmatrix}0\\ \Phi_i^T B_{force}\end{bmatrix}, \text{ and} \quad \textbf{(D-53)}$$

$$C_{c\_norm}=\begin{bmatrix}d_i\left(\left(\dfrac{\Im(b_i)}{\Re(b_i)}\sigma_i-\omega_i\right)\Im(c_i)-\left(\sigma_i+\dfrac{\Im(b_i)}{\Re(b_i)}\omega_i\right)\Re(c_i)\right)\\ d_i\left(\Re(c_i)-\dfrac{\Im(b_i)}{\Re(b_i)}\Im(c_i)\right)\end{bmatrix}^{\mathrm{T}}=\begin{bmatrix}\Phi_i C_{displ}\\ 0\end{bmatrix}^{\mathrm{T}} \quad \textbf{(D-54)}$$

Thus for co-location $C_{displ}=(B_{force})^{\mathrm{T}}$, and hence the scaling factor for each mode is given by

$$d_i^2=\frac{2\Re(b_i)}{\left(\dfrac{\Im(b_i)}{\Re(b_i)}\sigma_i-\omega_i\right)\Im(c_k)-\left(\sigma_i+\dfrac{\Im(b_i)}{\Re(b_i)}\omega_i\right)\Re(c_k)} \quad \textbf{(D-55)}$$

The need to transform the output influence matrix, C_{accel}, if acceleration were measured as opposed to displacement or velocity, should now be apparent.

Recalling the state-space form of the output influence matrix, if acceleration were measured, is of the form given in equation (D-36), hence there would not be a unique solution to equation (D-54) for the value of the scaling factor, d_i.

In summary the time domain identification procedure, for the extraction of modal parameters provides a robust method for the extraction of undamped frequencies, modal damping coefficients and mass normalised mode shapes.

However, the one potential limitation of the procedure is the assumption that the measured system exhibit proportional damping. The theoretical development, see equation (D-34), assumes proportional damping for the decoupling of the second-order differential equations. If the structure is not proportional damped, which is commonly the case unless the system is nearly undamped, the mode shapes obtained from C_{c_norm} will contain some combination of both the in-phase and out-of-phase components of the complex mode shapes. The relative magnitude of these two components are reflected by the magnitudes of the subsets of the output influence matrix, and thus is useful in assessing the degree of non-proportionality in the damping of the respective modes.

D.3 Solution of Mass, Stiffness & Damping Matrices.

The solution technique is discussed in the literature review of section D.1.1, and graphically depicted in figure D-1. The Guyan statically condensed matrices are defined in the first subsection. These matrices are expressed in terms of the measured modal parameters, in the second subsection. While the third subsection defines the expressions for Craig Bampton reduced mass and stiffness matrices. The final subsection presents the substitution of the Guyan reduced mass and stiffness matrices, expressed in terms of the modal parameters, into the Craig Bampton mass and stiffness matrices. This work is described in *Alvin et. al. (1995)*[1] *and Alvin et. al. (1995)*[2]

D.3.1 Classical Guyan Reduction.

If we partition the degrees of freedom of the second order differential equation, into those dofs measured, q_m, and those dofs not measured, q_i, then

$$\begin{bmatrix} M_{mm} & M_{mi} \\ M_{mi}^T & M_{ii} \end{bmatrix}\begin{bmatrix} \ddot{q}_m \\ \ddot{q}_i \end{bmatrix}+\begin{bmatrix} C_{mm} & C_{mi} \\ C_{mi}^T & C_{ii} \end{bmatrix}\begin{bmatrix} \dot{q}_m \\ \dot{q}_i \end{bmatrix}\begin{bmatrix} K_{mm} & K_{mi} \\ K_{mi}^T & K_{ii} \end{bmatrix}\begin{bmatrix} q_m \\ q_i \end{bmatrix}=\begin{bmatrix} B_{force_m} \\ B_{force_i} \end{bmatrix}u_f(t) \qquad \textbf{(D-56)}$$

Suppose also that the generalised eigenproblem corresponding to equation (D-56) is satisfied, (also see equation (D-32)).

$$\begin{aligned} &(M^{-1}K)\Phi = \Phi\Omega \\ &\text{such that} \\ &\Phi^T M\Phi = I_{mxm} \quad \text{(definition of mass normalized eigenvectors)} \\ &\Phi^T K\Phi = \Omega = diag(\omega_{nat_i}^2 \quad i = 1,.....,m) \\ &\Phi^T C\Phi = \Xi = diag(2\xi_i\omega_{nat_i} \quad i = 1,.....,m) \end{aligned} \qquad \textbf{(D-57)}$$

If the static equations of equation (D-56) are solved, for B_{forcei}=0, then

$$q_i = -K_{ii}^{-1}K_{mi}^T q_m \qquad \textbf{(D-58)}$$

and hence a transformation is possible

$$q = \begin{bmatrix} q_m \\ q_i \end{bmatrix} = \begin{bmatrix} I \\ -K_{ii}^{-1}K_{mi}^T \end{bmatrix} q_m = \Phi_c q_m \qquad \textbf{(D-59)}$$

then applying this transformation to equation (D-56), the so-called Guyan Reduced mass, damping and stiffness matrices result, *(Guyan 1965)*

$$\begin{aligned} \overline{M} &= \Phi_c^T M \Phi_c \\ \overline{C} &= \Phi_c^T C \Phi_c \\ \overline{K} &= \Phi_c^T K \Phi_c = \left(K_{mm} - K_{mi}K_{ii}^{-1}K_{mi}^T\right) \end{aligned} \qquad \textbf{(D-60)}$$

D.3.2 Alternative Representation of Guyan Reduced Matrices.

The Guyan reduced matrices given in equation (D-60) may be expressed in terms of the normal modes of the full system. If it is assumed that the measured modes from the test completely span the dynamics of equation (D-56), such that the model representation in modal co-ordinates is a complete equivalent realization. Then the physical degrees of freedom $q(t)$ may be expressed in terms of the modal variables $\eta(t)$,

$$q = \begin{bmatrix} q_m \\ q_i \end{bmatrix} = \Phi\eta = \begin{bmatrix} \Phi_m \\ \Phi_i \end{bmatrix}\eta \qquad \textbf{(D-61)}$$

where Φ_m and Φ_i are partitions of the eigenvectors at the measured and unmeasured degrees of freedom, respectively. Using the results of equation (D-57) and assuming that there are no rigid-body modes, such that Ω is non-singular, the **inverse vibration problem** may be stated as

$$\boxed{\begin{aligned} M^{-1} &= \Phi\,\Phi^T \\ C^{-1} &= \Phi\,\Xi^{-1}\,\Phi^T \\ K^{-1} &= \Phi\,\Omega^{-1}\,\Phi^T \end{aligned}} \qquad \textbf{(D-62)}$$

D.3.2.1 Mass Matrix

The mass matrix may be stated as

$$M = KK^{-1}MK^{-1}K \qquad \textbf{(D-63)}$$

Substituting K^{-1}, as given by equation (D-62) into equation (D-63)

$$\begin{aligned} M &= K\Phi\Omega^{-1}\left(\Phi^T M\Phi\right)\Omega^{-1}\Phi^T K \\ M &= K\Phi\Omega^{-2}\Phi^T K \end{aligned} \qquad \textbf{(D-64)}$$

Then applying the Guyan transformation of equation (D-61),

$$\begin{aligned} &\overline{M} = \Phi_c^T\left(K\Phi\Omega^{-2}\Phi^T K\right)\Phi_c \quad \text{hence} \\ &\boxed{\overline{M} = \overline{K}\Phi\Omega^{-2}\Phi^T\overline{K}} \end{aligned} \qquad \textbf{(D-65)}$$

D.3.2.2 Damping Matrix

Following an identical derivation, to that described for the mass matrix, the Guyan reduced damping matrix may be expressed in terms of the system's eigenvectors as

$$C = K\Phi\Omega^{-1}\left(\Phi^T C\Phi\right)\Omega^{-1}\Phi^T K$$
$$C = K\Phi\Omega^{-1}\Xi\Omega^{-1}\Phi^T K \qquad \textbf{(D-66)}$$

Then applying the Guyan transformation of equation (D-61),

$$\overline{C} = \Phi_c^T\left(K\Phi\Omega^{-1}\Xi\Omega^{-1}\Phi^T K\right)\Phi_c \quad \text{hence}$$
$$\boxed{\overline{C} = \overline{K}\Phi\Omega^{-1}\Xi\Omega^{-1}\Phi^T\overline{K}} \qquad \textbf{(D-67)}$$

D.3.2.3 Stiffness Matrix.

The inverse of the stiffness matrix, defined in equation (D-56), can be algebraically described by

$$K^{-1} = \begin{bmatrix} \overline{K}^{-1} & -\overline{K}^{-1}K_{mi}K_{ii}^{-1} \\ -K_{ii}^{-1}K_{mi}^T\overline{K}^{-1} & K_{ii}^{-1}\left(I + K_{mi}^T\overline{K}^{-1}K_{mi}K_{ii}^{-1}\right) \end{bmatrix} \qquad \textbf{(D-68)}$$

Using the partition of the system eigenvectors, Φ ; equation (D-61), and the inverse vibration results, K^{-1} may be stated

$$K^{-1} = \begin{bmatrix} \Phi_m\Omega^{-1}\Phi_m^T & \Phi_m\Omega^{-1}\Phi_i^T \\ \Phi_i\Omega^{-1}\Phi_m^T & \Phi_i\Omega^{-1}\Phi_i^T \end{bmatrix} \qquad \textbf{(D-69)}$$

and hence the Guyan Reduced stiffness matrix can be stated as

$$\boxed{\overline{K} = \left(\Phi_m\Omega^{-1}\Phi_m^T\right)^{-1}} \qquad \textbf{(D-70)}$$

D.3.3 Craig-Bampton Component Mode Synthesis Method

The Craig Bampton Component Mode Synthesis (CMS) method *Longman & Juang (1987)* defines

$$q_i = -K_{ii}^{-1} K_{mi}^T q_m + T_\xi \xi \tag{D-71}$$

where ξ is the augmented generalised degree of freedom and T_ξ are the displacements of q_i with respect to unit displacements of ξ . In the Craig Bampton CMS method ξ is defined as the fixed interface modal co-ordinates of the residual structure and related to T_ξ by the eigenvalue problem

$$\begin{aligned} &K_{ii} T_\xi = M_{ii} T_\xi \Omega_\xi \\ &\text{and} \\ &T_\xi^T K_{ii} T_\xi = \Omega_\xi \\ &T_\xi^T M_{ii} T_\xi = I \end{aligned} \tag{D-72}$$

Thus, the variable transformation, T_{CMS}, is

$$q = \begin{bmatrix} q_m \\ \xi \end{bmatrix} = \begin{bmatrix} I & 0 \\ -K_{ii}^{-1} K_{mi}^T & T_\xi \end{bmatrix} \begin{bmatrix} q_m \\ \xi \end{bmatrix} = T_{CMS}\, q \tag{D-73}$$

Applying this transformation the so-called Craig Bampton mass, damping and stiffness matrices result, *(Craig & Bampton 1968)*

$$\begin{aligned} \hat{M} &= T_{CMS}^T M T_{CMS} = \begin{bmatrix} \overline{M} & \left(M_{mi} T_\xi - K_{mi} K_{ii}^{-1} M_{ii} T_\xi\right) \\ \left(M_{mi} T_\xi - K_{mi} K_{ii}^{-1} M_{ii} T_\xi\right) & I \end{bmatrix} \\ \hat{K} &= T_{CMS}^T K T_{CMS} = \begin{bmatrix} \overline{K} & 0 \\ 0 & \Omega_\xi \end{bmatrix} \end{aligned} \tag{D-74}$$

D.3.4 Express Craig Bampton Matrices in terms of Measured Modal Parameters.

The Craig Bampton CMS representations for the mass, damping and stiffness matrices can now be expressed in terms of the alternative form of the Guyan reduced matrices. This allows the Craig Bampton CMS representations for the mass, damping and stiffness matrices to be expressed in terms of *the measured modal parameters ,*

I) the mass normalised mode shapes , Φ, and

ii) the undamped natural frequencies , Ω

Consider the eigenproblem

$$\hat{K} \begin{bmatrix} \Phi_m \\ \Phi_{resl} \end{bmatrix} = \hat{M} \begin{bmatrix} \Phi_m \\ \Phi_{res} \end{bmatrix} \Omega$$

then substituting (D-75)

$$\begin{bmatrix} \overline{K} & 0 \\ 0 & \Omega_\xi \end{bmatrix} \begin{bmatrix} \Phi_m \\ \Phi_{res} \end{bmatrix} = \begin{bmatrix} \overline{M} & \left(M_{mi} T_\xi - K_{mi} K_{ii}^{-1} M_{ii} T_\xi\right) \\ \left(M_{mi} T_\xi - K_{mi} K_{ii}^{-1} M_{ii} T_\xi\right)^T & I \end{bmatrix} \begin{bmatrix} \Phi_m \\ \Phi_{res} \end{bmatrix} \Omega$$

then normalising

$$\begin{bmatrix}\Phi_m^T & \Phi_{res}^T\end{bmatrix}\begin{bmatrix}\overline{K} & 0\\ 0 & \Omega_{res}\end{bmatrix}\begin{bmatrix}\Phi_m\\ \Phi_{res}\end{bmatrix}=\Omega \qquad \textbf{(D-76)}$$

substituting the definition for the Guyan Reduced form of stiffness matrix, equation (D-70), and solving for equation (D-76) results in

$$\begin{aligned}&\Phi_m^T\overline{K}\Phi_m+\Phi_{res}^T\Omega_{res}\Phi_{res}=\Omega\\ &\Phi_m^T\left(\Phi_m\Omega^{-1}\Phi_m^T\right)^{-1}\Phi_m+\Phi_{res}^T\Omega_{res}\Phi_{res}=\Omega\end{aligned} \qquad \textbf{(D-77)}$$

and hence maybe rewritten as

$$\Delta\Omega=\left(\Phi_{res}^T\Omega_{res}\Phi_{res}\right)=\Omega-\Phi_m^T\left(\Phi_m\Omega^{-1}\Phi_m^T\right)^{-1}\Phi_m \qquad \textbf{(D-78)}$$

The required minimal rank augmentation of q_m is determined through the dynamic residual matrix $\Delta\Omega$. To find the rank of Ω_{res} and a vector basis for Φ_m, the singular value decomposition technique is utilised

$$P\,S\,P^T = \textbf{svd}(\Delta\Omega) \qquad \textbf{(D-79)}$$

Then, examining the singular values of $\Delta\Omega$, i.e. the diagonal terms of S, the required dimension of the augmented co-ordinate ξ may be determined. Typically, with p independent spatial measurements, $\Phi_m^T\overline{K}\Phi_m$ will be typically of rank p, whereas Ω is rank n. Then the rank of $\Phi_{res}^T\Omega_{res}\Phi_{res}$ is $(n-p)$.

Having determined a basis P_p for the augmented co-ordinates

$$\Delta\Omega = P\,S\,P^T = P_p\,S_p\,P_p{}^T \qquad \textbf{(D-80)}$$

Φ_m can be augmented by the rows of P_p^T, which span the singular values and the inverse vibration problem solved , see equation (D-62)

$$\begin{aligned}&\begin{bmatrix}\overline{K} & 0\\ 0 & K_{res}\end{bmatrix}=\begin{bmatrix}\Phi_m\\ P_p^T\end{bmatrix}^{-T}\Omega\begin{bmatrix}\Phi_m\\ P_p^T\end{bmatrix}^{-1}\\ &\begin{bmatrix}\overline{M} & \tilde{M}\\ \tilde{M}^T & M_{res}\end{bmatrix}=\left(\begin{bmatrix}\Phi_m\\ P_p^T\end{bmatrix}\begin{bmatrix}\Phi_m^T & P_p\end{bmatrix}\right)^{-1}\end{aligned} \qquad \textbf{(D-81)}$$

Finally normalising

$$\begin{aligned}&K_{res}U=M_{rss}U\Omega_{res}\\ &\text{and}\\ &U^TK_{res}U=\Omega_{res}\\ &U^TM_{res}U=I\end{aligned} \qquad \textbf{(D-82)}$$

to result in the

$$\hat{K} = \begin{bmatrix} I & 0 \\ 0 & U^T \end{bmatrix} \begin{bmatrix} \overline{K} & 0 \\ 0 & K_{res} \end{bmatrix} \begin{bmatrix} I & 0 \\ 0 & U \end{bmatrix} = \begin{bmatrix} \overline{K} & 0 \\ 0 & \Omega_{res} \end{bmatrix}$$

$$\hat{M} = \begin{bmatrix} I & 0 \\ 0 & U^T \end{bmatrix} \begin{bmatrix} \overline{M} & \tilde{M} \\ \tilde{M}^T & M_{res} \end{bmatrix} \begin{bmatrix} I & 0 \\ 0 & U \end{bmatrix} = \begin{bmatrix} \overline{M} & \left(M_{mi}T_\xi - K_{mi}K_{ii}^{-1}M_{ii}T_\xi\right) \\ \left(M_{mi}T_\xi - K_{mi}K_{ii}^{-1}M_{ii}T_\xi\right)^T & I \end{bmatrix} \quad \textbf{(D-83)}$$

The Craig Bampton damping matrix may also be determined by

$$\begin{bmatrix} \overline{C} & 0 \\ 0 & C_{res} \end{bmatrix} = \begin{bmatrix} \Phi_m \\ P_p^T \end{bmatrix}^{-T} \Xi \begin{bmatrix} \Phi_m \\ P_p^T \end{bmatrix}^{-1} \quad \textbf{(D-84)}$$

and hence

$$\hat{C} = \begin{bmatrix} I & 0 \\ 0 & U^T \end{bmatrix} \begin{bmatrix} \overline{C} & 0 \\ 0 & C_{res} \end{bmatrix} \begin{bmatrix} I & 0 \\ 0 & U \end{bmatrix} \quad \textbf{(D-85)}$$

D.4 Software Implementation of the Time Domain Identification.

This section presents the software implementation of the Time Domain Identification procedure. The mathematical visualisation software, Matlab™ , was used as the principle development tool. Once the development was complete the Matlab files were translated, using the *matcom* translator, into C++ code and compiled into executable form using the Borland™ C++ V4.52 compiler. The software listing is given in **Appendix IV.**

The software programs combine in the sequence shown in figure D-2

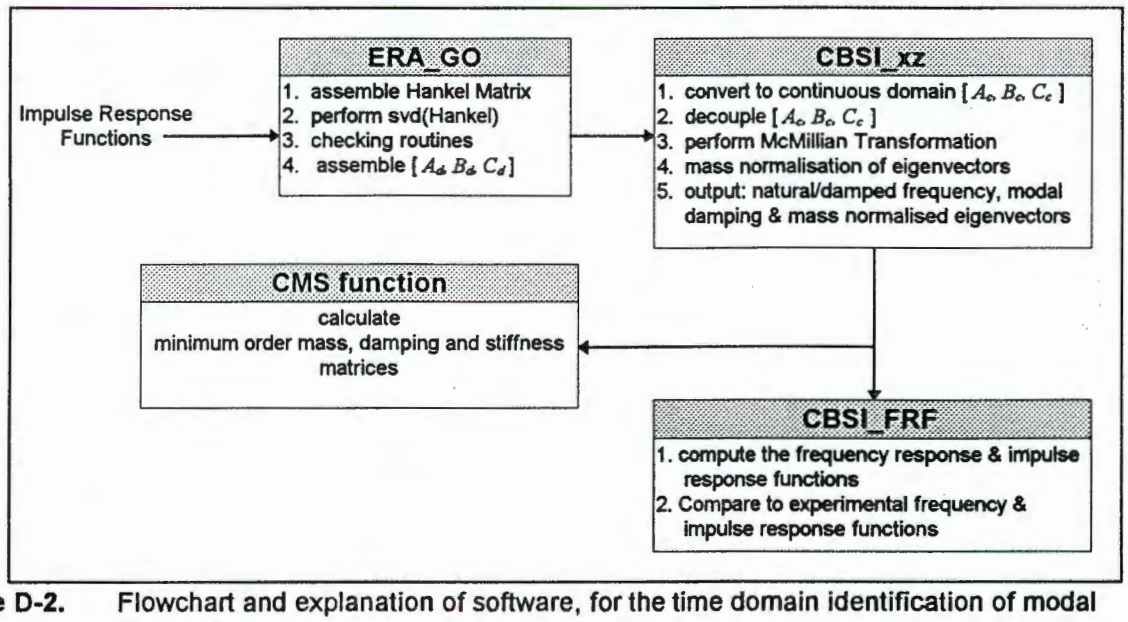

Figure D-2. Flowchart and explanation of software, for the time domain identification of modal Parameters.

Chapter E.

Experimental Details.

E. Experimental Details.

The experimental apparatus is shown schematically in figure E-1. The input force was applied by means of an impact hammer, the hammer head being fitted with a load cell. The vibration response of the structure was measured by three accelerometers. One of the accelerometers was located directly opposite the impact location on the structure.

Both the force and response signals were passed through signal conditioning equipment, which included low-pass and anti-aliasing filters, before being digitised. The frequency response, coherence function and impulse response functions were then calculated. The details of each component of the experimental apparatus are next described.

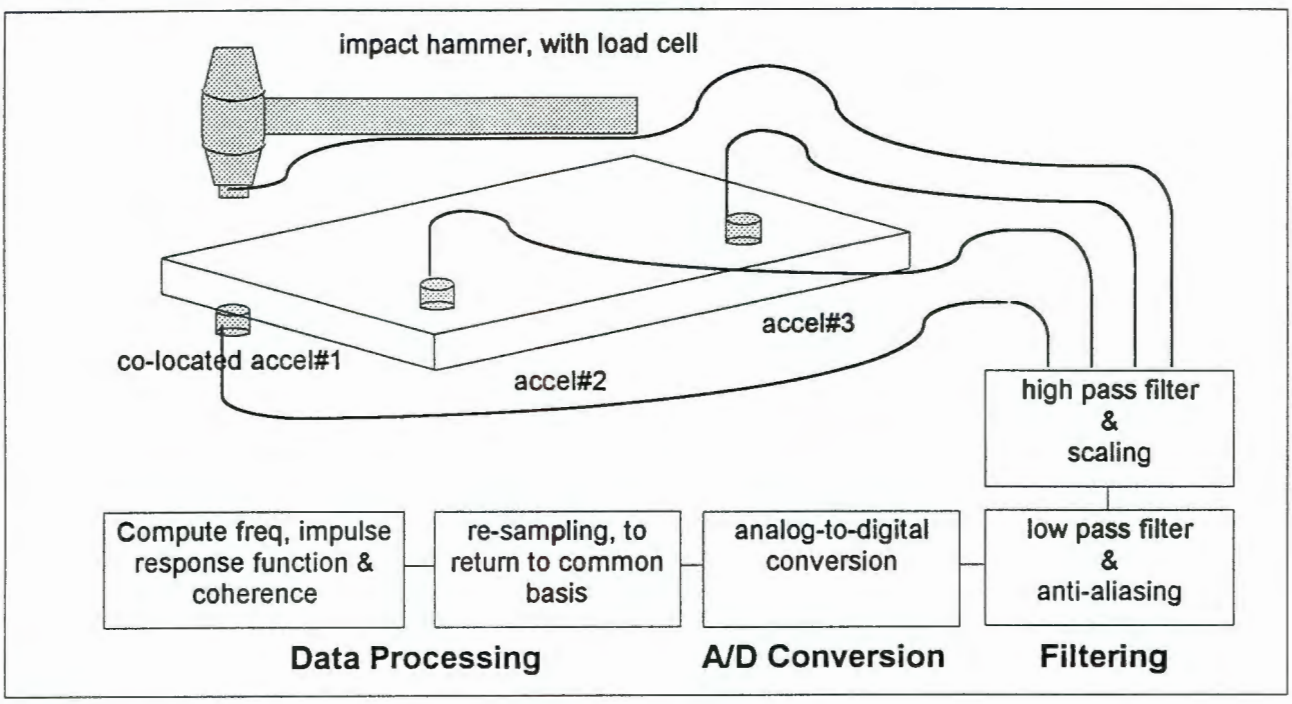

Figure E-1 Schematic of the experimental apparatus for the impulse response technique.

E.1 Impulse Response Technique.

The impulse response technique provides a fast way of performing transient vibration tests. The impact hammer is generally hand held, or may be suitably suspended. The impact hammer head has a load cell fitted which measures the input force directly.

In general, the impulse response technique enjoys several advantages, over traditional vibration measuring techniques:

- No fixtures are required for attachment to the test structure,
- no electro-mechanical, electromagnetic or electro-hydraulic exciters are required, and
- the impulse response method is faster and more portable than other traditional techniques.

However , the impulse response technique also has some disadvantages:

- Due to the variation in the shape and magnitude of the input force signal the power spectrum of the input force is not easily controlled.
- Since the total energy supplied by the impact is distributed over a broad frequency range, the actual excitation energy density is often quite small When testing large heavily damped structures the accuracy of the frequency response function may deteriorate due to the poor signal-to-noise ratio of the measurement. Ensemble averaging is advised to overcome the problem of poor signal-to-noise ratio.
- A further drawback is the degree of damping of the test structure. As the response signal decays to zero, its signal-to-noise ratio diminishes. If it has decayed to a small value inside the data window, the post data processing will be operating mostly on noise. This results in uncertainties in the frequency responses function measurement. This problem becomes more acute as higher frequency spans are required, as the measurement data window decreases in size.

  Also, as the measurement data window decreases, the damped transient response may not decay to zero. This windowing effect, is especially serious for lightly damped structures, which tend to vibrate for a long time and led to leakage in the frequency domain.

E.2 Description of Test Structure.

A uniform cross-section, low carbon steel beam was used as the test structure. In an effort to ensure optimum contact between the response accelerometers and the beam the mill scale was removed by machining. The density of the steel was calculated from the weight and volume of the beam. The mechanical properties that were used for the finite element model are given in Table E-1

Table E-1. The material properties of the test structure.

Parameter	Numerical Value & Units
length	500.0 mm
width	48.10 mm
height	19.20 mm
Poisson's Ratio, ν	0.3
Young's Modulus, E	204 GPa
Shear Modulus, G	78.4 GPa
density, ρ	7860 kg/m^3

During the vibration measurement procedure the beam was suspended by two rubber slings. The beam was excited in the plane orthogonal to the direction of the suspended rubber slings, so as not to extend the slings during the measurement of the vibration response.

The beam was thus free to swing in the plane of excitation, under it's own weight. The assumption was made that the vibration measurements were conducted with 'free-free' boundary conditions. This boundary condition assumption was used for the finite element model of the structure. In light of the experimental results this assumption seems valid.

E.3 Impact Hammer Design & Construction.

The magnitude of the impact force is determined by the mass of the hammer head and the velocity with which it is moving when it impacts the structure. Often, the operator will control the velocity rather than the force itself, and so an appropriate way of adjusting the magnitude of the impact force is by varying the mass of the hammer head.

The frequency range which is effectively excited is determined by the mass of the hammer head and the stiffness of the contacting surfaces. An initial resonant, *freq*, will occur at the frequency given by

$$freq = \sqrt{\left(\frac{\text{contact stiffness}}{\text{mass of hammer head}}\right)} \qquad \textbf{(E-1)}$$

Above the frequency of the first resonant it is difficult to input energy into the structure, thus it is desirable that the frequency range of interest is less than the first resonant frequency. Either the hammer head contact stiffness or hammer head mass should be adjusted to ensure this constraint.

Thus the hammer head mass influences both the magnitude of the force produced and the useful frequency span for vibration measurements. There is also a relation between the duration of the impact and the contact stiffness, the higher the contact stiffness the shorter the duration of the impact and hence the larger the useful frequency span. This is depicted graphically in figure E-2.

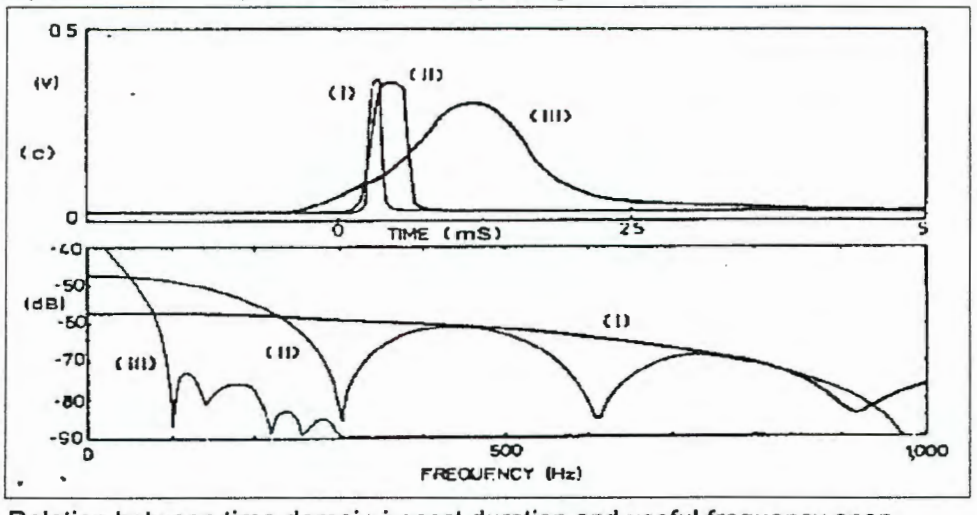

Figure E-2: Relation between time-domain impact duration and useful frequency span.

In order to gain some insight to the ideal mass of the hammer head, the brochures of a number of impact hammer manufactures were scrutinised. e.g. *PCB manual.* It was decided to use a hammer head mass of approximately 120 grams. This mass was slightly less than that specified for the general purpose impact hammer, 140 gram, offered by *PCB Piezotronics* as Model K291-A and Model 086-C03 respectively. In the design of the hammer head provision was made for an additional mass to be fastened to the unused contact surface of the hammer head, should greater input energy be required. This feature was not used.

The hammer handle should ideally be as stiff as possible, so as not to dampen the impact. This is contrary to the requirements of a normal hammer, where some damping may be desirable. The hammer handle should also be as light as possible, to ensure that the centre of percussion is coincident with the centre of the hammer head. This ensures that no torque reaction is experienced. A carbon fibre tube of dimensions OD 17.8 mm, ID 15.8 mm and length 260 mm was generously donated by Aerodyne Engineering, of Somerset West.

The impact hammer head was constructed in the Mechanical Engineering workshop, and subsequently the impact hammer was assembled and glued by Aerodyne Engineering. The construction drawings of the impact hammer head is shown in Figure E-3

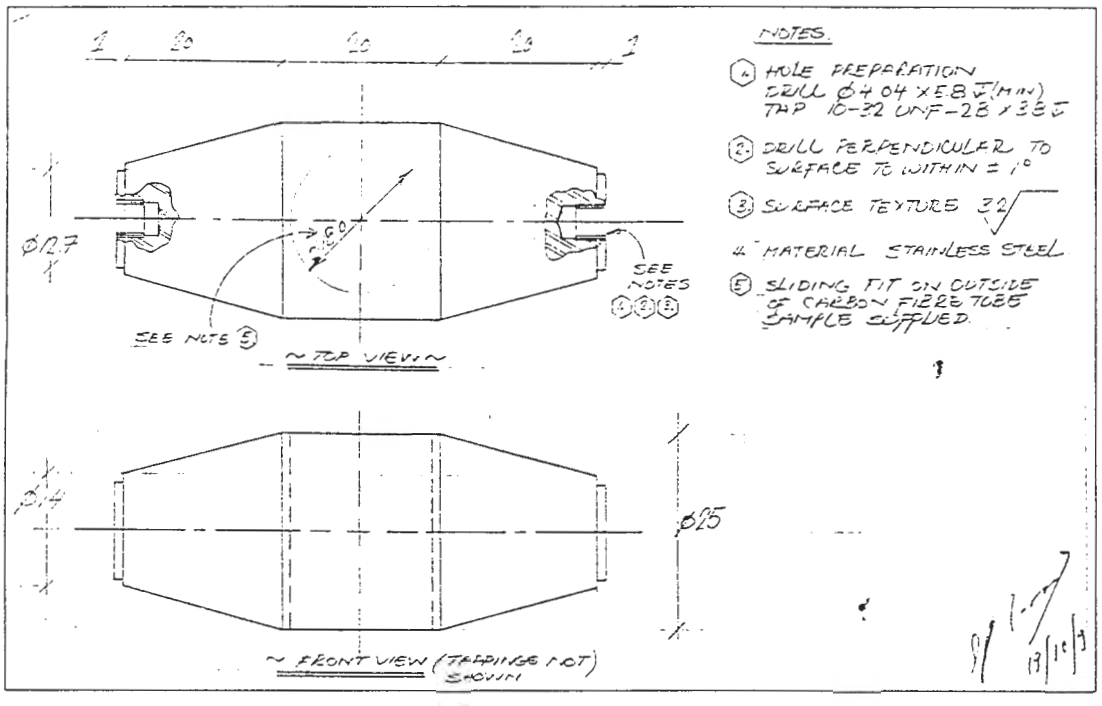

Figure E-3 Construction Drawing of Impact Hammer Head.

E.4 Force Transducer.

A *PCB Piezotronics Inc.*, ICP force sensor Model 208-B03, serial number 12465 was utilised. The force range of the force transducer was 0 to 500 lb., and the corresponding voltage range was 0 to 5V. A copy of the specifications are included in **Appendix III-1.1**

The power supply required by the force transducer was a 24-30 volt DC power source at 2.0mA current. The PCB Piezotronics Inc., Battery Powered Signal Conditioner model 480-D09, serial number 4077 was utilised. A copy of the specifications are similarly included in **Appendix III-1.1** Three additional power supply units, custom built within the Mechanical Engineering Department, were used for the accelerometers. Investigations showed that these custom built power supplies had similar power characteristics as the PCB Piezotronics Inc., Battery Powered Signal Conditioner.

E.5 Accelerometers.

Three *Wilcoxon Research* , ICP accelerometers were utilised: Model *736*, Serial numbers *747, 748* & *749*. A copy of the specifications are included in **Appendix III-1.2.**

E.5.1 Calibration.

The calibration of the response accelerometers was conducted within Stellenbosch University's Mechanical Engineering Department. *(personal correspondence Dr. N. Theron).* Each of the accelerometers were consecutively placed in series with a reference accelerometer. The assembly was secured to a mini-shaker, type *B&K* (model unknown), which was driven by a white noise signal. The response of both the reference accelerometer and test accelerometer were processed by the *Modal Plus software, version 3.* Typical comparative results for one accelerometer are shown in **Appendix III-1.3.** Each of the three accelerometers showed similar results within 2%. Hence it was decided not to correct for the deviation from the reference accelerometer.

E.5.2 Mounting Details.

The co-located accelerometer was stud mounted to the test structure, while the other two test accelerometers were attached to the test structure via magnetic bases. *Ewins (1984)* discusses the resonant characteristics of accelerometers when mounted in varying configurations, see figure E-4. The resonant frequency of the magnetically mounted accelerometer in the region of 5 kHz was not detected.

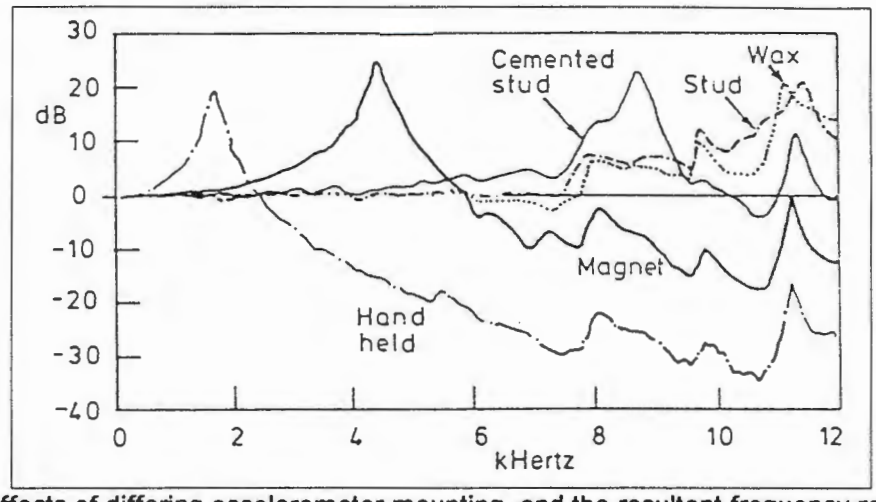

Figure E-4 The effects of differing accelerometer mounting, and the resultant frequency response.

E.5.3 Measurement Locations.

Two methods were used to decide the placement of the response accelerometers and impact location, on the test structure. First, predicted mode shapes from classical Euler beam theory were considered. The Timoshenko finite element beam software, as discussed in Chapter C, was then utilised to verify these mode shapes. Guided by the position of the respective mode shapes the measurement locations were finalised.

E.5.3.1 Mode Shapes Predicted by Euler Beam Theory.

The mode shapes of a free-free supported beam, are found from the solution of equation (E-2),

$$\frac{\partial^2}{\partial x^2}\left[EI(x)\frac{\partial^2 w(x,t)}{\partial x^2}\right]+\rho A(x)\frac{\partial^2 w(x,t)}{\partial t^2}=f(x,t) \qquad \textbf{(E-2)}$$

and for a uniform cross-section beam

$$\left[EI\frac{\partial^4 w(x,t)}{\partial x^4}\right]+\rho A\frac{\partial^2 w(x,t)}{\partial t^2}=f(x,t) \qquad \textbf{(E-3)}$$

The *free solution* can be found using the method of separation of variables as

$$w(x,t)=W(x)T(t) \qquad \textbf{(E-4)}$$

where it can be shown that

$$T(t)=A\cos(\omega t)+B\sin(\omega t) \qquad \textbf{(E-5)}$$

where A & B are constants found from the initial conditions, (typically both zero velocity and displacement), and

$$W(x)=C_1e^{\beta x}+C_2e^{-\beta x}+C_3e^{j\beta x}+C_4e^{-j\beta x} \qquad \textbf{(E-6)}$$

where C_1, C_2, C_3 & C_4 are constants found from the free-free boundary conditions,(E-7)

$$\text{bending moment} = EI\frac{\partial^2 w(x,t)}{\partial x^2} = 0$$

and **(E-7)**

$$\text{shear force} = \frac{\partial}{\partial x}\left(EI\frac{\partial^2 w(x,t)}{\partial x^2}\right) = 0$$

and the natural frequencies of the beam

$$\omega = \beta^2\sqrt{\frac{EI}{\rho A}} = (\beta l)^2\sqrt{\frac{EI}{\rho A l^4}} \qquad \textbf{(E-8)}$$

The mode shapes are for the first six natural frequencies are plotted in figure E-5. Notice that the mode shapes are invariant to both the dimensions and beam material. These parameters only influence the value of the natural frequencies, as shown in equation (E-8).

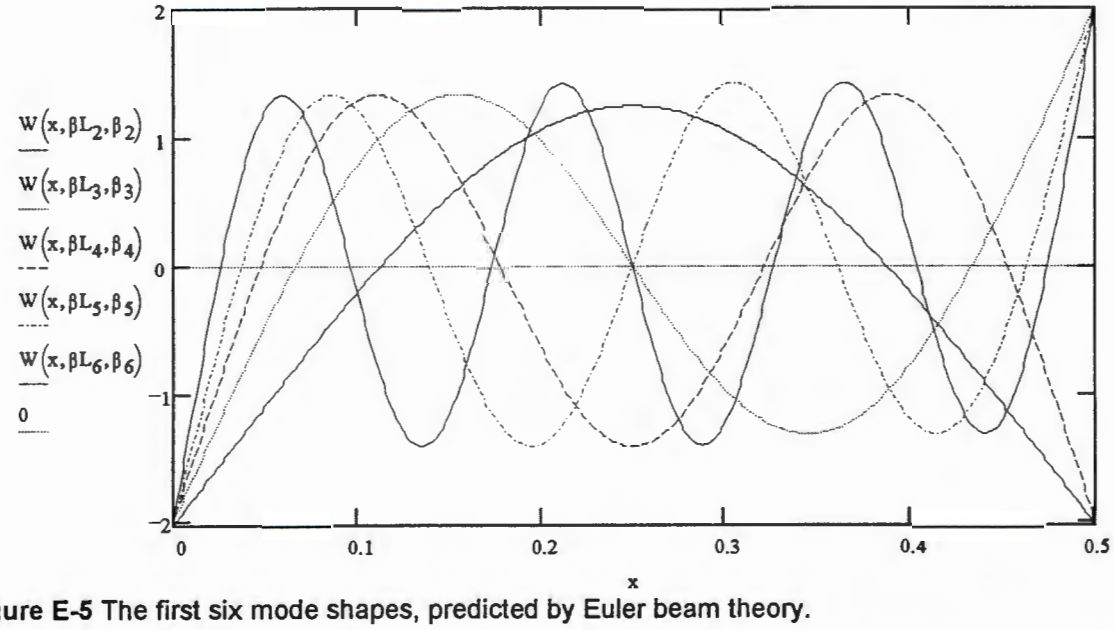

Figure E-5 The first six mode shapes, predicted by Euler beam theory.

From inspection of figure E-5, it was decided to impact the beam at 0.16m, while detecting the response at locations 0.3m and 0.35m. The motivation for these choices was that the majority of the first six modes anti-nodes are at maximum values at these locations. Thus, the respective responses would be most influenced by these modes. (In contrast, if an accelerometer were placed at 0.25m then only modes #1 and #4 would be detected)

E.5.3.2 Mode Shapes Predicted by Timoshenko Beam Element.

A similar analysis of mode shapes was conducted using the Timoshenko beam element, developed in chapter C. The mode shapes predicted form the finite element code are presented in figures E-6 & E-7. The mode shapes are similar to those predicted by Euler beam theory, and hence the previously defined locations were retained.

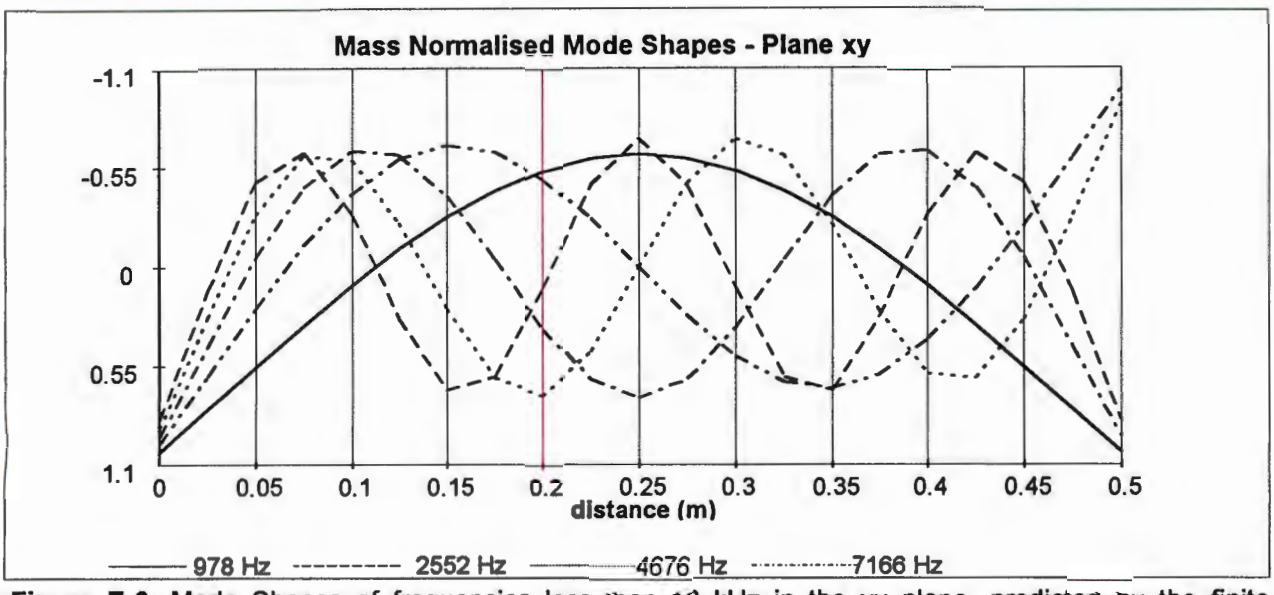

Figure E-6. Mode Shapes of frequencies less than 10 kHz in the xy plane, predicted by the finite element code developed in Chapter C.

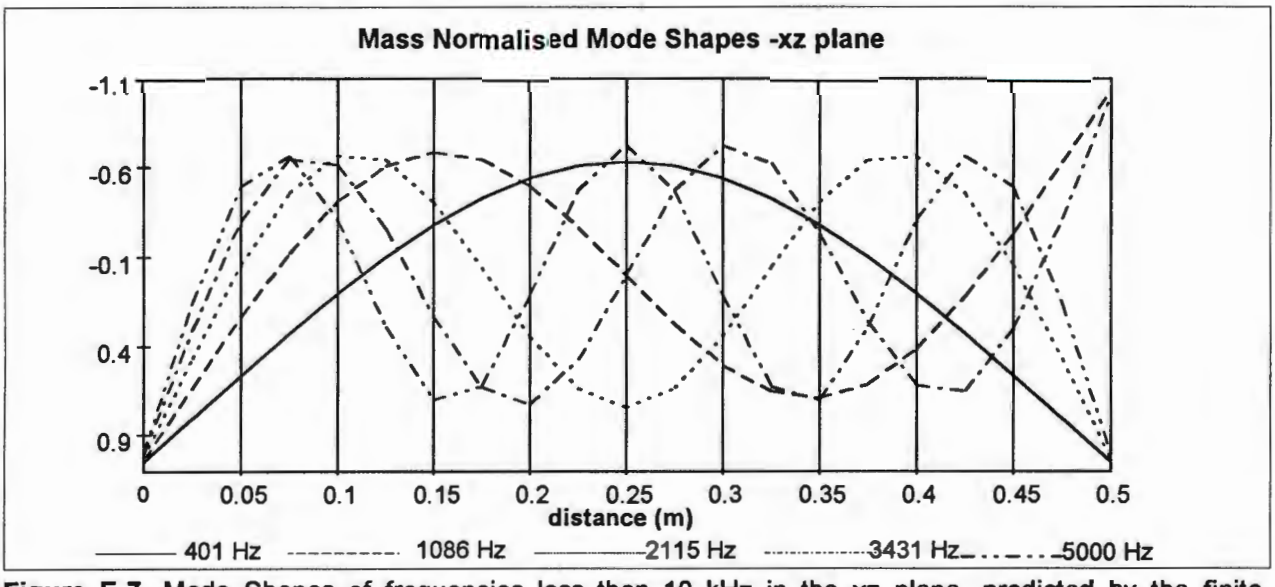

Figure E-7. Mode Shapes of frequencies less than 10 kHz in the xz plane, predicted by the finite element code developed in Chapter C.

E.5.4 Measurement Configuration.

The measurement locations for both the impact and response measurement locations are given in Table E.2. The letter designation referring to the specific force transducer or accelerometer are also given in the Table. These letter designations are also used to refer to the frequency and impulse response functions between the force transducer location and the response accelerometer location. For example the frequency response function, H_pq($j\omega$), refers to the frequency response function between the input location at 0.16m and response location at 0.30m.

Table E.2 Measurement locations and naming convention

	location on structure	channel	designation
Force Transducer	0.16 m	channel #1	p
Accelerometer #1	0.30 m	channel #2	q
Accelerometer #2	0.35 m	channel #3	r
Accelerometer #3	0.16 m	channel #4	s

E.6 Choice of Sampling Frequency.

If a signal $x(t) \overset{FFT}{\Leftrightarrow} X(\omega)$ is strictly band-limited in the frequency domain, to a maximum frequency content of ω_{max}. Then $x(t)$ can be completely specified by and can be exactly recovered from a sequence of equally spaced samples *'if and only if'* the sampling frequency, ω_s, satisfies the Nyquist criteria, equation (E-9).

$$\omega_s \geq 2\omega_{max} \qquad \textbf{(E-9)}$$

If $x(t)$ is not strictly band limited i.e. equation (E-9) is invalidated, then aliasing will occur. Recovery of the original signal will not be possible, as the frequency transform will be corrupted. In this case the signal should first be band-limited, by means of a low pass filter prior to sampling. In the context of this thesis both the signal of the force transducer and accelerometers process infinite frequency spectrums, thus low pass filtering prior to sampling is essential.

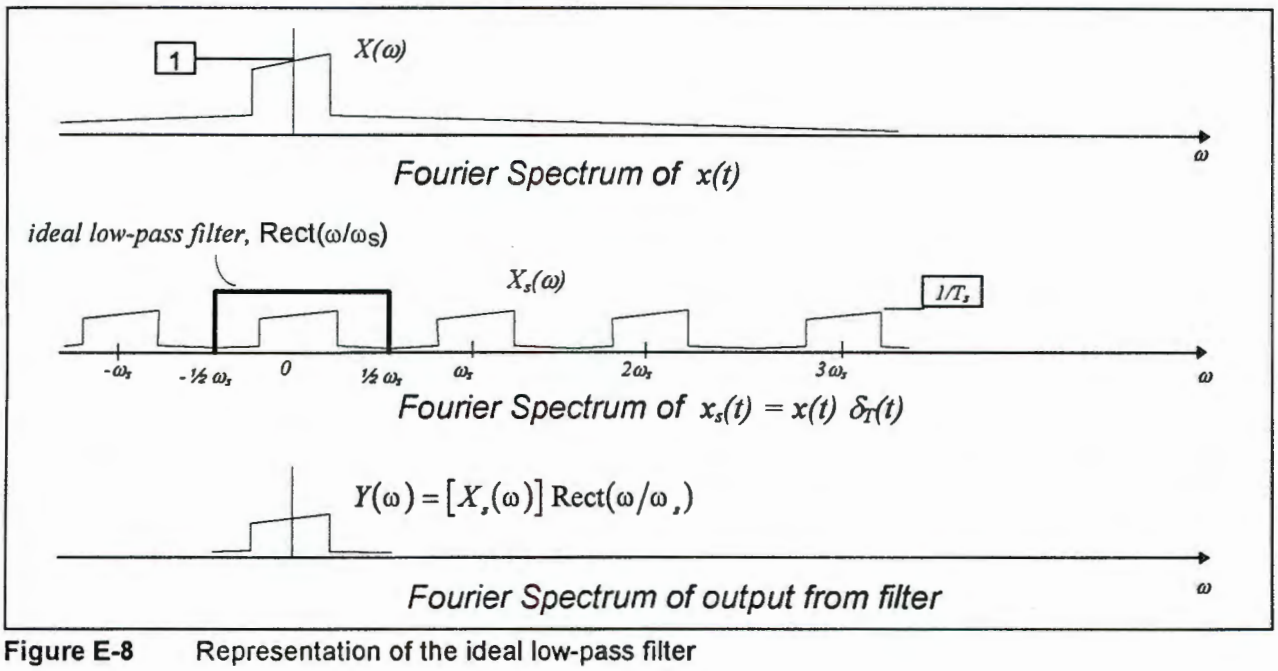

Figure E-8 Representation of the ideal low-pass filter

Two distinct types of time-domain signals are recovered:-

1. a finite span pulse in the time domain is recovered from the force transducer, while
2. a response of infinite span is recovered from each of the accelerometers.

To ensure accurate and adequate sampling of the frequency spectrum, the suitable choice of the sampling time and sampling frequency are essential.

The relation of sampling time and span of the response is given as

$$T_0 = NT_s \qquad \textbf{(E-10)}$$

where N is the number of samples and should always be chosen as large as practically possible. In this dissertation N is chosen as 2^{13}=8192 samples. The choice of T_0 is governed by the rate of decay of the accelerometer responses, rather than the finite pulse characteristics.

E.6.1 Infinite Span Pulse, Accelerometer Response.

The fourier transform cannot be used to estimate the fourier spectrum of pulses which do not decay to zero. For this reason *Halvorsen & Brown (1977)* recommend the use of an exponential window, which is multiplied by the infinite span pulse to force the resulting product to zero within the time period , T_0. However the result is to corrupt the fourier spectrum, as multiplication in the time domain is equivalent to convolution in the frequency domain. The corrupted spectrum is unable to correctly predict the modal damping coefficients, while the resonant frequencies and mode shapes remain invariant to the frequency domain convolution. In the context of this thesis it was considered that accurate knowledge of the modal damping coefficients was essential and thus discounted this method. Instead the time window was chosen to be large to enable the structure to naturally decay. The time period was chosen to be approximately

$$T_0 \cong 200 \text{ millisecond} \qquad \textbf{(E-11)}$$

thus by equation (E-10) the sampling time is

$$T_s = 25 \text{ microsecond} \qquad \textbf{(E-12)}$$

and hence the sampling frequency is

$$freq_s = 40 \text{ kHz} \qquad \textbf{(E-13)}$$

E.6.2 Finite Span Pulse, Force Transducer Response.

The sampling time, chosen for the infinite span signals, must be capable of accurately sampling the finite span of the force transducer. During preliminary investigations it was noticed that the average duration of the impact on a steel structure was 250 to 375 microseconds. Thus the finite span pulse is described by between 10 and 15 samples. This number was considered adequate, considering that a minimum of two samples are sufficient.

E.7 Filter Design & Construction.

As discussed in section D.6, both the response and input signals should be band-limited prior to the application of the fourier transform. This section discusses the specification and subsequent construction of such a band limiting filter.

The voltage characteristics of the respective signals to be filtered are listed in Table E-3. The DC offset is due to the operation of the ICP transducers and is usually automatically removed on Spectrum Analysers by activating the *'AC coupling'* feature. For this application, a high pass filter is necessary to remove the DC offset, prior to low pass filtering and sampling.

Table E-3 General characteristics of the respective signals

	Force Transducer	Accelerometers
AC Signal	0 ⇒ 5 V (overload if > 5V)	-5V ⇔ +5 V (overload if > +5V or < -5V)
approx. DC bias	12 ⇒ 15 V	12 ⇒ 15 V

E.7.1 Assessment of Desirable Frequency Range.

Two requirements were considered in defining the desirable frequency range. One requirement was ensuring that sufficient natural modes were within the frequency range, while the second requirement was to ensure that the sampling theory criteria were not violated.

- In the frequency range below 10 kHz, the finite element model of the test structure predicted six natural flexural modes in the *xz* plane, and four in the orthogonal *xy* plane of the test structure. (excluding rigid body-motions) This number of natural modes within the frequency bandwidth was considered adequate for the purpose of this dissertation.

- The Nyquist Criteria, as discussed in section D.6, requires that the sampling frequency be at least twice the highest frequency content of the signal to be sampled. Due to the fall-off of the low pass filter it was decided to assign the low pass filter cut-off at approximately 8 to 10 kHz.

E.7.2 High Pass Filter.

A classical high pass, leading phase, filter circuit was designed for each channel. The transfer function and phase characteristics of the circuit are defined by equation (E-14).

$$H(j\omega) = \frac{j\omega}{j\omega + \omega_{nat}} \qquad \textbf{(E-14)}$$

where ω_{nat} is the cut-off frequency of the circuit

$$\omega_{nat} = {}^{1}\!/_{R_1 C} \qquad \textbf{(E-15)}$$

The cut-off frequency was chosen to be below 1.0 Hz. From equation (E-15) the components R_1 and C were set as R_1=100KΩ and C=2.2μF, as shown in figure E-9. The theoretical cut-off frequency is thus 0.723 Hz. The reader is referred to the section on calibration of the completed filter, where the actual characteristics of the high pass filter can be better appreciated.

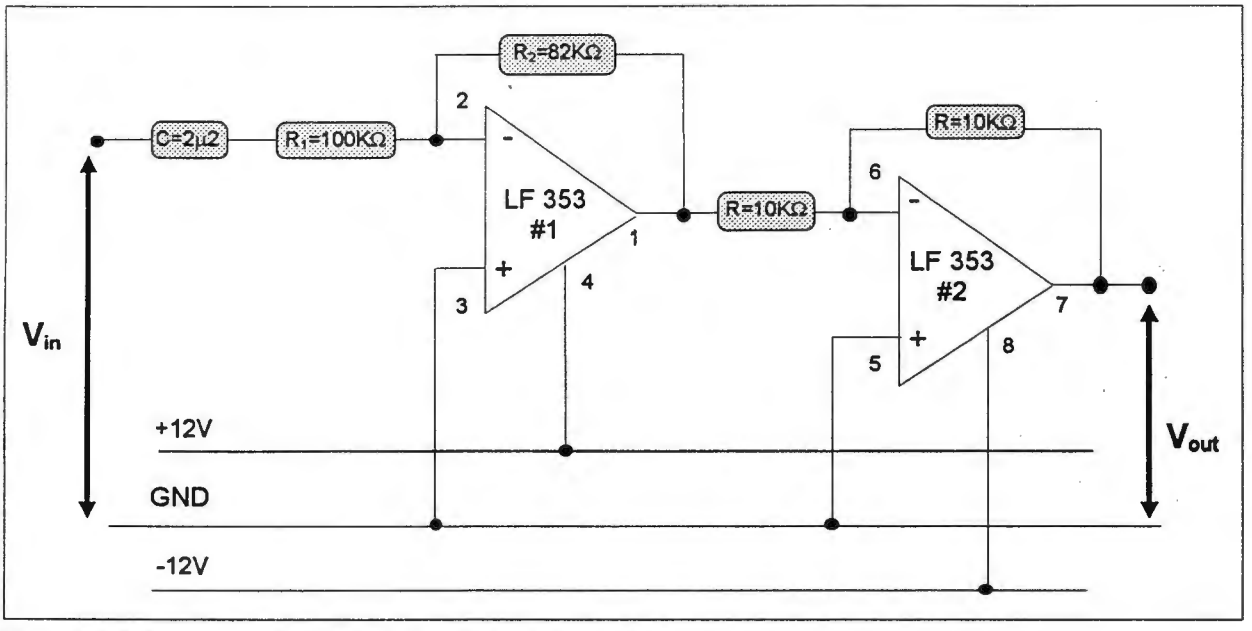

Figure E-9 Schematic circuit diagram of high pass filter.

E.7.3 Butterworth Low Pass Filter.

The complex transfer function, known as the *Butterworth response* is given in equation (E-16).

$$\left|H_n(j\omega)\right|^2 = \frac{1}{1+\left(\omega/\omega_0\right)^{2n}} \qquad \textbf{(E-16)}$$

If the frequency ω_0 is normalised to unity, then equation (E-16) may be re-written as

$$\left|H_n(j\omega)\right| = \frac{1}{\sqrt{1+\omega^{2n}}} \qquad \textbf{(E-17)}$$

Observe in equation (E-17), that

1. $\left|H_n(0)\right| = 1$, for all values of n
2. $\left|H_n(j)\right| = \frac{1}{\sqrt{2}}$, for all values of n
3. for large values of ω, $\left|H_n(j\omega)\right|$ exhibits *n-pole* roll-off
4. the derivatives of $\left|H_n(j\omega)\right|$ for small values of $\omega \approx 0$, are all zero but one. Hence the response is also known as *maximally flat.*

These properties of the Butterworth filter are shown in figure E-10, for increasing values of n. Notice that the case of $n=10$ approaches the ideal cut-off filter.

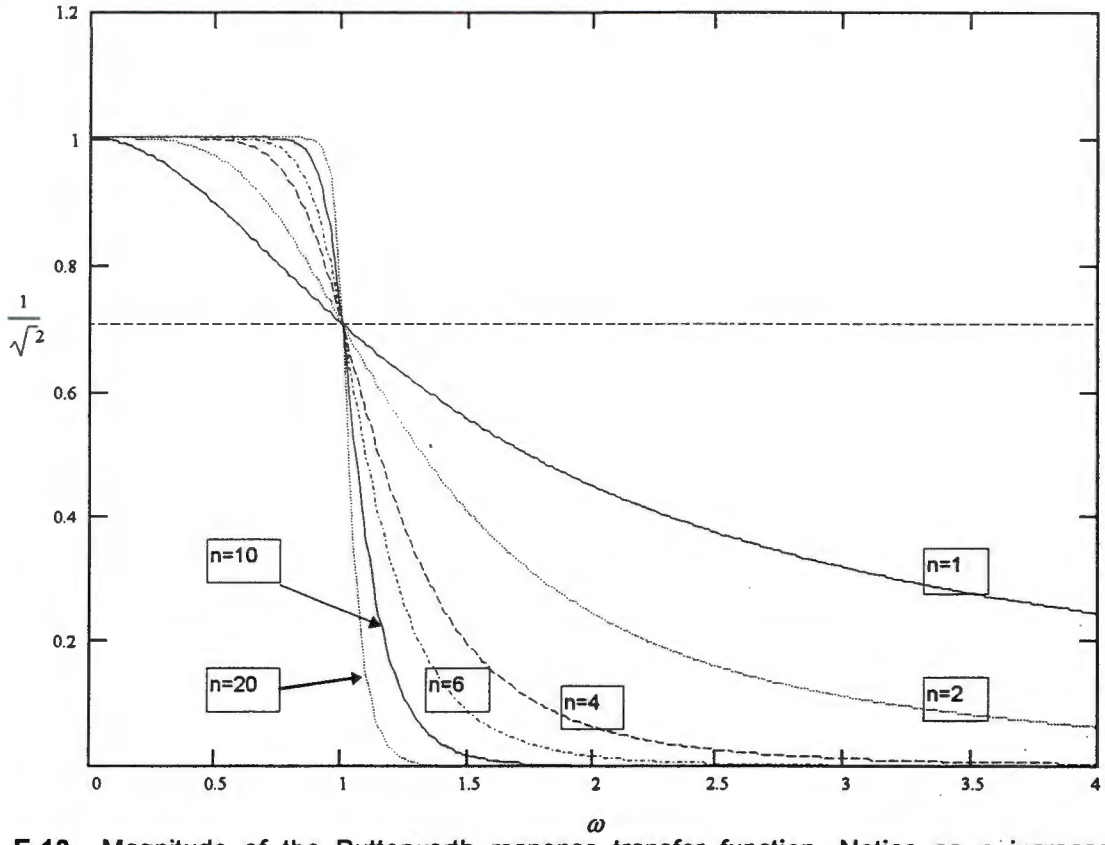

Figure E-10 Magnitude of the Butterworth response transfer function. Notice as n increases the response tends toward the ideal cut-off filter.

Filter characteristics may be defined in terms of a parameter, attenuation, defined as

$$\alpha = -20\log|H_n(j\omega)| \qquad \textbf{(E-18)}$$

For a pass band extending from $0 \leq \omega \leq \omega_p$, the attenuation should not exceed α_{max}. Between ω_p and ω_s, there is a transition band. From ω_s and all higher frequencies the attenuation should not be less than α_{min}. An interpretation is that the filter response should fall inside the diagonally shaded region of figure E-11.

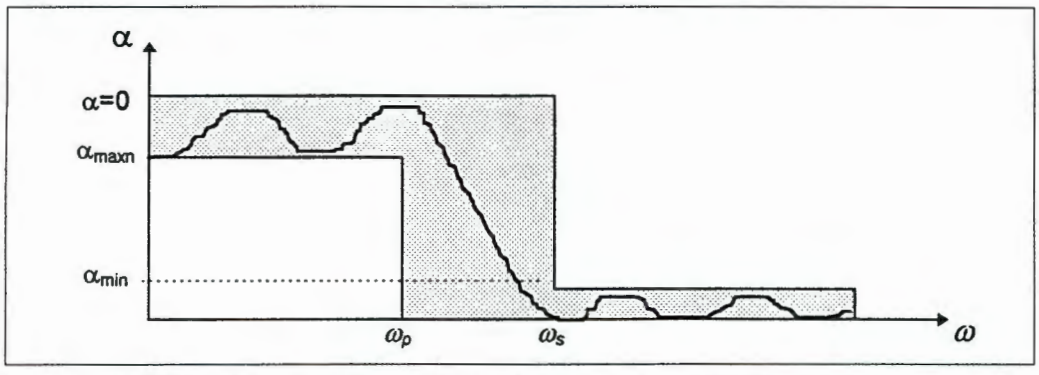

Figure E-11 Specification of attenuation characteristics versus frequency , for a typical low pass filter.

From equation (E-18), attenuation may be written

$$\alpha = -20\log\left[1+\left(\frac{\omega}{\omega_0}\right)^{2n}\right] \qquad \textbf{(E-19)}$$

To determine the order of the Butterworth filter required for the attenuation characteristics and bandwidth frequencies specified, the appropriate bandwidth frequencies values may be substituted into equation (E-19) and rewritten in terms of frequencies. These two equations may be divided by each other, and solving for n gives the desired result

$$n = \frac{\log\left[\left(10^{\alpha_{min}/10}-1\right)\Big/\left(10^{\alpha_{max}/10}-1\right)\right]}{2\log\left(\omega_s/\omega_p\right)} \qquad \textbf{(E-20)}$$

In terms of this thesis, the values assigned to these parameters in equation (E-20) were $\omega_p = 8000(2\pi)$ rad/s & $\alpha_{max} = 1$ dB and $\omega_s = 16000(2\pi)$ rad/s & $\alpha_{min} = 30$ dB. Thus a 6^{th} order Butterworth filter was required with cut-off of $\omega_0 = 8950(2\pi)$ rad/s.

The LMF60-100 non-inverting, unity gain, 6^{th} order switched capacitor Butterworth lowpass filter was used. Switched capacitor techniques minimise external components required and allow a clock-tuneable cut-off frequency to be used. The ratio of the clock frequency to the low pass cut-off frequency is internally set to 100:1. A Schmitt trigger clock input stage allows two clocking options, either self-clocking or a TTL or CMOS logic compatible clock.

In addition to the low pass circuit, there are three additional circuits:-

1. Schmitt trigger,
2. offset adjustment and
3. anti-aliasing filtering.

1. *The Schmitt Trigger.*

The clock frequency, ω_{clock} , must equal 100 times the cut-off frequency, ω_0=8950(2π) rad/s, that is ω_{clock}=895000(2π) rad/s. Using formula supplied by the filter manufacturer, the respective resistor and capacitor were selected. An adjustment resistor pot was provided to allow minor adjustment of the clock frequency and hence cut-off frequency for each individual channel.

2. *Offset Adjustment.*

The $V_{os}adj$ pin (pin #7 in figures E-12 & E-13) sets the zero reference of the output of the filter. One of the two op-amps provided on the chip was used as an integrator circuit to maintain the average DC output at GND.

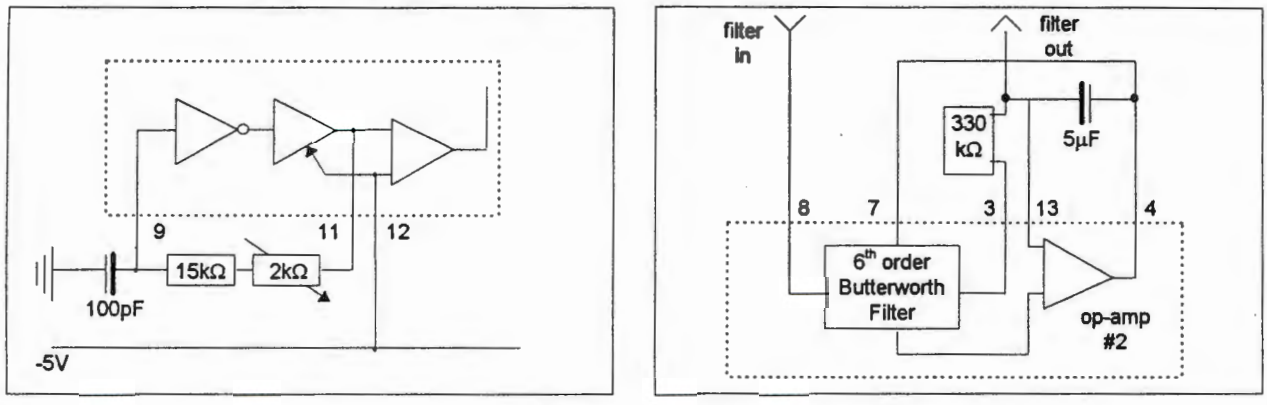

Figure E-12 Sub-circuits showing Schmitt trigger (left) and offset adjustment (right)

3. *Anti-aliasing Filtering.*

A second order Butterworth anti-aliasing filter was constructed using the last of the uncommitted op-amps. This filter had the following characteristics ω_p = 16000(2π)rad/s & α_{max}= 1dB and ω_s = 25000(2π)rad/s & α_{min}= ~30dB. Following the recommendations of the filter manufacturer, the appropriate resistors and capacitors were chosen, as illustrated in Figure E-13.

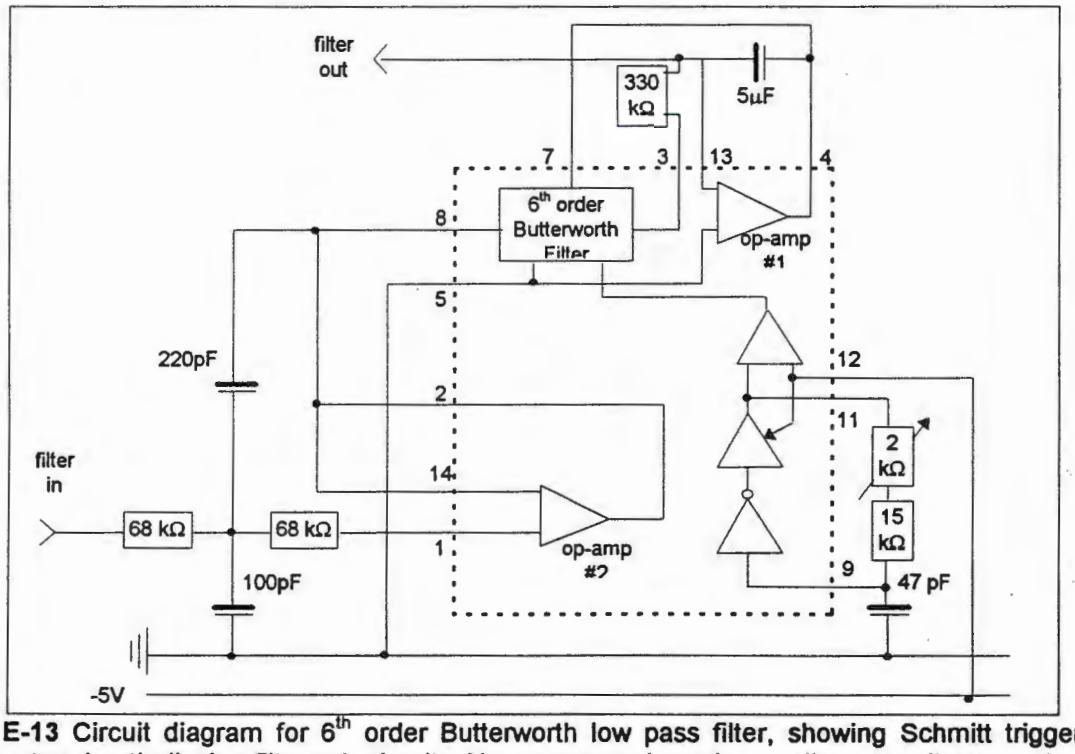

Figure E-13 Circuit diagram for 6th order Butterworth low pass filter, showing Schmitt trigger, offset adjustment and anti-aliasing filter sub-circuits. No power supply or de-coupling capacitors are shown.

E.7.4 DC Power Supply.

As a portable adjustable DC power supply was available, no AC to DC rectification was required. Instead, an external DC supply voltage was suitably reduced on the circuit board by means of transistors. The high pass filter op-amps required a ±12V supply, while the low pass filter required ±5V. Decoupling capacitors were used where appropriate. Figure E-14 presents a schematic representation of the power supply.

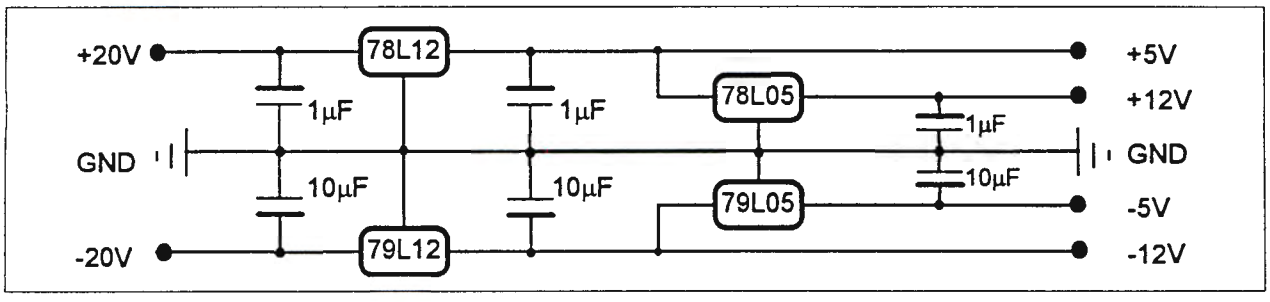

Figure E-14 Schematic representation of the power supply. (The transistor codes are given.)

E.7.5 Calibration.

Initially the cut-off frequency adjustment of each channel was conducted with the use of a signal generator and digital oscilloscope. Later at the University of Stellenbosch the filter was accurately analysed. A broad-band white noise source was used as input to the filter, while recording the output. Both the attenuation and phase characteristics of each channel are shown in figure E-15. The results were surprisingly consistent, and it was decided not to correct the measured vibration response for the phase shift, as all channels were equally distorted.

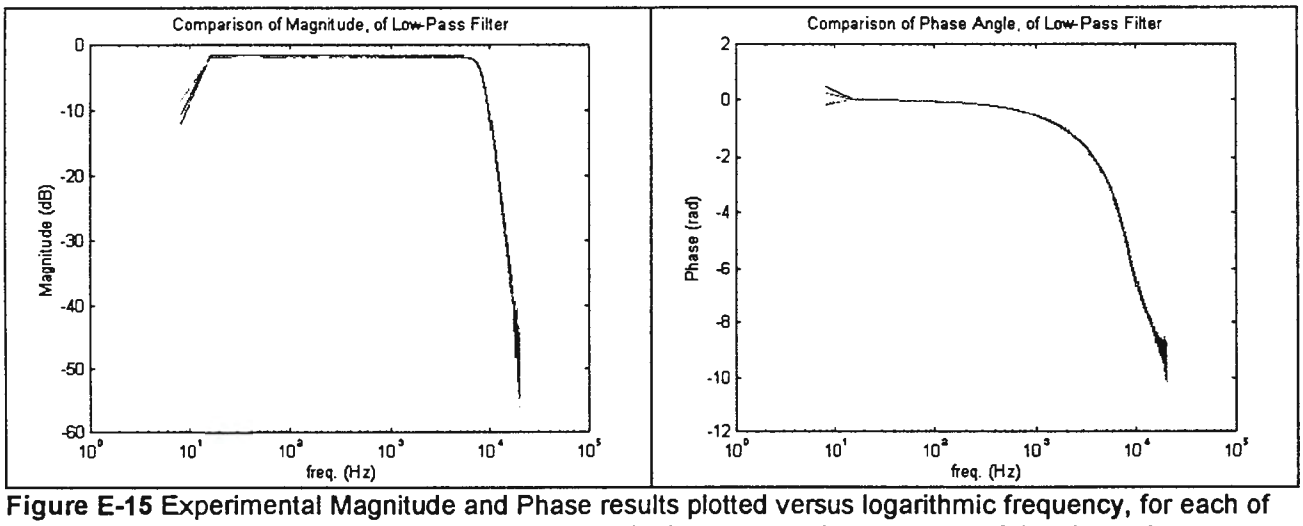

Figure E-15 Experimental Magnitude and Phase results plotted versus logarithmic frequency, for each of the four channels. There is no significant difference in the response between any of the channels.

E.8 Analog to Digital Conversion.

An Eagle Technology PC-30D analog-to-digital (A/D) card was made available by the Biomedical Engineering Department ,U.C.T, for the duration of the data collection. The A/D card supported an accumulative sampling rate of 200 kHz for all of the 16 channels. However, the A/D card was unable to simultaneous sample all the channels and hence the respective digitised records were time shifted by multiples of 5μs, relative to channel zero. To correct this the sampled data was re-sampled at five times the sampling rate, and then re-sampled at the correct time instance. This is discussed in section E.9, on the post data processing.

Initially the threshold trigger, on channel zero, was utilised to trigger the sampling process. However, much of the force transducer signal was truncated due to the low sensitivity of the trigger and hence software was written to customise the operation of the trigger. After an initial delay, the software automatically streamed the four channels, for the appropriate time period.

The input voltage ranges were hardware adjustable at either -5V to +5V or 0 to 10V. As was stated in Table E-1, the typical input voltage range for both the response accelerometers and force transducer are within the -5V to +5V range and hence this was the obvious choice. However, during the capture of responses it was noted that to avoid overloading the accelerometers, the force transducer signal could generally not exceed +1.5V. Thus the voltage resolution for the force transducer signal was not optimum, but unfortunately the A/D card could not support adjustable/programmable gain.

The discretised time histories of the respective channels were saved in binary format, for later post data processing.

E.9 Post Data Processing.

This section refers to the data processing that occurred following the capture and storage of the vibration response. The purpose of the post data processing is to extract the impulse response function, required for the identification of the modal parameters.

E.9.1 Re-sampling and Averaging of Data.

Each stored response was checked for excessive voltages outside the acceptable range, see Table E-3, and if detected that data file was excluded from all further analysis. The initial scaling due to the scaling ratio present in the high pass filter was corrected. Finally the appropriate voltages were converted to either force (N) or acceleration (m/s^2).

The time shift phenomena between channels, discussed in section D.8, was corrected. The situation is best appreciated by considering figure E-16. The circles with a '+' indicate where the actual digitised points are located, for the particular response. The empty circles depict an interpolated curve fit to the digitised points, sampled at five times the actual sampling rate, i.e. 200 kHz. Finally, the circles with both an '+' & 'x' are the new samples used in subsequent analysis, sampled in unison with the force transducer signal.

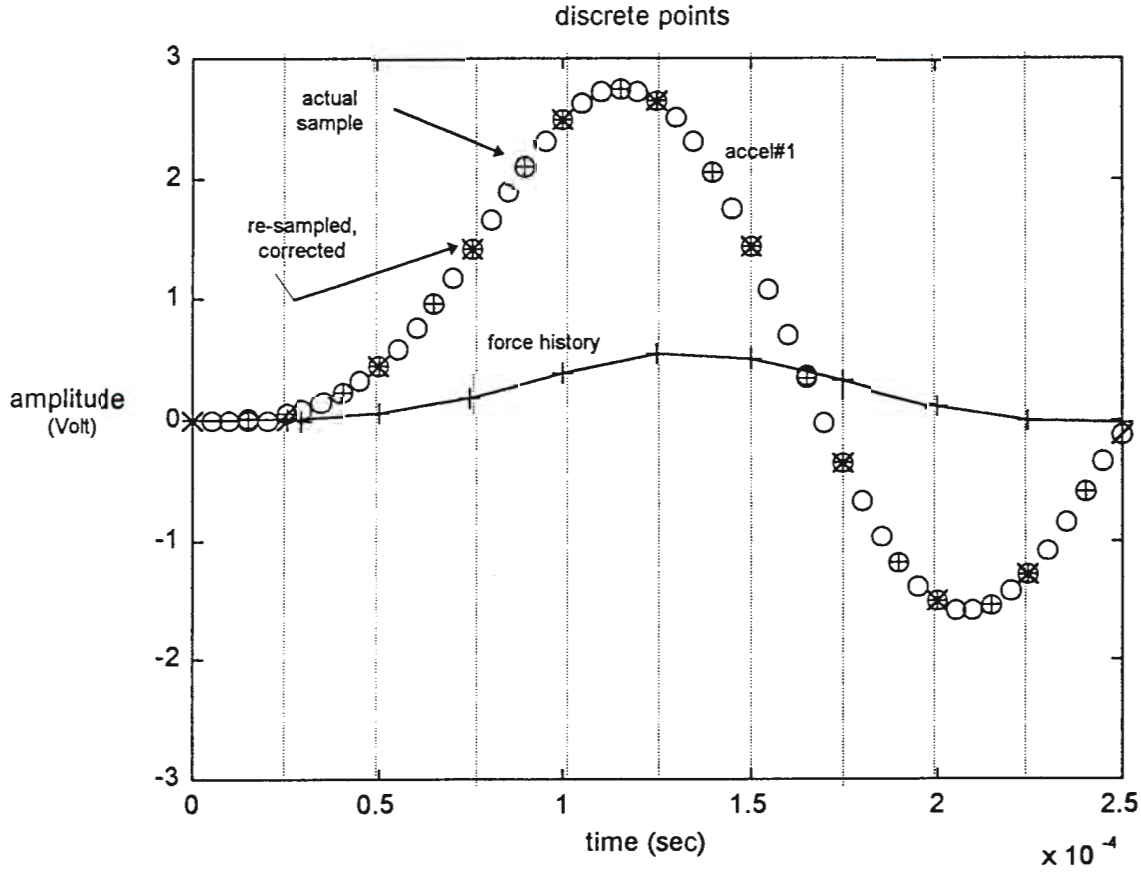

Figure E-16 Illustration of the interpolation and re-sampling procedure, to correct for the time-shift of the A/D card. Indicated are the reference force time history, (+), and the response acceleration (o). The correctly re-sampled samples are indicated by (x), while the time shifted samples are label (+).

E.9.2 Calculation of the Frequency Response Function.

The general scheme for measuring the frequency response function $H(j\omega)$ in terms of the single input/output system consists of measuring simultaneously an input, $u(t)$, and a response signal, $v(t)$, in the time domain.

Figure E-17 Idealisation of the relationship of input and output signals to the frequency response function.

The fourier transform is then applied to each time history, forming the system transfer function by dividing the transformed response by the transformed input.

$$H(j\omega) = \frac{V(j\omega)}{U(j\omega)} \qquad \textbf{(E-21)}$$

where $V(j\omega)$ = fourier transform of the system output $v(t)$
$U(j\omega)$ = fourier transform of the system input $u(t)$

The only requirements for a complete description of the frequency response are that the input and output signals be fourier transformable, a condition that is met by all physically realisable systems. An additional requirement is that the input signal be non-zero at all frequencies of interest.

The frequency response function may be computed directly from the equation (E-21). However, better results are obtained in practise by computing the frequency response function as the ratio of the cross-spectrum between the input and output to the power spectrum of the input, *Halvorsen (1977), Ramsey (1975) & Ewins (1984)*

$$H(j\omega) = \frac{G_{uv}(j\omega)}{G_u(j\omega)} \qquad \textbf{(E-22)}$$

where

$G_{uv}(j\omega) = U^*(j\omega)V(j\omega)$, cross-spectrum between $u(t)$ and $v(t)$

$G_u(j\omega) = U^*(j\omega)U(j\omega)$, power-spectrum between of $u(t)$

$U^*(j\omega)$, is the complex conjugate of $U(j\omega)$

The usefulness of this form of the frequency response function may be seen by considering the practical single input/output measurement situation, as illustrated in Figure E-24. Signals $m(t)$ and $n(t)$ represent noise at the input and output measurement points respectively.

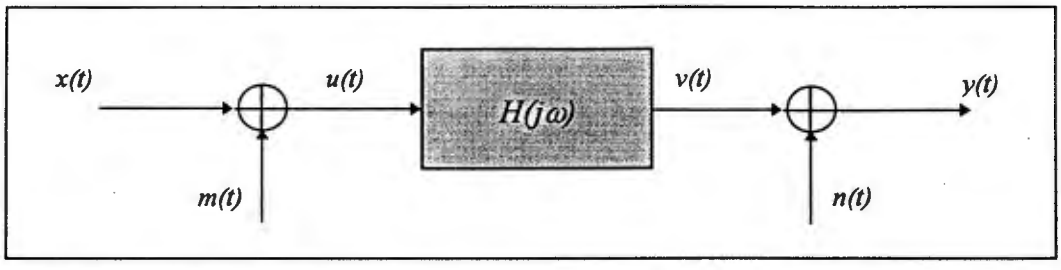

Figure E-18 General single input/output measurement system. **note** that $u(t)=x(t)+m(t)$ *and* $y(t)=v(t)+n(t)$

The measured frequency response function $H'(j\omega)$ is then given by

$$H'(j\omega) = \frac{Y(j\omega)}{X(j\omega)} = \frac{V(j\omega)+N(j\omega)}{U(j\omega)+M(j\omega)} \qquad \textbf{(E-23)}$$

In this form the measured frequency response function will be a good approximation of the true frequency response function only if the measurement noise at both the input and output measurement points is small relative to the input and output signals. This can be demonstrated by multiplying equation (E-23) by the conjugate of $X(j\omega)$. If the measurement noise signals $m(t)$ and $n(t)$ are non-coherent with each other and with the input signal $u(t)$, then the expected value of the cross-spectrum terms involving m and n will equal zero. Thus after simplification equation (E-23) may be re-stated as

$$H'(j\omega) = \frac{G_{uv}(j\omega)}{G_u(j\omega)+G_m(j\omega)} = \frac{H(j\omega)}{1+\left(\frac{G_m(j\omega)}{G_u(j\omega)}\right)} \qquad \textbf{(E-24)}$$

Thus, if the noise-to-signal ratio at the input measurement point $G_m(j\omega)/G_u(j\omega)$ is much less that 1, the measured frequency response will closely approximate the desired true frequency function, $H(j\omega)$.

A further advantage of calculating the frequency response function using equation E-22 is that the phase characteristics are considered, since the cross power spectrum contains phase information. An additional advantage, is that ensemble averaging of the measurements may easily be applied. This is an important consideration due to the large variance in the transfer function estimate when only one measurement is used. Equation (E-22) may be restated as

$$H(j\omega) = \frac{\overline{G}_{uv}(j\omega)}{\overline{G}_u(j\omega)} \qquad \textbf{(E-25)}$$

where

$\overline{G}_{uv}(j\omega) = U^*(j\omega)V(j\omega)$, ensemble average cross-spectrum between $u(t)$ and $v(t)$

$\overline{G}_u(j\omega) = U^*(j\omega)U(j\omega)$, ensemble average power-spectrum between of $u(t)$

$U^*(j\omega)$, is the complex conjugate of $U(j\omega)$

It should be pointed out that there is an inherent bias error associated with the computation of the cross-spectrum and the magnitude of this bias error is inversely proportional to the number of averages in the computation. Thus, the greater the measurement noise the greater number of averages required to approach the expected value of the cross-spectrum between input and the output measurement signals.

A simple test to assess the bias error, described by *Halvorsen & Bendat (1975)*, is to double the number of time samples used in the ensemble averaging and observe the change in the overall level of the coherence output power spectrum. If the change is approximately 3dB, then the bias error is significant and the number of samples should be increased. In this dissertation 20 samples were used in the ensemble averaging.

E.9.3 Calculation of the Coherence Function.

The true coherence function is defined by the equation

$$\chi^2_{uv}(j\omega) = \frac{\text{response power caused by the applied input}}{\text{measured response power}} \qquad \textbf{(E-26)}$$

and hence as

$$\chi^2_{uv}(j\omega) = \frac{\left|\overline{G}_{uv}(j\omega)\right|^2}{\overline{G}_u(j\omega)\overline{G}_v(j\omega)} \qquad \textbf{(E-27)}$$

According to the definitions of the power spectrum and the cross-spectrum, the coherence function will be identically equal to 1 if there is no measurement noise and the system is linear.

The measured coherence function as defined in Figure E-18, may be stated as

$$\begin{aligned}\chi^2_{xy}(j\omega) &= \frac{\left|G_{xy}(j\omega)\right|^2}{G_x(j\omega)G_y(j\omega)} \\ &= \frac{\left|G_{uv}(j\omega)\right|^2}{[G_u(j\omega)+G_m(j\omega)][G_v(j\omega)+G_n(j\omega)]} \\ &= \frac{\gamma^2_{uv}(j\omega)}{\left[1+\dfrac{G_m(j\omega)}{G_u(j\omega)}\right]\left[1+\dfrac{G_n(j\omega)}{G_v(j\omega)}\right]}\end{aligned} \qquad \textbf{(E-28)}$$

Thus the measured value of the coherence function is diminished from the true value by terms involving the measurement signal-to-noise ratios. *Ewins (1984).*

E.9.4 Calculation of the Impulse Response Function.

The impulse response function, *h(t)* ,of a linear system is merely the inverse fourier transform of the frequency response function,

$$h(t) \overset{FFT^{-1}}{\Leftrightarrow} \left\{\frac{\overline{G}_{uv}(j\omega)}{\overline{G}_u(j\omega)}\right\} \qquad \textbf{(E-29)}$$

E.9.5 Software Implementation of the Data Processing.

This section presents the software implementation of the data processing procedure. The mathematical visualisation software, Matlab™, was used as the principle development tool. Once the development was complete the matlab files were translated, using the *matcom* translator, into C++ code and compiled into executable form using the Borland™ C++ V4.52 compiler. The software listing is given in **Appendix III-2.**

Chapter F.

Discussion of Results.

F. Discussion of Results.

In the first section of this chapter the experimental vibration results and post data processed results are presented and discussed. The second section investigates the influence of both the Hankel matrix dimensions and the number of retained singular values on the accuracy of the realized modal parameters. Section two concludes by presenting and discussing the finalised modal parameters.

In the third section the least order mass, stiffness and damping matrices are graphically depicted. In the final section the finite element predictions for the resonant frequencies are compared to the experimentally measured modes. The finite element predictions for the response functions are also compared to those experimentally measured.

The organisation of this chapter is depicted in figure F.1.

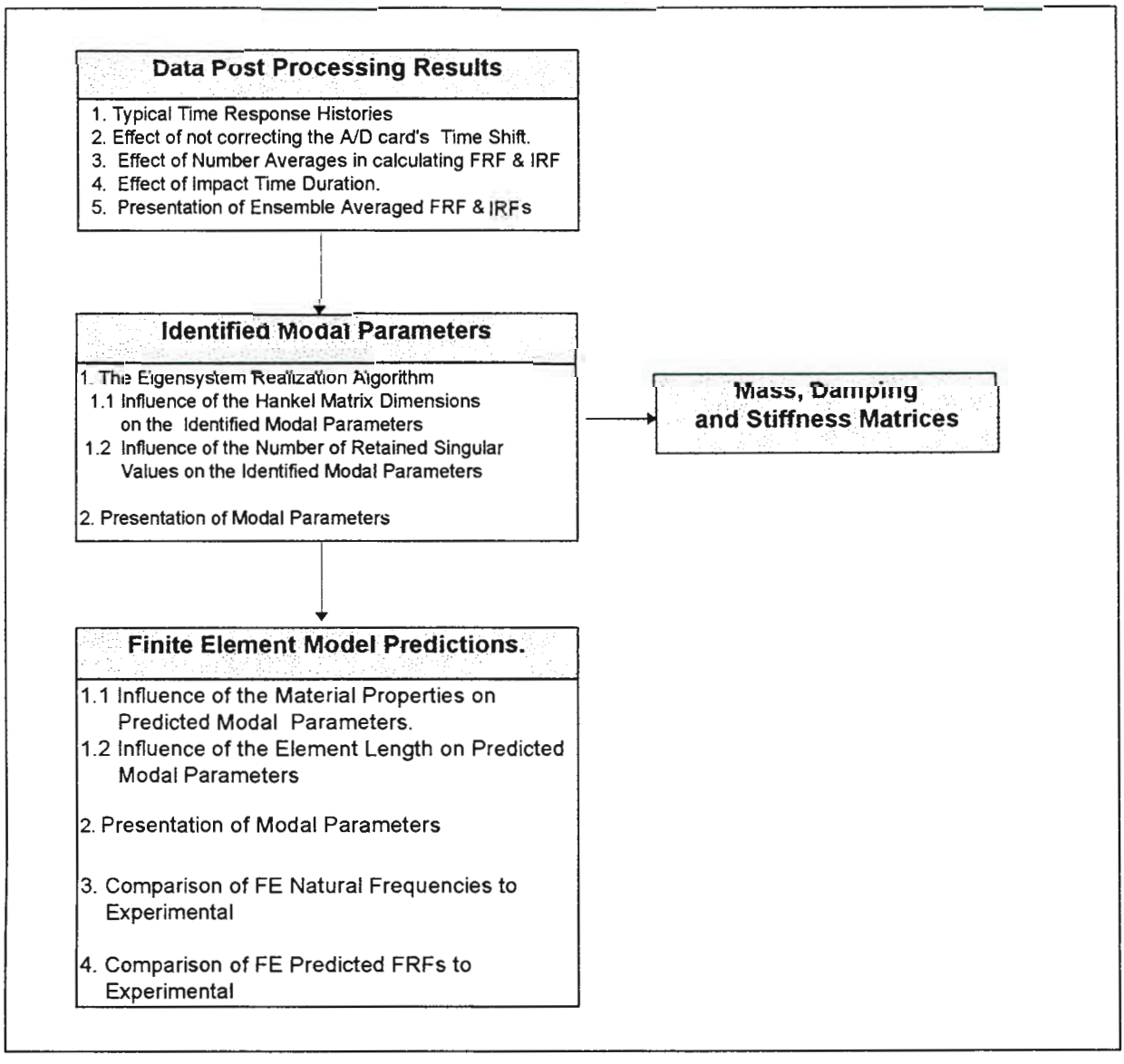

Figure F.1 Organisation of Chapter F.

F.1 Data Post Processing Results.

This section begins by presenting typical time histories of both the impact and acceleration responses. The frequency spectrum of typical impact force time histories are also analysed, as the frequency spectrum of the impact force governs the practical bandwidth that may be measured.

The influence of not resampling the acceleration time history data to account for the time-shift of the A/D card is considered. The influence of the number of averages used in the calculation of the ensemble averaged frequency and impulse response functions is then considered.

The section concludes by presenting and commenting on the final post-processed frequency and impulse response function results.

F.1.1 Typical Time Response Histories.

Figures F.2(a) & F.2(b) depict typical acceleration history responses for vibration in the xy and xz planes, respectively. The following observations may be made: the acceleration responses exhibit the classical exponential decay, characteristic of the damping of the structure under test. A steady state of vibration is reached after approximately 0.1s, in each of the responses. The magnitude of each of the respective responses is non-zero within the time window.

During the sampling procedure, the number of samples that were captured was 2^{13} or 8196. However due to the observed steady state response after 0.1s, only the initial 4096 time samples were used in subsequent data post-processing.

As the magnitude of each of the respective acceleration responses was non-zero at time sample 4096, there is the possibility that leakage and aliasing of the response could have occurred. However, as may be seen in the presented results of the respective impulse response functions, due to anti-aliasing filtering, the aliasing effect is insignificant.

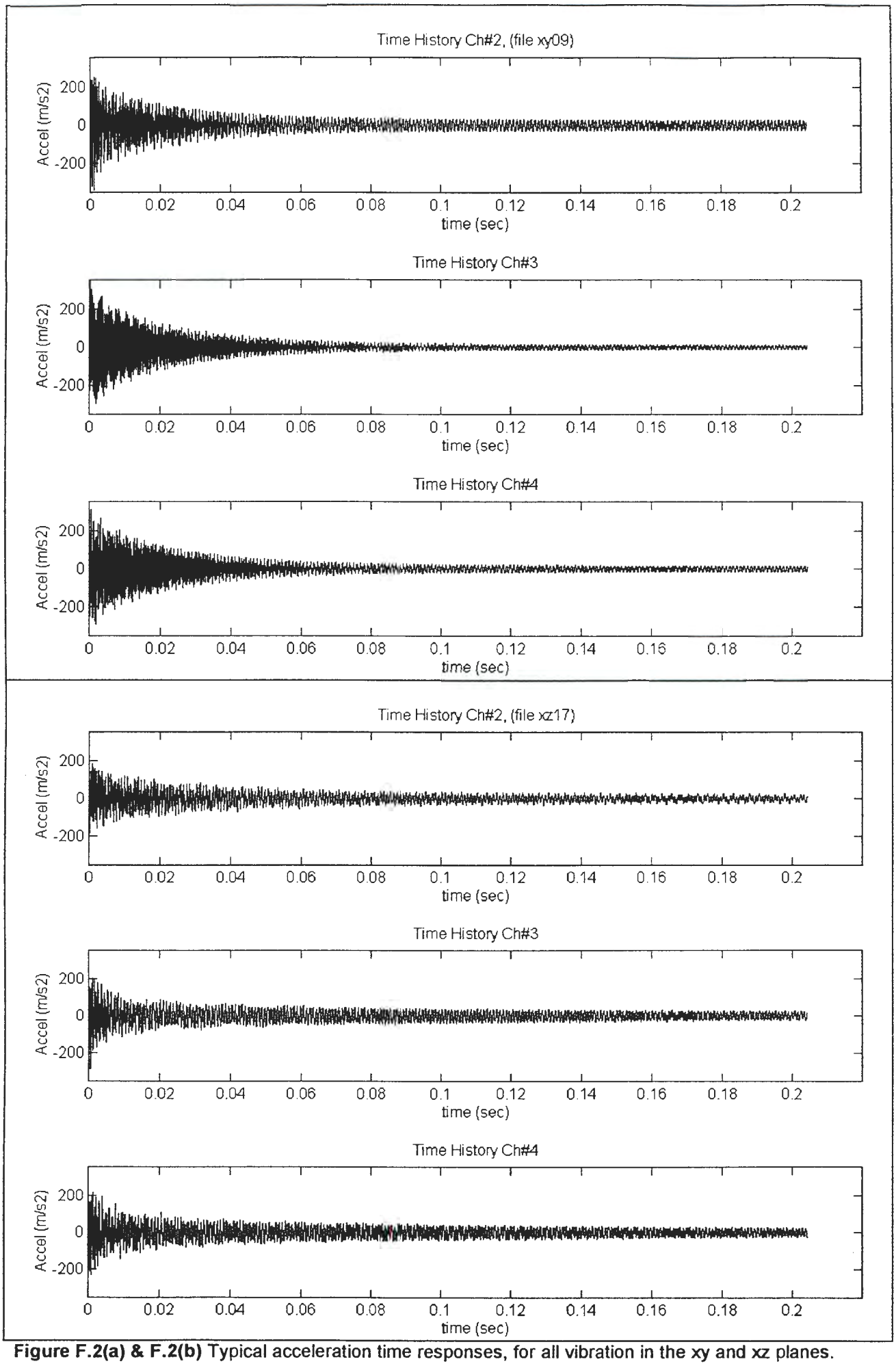

Figure F.2(a) & F.2(b) Typical acceleration time responses, for all vibration in the xy and xz planes.

F.1.2 Typical Time Histories of the Force Impact.

As discussed in section E.3, there is a relationship between the duration of the impact and the resulting frequency spectrum. The bandwidth of the resulting frequency spectrum governs the bandwidth over which realistic vibration data of the test structure may be extracted. At frequencies outside the bandwidth of the impact frequency spectrum, the input energy into the structure is no longer linear. Hence there is some uncertainty if modes outside the bandwidth are being satisfactorily excited

Presented as figures F.3(a) & F.3(b) are typical time histories of the force impact, for the xy and xz planes respectively. Notice, although the magnitude of the impacts differ by an approximate factor of two, the duration of the impacts is similar. The frequency bandwidth is related to the impact duration, while independent of the magnitude. This may be observed in the respective frequency spectra, where the magnitudes differ but the useful bandwidths are similar.

The useful frequency bandwidth was estimated to be 8000 Hz, which corresponds to an approximate 10 dB drop-off in the magnitude of the impact frequency spectrum. The cut-off frequency of the filter was made to coincide with the 8000 Hz bandwidth.

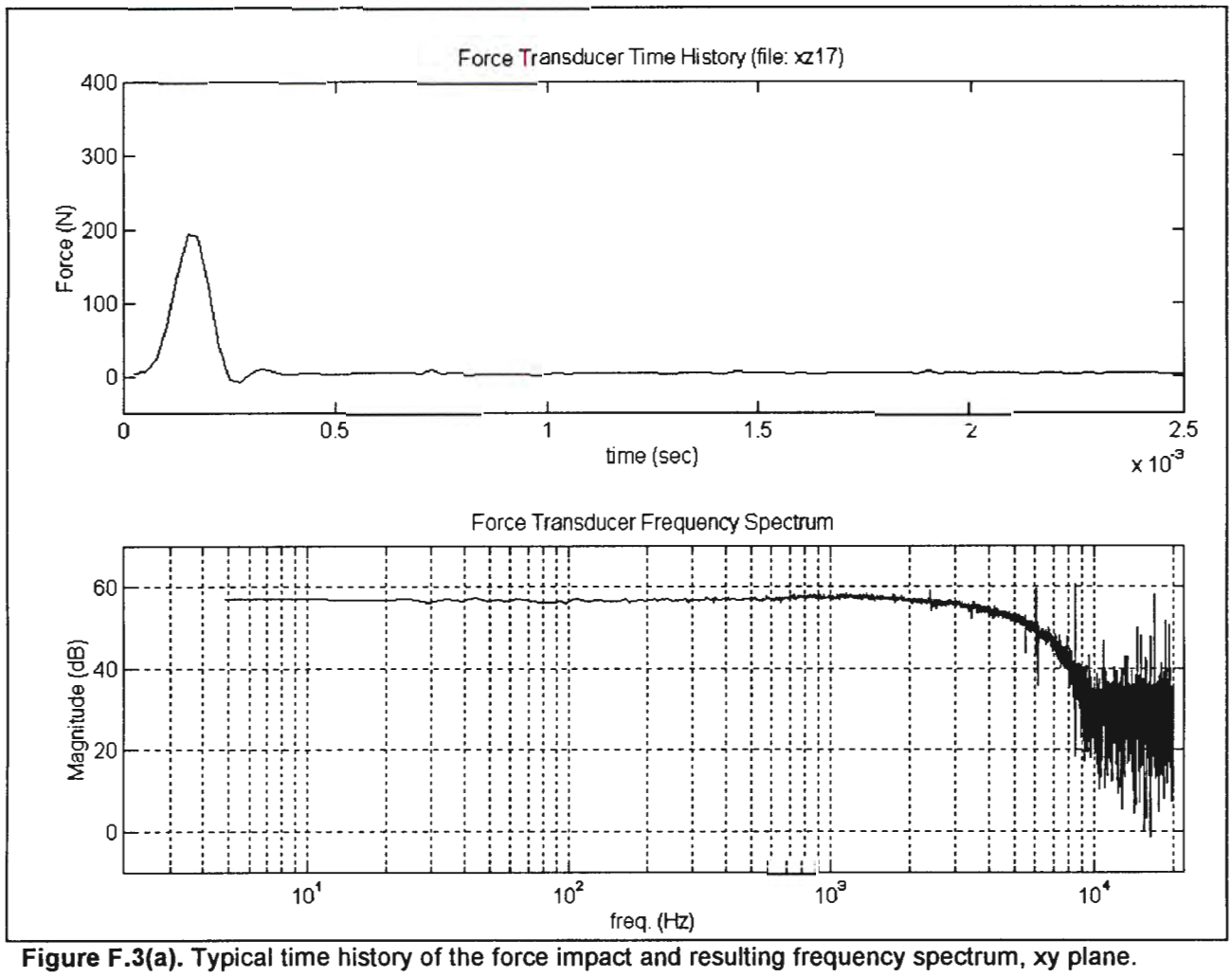

Figure F.3(a). Typical time history of the force impact and resulting frequency spectrum, xy plane.

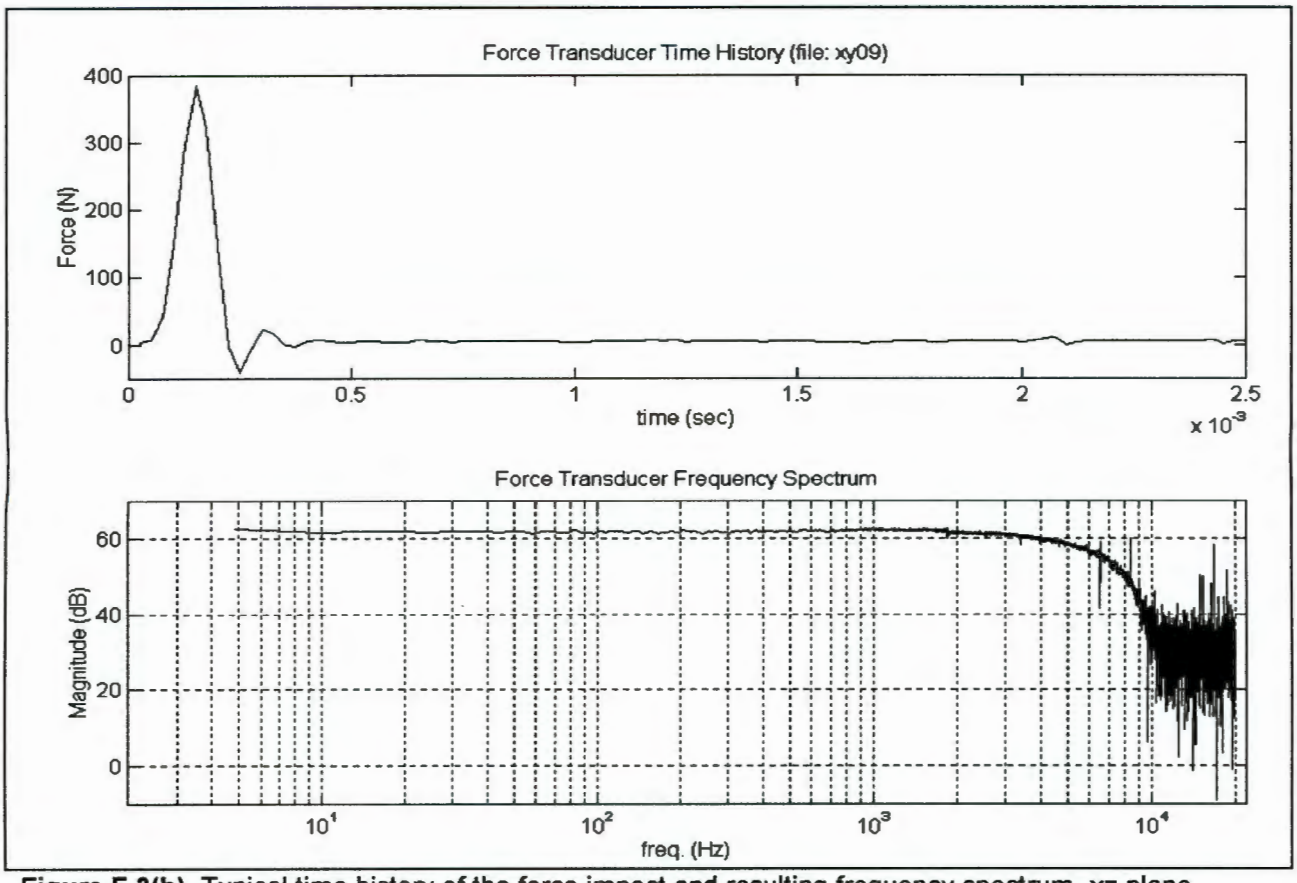

Figure F.3(b). Typical time history of the force impact and resulting frequency spectrum, xz plane.

F.1.3 The Effect of Not Correcting the A/D card's Time Shift.

As discussed in section E.9.1, the time-shift phenomena is a hardware related shortcoming, outside of the operators control. To correct the time-shift the data was numerically interpolated, at five times the sampling rate, and then reassembled at the correct time instances. Figure F.4 shows the procedure graphically.

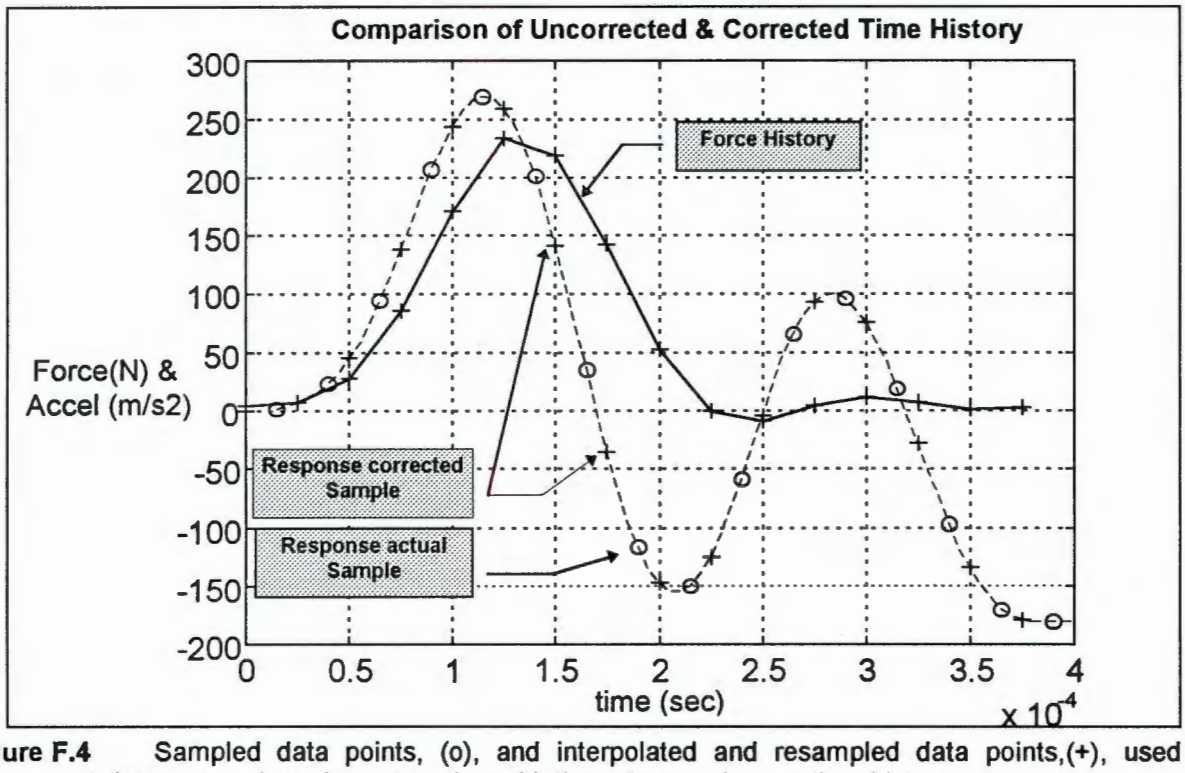

Figure F.4 Sampled data points, (o), and interpolated and resampled data points,(+), used in subsequent data processing, shown together with the reference impact time history.

To investigate the effect of not correcting the time history data, the resulting frequency response functions (FRF), of both the corrected and un-corrected time histories were compared.

The real and imaginary components of both the corrected and un-corrected FRFs are shown in figures F.5(a) & F.5(b). The location and magnitude of the resonant peaks are unaffected. However the anti-resonant troughs of the imaginary components differ greatly, but not so for the real component. The effect on the real component is predominately a high frequency effect.

From the comparison of the magnitude and phase of the corrected and un-corrected FRFs, see figures F.5(c) & F.5(d), it would seem that the effect of not correcting the time-shift of the time data is minimal. Neither the magnitude or phase characteristics of the respective frequency response functions vary, except at high frequency.

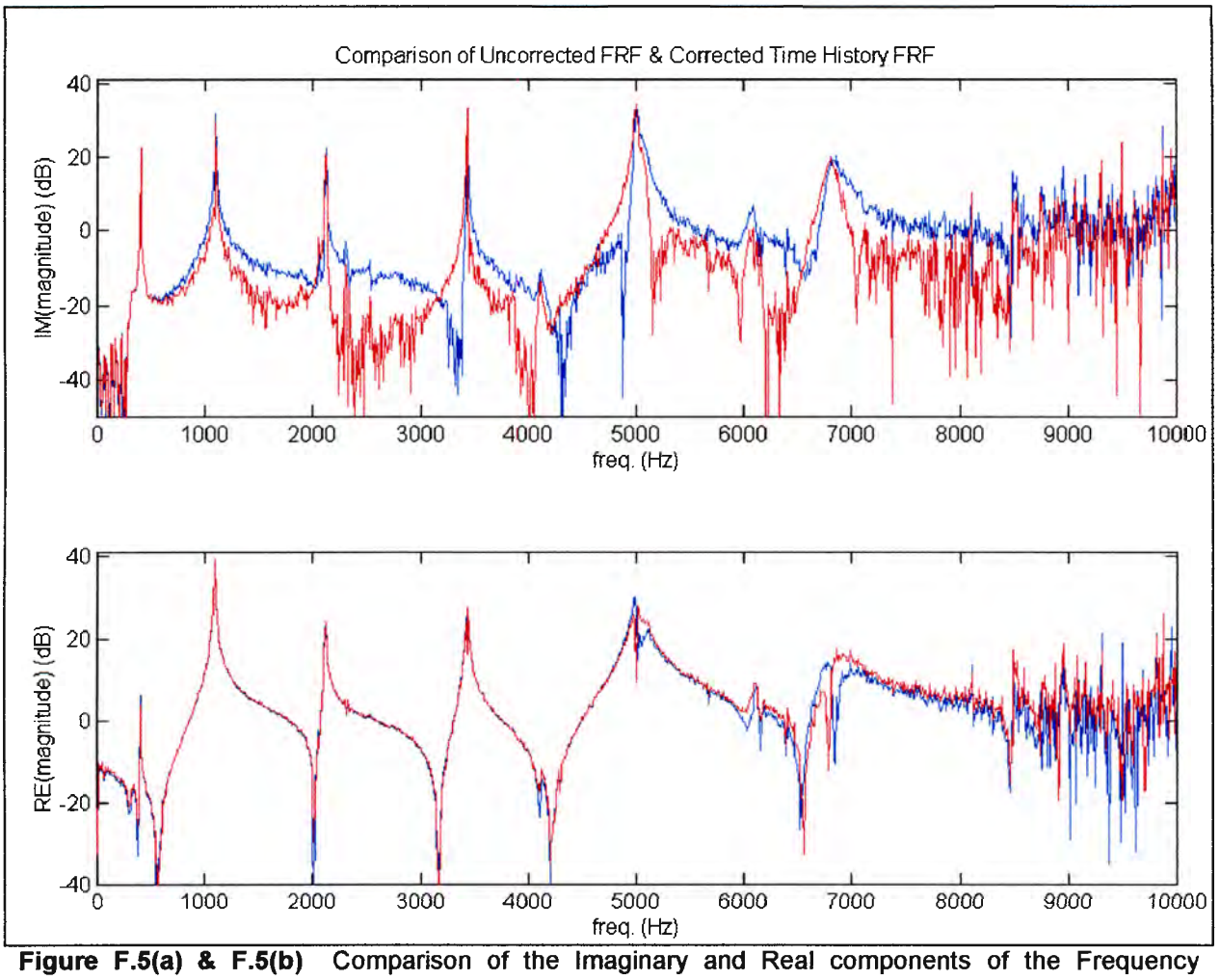

Figure F.5(a) & F.5(b) Comparison of the Imaginary and Real components of the Frequency Response Functions, for the corrected (blue) and un-corrected (red) time histories.

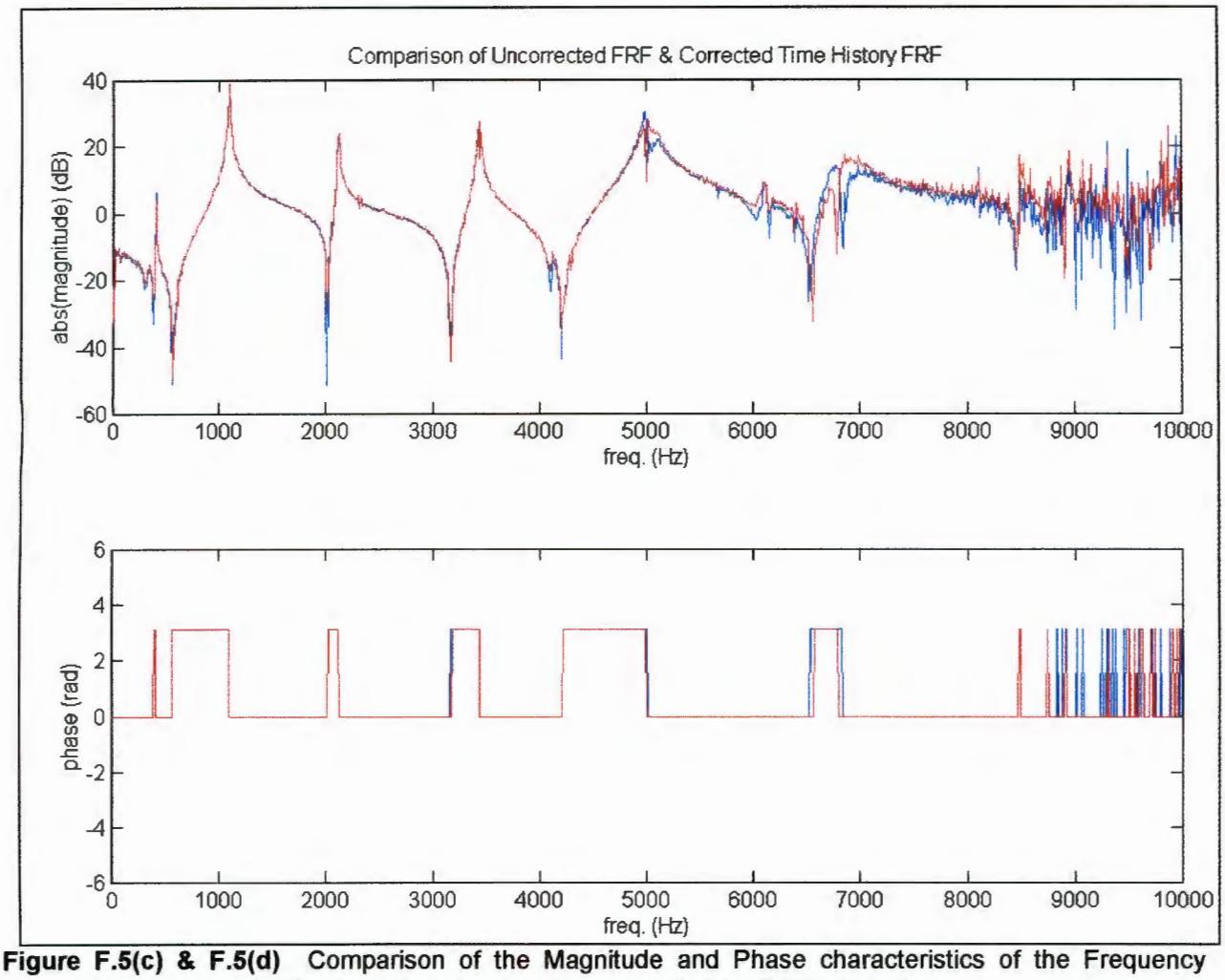

Figure F.5(c) & F.5(d) Comparison of the Magnitude and Phase characteristics of the Frequency Response Functions, for the corrected (blue) and un-corrected (red) time histories.

F.1.4 The Effect of the Number of Ensemble Averages used to Calculate the FRFs.

The theory and motivation for the use of ensemble averaging was presented in section E.9.2. In this section the results of a parametric study are presented, to assess the effect of the number of averages used for the ensemble average calculation of the frequency response function. The number of averages used to calculate the respective FRF and IRFs were increased in the sequence [1,5,10,15,20, 25]. A representative sample of the results, for vibration in the xy plane, are presented as figures F.6(a) ⇒ F.6(d).

As expected the coherence function is unity for the single sample, see figure F.6(a), as the there is no other 'contaminating' data. Ideally, the coherence function should degrade to zero in regions of anti-resonance and outside the filter bandwidth. Notice that both of these phenomena are more accurately fulfilled as the number of ensemble averages increases, see figures F.6(a) ⇒ F.6(d). However, in the region of the ≈9000 Hz anti-resonance, the coherence function seems to have become less well defined as the number of averages was increased. This seems to imply that the anti-resonant region was not reliably defined by the respective time histories.

Due to the averaging effect, both the FRF and IRFs generally become more 'smooth' as the number of averages is increased. Extraneous noise effects and weakly excited high frequency modes are averaged out, thus resulting in the smoothing. This is especially prominent by inspecting the IRF of figure F.6(a) and figure F.6(d).

From this limited parametric study it would seem that the greater the number of averages used, the more confidence one may place on the reliability of the results.

The results of this study indicate that 25 average samples were sufficient, as no change was observed from the results of 20 averages.

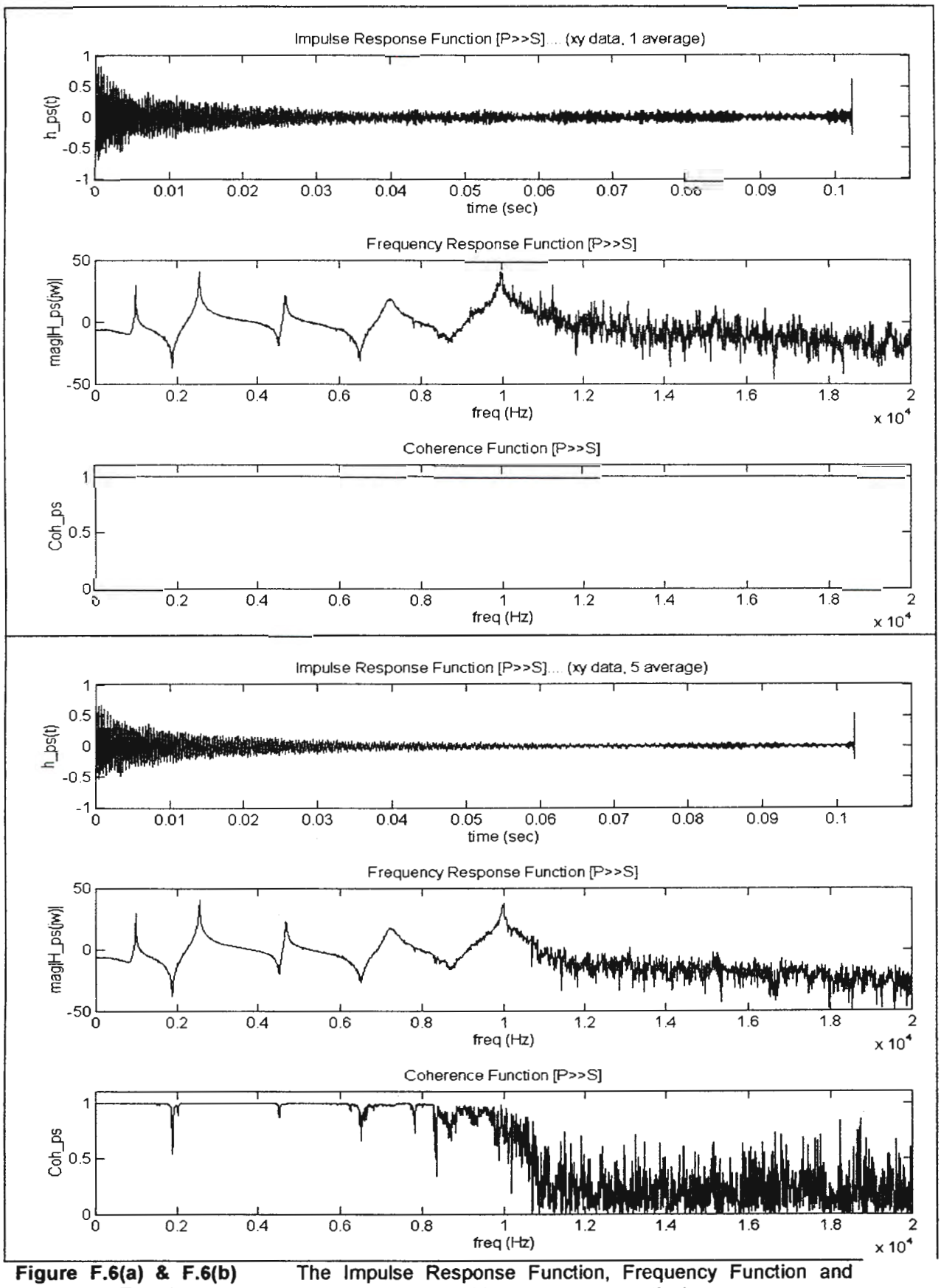

Figure F.6(a) & F.6(b) The Impulse Response Function, Frequency Function and Coherence Function plotted for one and five ensemble averages respectively.

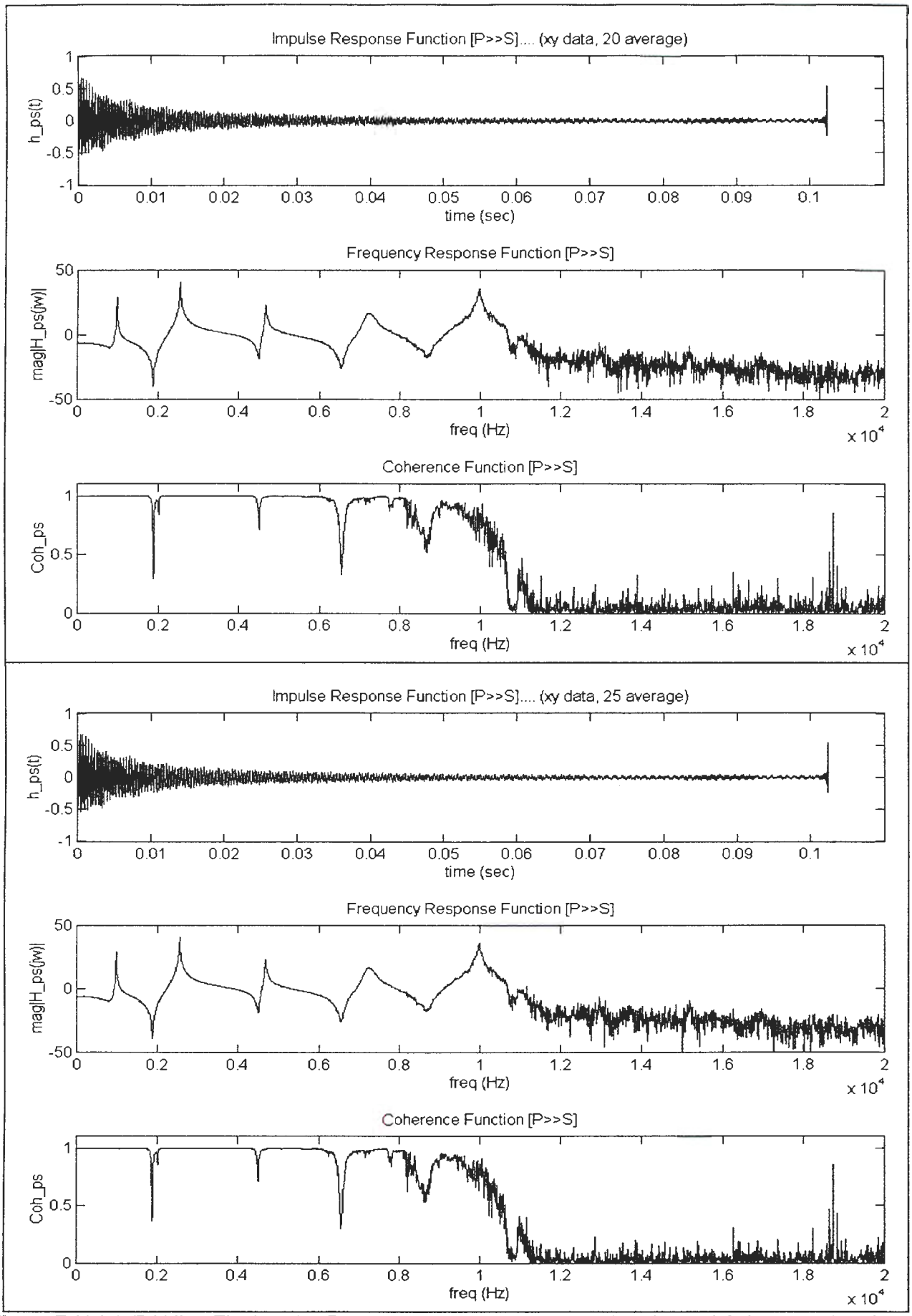

Figure F.6(c) & F.6(d) The Impulse Response Function, Frequency Function and Coherence Function plotted for twenty and twenty-five ensemble averages respectively.

F.1.5 Presentation of the Ensemble Averaged FRF & IRFs.

The final ensemble averaged frequency and impulse response functions are now presented and discussed, for each of the vibration planes.

F.1.5.1 xy Vibration Plane Results.

Generally the xy vibration plane results are satisfactory, see figures F.7(a), F.7(b) & F.7(c). Four sharp, well defined modes are identified within the bandwidth. The corresponding coherence function indicates that these modes were consistently defined. An additional mode, ≈10000 Hz, outside the bandwidth was also strongly excited. The anti-resonances are in general poorly defined, being a combination of anti-resonant peaks and minimum. As expected for the co-located response, H_ps($j\omega$), it was characterised by a succession of resonant and anti-resonant peaks. While for the other two responses H_pq($j\omega$) & H_pr($j\omega$) there is a combination of anti-resonate peaks and minimum.

Notice the correlation between frequency regions of: poorly defined anti-resonance, ill-defined phase and broad band 'zero' coherence. In each response such regions may be identified:-

- For the H_pq($j\omega$) response, two regions may be identified. The anti-resonant peak between the second and third mode and third and forth mode.
- For the H_pr($j\omega$) response, a single region may be identified between the third and forth modes.
- No regions of poorly defined anti-resonance are present in the H_ps($j\omega$) response.

The presence of these regions of poorly defined anti-resonance peaks, imply that there is considerable uncertainty in the definition of these regions. It should be anticipated that the predictions of the modal identification procedure would not correlate well in these regions.

The time domain impulse response functions, h_pq(t), h_pr(t) & h_ps(t), indicate that after an initial decay period the structure vibrates in a virtual steady state. This was observed in the acceleration time histories. Both the impulse response functions h_pr(t) and h_ps(t) seem to exhibit high frequency influences, characterised by the complex waveforms in the steady state response regions. This is not observed in the impulse response function of h_pq(t).

Aliasing of the impulse response function has occurred, characterised by the vertical 'line' at the end of the time datum. The degree of aliasing was judged to be insignificant and hence ignored.

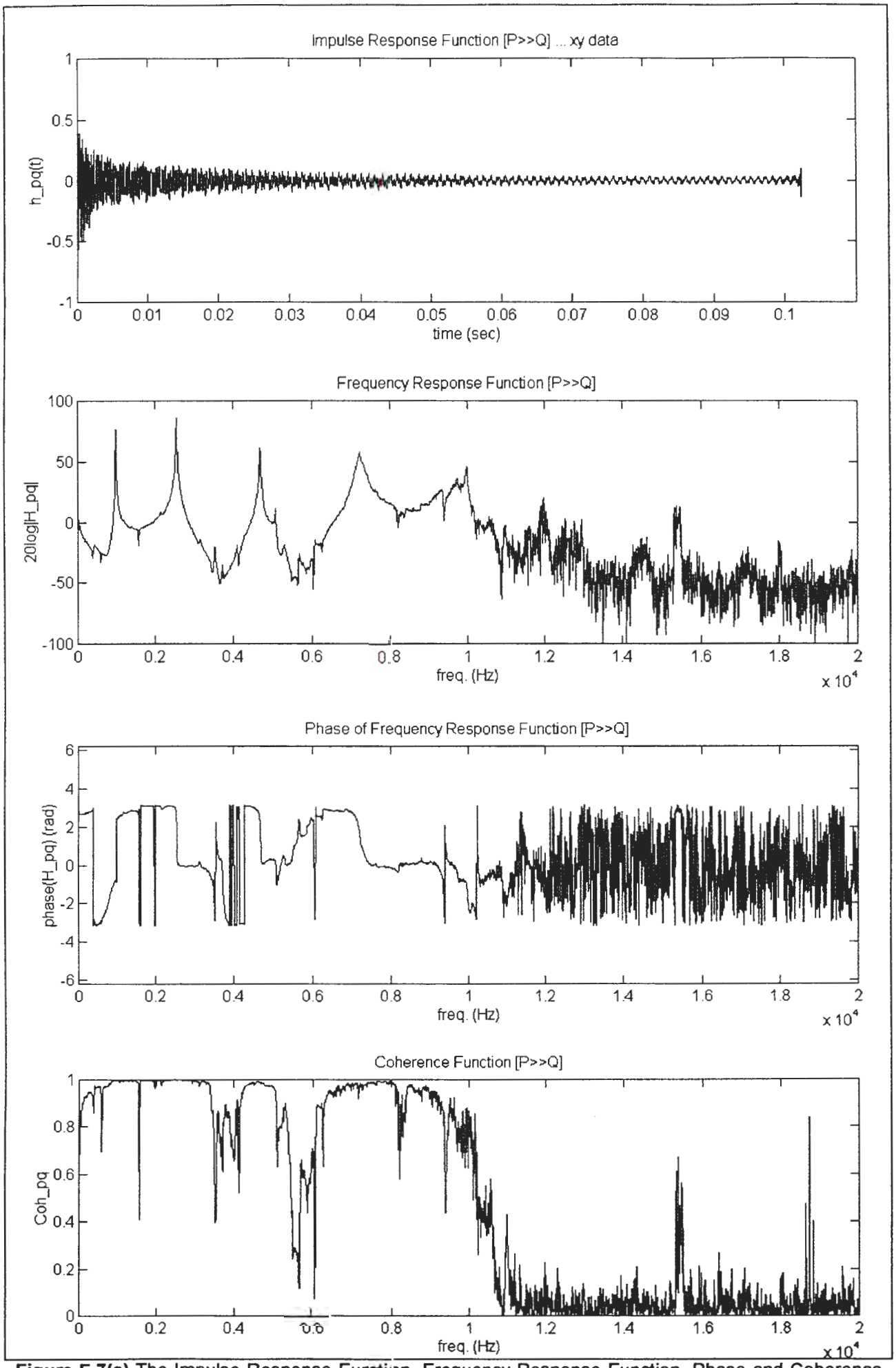

Figure F.7(a) The Impulse Response Function, Frequency Response Function, Phase and Coherence Function for vibration in the xy plane, at location pq.

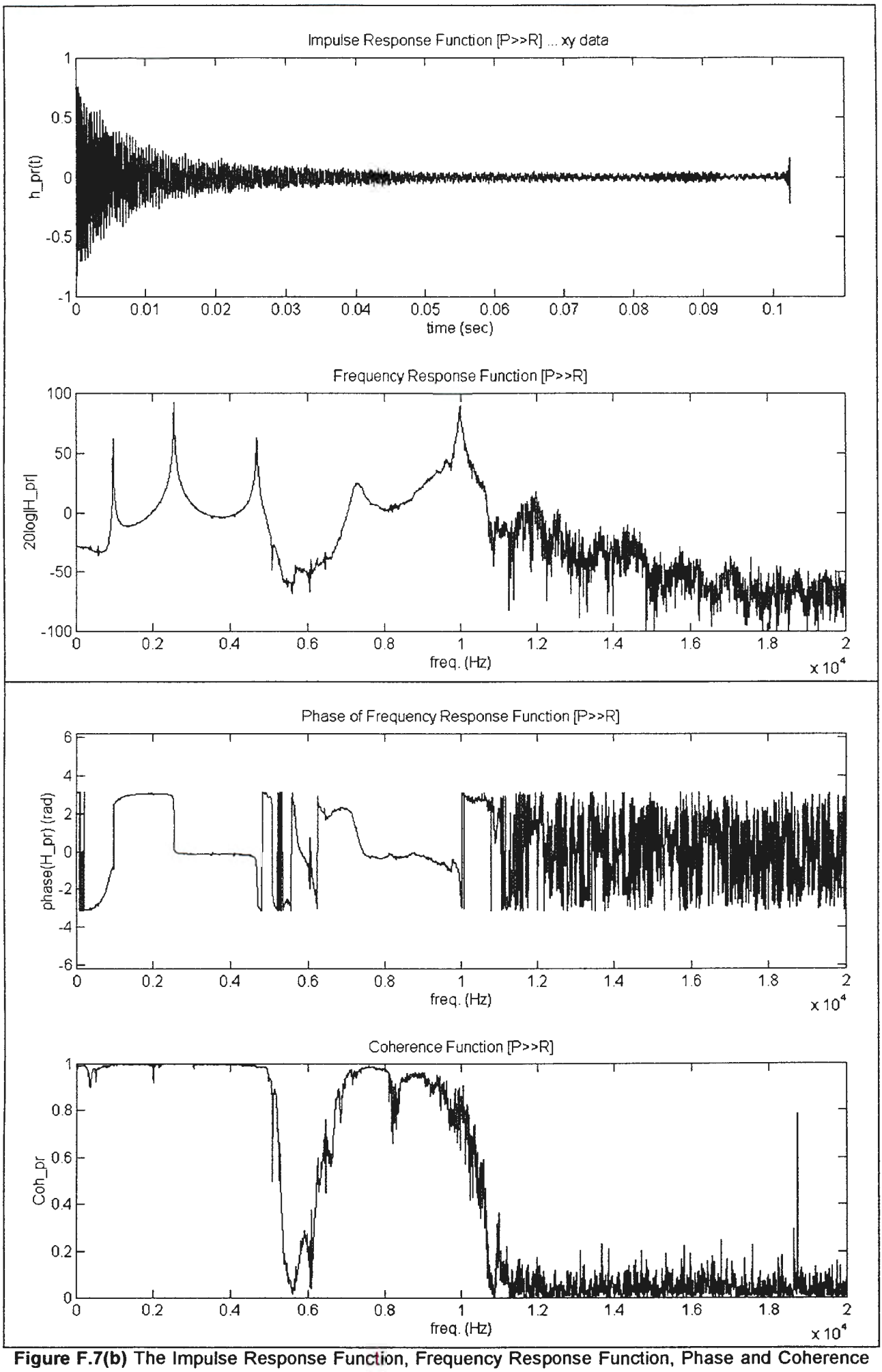

Figure F.7(b) The Impulse Response Function, Frequency Response Function, Phase and Coherence Function for vibration in the xy plane, at location pr.

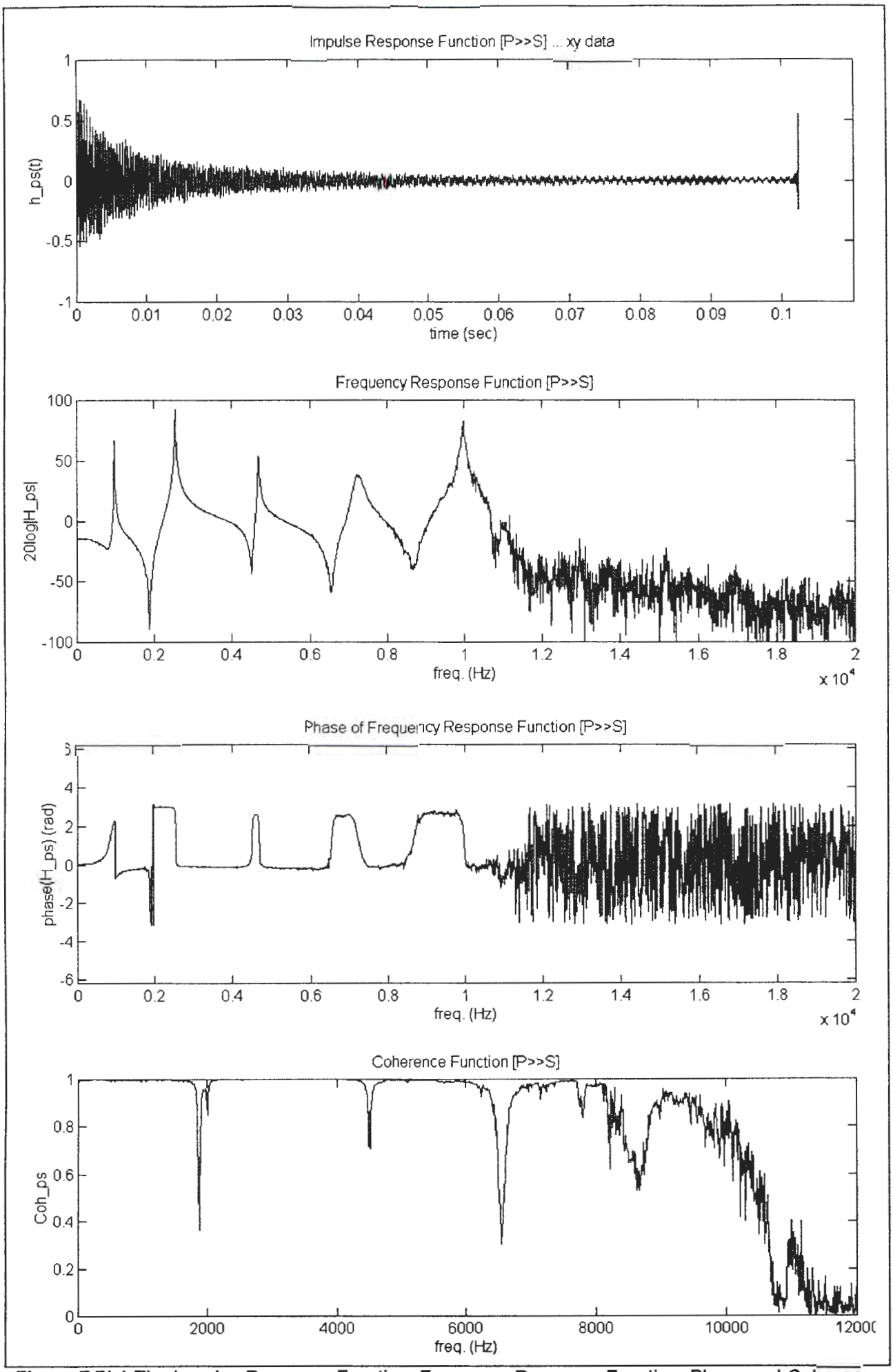

Figure F.7(c) The Impulse Response Function, Frequency Response Function, Phase and Coherence Function for vibration in the xy plane, at location ps.

F.1.5.2 xz Vibration Plane Results.

Similar comments can be made concerning the quality of the resonant and anti-resonant modes, as those made for the xy vibration plane.

Again, in general the xz vibration plane results are satisfactory, as presented in figures F.8(a), F.8(b) & F.8(c). Six sharp well defined modes are identified within the bandwidth. The corresponding coherence function indicates that these modes were consistently defined. Present in the H_pq($j\omega$) frequency response are two additional excited modes, ≈9000 Hz & ≈10000 Hz, outside the bandwidth. While only the ≈9000 Hz mode is present in H_ps($j\omega$) response.

The anti-resonants are in general well defined, compared to the xy vibration plane results. As expected the anti-resonants are a combination of anti-resonant peaks and minimum. The co-located response, H_ps($j\omega$), is once again characterised by a succession of resonant and anti-resonant peaks. While for the other two responses H_pq($j\omega$) & H_pr($j\omega$) there is a combination of anti-resonate peaks and minimum.

The correlation between frequency regions of poorly defined anti-resonant, ill-defined phase and broad band 'zero' coherence is once again noticeable. In each response these regions may be identified:-

- For the H_pq($j\omega$) response, a single region may be identified, the anti-resonant peak between the fifth and sixth mode.
- For the H_pr($j\omega$) response, a single region may be identified between the third and forth modes.
- No regions of poorly defined anti-resonance are present in the H_ps($j\omega$) response.

The presence of these regions of poorly defined anti-resonance peaks imply that there is considerable uncertainty in the definition of these regions. It should again be anticipated that the predictions of the modal identification procedure will not correlate well in these regions.

As observed in the xy vibration plane results, the time domain impulse response functions, h_pq(t), h_pr(t) & h_ps(t), naturally decay to a steady state response. The impulse response function, h_pq(t), exhibits considerable high frequency influences, characterised by the complex waveform in the steady state response region. This is not observed in the impulse response function of h_pr(t) or h_ps(t). The high frequency influence is probably derived from the two strongly excited modes outside the bandwidth, in the H_pq($j\omega$) response.

Aliasing of the impulse response function has once again occurred, characterised by the vertical 'line' at the end of the time datum. The degree of aliasing was judged to be insignificant and hence ignored, even though the h_pq(t) aliasing is easily noticeable.

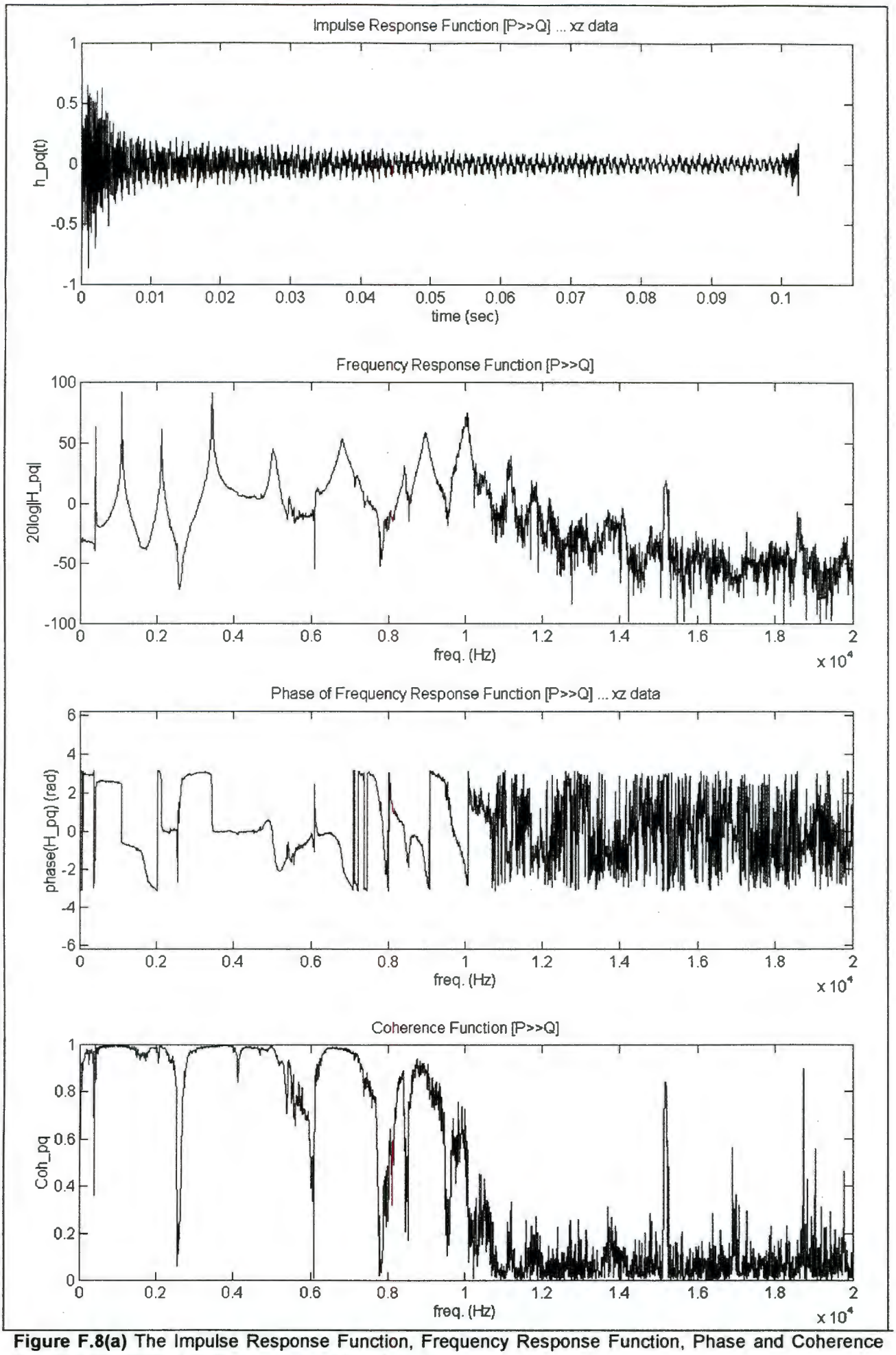

Figure F.8(a) The Impulse Response Function, Frequency Response Function, Phase and Coherence Function for vibration in the xz plane, at location pq.

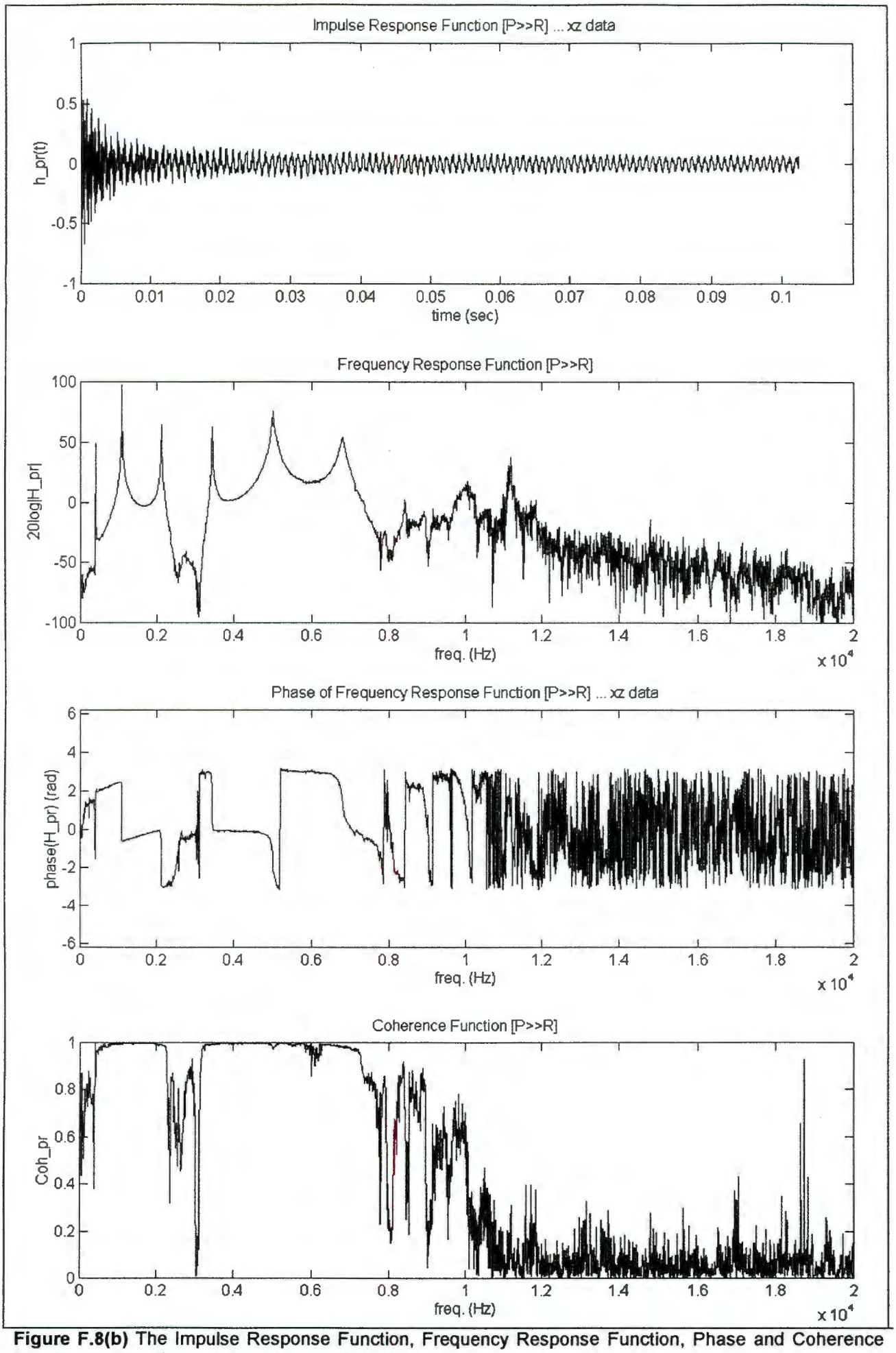

Figure F.8(b) The Impulse Response Function, Frequency Response Function, Phase and Coherence Function for vibration in the xz plane, at location pr.

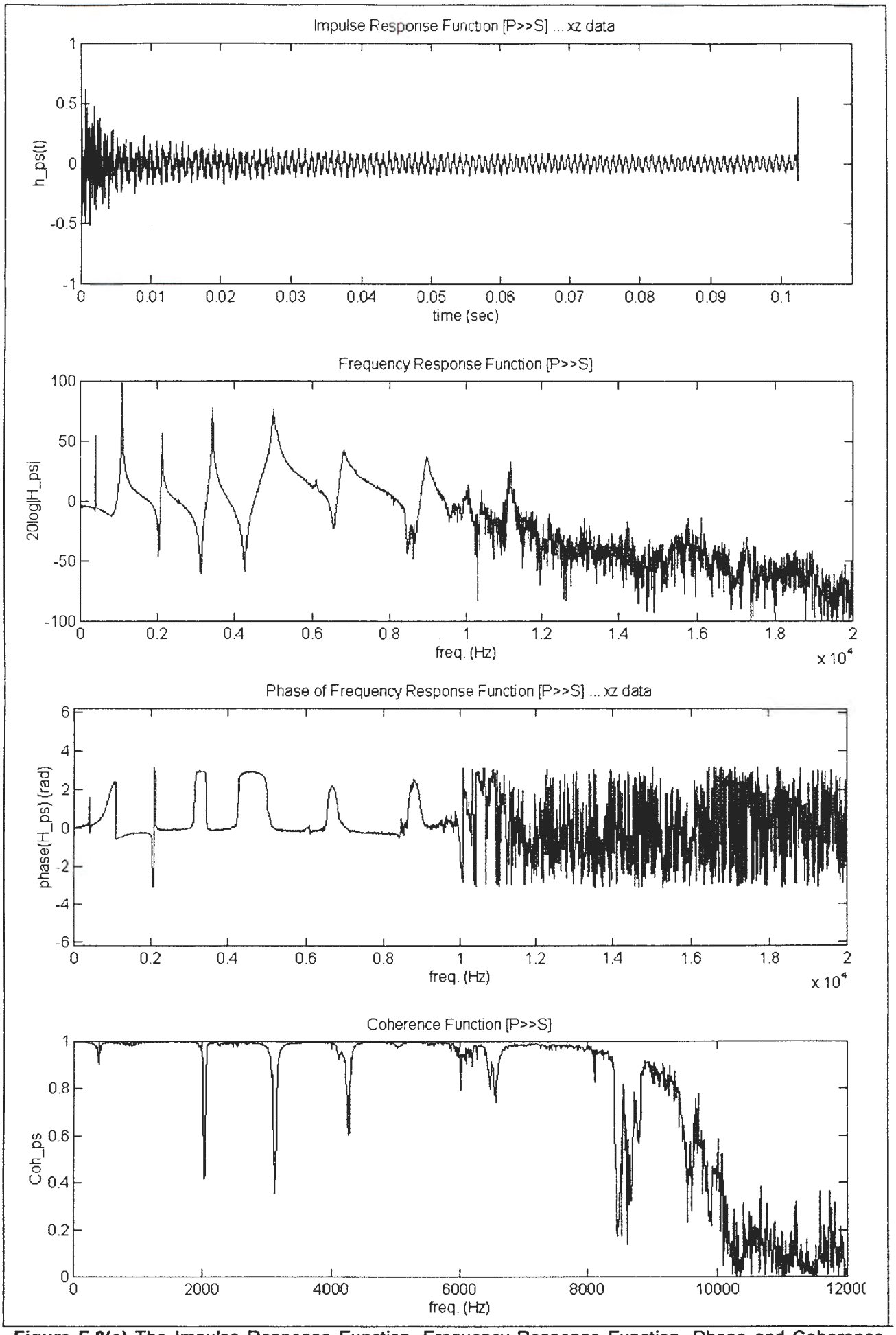

Figure F.8(c) The Impulse Response Function, Frequency Response Function, Phase and Coherence Function for vibration in the xz plane, at location ps.

F.2 Discussion of the Identified Modal Parameters.

In this section the influence of the Hankel matrix dimensions and the number of retained singular values are considered on the accuracy of the identified modal parameters. This section concludes by presenting and discussing the final identified modal parameters.

F.2.1 Influence of the Hankel Matrix Dimensions on the Identified Modal Parameters.

As described in section E.2.1 the Eigensystem Realization Algorithm (ERA) begins by forming the [r x s] generalised Hankel matrix, defined by equation (E-19). As the chosen integer values r & s determine the Hankel matrix dimensions, they also determine the number of discrete time samples used in the realization, from each of the respective impulse response functions (IRF). It is therefore reasonable to anticipate that the dimensions of the Hankel matrix would influence the accuracy of the resultant identified modal parameters.

To investigate the influence of the Hankel matrix dimensions on the identified modal parameters, the Hankel matrix dimensions were systematically increased. The number of retained singular values were chosen to yield a normalised average 'error' of $\approx 10^{-3}$. (The 'error' here refers to the magnitude of the last retained singular value as a fraction of the most dominant singular value.)

The sequence of Hankel matrix dimensions used in the investigation is shown in Table F.1. For this investigation only the processed vibration results in the xy plane are presented.

Table F.1 Hankel matrix dimensions used in the investigation.

file name	integer values s	r	effective Hankel matrix dimension	no. of time samples used in realization	time span of samples used in realization	No. of retained singular values
s3r1y_100	300	100	300 x 300	400	10 ms	100
s3r3y_100	300	300	900 x 300	600	15 ms	100
s6r3y_400	600	300	900 x 600	900	22.5 ms	400
s12r3y_400	1200	300	900 x 1200	1500	37.5 ms	400

The available computer memory storage proved the limiting factor for the maximum possible dimension of the Hankel matrix. For example, considering the s12r3y_400 case, after singular value decomposition the computer memory storage requirements were 38.88 Mbytes, as detailed in Table F.2. Thus for the computer hardware available the [900 x 1200] Hankel matrix dimensions were the largest attainable.

Table F.2 Storage requirements for the s12r3y realization. These storage value excludes additional workspace required during computation and other stored variables. (For an explanation of the matrices refer to equation (E-19)).

Matrix	Matrix Dimensions	Storage Requirements
$H_{rs}(1)$	900 x 1200	8.64 Mbytes
$H_{rs}(0)$	900 x 1200	8.64 Mbytes
P	900 x 900	6.48 Mbytes
D	900 x 900	6.48 Mbytes
Q	1200 x 900	8.64 Mbytes
workspace	-	≈ 15 Mbytes
		$\Sigma \approx$ 54 Mbytes

The Hankel matrix dimensions also determine the number of singular values available, following the singular value decomposition procedure. Plotted on a logarithmic scale, in figure F.9, are the normalised magnitudes of the singular values as a function of the number of singular values available, for each of the four analysed systems.

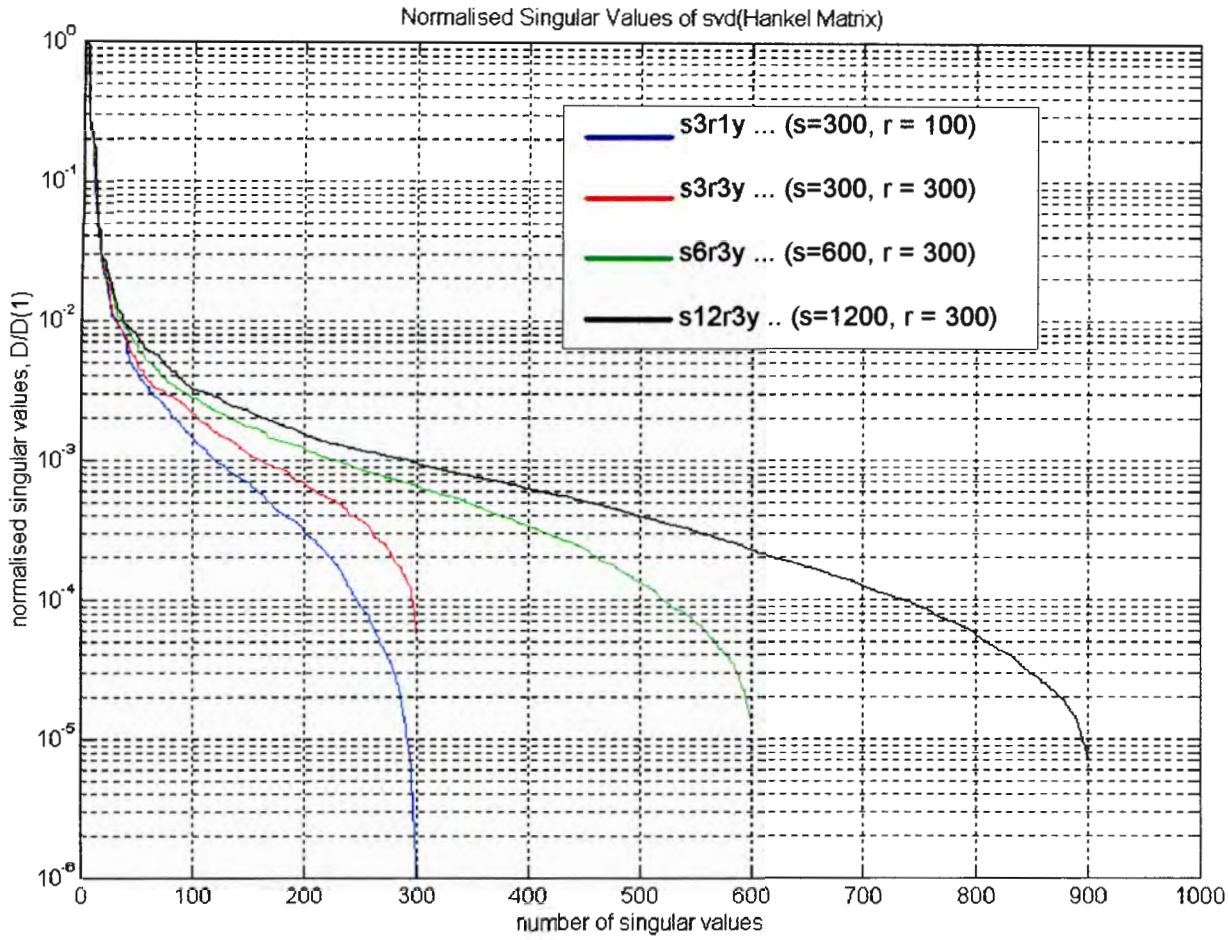

Figure F.9 The sorted, normalised magnitude of the singular values as a function of the number of singular values available, for each of the four realized systems.

It is apparent that there exists three regions for each of the normalised magnitude curves.

- Region #1: A rapid decrease in the normalised magnitude of the singular values, occurring within the initial ≈10% of the total number of singular values. The gradient of all four curves are very similar in this region.
  The consistent gradient obtained for each of the curves in region #1 may be due in part to the normalisation of the singular values, as the actual normalising value differed for each of the investigated cases. Even so, the consistent gradient does indicate that the most predominant singular values occur within the initial ≈10% of singular values.

- Region #2: This region predominates within the ≈10% ⇒ ≈90% bandwidth of possible singular values. Four unique gradients exist, less steep than for region #1. This region demonstrates the linear relationship between the retained number of singular values and the 'error' which could be expected. The 'error' here refers to the magnitude of the last retained singular value as a fraction of the most dominant singular value.

There is a systematic decrease in the gradient within this region, from the most steep gradient of s3r1xy to the least steep gradient of the s12r3xy case. This would seem to indicate that the s3r1xy case would be the most economical, as the 'error' is smallest for the least number of retained singular values. However that is too simplistic, as the s3r1xy case was constructed using the least number of actual samples of the respective IRFs, and hence may not be fully representative.
In the absence of noise or any extraneous high frequency components in the IRFs, it is this author's opinion that the gradient of this region would tend to unity. This has not been substantiated.

- Region #3: This region is of little interest, extending from ≈90% ⇒ ≈100% of possible singular values.

Completing the realizations, for each of the four cases, the identified modal parameters are presented in Table F.3. Only the response results at response location 'pq' are presented.

Table F.3 Identified Modal Parameters, for response location 'pq', for frequencies below the filter cut-off.

file name	s3r1y_100	s3r3y_100	s6r3y_400	s12r3y_400
1st Resonant				
Freq.	979 Hz	979 Hz	979 Hz	979 Hz
Ξ	0.0001	0.0002	0.0005	0.0005
mode	[0.5162]	[0.5197]	[-0.5366]	[0.5385]
2nd Resonant				
Freq.	2541 Hz	2541 Hz	2541 Hz	2541 Hz
Ξ	0.0067	0.0066	0.0066	0.0067
mode	[0.4913]	[-0.4868]	[-0.4949]	[0.4976]
3rd Resonant				
Freq.	4680 Hz	4681 Hz	4681 Hz	4681 Hz
Ξ	0.0154	0.0142	0.0116	0.0113
mode	[-0.3460]	[0.3347]	[-0.3141]	[-0.3041]
4th Resonant				
Freq.	7212 Hz	7218 Hz	7212 Hz	7191 Hz
Ξ	0.1199	0.1342	0.1170	0.1147
mode	[-0.9824]	[-1.0366]	[0.8703]	[-0.8107]

The initial three resonant frequencies are consistently identified. However the higher resonant frequency is sensitive to the Hankel matrix dimensions. Both the damping and mode shapes appear to be highly sensitive to the Hankel matrix dimensions and it would seem that these modal parameters converge as the Hankel matrix dimensions increase. Unfortunately the true numerical value of the modal parameters are unknown and so these comments can only be subjective.

Presented overleaf, figures F.10(a) & F.10(b), are plots of the s3r1_100y and s12r3_400y realized systems compared to the experimental results. As may be expected due to the close correlation of the resonant frequencies seen in Table F.3, there are only minor variations between the two realized systems:

- Most noticeable is the variation in the magnitude of the fourth resonant frequency, between the s3r1_100y and s12r3_400y realized systems. The experimentally identified resonant frequency is undoubtedly closer to 7212 Hz than to 7191 Hz.

- Also noticeable is that the 3rd and 4th anti-resonance peaks have biased more toward the lower frequency region for the s12r3_400y system, when compared to the s3r1_100y realised system. Table F.3 indicates that both the 3rd and 4th realized mode shapes for the s12r3_400y realization have decreased greatly compared to the s3r1_100y case, which would explain this effect. It is difficult to comment on the correctness of these mode shapes, as the experimental anti-resonant peaks are unrealistic.

- Conversely, the 1st anti-resonant peaks are biased toward the higher frequency region for the s12r3_400y system, when compared to the s3r1_100y realised system. The discrepancy may once again be explained from the mode shapes of Table F.3, were the mode shape for the s12r3_400y mode is larger than that for the s3r1_100y realization.

- A smaller error in the difference between the experimental impulse response function (IRF) and the realized IRF for the s12r3_400y system is observed than for the s3r1_100y realization. This should not be surprising as more time samples of each of the experimental IRF were used in the realization.

In summary, the influence of the Hankel matrix dimensions on the realized modal parameters is complex. Figure F.9 shows that irrespective of the Hankel matrix dimensions there exists an initial region (region #1) of rapid decrease in the magnitude of the normalised singular values, followed by a more gentle decline (region #2). The most dominant singular values consistently appear in the initial region, hence the close correlation of modal parameters in Table F.3.

In this case moderate Hankel matrix dimensions proved satisfactory in correctly realizing the resonant frequencies. It should be appreciated that this is the inherent strength of the Eigensystem Realization Algorithm (ERA), i.e. the ability to realize a system, to a given accuracy, using only the most dominant singular values. Unfortunately the true values of the other modal parameters are unknown and hence a more definite judgement on the correctness of these modal parameters could not be made.

The largest Hankel matrix dimensions were used in subsequent realizations, due to the small gain in accuracy observed in predicting the impulse response function.

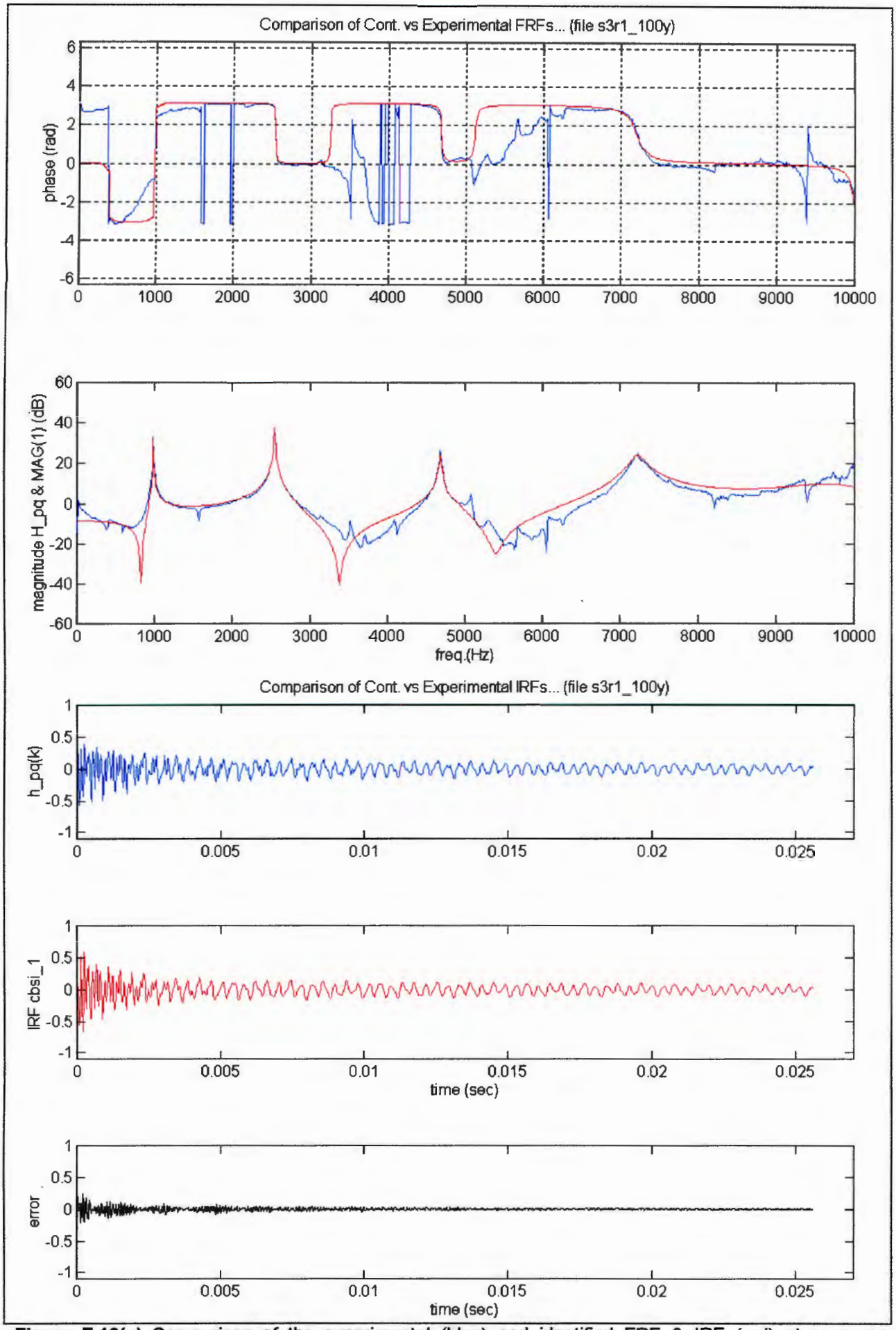

Figure F.10(a) Comparison of the experimental (blue) and identified FRF & IRF (red) at response location 'pq', for the s3r1y_100 realization. (The plot labelled 'error' refers to the difference between the experimental and identified IRFs)

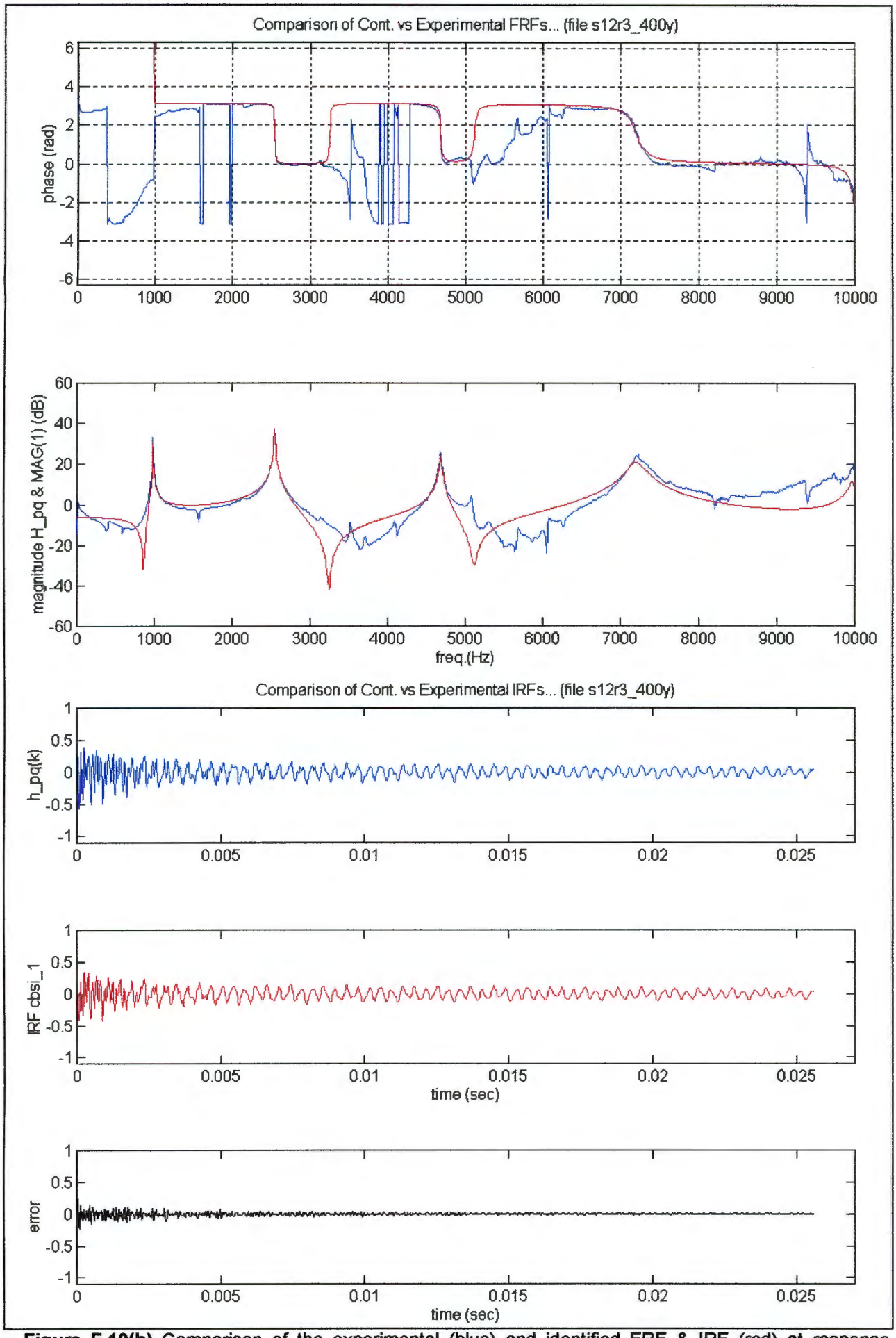

Figure F.10(b) Comparison of the experimental (blue) and identified FRF & IRF (red) at response location 'pq', for the s12r3y_400 realization. (The plot labelled 'error' refers to the difference between the experimental and identified IRFs)

F.2.2 Influence of the Number of Retained Singular Values on the Identified Modal Parameters.

For this investigation the Hankel matrix dimensions of s=1200 and r=300 where chosen. Four realizations were analysed, each having a different number of retained singular values. The details of the four realizations are given in Table F.4

Table F.4 Details of the four analysed realizations

file name	Number of retained *singular values*	Normalised magnitude, at the corresponding number of retained singular values
s12r3z_50	50	0.0176
s12r3z_100	100	0.0056
s12r3z_200	200	0.0027
s12r3z_400	400	0.0012

The normalised magnitude of the singular values are plotted against the number of realized singular values, in Figure F-11. For this investigation only the results at the response location 'pr' in the xz plane are presented.

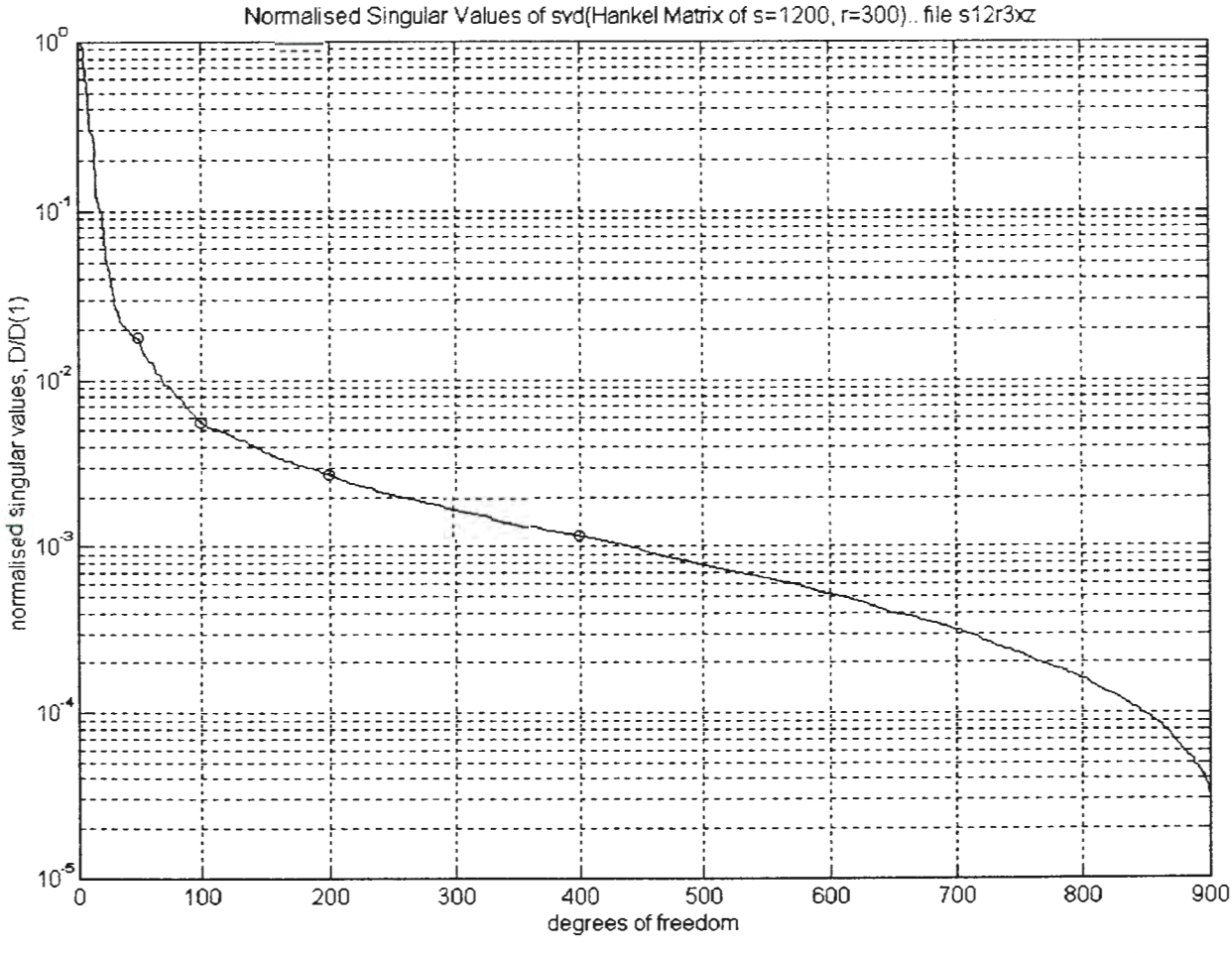

Figure F.11 Normalised magnitude of the singular values are plotted against the number of realized singular values, for the realization of the vibration response in the xz plane.

Notice that, as for the realization of the xy vibration plane results discussed in the previous section, figure F.11 depicts an initial rapid decrease in the magnitude of the normalised singular values followed by a more gradual decrease. The respective normalised magnitudes at the final selected retained singular value are given in Table F.4.

The realized modal parameters are given in Table F.5, for the six resonant modes within the 8000 Hz bandwidth.

Table F.5 Comparison of Identified Modal Parameters, at response location 'pr'. (the ⇔ symbol indicates the presence of two identified resonant modes, so-called 'split modes')

file name	s12r3z_50	s12r3z_100	s12r3z_200	s12r3z_400
1st Resonant Freq.	401 Hz	401 Hz	401 Hz	401 Hz
Ξ	0.0002	0.0001	0.0001	0.0001
mode	[0.2762]	[0.2727]	[0.2733]	[0.2732]
2nd Resonant Freq.	1086 Hz	1086 Hz	1086 Hz	1086 Hz
Ξ	0.0009	0.0010	0.0010	0.0010
mode	[0.5204]	[0.6960]	[0.6956]	[0.6957]
3rd Resonant Freq.	2115 Hz	2115 Hz	2115 Hz	2115 Hz
Ξ	0.0045	0.0047	0.0047	0.0047
mode	[0.4271]	[0.4231]	[0.4228]	[0.4225]
4th Resonant Freq.	3431 Hz	3431 Hz	3431 Hz	3431 Hz
Ξ	0.0052	0.0054	0.0054	0.0054
mode	[0.1846]	[-0.1851]	[0.1846]	[0.1846]
5th Resonant Freq.	5001 Hz ⇔ 5064 Hz	5002 Hz ⇔ 5034 Hz	5000 Hz ⇔ 5007 Hz	5000 Hz ⇔ 5007 Hz
Ξ	0.0267 ⇔ 0.0522	0.0208 ⇔ 0.0681	0.0201 ⇔ 0.1032	0.0206 ⇔ 0.0658
mode	[0.5276 ⇔ 0.3557]	[0.4058 ⇔ -0.5266]	[-0.4127 ⇔ 0.5935]	[0.4021 ⇔ 0.5050]
6th Resonant Freq.	6804 Hz	6806 Hz ⇔ 6868 Hz	6809 Hz ⇔ 6881 Hz	6798 Hz ⇔ 6881 Hz
Ξ	0.0815	0.0649 ⇔ 0.1437	0.0621 ⇔ 0.2760	0.1300 ⇔ 0.0510
mode	[-0.5627]	[0.4883 ⇔ 0.3058]	[0.4486 ⇔ 0.1122]	[0.5856 ⇔ -0.3598]

The modal parameters for the first four modes are virtually exact. This would imply that the first four resonances are well-defined and consistently realized irrespective of the number of retained singular values. Variations in the modal parameters are observed for the fifth and sixth modes. The Eigensystem Realization Algorithm yielded two dominant modes around both the fifth and sixth resonant peaks. This implies that both the fifth and sixth resonant peaks were not uniquely defined experimentally. Notice that the corresponding coherence function, see figure F.8(b), for both of these resonant modes is not unity. Thus there is indeed some uncertainty in their definition. Notice that the second resonant mode, or split mode, around the sixth resonant was not identified when only 50 singular values were retained.

The modal parameters of the fifth and sixth resonant seem to converging as the number of retained singular values is increased. Unfortunately the true modal parameters for the test structure are unknown, thus this assumption can only be made by comparing realized frequency and impulse response functions to their experimental counterparts. These plots are shown overleaf as Figure F.12(a), for the s12r3z_50 realization and F.12(b) for the s12r3_400z realization.

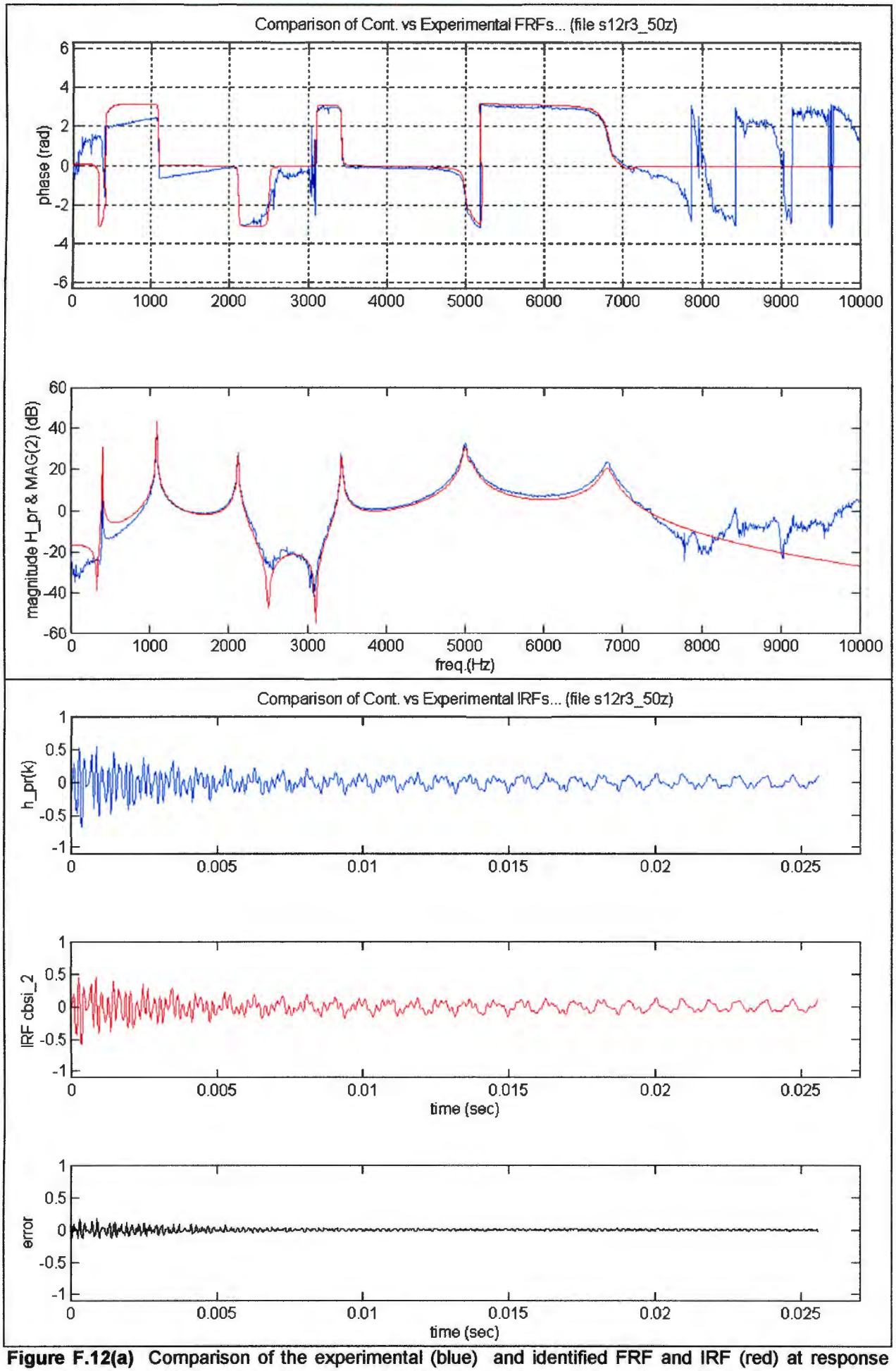

Figure F.12(a) Comparison of the experimental (blue) and identified FRF and IRF (red) at response location 'pr', for case s12r3z_50. (The plot labelled 'error' refers to the difference between the experimental and identified IRFs)

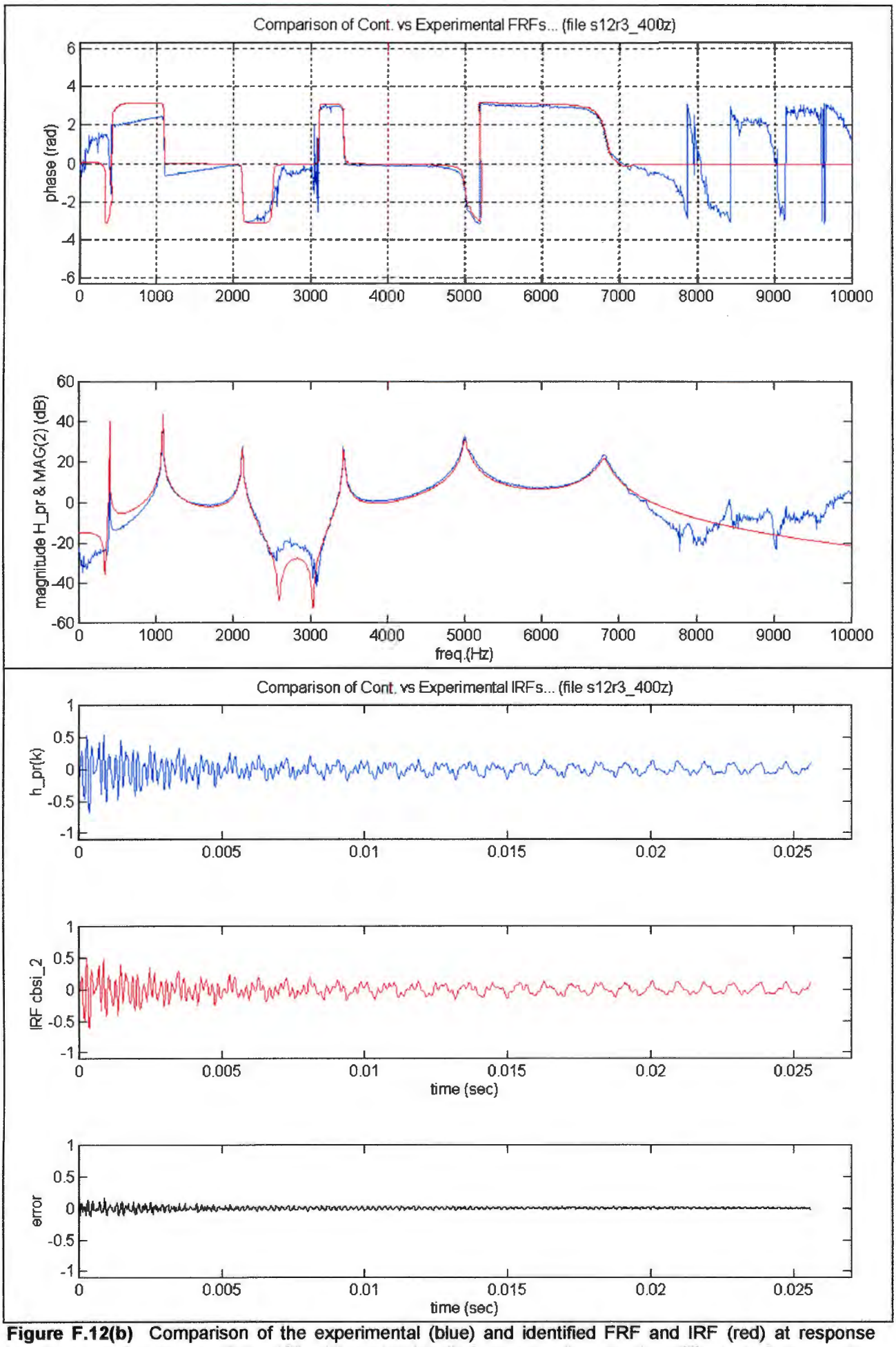

Figure F.12(b) Comparison of the experimental (blue) and identified FRF and IRF (red) at response location 'pr', for case s12r3z_400. (The plot labelled 'error' refers to the difference between the experimental and identified IRFs)

Notice from figures F.12(a) and F.12(b) that the first four resonant peaks correlate well to the experimental FRF, as may be expected due to the consistency of the identified modal parameters in Table F.5 for these modes. Also notice the marked improvement in correlation between the s12r3z_400 realized FRF and the experimental FRF for both the fifth anti-resonant peak and sixth resonant peak. Compare this to the poor correlation between the s12r3z_50 realized FRF and the experimental FRF.

The error in the difference between the realized IRF and the experimentally measured IRF is also smaller for the s12r3z_400 realization than for the s12r3z_50 realization.

In summary, the results of this investigation suggest that while the low frequency characteristics may be adequately described by a small number of retained singular values, to adequately model the higher frequency behaviour additional singular values should be retained. Reflecting on the findings of the previous investigation, it is apparent that the dimensions of the Hankel matrix and the number of retained singular values are associated. The optimal course is to utilise the largest possible Hankel matrix dimensions and retain the largest possible number of singular values practical. This will ensure that both the low and high frequency characteristics of the realized system will be adequately modelled.

F.2.3 Presentation of Modal Parameters.

In this section the realized modal parameters are presented. Based on the discussion of the influence of the Hankel matrix dimensions and the number of retained singular values, the final values for these variables are given in Table F.6

Table F.6 Details of the final realizations, for both the xz & xy vibration planes

file name	Number of retained singular values	integer values r	s
s12r3z_400	400	1200	300
s12r3y_400	400	1200	300

The identified modal parameters are listed in Table F.7. Only natural frequencies below the filter cut-off are tabulated, although the higher natural modes where identified.

Table F.7 Identified Modal Parameters, for both the xz & xy vibration planes. The mode shape vector refers to the mode shape at the locations [q,r,s] respectively.

	s12r3z_400 vibration plane xz		s12r3y_400 vibration plane xy
1st Resonant			
Freq.	401 Hz		979 Hz
Ξ	0.0001		0.0005
mode shape	[0.5616, 0.2732, -0.3489]		[0.5385, 0.2683, -0.3358]
2nd Resonant			
Freq.	1086 Hz		2541 Hz
Ξ	0.0010		0.0067
mode shape	[0.5215, 0.6957, 0.7225]		[0.4976, 0.6584, 0.6754]
3rd Resonant			
Freq.	2115 Hz		4681 Hz
Ξ	0.0047		0.0113
mode shape	[-0.33596, 0.4225, -0.2736]		[-0.3041, 0.3257, -0.2126]
4th Resonant			
Freq.	3431 Hz		7191 Hz
Ξ	0.0054		0.1147
mode shape	[0.7383, 0.1846, 0.3878]		[-0.8107, -0.1216, -0.3565]
5th Resonant			
Freq.	5000 Hz	5007 Hz	-
Ξ	0.0206	0.0658	-
mode shape	[0.0598, 0.4021, -0.4139]	[0.1459, 0.5050, -0.5325]	-
6th Resonant			
Freq.	6798 Hz	6881 Hz	-
Ξ	0.1300	0.0510	-
mode shape	[-0.5230, 0.5856, 0.3111]	[0.4341, -0.3598, -0.2105]	-

The respective FRF and IRFs, for all the respective input/output combinations, are presented.

F.2.3.1 Description of results for the xy vibration plane

- Response at location 'pq', see figure F.13(a)
  The location and magnitude of the initial three resonant peaks correlate exactly with their experimental counterparts. There is a minor discrepancy at the forth resonant peak, where a slight deviation in magnitude occurs. The first and second anti-resonant minimum correlate well with the experimental minimum. However, the third and forth anti-resonant peaks deviate significantly from the experimental anti-resonance. As commented previously, (sections F.1.5.1 & F.2.1), there is uncertainty in the reliability of both of these anti-resonant peaks due to the poor coherence definition in these regions. It is proposed that the identified anti-resonant peaks are a more realistic representation.

  The phase characteristics of the identified FRF correlate well to the experimental FRF's phase. Again it is proposed that the identified phase characteristics are a more realistic representation, in the regions of the third and forth anti-resonant peaks. Considering the identified time domain response, the difference between the experimental and realized impulse response functions is acceptable.

- Response at location 'pr', see figure F.13(b)
  The correlation between both the experimental and identified FRF and phase characteristics of the initial three resonant and anti-resonant peaks are acceptable. While the location and magnitude of the forth resonant peak is less well correlated. The fourth anti-resonant peak does not correlate to the experimental peak, although it is proposed that the identified anti-resonant peak is more realistic. It is argued that the poor coherence definition and ill-defined phase characteristics in this region, indicate that the anti-resonant peak is poorly defined.

  There is a significant difference between the experimental and identified IRFs. Clearly , the experimental IRF contains high frequency contributions not modelled in the identified response. Notice the strongly excited mode in the region of ≈10000 Hz, see figure F.7(b), but not included in the time domain realization.

- Response at location 'ps', see figure F.13(c)
  Notice that while acceptable correlation is achieved for both the location and magnitude of the resonant peaks, the anti-resonant peaks are incorrectly shifted toward the lower frequency spectrum. The phase characteristics similarly indicate this shift in the location of the anti-resonant peaks.

  Dr. Peterson (*personal correspondence*) suggested either neglecting the co-located response or implementing a curve-fitting procedure to correct for the 'phase lag'. The curve fitting procedure, however, would invalidate the linear state space modelling assumption on which the modal identification procedure was based. In addition, a residual flexibility term would be introduced, to account for the omitted high frequency resonance modes, which cannot be incorporated into the formulation of the mass, damping and stiffness matrices. Thus the curve fitting procedure was not implemented and the 'ps' response was omitted from the formulation of the mass, damping and stiffness matrices.

  The difference between the experimental and identified IRFs is once again significant. Truncated high frequency modes are thought to be responsible.

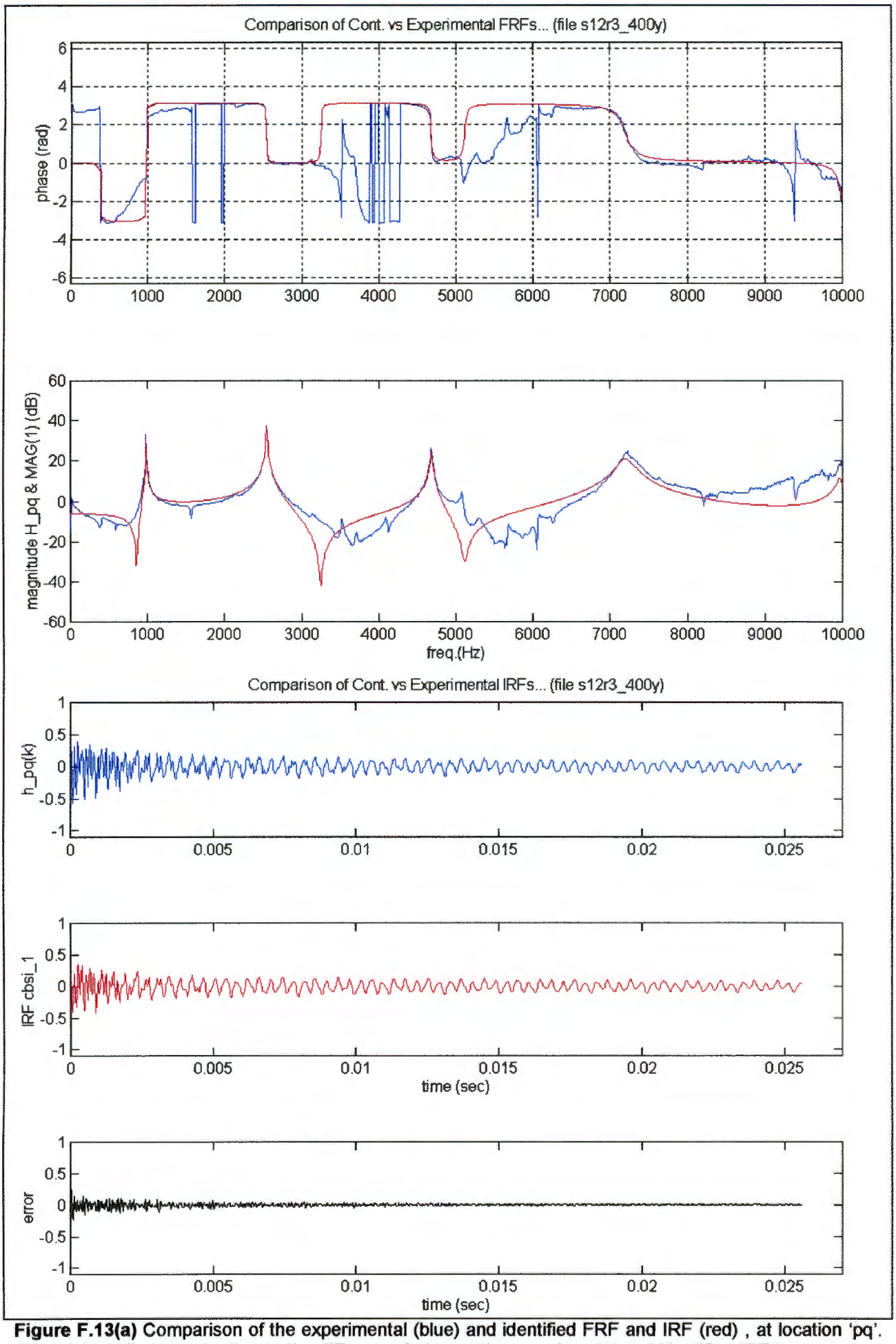

Figure F.13(a) Comparison of the experimental (blue) and identified FRF and IRF (red) , at location 'pq'. (The plot labelled 'error' refers to the difference between the experimental and identified IRFs)

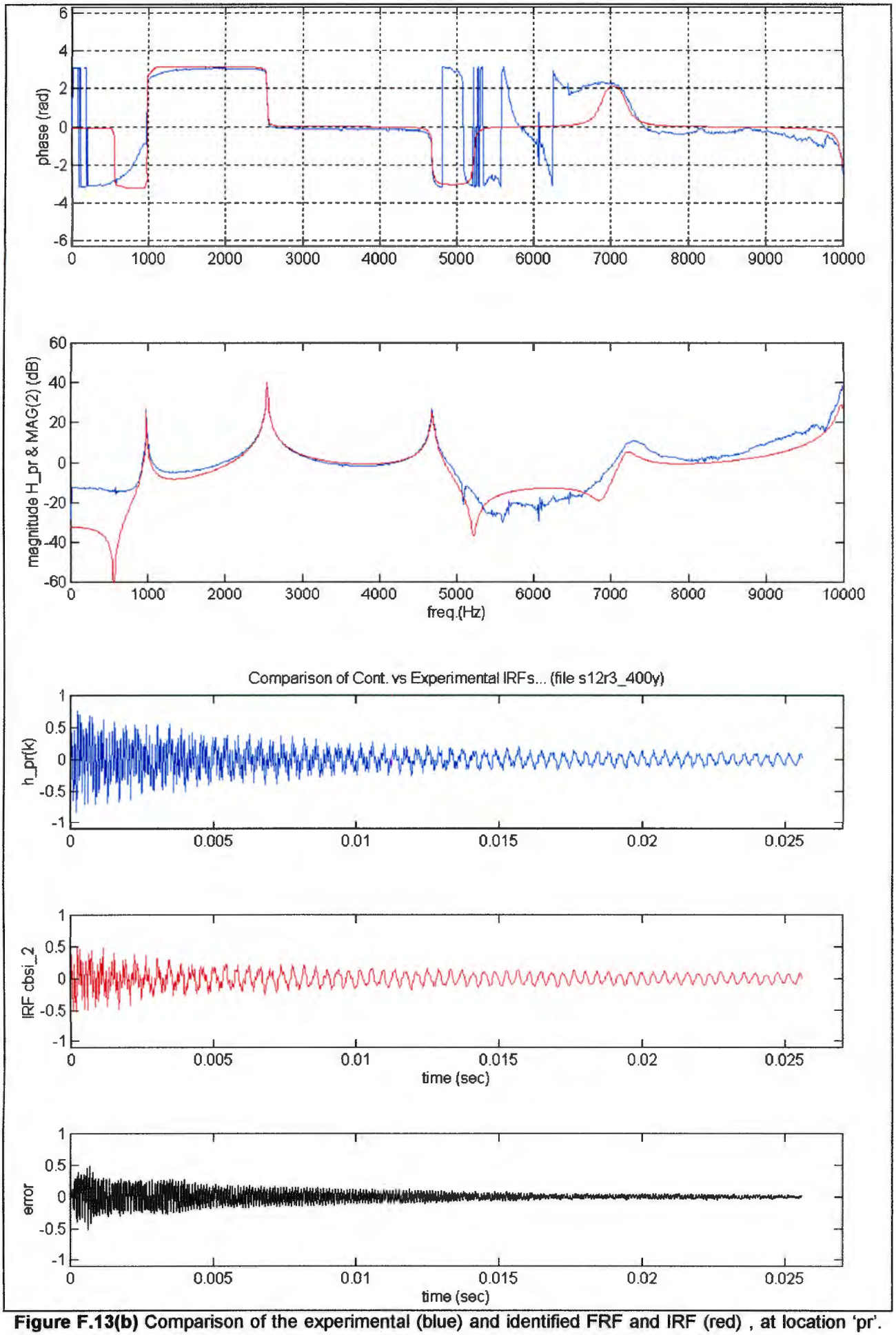

Figure F.13(b) Comparison of the experimental (blue) and identified FRF and IRF (red) , at location 'pr'. (The plot labelled 'error' refers to the difference between the experimental and identified IRFs)

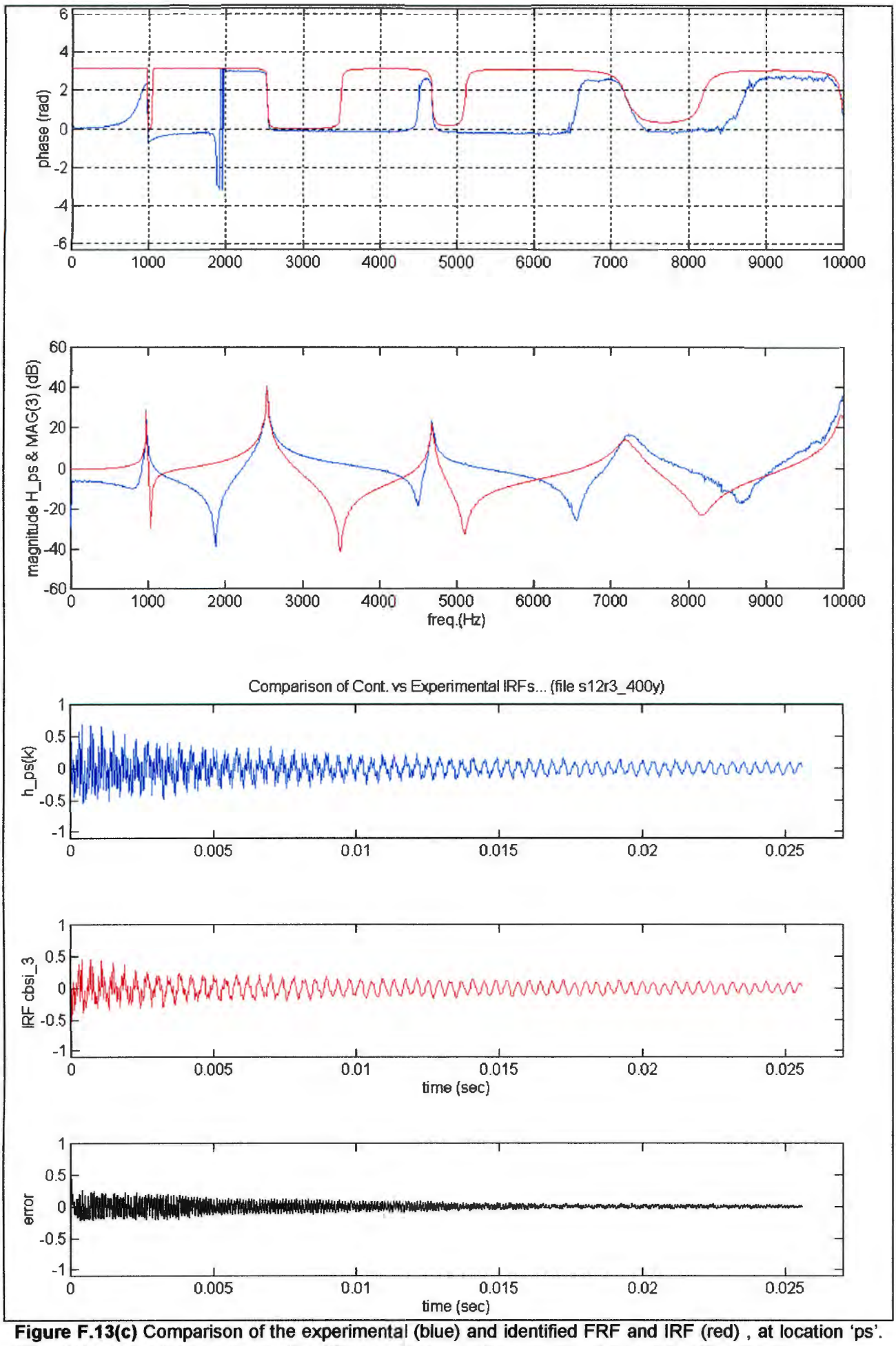

Figure F.13(c) Comparison of the experimental (blue) and identified FRF and IRF (red) , at location 'ps'. (The plot labelled 'error' refers to the difference between the experimental and identified IRFs)

F.2.3.2 Description of results for the xz vibration plane

- Response at location 'pq', see figure F.14(a)
  The location and magnitude of the six resonant peaks correlate exactly with their experimental counterparts. A minor exception is the fifth resonant peak, where a slight deviation occurs. The anti-resonant peaks correlate well for the initial five anti-resonant peaks. The identified FRF's representation of the sixth anti-resonant peak is probably a more realistic representation, than the experimental FRF. Noting the comments of section F.1.5.2, concerning the poor definition of the coherence function in this region.

  The phase characteristics of the identified FRF correlate well to the experimental FRF's phase. An exception is the opposing direction of the phase for the third anti-resonant peak.

  Considering the identified time domain response, the difference between the experimental and realized impulse response functions is significant during the initial 5ms. This is due to the omission of the strongly excited resonant peaks of ≈9000 Hz and ≈10000 Hz from the realization. These modes were omitted as they both are greater than the measured bandwidth.

- Response at location 'pr', see figure F.14(b)
  The correlation between both the FRF and phase characteristics of the experimental and identified results are excellent. The location and magnitude of the resonant peaks and anti-resonant peaks are well correlated.

  As both the resonant modes outside the measured bandwidth are weakly excited, the difference between the experimental and identified IRFs is minimal.

- Response at location 'ps', see figure F.14(c)
  Most noticeable in these comparative results, are that while the location and magnitude of the resonant peaks correlate exactly, the anti-resonant peaks are incorrectly shifted toward the lower frequency spectrum. The phase characteristics similarly indicate this shift in the location of the anti-resonant peaks. Initially it was thought that there was significant high frequency content in the signal, which while neglected was distorting the identified phase characteristics. This was discounted as the time domain realization closely predicts the experimental impulse response function.

  Dr. Peterson (*personal correspondence*) suggested either neglecting the co-located response or implementing a curve-fitting procedure to correct for the 'phase lag'. The curve fitting procedure, however, would invalidate the linear state space modelling assumption on which the modal identification procedure was based. In addition, a residual flexibility term would be introduced, to account for the omitted high frequency resonance modes, which cannot be incorporated into the formulation of the mass, damping and stiffness matrices. Thus the curve fitting procedure was not implemented and the 'ps' response was omitted from the formulation of the mass, damping and stiffness matrices.

  The difference between the experimental and identified IRFs is acceptable, but larger in magnitude than for the 'pr' response. This may be due to the strongly excited ≈9000 Hz resonant modes outside the measured bandwidth.

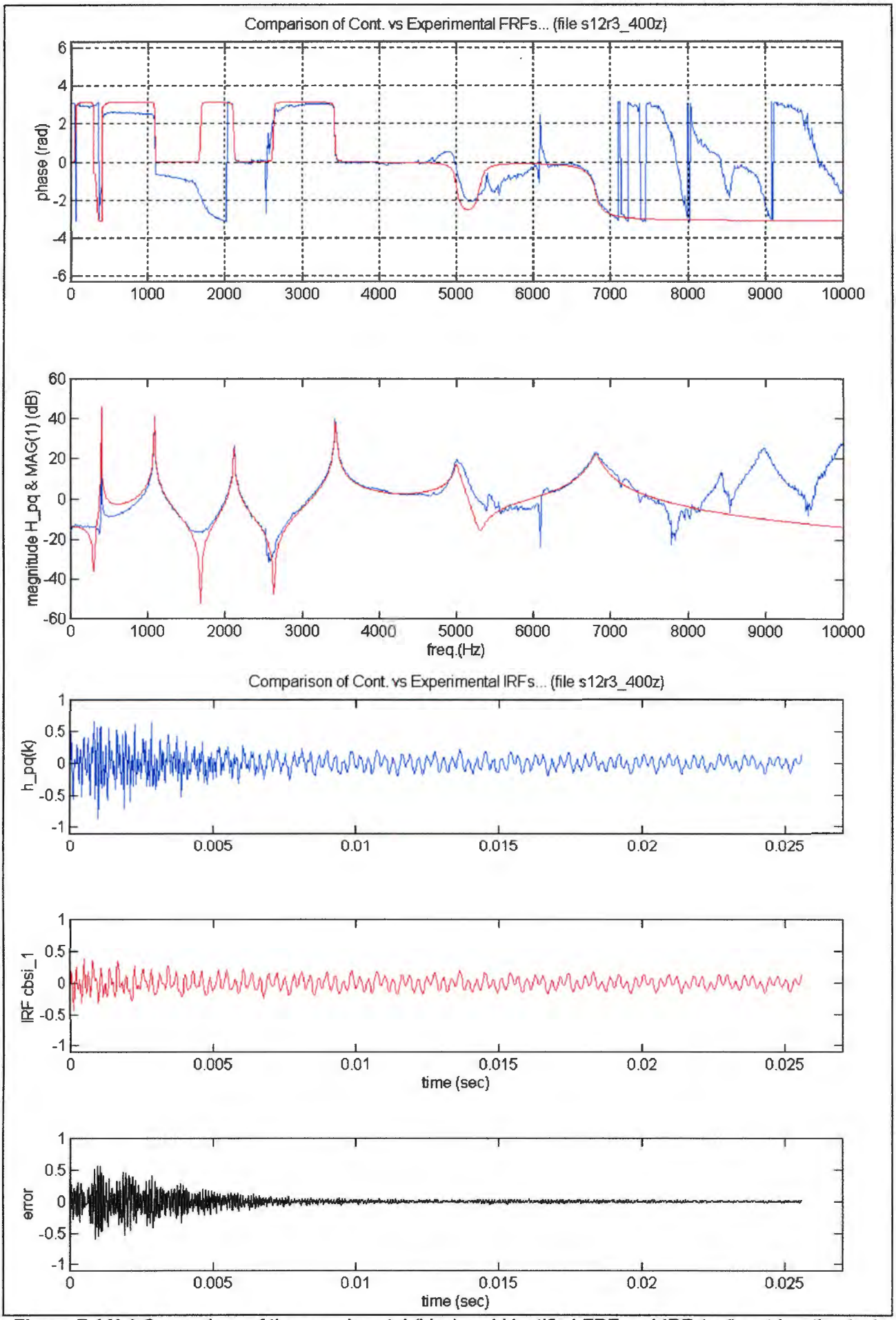

Figure F.14(a) Comparison of the experimental (blue) and identified FRF and IRF (red) , at location 'pq'. (The plot labelled 'error' refers to the difference between the experimental and identified IRFs)

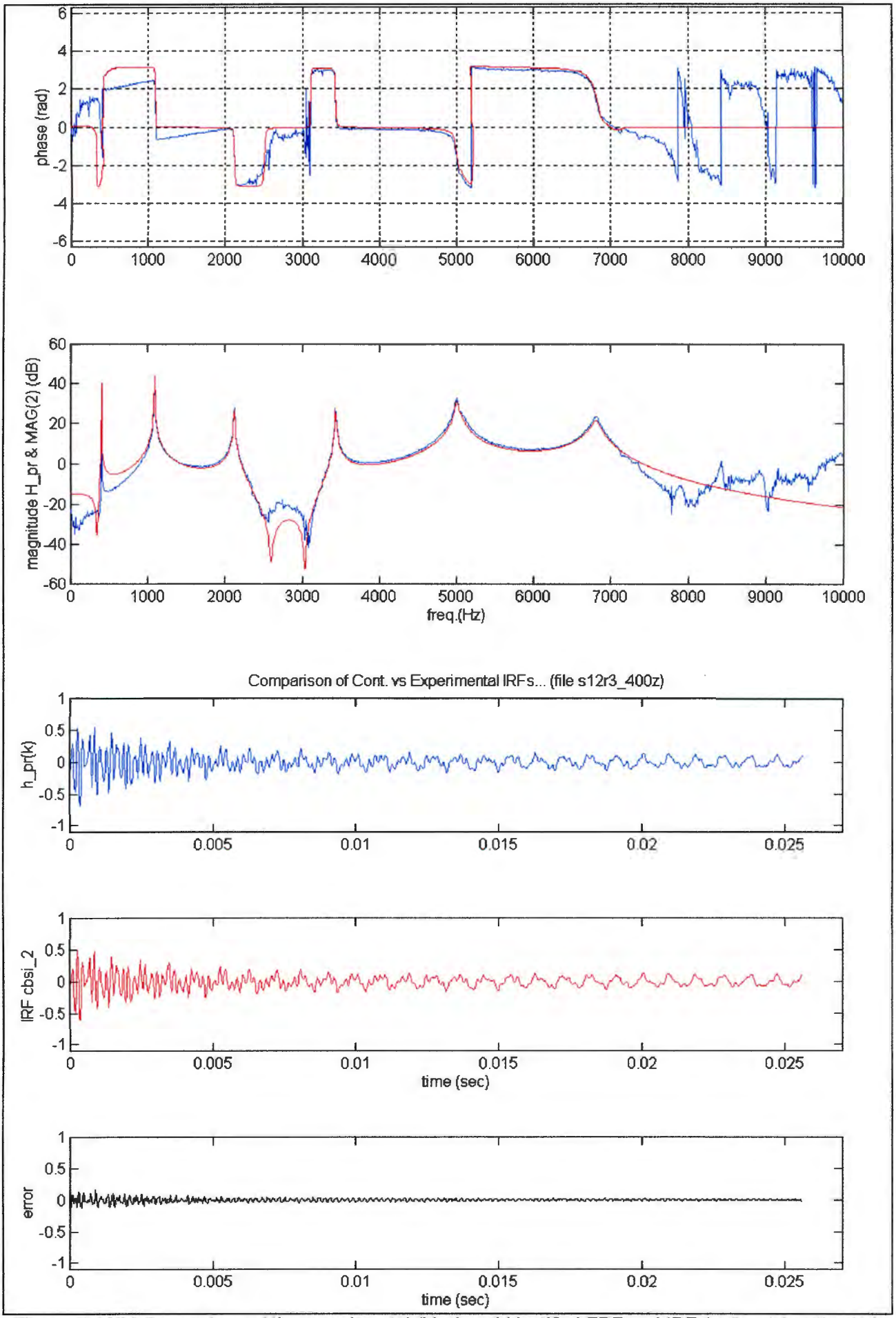

Figure F.14(b) Comparison of the experimental (blue) and identified FRF and IRF (red) , at location 'pr'. (The plot labelled 'error' refers to the difference between the experimental and identified IRFs)

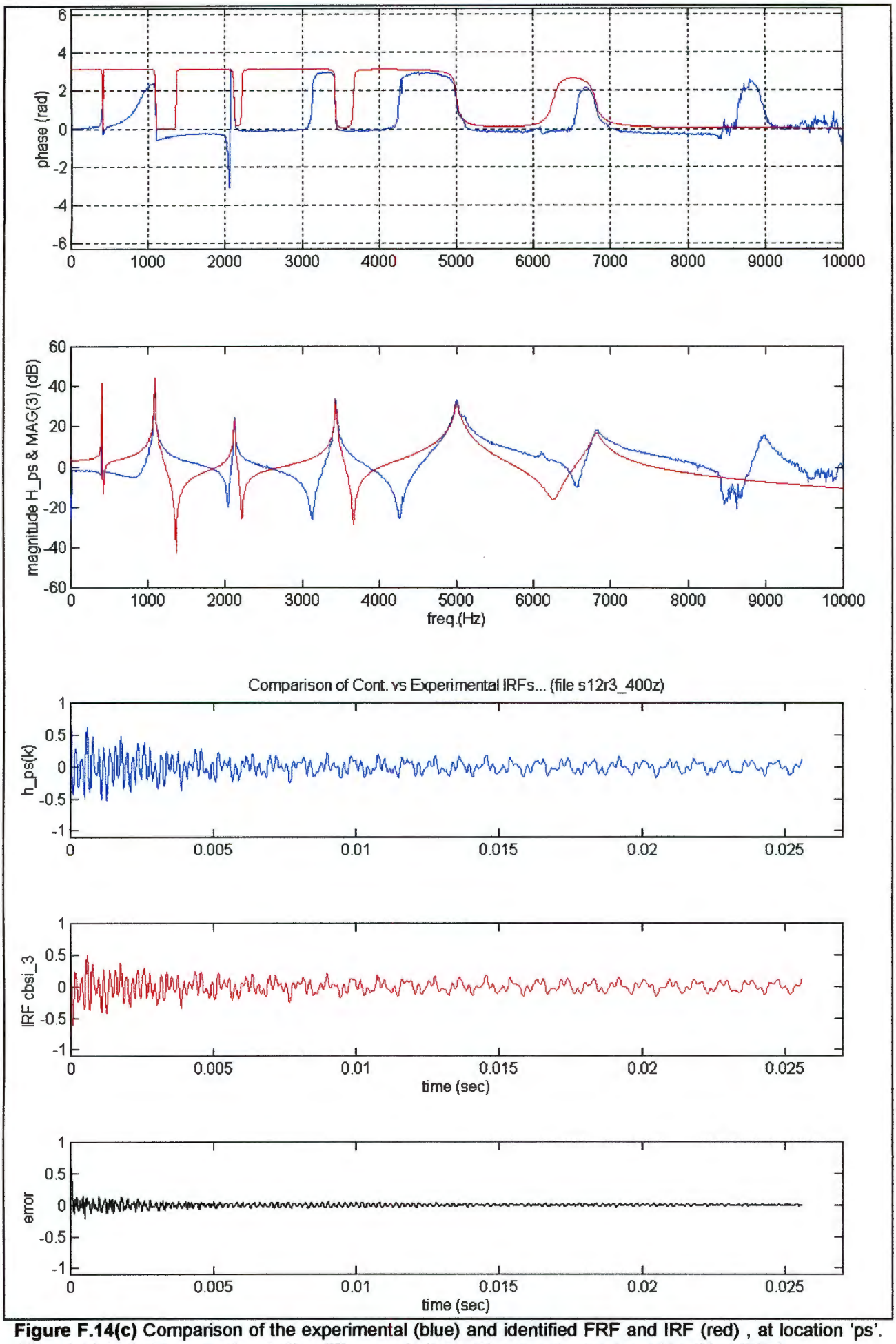

Figure F.14(c) Comparison of the experimental (blue) and identified FRF and IRF (red) , at location 'ps'. (The plot labelled 'error' refers to the difference between the experimental and identified IRFs)

In summary, the respective identified systems predicted the experimental vibration responses very well. The majority of the discrepancies resulted from truncated high frequency modes. Poorly defined anti-resonant regions, in the frequency response functions, were more realistically represented by the identified frequency response functions. The identified frequency and impulse response functions are 'smoothed' versions of the experimental data, as all poorly excited modes and extraneous noise artefact were removed from the identified functions.

F.3 Mass, Damping and Stiffness Matrices.

The identified mass normalised eigenvectors, undamped resonant frequencies and modal damping coefficients were applied to the software routine, **cms**. The underlying theory and construction of this routine was discussed in section E.3 and E.4.

For the identified data, ten non-zero singular values resulted from the singular decomposition of the dynamic residual matrix, $\Delta\Omega$. This quantity thus defined the dimensions of the resultant mass, stiffness and damping matrices. These matrices are presented in Figure F.15(a) & F.15(b), for both the xy and xz vibration planes respectively.

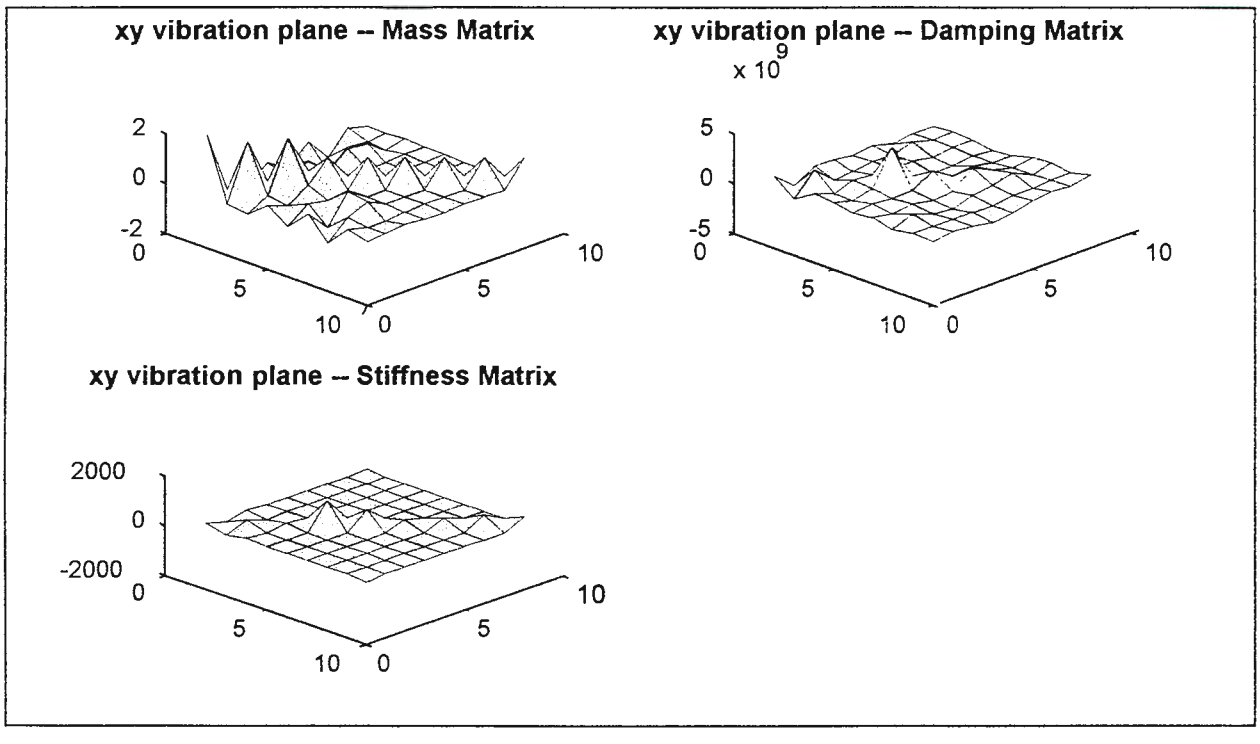

Figure F. 15(a) The Mass, Damping and Stiffness Matrices in the xy vibration planes.

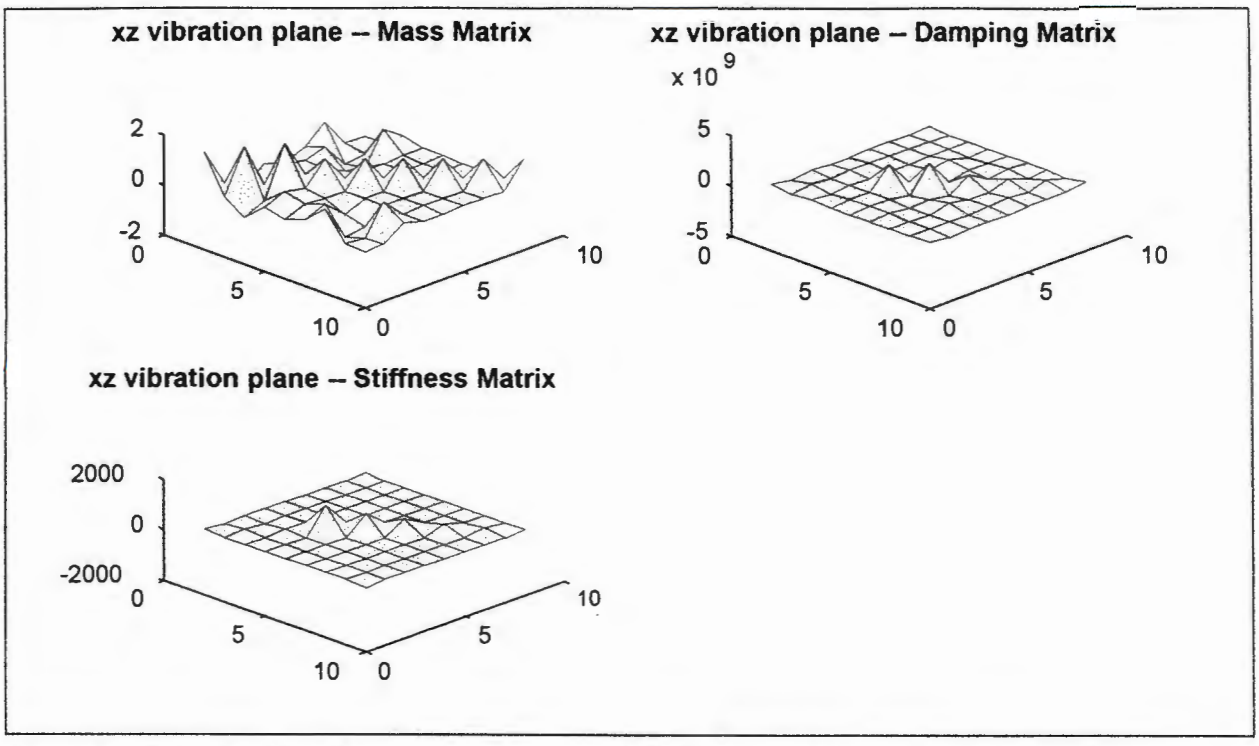

Figure F. 15(b) The Mass, Damping and Stiffness Matrices in the xz vibration planes.

Notice the characteristic diagonal dominance in all of the matrices. Interpretation of the respective matrices is difficult as there is no theoretical basis against which to evaluate their correctness. It should be appreciated that one of the motivations for the formulation of these least-order matrices was to allow comparisons to be made between the vibration response of a number of test structures (patient's tibia). For this purpose these matrices may still provide a useful way of representing the 'complete' vibration response.

F.4 Finite Element Model Predictions.

In the following section the finite element model predictions will be presented. The influence of both the material properties and degree of mesh refinement, on the predicted flexural resonant frequencies are considered. The section concludes by presenting and comparing the finite element predictions to the experimental vibration responses.

F.4.1 Influence of the Material Properties on Predicted Modal Parameters.

As might be expected the material properties influence the model parameters predicted by the finite element beam element. The Young's modulus, shear modulus and Poisson ratio were unknown for the test structure and hence were estimated. The value of both Young's modulus and the shear modulus are required for the formulation of the stiffness matrix, see equations (C-40) and (C-41). The Poisson ratio defines the relationship between these moduli, see equation (F-1).

The Poisson ratio was assumed to be equal to 0.3, which is an acceptable value for the mild steel test structure. Hence the shear and Young's modulus are related via equation (F-1)

$$G = \frac{E}{2(\nu+1)} \quad \text{or since } \nu = 0.3$$
$$G = \frac{E}{2.6} \qquad \textbf{(F-1)}$$

Within limits it is now possible to vary the magnitude of either the shear modulus or Young's modulus to match the experimental modal parameters. This procedure was described in the literature review of section C.1.1.3. Table F.8 tabulates the sequence of values assigned to both the shear, Young's modulus and the corresponding solved resonant frequencies.

Table F.8 The influence of material properties on the predicted finite element resonant frequencies, for vibration in the xz plane. (10 elements used)

	E=200 GPa and G=77GPa xz	E=202 GPa and G=77.7GPa xz	E=204 GPa and G=78.5GPa xz	Identified Modal Parameters xz
1st Resonant Freq.	396 Hz	398 Hz	400 Hz	401 Hz
2nd Resonant Freq.	1081 Hz	1086 Hz	1091 Hz	1086 Hz
3rd Resonant Freq.	2089 Hz	2100 Hz	2110 Hz	2115 Hz
4th Resonant Freq.	3393 Hz	3410 Hz	3426 Hz	3431 Hz
5th Resonant Freq.	4966 Hz	4986 Hz	5010 Hz	5000 Hz to 5007 Hz
6th Resonant Freq.	6766 Hz	6799 Hz	6831 Hz	6798 Hz to 6881 Hz

No formal attempt was made to optimise either the value for the shear or Young's modulus. Table F.8 clearly demonstrates the convergence of the predicted resonant frequencies toward the experimental resonant frequencies, as the value of the Young's modulus is increased. A similar trend was observed for the results in the xy vibration plane. Thus the material properties that were used in the subsequent finite element analysis were:- E=204 GPa, G=78.5 GPa and ν=0.3

F.4.2 Influence of Mesh Refinement on the Predicted Modal Parameters.

The refinement of the finite element mesh was considered to be an influential parameter on the convergence of the predicted modal parameters. As a result the element length was progressively deduced and the resonant frequencies compared to the experimental modes. Table F.9 lists the three cases that were analysed, together with the predicted natural frequencies.

Table F.9 The influence of the element length on the predicted finite element resonant frequencies, for vibration in the xz plane. (The material properties E=204 GPa and G=78.5GPa). Also given are the natural frequencies predicted by Euler beam theory, for comparison.

	Euler Beam Theory	10 elements xz	20 elements xz	50 elements xz	Identified Modal Parameters xz
Element Length	n/a	50 mm	25 mm	10 mm	n/a
1st Resonant Freq. xz	402 Hz	400 Hz	400 Hz	401 Hz	401 Hz
2nd Resonant Freq.	1109 Hz	1091 Hz	1092 Hz	1092 Hz	1086 Hz
3rd Resonant Freq.	2173 Hz	2110 Hz	2111 Hz	2111 Hz	2115 Hz
4th Resonant Freq.	3593 Hz	3426 Hz	3427 Hz	3426 Hz	3431 Hz
5th Resonant Freq.	5367 Hz	5010 Hz	5011 Hz	5010 Hz	5000 Hz to 5007 Hz
6th Resonant Freq.	7496 Hz	6831 Hz	6832 Hz	6833 Hz	6798 Hz to 6881 Hz

The results of Table F.9 indicate that the initial six predicted resonant modes are insensitive to the element length. Typically, convergence of the resonant frequencies would normally be observed as the degree of mesh refinement is increased. As this is not observed, the implication is that the finite element model has converged. (Convergence of the resonant frequencies was observed at frequencies greater than the measured bandwidth)

The 10 element solution was used in subsequent finite element analysis. However, for more complex varying geometry and material properties, a finer element mesh would be required.

The results also indicate the value of developing the three-node Timoshenko beam element over the Euler beam formulation. While direct comparisons of the 'element length to convergence' have not been made between the Euler and Timoshenko beam, the difference should be appreciated by comparing the frequencies predicted by Euler beam theory and Timoshenko finite element model.

F.4.3 Comparison of the Finite Element Predictions to Experimental Vibration Results.

The comparison of the finite element model predictions to the experimental vibration results are presented in two phases. The initial phase compares the predicted resonant frequencies, while the second phase considers the effect of damping on the comparison of the predicted frequency and impulse response functions.

F.4.3.1 Comparison of the Predicted and Measured Resonant Frequency.

The predicted finite element flexural resonant frequencies are tabulated in Table F-10, together with the experimentally identified resonant frequencies.

Table F.10 Comparison of the finite element and experimentally identified resonant frequencies, for both the xz & xy vibration planes.

	s12r3z_400 vibration plane xz		Finite Element Predictions	s12r3y_400 vibration plane xy	Finite Element Predictions
1st Resonant Freq.	401 Hz		401 Hz	979 Hz	978 Hz
2nd Resonant Freq.	1086 Hz		1092 Hz	2541 Hz	2553 Hz
3rd Resonant Freq.	2115 Hz		2111 Hz	4681 Hz	4676 Hz
4th Resonant Freq.	3431 Hz		3426 Hz	7191 Hz	7166 Hz
5th Resonant Freq.	5000 Hz	5007 Hz	5010 Hz	exceeds cut-off freq.	-
6th Resonant Freq.	6798 Hz	6881 Hz	6833 Hz	exceeds cut-off freq.	-

The correlation is acceptable and on average the finite element prediction do not deviate by more than 1% from the experimentally identified resonant frequencies. As may be expected the largest derivation is for the higher frequency modes.

F.4.3.2 The Effect of Damping on the Comparison of the Predicted and Measured Response Functions.

The effect of damping is best illustrated by comparing the frequency and impulse response functions for the undamped and damped case. The undamping finite element response functions are given in Figure F-16(a), while the damped predicted response functions are given in Figure F-16(b) for vibration in the xy plane. Figures F-17(a) & F-17(b) are similar plots for the xz plane.

The predicted modal damped coefficients for the proportional, mass-proportional and stiffness-proportional damping cases were similar. As the predicted damped resonant frequencies, using proportional damping values α=1.0E-06 & β=1.0E-06, resulted in marginally lower damped frequencies these values were used in the comparison.

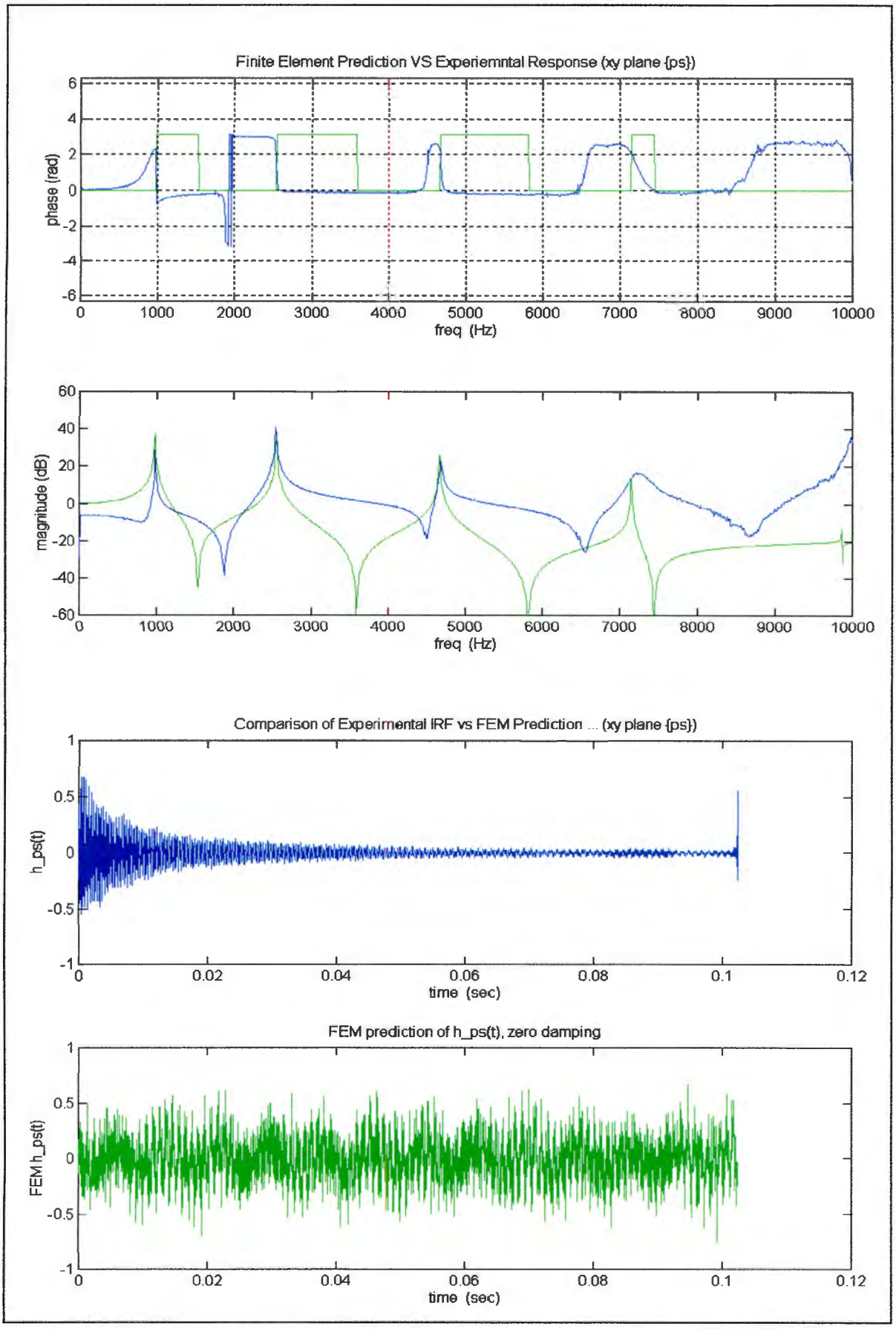

Figure F.16(a) Comparison of the Finite Element prediction (green) and the experimentally measured frequency and impulse response functions (blue), at location 'ps'. The finite element analysis was conducted with zero damping.

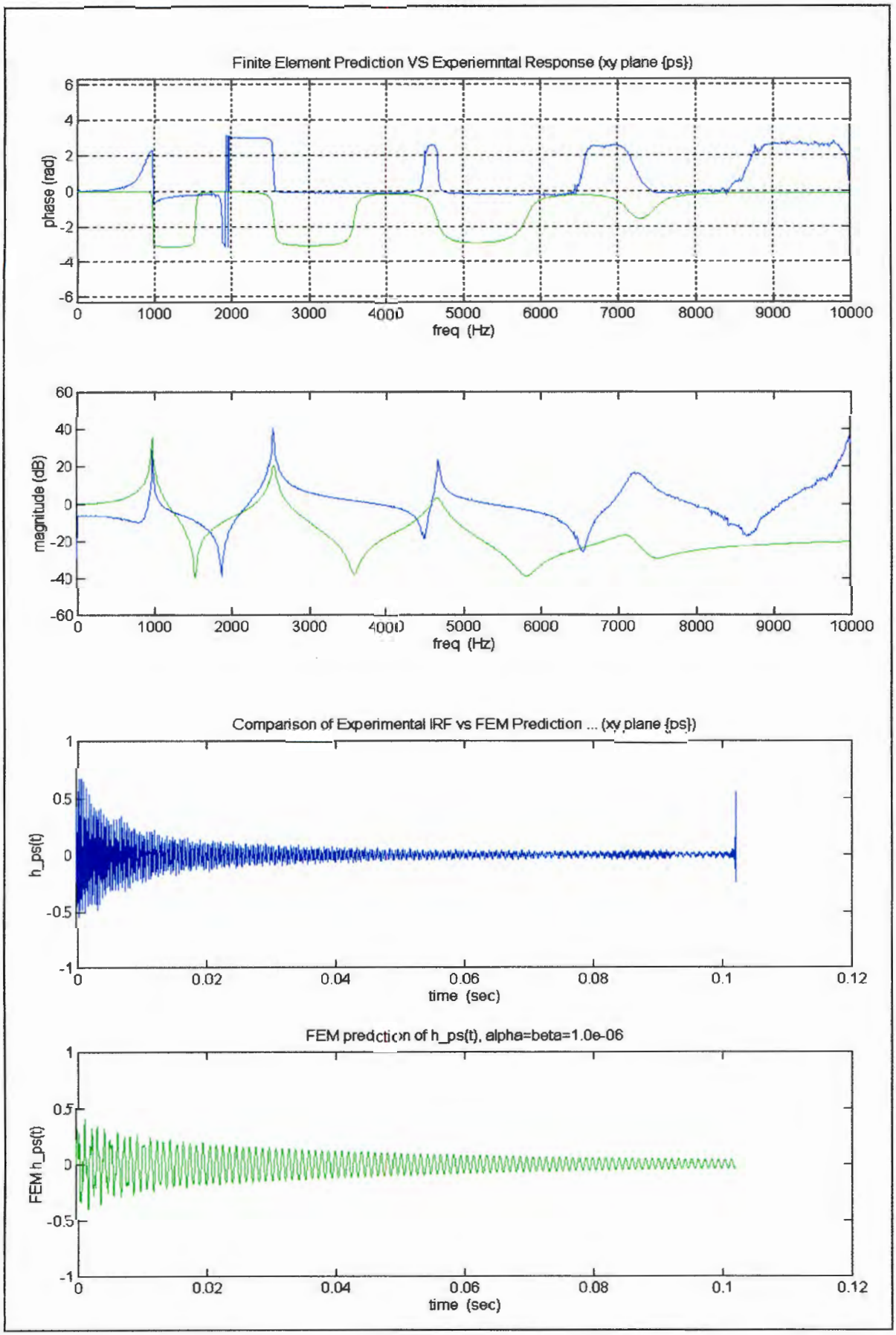

Figure F.16(b) Comparison of the Finite Element prediction (green) and the experimentally measured frequency and impulse response function (blue), at location 'ps'. The finite element analysis was conducted with damping, α=1.0E-06 & β=1.0E-06.

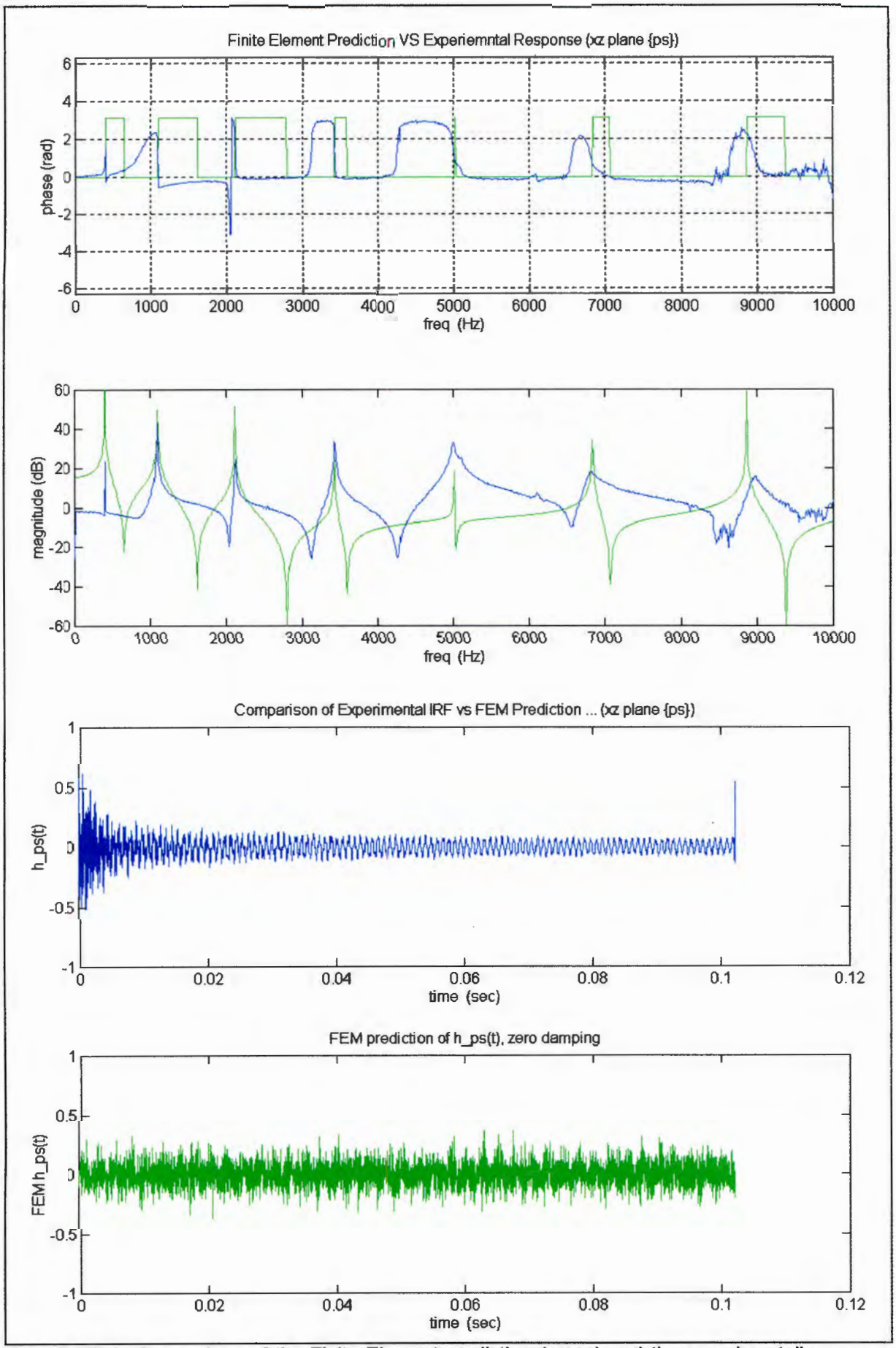

Figure F.17(a) Comparison of the Finite Element prediction (green) and the experimentally measured frequency and impulse response functions (blue), at location 'ps'. The finite element analysis was conducted with zero damping.

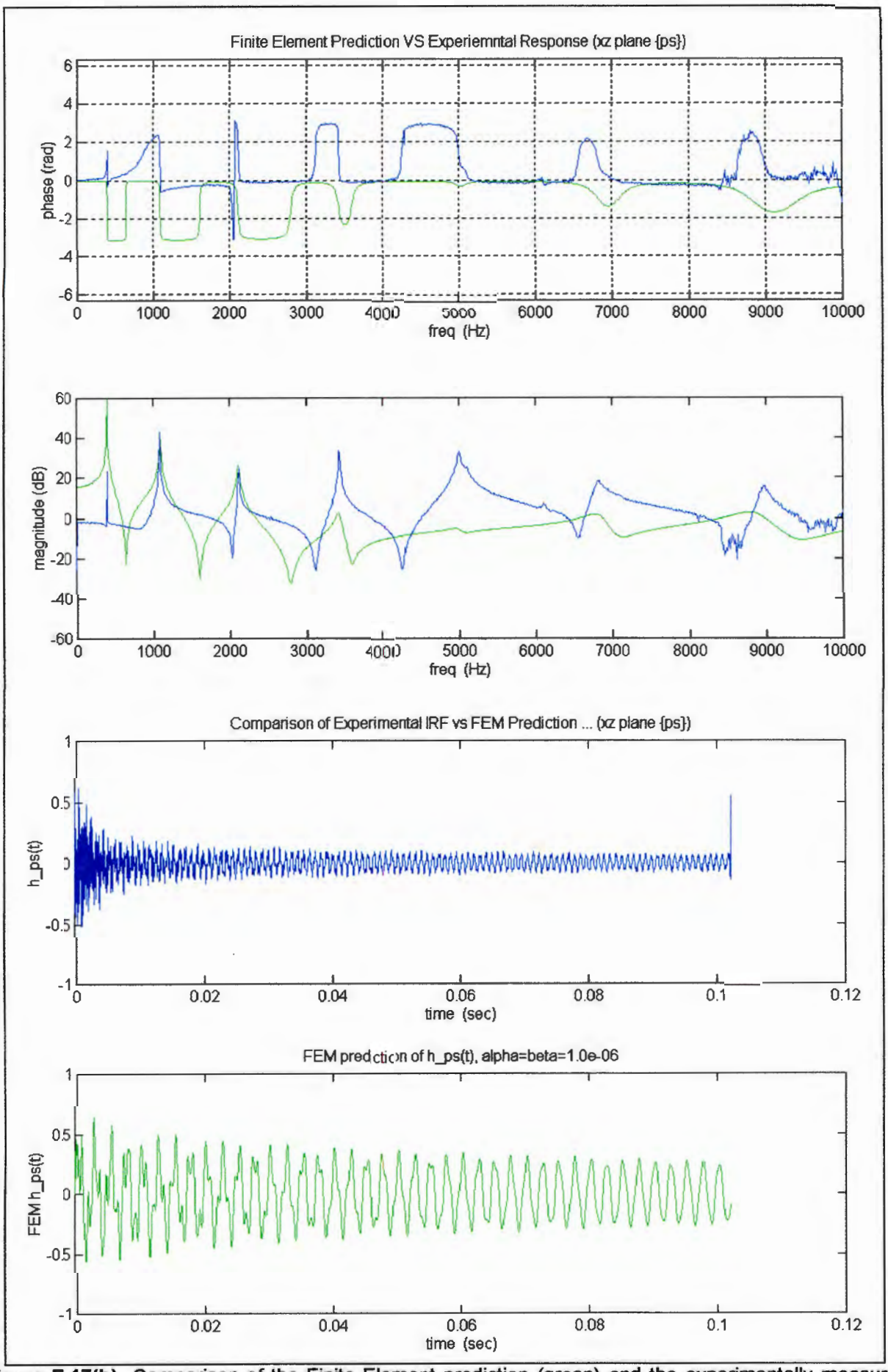

Figure F.17(b) Comparison of the Finite Element prediction (green) and the experimentally measured frequency and impulse response function (blue), at location 'ps'. The finite element analysis was conducted with damping, α=1.0E-06 & β=1.0E-06.

Notice immediately that reasonable correlation is achieved for both the location and magnitude of the resonant peaks for the finite element models. For the frequency response function of the damped models, see figure F.16(b) & F.17(b), the initial resonant peaks are well matched but as the frequency of the resonant modes increase this correlation weakens. It is suggested that the proportional damping strategy which is instituted in the finite element code is inappropriate, as the modal damping in the higher frequency modes is obviously too great.

For both finite element predictions the anti-resonant peaks poorly match the experimental anti-resonant peaks. This trend may be similarly observed from the poor correlation of the phase characteristics. It is apparent that the eigenvectors predicted by the finite element code and the actual mode shapes do not correlate, as this would explain the poor anti-resonant peak correlation.

The finite element predicted impulse response functions do not accurately represent the experimental impulse responses. Due to the obvious deviation of the finite element predicted response functions, no further comparisons are presented.

Chapter G.

Conclusions and Recommendations.

G. Conclusions and Recommendations.

1. From the literature review it may be concluded that osteoporosis could be successfully diagnosed by the non-invasive measurement of the vibration response of the patient's tibia or ulna. The diagnosis is based on the measured values for the resonant frequencies. Prior to the application in patients, additional research is required to overcome the difficulties in reliably measuring the dynamic response of the tibia or ulna.

2. The Timoshenko beam element was shown to accurately predict the measured natural resonant frequencies of the test structure. However, the predictions for the dynamic responses did not correlate well. It appears that the implementation of the viscous damping model in the finite element modal solution was responsible.

   It is recommended that allowance be made in the finite element code for the input of the experimental damping values. It is anticipated that following this modification the finite element model predictions of the dynamic response of the test structure would improve.

3.1 An impact hammer and low-pass filter were successfully constructed. The low-pass filter's response characteristics were successfully measured and calibrated. In an effort to reduce the high frequency content of the captured signals, it is recommended that the attenuation of the low-pass filter be increased. It is hoped that this will reduce the inclusion of all frequency components above the cut-off frequency.

3.2 The choice for the placement of the respective accelerometers and impact location on the test structure, was not successful. Significant high frequency resonant modes, above the cut-off frequency, were excited in many of the responses. This was observed in the xz vibration responses at the ≈9000 Hz and ≈10000 Hz modes and similarly in the xy vibration responses at the ≈10000 Hz mode. The presence of these high frequency modes generally resulted in the poor correlation between the measured and identified impulse response functions. Therefore the re-evaluation of the placement of both the response accelerometers and impact location on the test structure, is recommended.

3.3 In the ensemble averaged frequency response functions, anti-resonant frequency regions were identified where the anti-resonant peak, coherence function and phase characteristics were poorly defined. It was reasoned that these anti-resonant peaks were not consistently defined by successive captured vibration responses.

   An understanding of the causes of the ill-defined anti-resonant peaks is lacking. It is recommended that both the effect of ensemble averaging on the quality of these ill-defined anti-resonant peaks and the influence of the location of the response transducers be investigated.

4.1 The time-domain identification procedure, i.e. the Eigensystem Realization Algorithm, was successful in identifying the resonant modes, damping ratio and mode shapes. Acceptable correlation was demonstrated between the identified and experimental response functions. In regions of ill-defined anti-resonant peaks the identified frequency response functions provided a more realistic representation, although this cannot be substantiated. Where deviations occurred between the identified and experimental impulse response functions, these differences were generally as a result of strongly excited high frequency modes in the experimental responses.

A possible enhancement of the time-domain identification procedure, is to overcome the present limitation of the Hankel matrix dimensions. It is recommended that either additional computer hardware be acquired or that the time-domain identification software be ported to a workstation, where memory constraints will no longer be an obstacle.

4.2 Least order mass, stiffness and damping matrices were successfully calculated for both planes of vibration. However, the physical interpretation of these matrices is less clear, and the vibration response of the resultant second-order differential equation was not pursued. The value of these matrices in comparing the vibration response of different structures, such as the tibia response of two patients, was also not pursued.

Further investigation is required to gain a complete understanding of the least order mass, stiffness and damping matrices. Also, the dynamic response of the resultant second-order differential equation should be compared to the response of the experimental data. Finally, the sensitivity of these least order matrices to subtle changes in the test structure should be investigated.

5. The proposed validation of both the experimental protocol and modal identification procedure by the finite element method, was only partially successful. As the comparative results indicate, the finite element model predictions for the resonant frequencies correlate well with both the experimentally measured and identified resonant frequencies. However, the finite element predictions for the response functions were unrealistic and hence the validation of the response functions was not possible.

Chapter H.

References.

H. References.

H.1 References Cited in Chapter B.

Ashman R.B., Rho J.Y. (1988) **Elastic modulus of Trabecular Bone Material**. Journal of Biomechanics vol. 21(3) pages 177 to 181

Ashman R.B., Rho J.Y. and Turner C.H. (1989) **Anatomical Variation of Orthotropic elastic moduli of the proximal human tibia**. Journal of Biomechanics vol. 22(8,9) pages 895 to 900

Bentzen S.M, Hvid I. and Jorgensen J. (1987) **Mechanical Strength of tibia trabecular bone evaluated by x-ray computed tomography**. Journal of Biomechanics vol 20(8) pages 743-752

Campbell J.N. and Jurist J.M.(1971) **Mechanical impedance of the femur: a preliminary report.** Journal of Biomechanics vol. 4 pages 319 to 322

Carter D.R. and Hayes W.C. (1977) **The compressive behaviour of bone as a two-phase porous structure**. J Bone Jt Surg, vol.59(A), pages 954-962

Chen I.I.H and Saha S. (1987) **Wave propagation characteristics in long bones to diagnose Osteoporosis** Journal of Biomechanics vol. 20(5) pages 523 to 527

Cornelissen P., Cornelissen M., Van der Perre G. et al (1986) **Assessment of tibial stiffness by vibration testing in situ-II. Influence of soft tissues, joints and fibula.** Journal of Biomechanics vol. 19(7) pages 551 to 561

Cunningham J.L, Kenwright J. and Kershaw C.J. (1990) **Biomechanical measurement of fracture healing**, Journal of Medical Engineering & Technology vol14,(3), pages 92 to 101

Currey J.D. (1986) **Power law models for the mechanical properties of cancellous bone**. Engng Med, vol. 15,pages 153-154

Doherty W.P., Bovill E.G. and Wilson E.L. (1974): **Evaluation of the use of resonant frequencies to characterise physical properties of human long bones.** Journal of Biomechanics vol 7, pages 559 to 561

Fah D. and Stussi E. (1988) **Phase velocity measurement of flexural waves in human tibia.** Journal of Biomechanics vol. 21 (11) pages 975 to 983

Galante J., Rostoker W. and Ray R.D. (1970) **Physical properties of trabecular bone**. Calcif. Tissue Res 5, pages 236-246

Hvid I, Bentzen S.M, et al(1989) **X-ray quantitative computed tomography: The relations to physical properties of proximal tibial trabecular bone specimens**. Journal of Biomechanics vol 22(8/9) pages 837-844

Jurist J.M. (1970) ***In vivo*** **determination of the elastic response of bone. II Ulnar resonant frequency in osteoporotic, diabetic and normal subjects**, Physical Medicine and Biology vol. 15, pages 427 to 434

Love A.E.H.(1927) **The Mathematical Theory of Elasticity** 4th edition Cambridge University Press, Cambridge

Marom S.A and Linden M.J. (1990) **Computer aided stress analysis of long bones utilising computer tomography.** Journal of Biomechanics vol 23(5) pages 399-404

Martin R.B. and Atkinson P.J. (1977) **Age and sex-related changes in the structure and strength of the human femoral shaft** Journal of Biomechanics vol. 10 pages 223 to 231

Orne D. (1974) **The *in vivo* driving point impedance of the human ulna, a visco-elastic model.** Journal of Biomechanics vol. 7 pages 249 to 257

Peck W.A. (1987) **Physician's resource manual on Osteoporosis**. National Osteoporosis Foundation

Pelker R.R and Saha S. (1983) **Stress wave propagation in bone.** Journal of Biomechanics vol. 16(7) pages 481 to 489

Rice J.C., Cowin S.C. and Bowman J.A.(1988) **On the dependence of the elasticity and strength of cancellous bone on apparent density**. Journal of Biomechanics vol. 21(3) pages 155 to 168

Richards J. (1987) **Stiffness in healing Structures.** CRC Critical reviews in Biomedical Engineering vol. 15, pages 145 to 185

Saha S. and Lakes R.S. (1977) **The effect of soft tissue on wave propagation and vibration tests for determining the *in-vivo* properties of bone.** Journal of Biomechanics vol. 10 pages 393 to 401

Sonstegard D.A. and Mattews L.S. (1976) **Sonic diagnosis of bone fracture healing: a preliminary report.** Journal of Biomechanics vol. 9 pages 686 to 694

Steele C.R., Zhou L.J., Guido D. et al (1988) **Non-invasive determination of Ulnar stiffness from mechanical - *in vivo* comparison of stiffness and bone mineral content in humans,** Journal of Biomechanical Engineering vol. 110, pages 87 to 96

Stussi E. and Fah D. (1988) **Assessment of bone mineral content by *in vivo* measurement of flexural wave velocities,** Medical and Biological Engineering and Computing vol. 26, pages 349 to 354

Thompson G.A., Orne D. and Young D.R. (1976): ***In vivo*** **determination of the mechanical properties of the human ulna by means of mechanical impedance tests: experimental results and improved mathematical model.** Medical and Biological Engineering, vol 14, pages 253 to 262

Van der Perre G., Van Audekercke R., Martens M. and Mulier J.C. (1983) **Identification of in-vivo vibration modes of human tibiae by modal analysis.** Transactions ASME vol.105(8), pages 244-248

H.2 References Cited in Chapter C.

Bourgery J.M. (1832) **Traite Complet de l'Anatomis de l'Homme.** I. Osteologie, Paris, France

Carnegie W. , Thomas J. and Dokumaci E (1969)**: An improved method of matrix displacement analysis in vibration problems.** The Aeronautical Quarterly vol(20) pages 321-332

Collier R.J, Nadav O, and Thomas T.G (1982) **The Mechanical Resonance of a Human Tibia: Part I- in vivo** Journal of Biomechanics. 15(8), pages 545-553

Cowin S.C., Hart R.T. and Balser J.R. (1985) **Functional adaptation in long bones: establishing in vivo values for surface remodelling rate coefficients.** Journal of Biomechanics vol. 18, pages 665 to 684

Davis R. , Henshell R.D. and Warburton G.B. (1972): **A Timoshenko beam Element.** Journal of Sound and Vibration vol (22) pages 475- 487

Dawe D.J.(1978): **A Finite Element for the Vibration Analysis of Timoshenko Beams.** Journal of Sound and Vibration vol (60-3) pages 11 - 20

Galileo G. (1638) **Discorsi e Dimostrazioni Matematiche,**Intorno a Due Nuove Scienze. Elsevier, Leiden

Hight T.K, Piziali R.L and Nagel D.A (1980) **Natural frequency analysis of a human tibia** Journal of Biomechanics. 13, pages 139-147

Hobatho M.C, Darmana R, Barrau P., et al (1991) **Development of a three-dimensional finite element model of a human tibia using experimental modal analysis** Journal of Biomechanics. 24(6), pages 371-383,

Huiskes R. (1982) **On the modelling of long bones in structural analysis** Journal of Biomechanics vol. 15, pages 65 to 69

Kapur K.K. (1966): **Vibrations of a Timoshenko Beam, using Finite Element Approach.** Journal of the Acoustical Society of America. vol(40) pages 1058-1063

Khalil, T.B, Viano D.C and Taber L.A (1981): **Vibrational Characteristics of the Embalmed Human Femur** Journal of Sound and Vibration. 75(3), pages 417-436,

Koch J.C. (1917) **The laws of bone architecture.** American Journal of Anatomy vol. 21, pages 177-208

Nickell R.E. and Secor G.A (1972)**: Convergence of consistently derived Timoshenko Beam Finite Elements.** International Journal of Numerical Methods in Engineering. vol(5) pages 243 - 253.

Severn R.T. (1970): **Inclusion of Shear Deformation in the Stiffness Matrix for a beam element.** Journal of Strain analysis. vol(5), pages 239-241

Thomas D.L. Wilson J.M. and Wilson R.R. (1973): **Timoshenko Beam Finite Elements.** Journal of Sound and Vibration vol (31-3) pages 315- 330

Thomsen J.J (1990) **Modelling Human Tibia Structural Vibrations** Journal of Biomechanics. 23(3), pages 215-228,

Timoshenko S. **Strength of Materials.** (3rd edn), Parts I & II, Van Nostrand Reinhold, New York, 1955

Viano D, Helfenstein U, Anliker M and Ruegsegger P (1976) **Elastic properties of Cortical Bone in Female Human Femurs** Journal of Biomechanics. 9, pages 703-710,

Watcom FORTRAN, **Graphics Library Reference & Language Reference 4th Edition,** WATCOM International Corporation, Waterloo, Ontario Canada.

Wolff J. (1870) **Über die innere architektur der knochen und ihre bedeutung für die frage vom knochenwachstum.** Virchows Arch. path. Anat. Physiol. vol. 50, pages 389

H.3 References Cited in Chapter D.

Alvin K.F. and Park K.C (1994): **Second Order Structural Identification Procedure via State Space Based System Identification.**, AIAA Journal, vol 32(2), pages 397 -

Alvin K.F., Peterson L.D. and Park K.C. (1995)[1]**:Method for Determining Minimum-Order Mass and Stiffness Matrices from Modal test Data.** AIAA Journal, vol 33(1), pages 128 -

Alvin K.F., Peterson L.D. and Park K.C.(1995)[2]**: Minimum-Order Experimental Component Mode Synthesis: New Results and Challenges,** AIAA Journal, vol 33(8), pages 1477 -

Alvin K.F. **Personal Correspondence.**

Borland™ C++ , Borland International

Chen J.C (1984), **Evaluation of Modal Testing Methods.** AIAA Paper 84-1071 May 1984

Craig R.R. and Bampton M.C.(1968): **Coupling of Substructures for Dynamic Analysis,** AIAA Journal, vol 6(7), pages 1313 to 1319

Ewins D.J. (1984) **Modal Testing: Theory and Practice**, Wiley New York

Franklin G.F. , Powell J.D. and Workman M.L. (1990): **Digital Control of Dynamic Systems.** (2nd Edition) Addison-Wesley Publishing Company

Gilbert E.G. (1963) **Controllability and Observability in Multivariable Control Systems.** SIAM Journal of Control Vol 1(2) pages 128-151

Golub G.H and Reinsch C. (1970): **Singular Value Decomposition and Least Squares Solutions.** Numerical Mathematics, Vol 14, pages 403 to 420

Guyan R.J.(1965): **Reduction of Stiffness and Mass Matrices,** AIAA Journal, vol 3(2), pages 380

Ho B.L. and Kalman R.E. (1965) **Effective Construction of linear State variable Models from Input/Output Data.** Proceedings of the 3rd Annual Allerton Conference on Circuit and System Theory. pages 449 - 459

Ibrahim S.R. and Mikulcik E.C. (1973) **A Time Modal Vibration Test Technique.** Shock and Vibration Bulletin. Bulletin 43, Pt. 4, pages 21 to 37

Juang J.J. (1987) **Mathematical Correlation of Modal Parameters Identification methods via System Realization Theory**, Journal of Modal Analysis Jan 1986, pages 1 to 18

Juang J.J and Pappa R.S (1983), **An Eigensystem Realization Algorithm for Modal Parameter Identification and Model Reduction.** Journal of Guidance, Control, and Dynamics Vol 8(5) pages 620-627

Kalman R.E. (1963) **Mathematical Description of Linear Dynamic Systems.** SIAM Journal of Control Vol 1(2) pages 152-192

Longman R.W. and Juang J.J. (1987): ***A Variance Based Confidence Criterion for ERA Identified Modal Parameters.*** *AAS Paper 87-454, AIAA*

Matlab™ , The MathWorks, Inc

Matcom, is a shareware utility written by Yaron and is available at his internet home-page http://techunix.technion.ac.il/~yak/matcom.html

Pappa R.S and Juang J.J (1988), **Some experiences with the Eigensystem Realization Algorithm.** Sound and Vibration, Jan 1988, pages 30 to 34

Peterson L.D. **Personal Correspondence**

Van Blaricum M.L. and Mittra R. (1978): **Problems and Solutions Associated with Prony's Method for Progressing Transient Data.** IEEE Trans. Antennas Propagat, Vol AP-26(1) Jan 1978, pages 174 to 182

Vold H., Kundrat J., Rocklin G.T., and Russell R.(1982) **A Multi-Input Modal Estimation Algorithm for mini-computers.** Society of Automotive Engineers, Paper 820194, Warrendale, PA, Feb 1982

Vold, H and Russell, R. (1983) **Advanced Analysis Methods Improve Modal Test Results**, Sound and Vibration, March 1983, pages 36 to 40

Wagie D.A. , Skelton R.E. (1986): **A Projection Approach to Covariance equivalent Realizations of Discrete Systems.** IEEE Trans. Automatic Control Vol AC-31(12), pages 1114

Yang C. and Yeh F. (1990): **Identification, Reduction, and Refinement of Modal Parameters by the Eigensystem Realization Algorithm.** Journal of Guidance, Control, and Dynamics Vol 13(6) pages 1051-1055

Zeiger H.P. and McEwen A.J. (1974): **Approximate Linear Realizations of given dimension via Ho's Algorithm.** IEEE Trans. Automatic Control Vol AC-19(2) April 1974, pages 153

H.4 References cited in Chapter E.

Borland™ C++, Borland International

Ewins D.J. (1984) **Modal Testing: Theory and Practise.** Research Studies Press Ltd, London

Halvorsen W.G. and Bendat J.S.(1975): **Noise Source Identification using Coherent output power Spectra.** Sound and Vibration vol. 9 (8) pages 15 to 22.

Halvorsen W.G. and Brown D.L.(1977): **Impulse Technique for Structural Frequency Response Testing.** Sound and Vibration vol. 11 (11) pages 8 to 21.

Matlab , The MathWorks , Inc, USA

Matcom, is a shareware utility written by Yaron and is available at his internet home-page http://techunix.technion.ac.il/~yak/matcom.html

Modal Plus, Structural Dynamics Research Corporation, USA

Ramsey K.A. (1976): **Effective Measurements for Structural Dynamics Testing - Part 2.** Sound and Vibration vol. 10 (4) pages 18 to 31.

Ramsey K.A. (1975): **Effective Measurements for Structural Dynamics Testing - Part 1.** Sound and Vibration vol. 9 (11) pages 24 to 35.

Appendix I

Courses Completed in Partial Fulfilment of the Masters of Science in Engineering.

Appendix I

Courses Completed in Partial Fulfilment of the
Master of Science in Engineering
at the
University of Cape Town.

Course	Description	Date	Credits
	Biomedical Coursework (Department of Biomedical Engineering, UCT)		
ANT 209W	Anatomy	1995	5
PGY 204W	Physiology	1995	5
	Mechanical Engineering Coursework (Department of Mechanical Engineering, UCT)		
AMU 502Z	Finite Element Analysis	1995	3
MEC 505Z	Vehicle Dynamics	1995	3
AMU 550F	Continuum Mechanics I	1995	3
CAM 504Z	Engineering Software Design and Development	1994	3
MEC 500W	Dissertation	1996	20
		Σ	42

Minimum Credit Requirement for the M.Sc (Eng) Degree : 40

Appendix II

Finite Element Modelling.

II-1 STRAIN ENERGY & KINETIC OF A LINEAR ELASTIC SYSTEM.

II-1.1 Strain Energy.

Consider a general linear elastic system secured to fixed supports. Suppose also that it has m degrees of freedom so that is geometrical configuration is completely described by m displacement co-ordinates

$$q_r, \text{ for } r=1 \text{ to } m \tag{II.1}$$

When all of these displacements are zero, the system is assumed to be in a state of stable equilibrium. Now let a set of externally applied generalised forces be slowly applied to the system.

$$(u_f)_r, \text{ for } r=1 \text{ to } m \tag{II.2}$$

Define a [m x m] matrix α, such that

$$q = \alpha\ u_f \tag{II.3}$$

Now suppose that initially, no forces are applied, so that the system is at rest with all the displacements $q_r=0$, *for* $r=1$ *to* m. If a force $(u_f)_1$ is applied slowly the resultant static displacement will be q_r, then the elastic-strain energy stored by the body is

$$U = \tfrac{1}{2}(u_f)_r q_r = \tfrac{1}{2}\alpha_{rr}(u_f)_r^2 \tag{II.4}$$

Similarly, if force $(u_f)_s$ is slowly applied, with $(u_f)_r$ remaining in action, the additional deflection under $(u_f)_r$ is $\alpha_{rs}(u_f)_s$ and the strain energy increase to

$$U = \tfrac{1}{2}\alpha_{rr}(u_f)_r^2 + \alpha_{rs}(u_f)_r(u_f)_s + \tfrac{1}{2}\alpha_{ss}(u_f)_s^2 \tag{II.5}$$

This expression for the strain energy as a result of two generalised forces may be rewritten as

$$U = \tfrac{1}{2}\alpha_{rr}(u_f)_r^2 + \tfrac{1}{2}\alpha_{rs}(u_f)_r(u_f)_s + \tfrac{1}{2}\alpha_{sr}(u_f)_s(u_f)_r + \tfrac{1}{2}\alpha_{ss}(u_f)_s^2 \tag{II.6}$$

due to $\alpha = \alpha^T$ as the linear system is independent of the order in which the loads are applied. Or more generally

$$U = \tfrac{1}{2}(u_f)^T \alpha (u_f) \tag{II.7}$$

Now if we consider the [m x m] stiffness matrix, K, which satisfies the equation $u_f=K\,q$. From the definition of [α], we see that $I=\alpha K$, $I=\alpha^T K^T$ and $I=\alpha K^T$. Finally $K^T = K$.

By substitution an alternative expression for the strain energy can be stated

$$\boxed{U = \tfrac{1}{2} q^T K q} \tag{II.8}$$

The following inferences can be drawn from the last two equations.

- Strain energy is always positive, or in the exceptional case of zero stiffness, it is zero.
- The stiffness matrix is thus ***real, symmetric*** and ***positive semi-definite matrix.***

II-1.2 Formulation of the Kinetic Energy.

Consider the kinetic energy of a system subject to the same conditions as defined in the potential energy formulation. The total kinetic energy is the sum of the kinetic energy of the component parts. If every part is thought to be composed of mass particles, the total kinetic energy T ,is the sum of the kinetic energies of the particles, so that

$$T = \tfrac{1}{2}\sum_{i=1}^{m} m_i \dot{q}_i^2 \tag{II.9}$$

where $\dot{q}_i$ is the absolute velocity of the i^{th} particle of mass $mass_i$. If the position vector r_i, is a function of the generalised co-ordinates, locates $mass_i$ from a fixed origin, then

$$\dot{q}_i = \frac{\mathrm{d}}{\mathrm{d}t} r_i = \sum_{r=1}^{m} \frac{\partial r_i}{\partial q_r} \frac{\mathrm{d}q_r}{\mathrm{d}t} \quad \text{so that} \tag{II.10}$$

$$\dot{q}_i^2 = \sum_{r=1}^{m} \sum_{s=1}^{m} \frac{\partial r_i}{\partial q_s} \frac{\partial r_i}{\partial q_r} \frac{\mathrm{d}q_r}{\mathrm{d}t} \frac{\mathrm{d}q_s}{\mathrm{d}t} \tag{II.11}$$

Now if we consider the [m x m] mass matrix, M. The kinetic energy may be formulated as

$$\boxed{T = \tfrac{1}{2} \dot{q}^T M \dot{q}} \tag{II.12}$$

The mass matrix, M, is a real, symmetric matrix. Also, since kinetic energy cannot be negative, the product $\dot{q}^T M \dot{q}$ can never be negative. Provided that none of the degrees of freedom has zero mass, $\dot{q}^T M \dot{q}$ is never zero unless $\dot{q}$ is a null vector, and so M must be a positive definite matrix.

II-2 TIMOSHENKO BEAM ELEMENT ENERGY FORMULATION.

In deriving the energy functions for a beam element it is assumed that the vibration occurs in one of the principle planes of the beam, namely plane xy and or plane xz. Consider a beam element of constant cross-sectional area , A, and length L as shown in *figure II-1*, subjected to a uniformly distributed load of magnitude p_y per unit length.

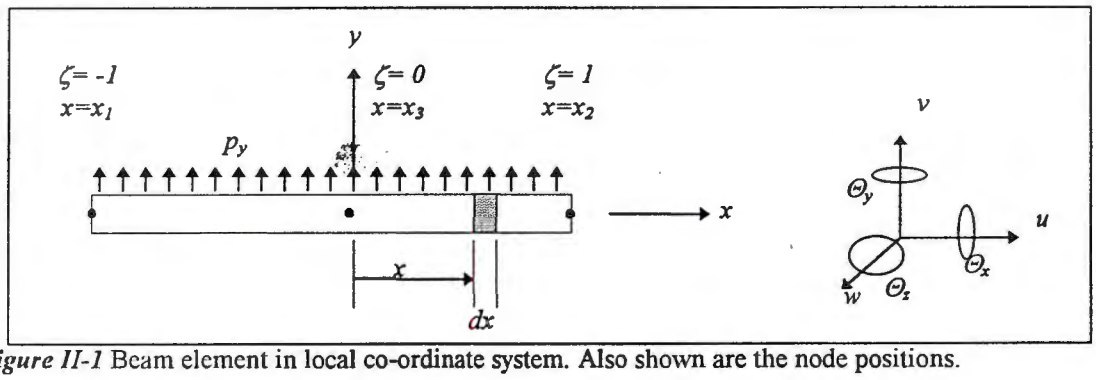

Figure II-1 Beam element in local co-ordinate system. Also shown are the node positions.

The assumption that plane sections which are normal to the un-deformed centroidal axis remain plane after bending is retained. However, it will no longer be assumed that these sections remain normal to the deformed axis. Consequently, the axial displacement, u, at a distance y from the centroidal axis is

$$u(x,y) = -y\theta_z(x) \tag{II-13}$$

The strain components ε_x and γ_{xy} are given by

$$\varepsilon_x = \frac{\partial u}{\partial x} = -y \frac{\partial \theta_z}{\partial x} \tag{II-14}$$

$$\gamma_{xy} = \frac{\partial u}{\partial y} + \frac{\partial v}{\partial x} = -\theta_z \frac{\partial v}{\partial x} \tag{II-15}$$

The strain energy stored in the element is the sum of the energies due to bending and shear deformation, which is given as

$$U = \tfrac{1}{2} \int_V \sigma_x \varepsilon_x dV + \tfrac{1}{2} \int_V \tau_{xy} \gamma_{xy} dV \tag{II-16}$$

The normal stress is related to strain, via $\sigma_x = E\varepsilon_x$. While the a numerical factor is introduced, κ, which depends on the shape of the cross-section, to account for the variation of strain through the cross-section. The shear stress may then be stated as $\tau_{xy} = \kappa G \gamma_{xy}$. Substituting into equation (II-16) and making use of the $dV = dA.dx$

$$U = \tfrac{1}{2}\int_{x_1}^{x_2} EI_z\left(\frac{\partial\theta_z}{\partial x}\right)^2 dx + \tfrac{1}{2}\int_{x_1}^{x_2} \kappa AG\left(\frac{\partial v}{\partial x} - \theta_z\right)^2 dx \qquad \textbf{(II-17)}$$

The kinetic energy of beam consists of the kinetic energy of translation and the kinetic energy of rotation, which may be expressed as

$$T = \tfrac{1}{2}\int_{x_1}^{x_2} \rho\, I_z\left(\dot{\theta}_z\right)^2 dx + \tfrac{1}{2}\int_{x_1}^{x_2} \rho A\dot{v}^2 dx \qquad \textbf{(II-18)}$$

The virtual work of the distributed loading is given by

$$\delta W = \int_{x_1}^{x_2} p_y \delta v\, dx \qquad \textbf{(II-19)}$$

II-3 DERIVATION OF THE TIMOSHENKO SHAPE FUNCTIONS.

The deflection, v, and the beam slope, θ_Z, vary along the length of the beam as stated by the polynomial approximations in equations (C-31) and (C-32). These equations are repeated for clarity

$$v = a_1 + a_2\zeta + a_3\zeta^2 + a_4\zeta^3 + a_5\zeta^4 + a_6\zeta^5 \qquad \textbf{(II-20)}$$

$$\theta_z = b_1 + b_2\zeta + b_3\zeta^2 + b_4\zeta^3 + b_5\zeta^4 \qquad \textbf{(II-21)}$$

As discussed in section C.3.2.2 the polynomial approximations must satisfy the modified dynamic and static equilibrium equations, equation (C-30). This equation is restated for clarity as equation (II-22)

$$EI_z\frac{d^2\theta_z}{dx^2} = \kappa AG\left(\theta_z - \frac{dv}{dx}\right) \qquad \textbf{(II-22)}$$

Equation (II-22) must first be transformed into iso-parametric space via the transform given as equation (C-35). Substituting the polynomial approximations into the transformed equation (II-22), yields

$$\left[\left[\frac{2EI_z b_3}{J^2} + \kappa AG\left(\frac{a_2}{J} - b_1\right)\right] \left[\frac{6EI_z b_4}{J^2} + \kappa AG\left(\frac{2a_3}{J} - b_2\right)\right] \left[\frac{12EI_z b_5}{J^2} + \kappa AG\left(\frac{3a_4}{J} - b_3\right)\right] \kappa AG\left(\frac{4a_5}{J} - b_4\right) \kappa AG\left(\frac{5a_6}{J} - b_5\right)\right] \begin{bmatrix} 1 \\ \zeta \\ \zeta^2 \\ \zeta^3 \\ \zeta^4 \end{bmatrix} = 0$$

(II-23)

Solving for the non-independent variables, ($b_1, b_2, \ldots b_5$).

$$\left\{\begin{array}{lll} \dfrac{5a_6}{J} = b_5\,, & \dfrac{4a_5}{J} = b_4\,, & \left[\dfrac{60EI_z a_6}{J^3} + \kappa AG\left(\dfrac{3a_4}{J}\right)\right] \Big/ [\kappa AG] = b_3 \\ \left[\dfrac{24EI_z a_5}{J^3} + \kappa AG\left(\dfrac{2a_3}{J}\right)\right] \Big/ [\kappa AG] = b_2 \text{ and} & \left[\dfrac{6EI_z a_4}{J^3} + \kappa AG\left(\dfrac{a_2}{J}\right) + \dfrac{120E^2 I_Z^2 a_6}{\kappa AGJ^5}\right] \Big/ [\kappa AG] = b_1 & \end{array}\right\} \qquad \textbf{(II-24)}$$

Hence equation (II-21) may be re-stated in terms of (a_1 , a_2, ... a_6), eliminating the non-independent variables, ($b_1, b_2, \ldots b_5$).

$$\theta_z = \left[0 \quad \frac{1}{J} \quad \frac{2\zeta}{J} \quad \left(\frac{6\varpi}{J^3} + \frac{3\zeta^2}{J}\right) \quad \left(\frac{4\zeta^3}{J} + \frac{24\varpi\zeta}{J^3}\right) \quad \left(\frac{5\zeta^4}{J} + \frac{60\varpi\zeta^2}{J^3} + \frac{120\varpi^2}{J^5}\right)\right] \begin{bmatrix} a_1 \\ a_2 \\ a_3 \\ a_4 \\ a_5 \\ a_6 \end{bmatrix} \qquad \textbf{(II-25)}$$

where $\varpi = \dfrac{EI_Z}{\kappa AG}$

Thus the approximate polynomial functions, equations (II-20) and (II-25), may be evaluated over the element, i.e. at node #1, #2 and node #3. (See figure II-1 for node positions.) These node positions correspond, in iso-parametric space, to ζ= -1, +1, 0. The matrix equation (II-25) results.

$$\begin{bmatrix} v_1 \\ \theta_{z_1} \\ v_2 \\ \theta_{z_2} \\ v_3 \\ \theta_{z_3} \end{bmatrix} = \begin{bmatrix} 1 & -1 & 1 & -1 & 1 & -1 \\ 0 & \left(\frac{1}{J}\right) & \left(\frac{-2}{J}\right) & \left(\frac{6\varpi}{J^3}+\frac{3}{J}\right) & \left(\frac{-4}{J}-\frac{24\varpi}{J^3}\right) & \left(\frac{5}{J}+\frac{60\varpi}{J^3}+\frac{120\varpi^2}{J^5}\right) \\ 1 & 1 & 1 & 1 & 1 & 1 \\ 0 & \left(\frac{1}{J}\right) & \left(\frac{2}{J}\right) & \left(\frac{6\varpi}{J^3}+\frac{3}{J}\right) & \left(\frac{4}{J}+\frac{24\varpi}{J^3}\right) & \left(\frac{5}{J}+\frac{60\varpi}{J^3}+\frac{120\varpi^2}{J^5}\right) \\ 1 & 0 & 0 & 0 & 0 & 0 \\ 0 & \left(\frac{1}{J}\right) & 0 & \left(\frac{6\varpi}{J^3}\right) & 0 & \left(\frac{120\varpi^2}{J^5}\right) \end{bmatrix} \cdot \begin{bmatrix} a_1 \\ a_2 \\ a_3 \\ a_4 \\ a_5 \\ a_6 \end{bmatrix} \quad \textbf{(II-26)}$$

The definition of the shape functions described by equations (C-33) and (C-34), restated for clarity, are required.

$$\theta_z = \begin{bmatrix} \Gamma_1 & \Gamma_2 & \Gamma_3 & \Gamma_4 & \Gamma_5 & \Gamma_6 \end{bmatrix} \begin{bmatrix} v_1 \\ \theta_{z_1} \\ v_2 \\ \theta_{z_2} \\ v_3 \\ \theta_{z_3} \end{bmatrix} \quad \textbf{(II-27)} \qquad v = \begin{bmatrix} \Lambda_1 & \Lambda_2 & \Lambda_3 & \Lambda_4 & \Lambda_5 & \Lambda_6 \end{bmatrix} \begin{bmatrix} v_1 \\ \theta_{z_1} \\ v_2 \\ \theta_{z_2} \\ v_3 \\ \theta_{z_3} \end{bmatrix} \quad \textbf{(II-28)}$$

To achieve this the equations (II-20) and (II-25) are respectively substituted into equations (II-28) and (II-27). Similarly equation (II-26) may be substituted into the resulting equations. The resulting equation is given as equation (II-29), for the shape functions describing the beam deflection.

$$\begin{bmatrix} 1 \\ \zeta \\ \zeta^2 \\ \zeta^3 \\ \zeta^4 \\ \zeta^5 \end{bmatrix}^T = \begin{bmatrix} \Lambda_1 \\ \Lambda_2 \\ \Lambda_3 \\ \Lambda_4 \\ \Lambda_5 \\ \Lambda_6 \end{bmatrix}^T \begin{bmatrix} 1 & -1 & 1 & -1 & 1 & -1 \\ 0 & \left(\frac{1}{J}\right) & \left(\frac{-2}{J}\right) & \left(\frac{6\varpi}{J^3}+\frac{3}{J}\right) & \left(\frac{-4}{J}-\frac{24\varpi}{J^3}\right) & \left(\frac{5}{J}+\frac{60\varpi}{J^3}+\frac{120\varpi^2}{J^5}\right) \\ 1 & 1 & 1 & 1 & 1 & 1 \\ 0 & \left(\frac{1}{J}\right) & \left(\frac{2}{J}\right) & \left(\frac{6\varpi}{J^3}+\frac{3}{J}\right) & \left(\frac{4}{J}+\frac{24\varpi}{J^3}\right) & \left(\frac{5}{J}+\frac{60\varpi}{J^3}+\frac{120\varpi^2}{J^5}\right) \\ 1 & 0 & 0 & 0 & 0 & 0 \\ 0 & \left(\frac{1}{J}\right) & 0 & \left(\frac{6\varpi}{J^3}\right) & 0 & \left(\frac{120\varpi^2}{J^5}\right) \end{bmatrix} \quad \textbf{(II-29)}$$

Equation (II-29) and the similar equation describing the shape functions for the beam slope, may be solved algebraically and hence the shape functions, Γ and Λ, may be directly stated as

$$\begin{cases} \Lambda_1 = \dfrac{\zeta(\zeta-1)}{4}\left(\dfrac{\left(3J^4+36J^2\varpi\right)\zeta^3+\left(J^4+6J^2\varpi\right)\zeta^2-\left(4J^4+114J^2\varpi+720J^2\right)\zeta-30J^2-360\varpi^2}{\left(J^2+12\varpi\right)\left(J^2+15\varpi\right)}\right) \\ \Lambda_2 = \dfrac{\zeta(\zeta+1)(\zeta-1)}{4J}\left(\dfrac{\left(J^6+6J^4\varpi-72J^2\varpi^2\right)\zeta^2-\left(J^6+15J^4\varpi\right)\zeta+\left(-6J^4\varpi+48J^2\varpi^2+1440\varpi^3\right)}{\left(J^2+12\varpi\right)\left(J^2+15\varpi\right)}\right) \\ \Lambda_3 = \dfrac{-\zeta(\zeta+1)}{4}\left(\dfrac{\left(3J^4+36J^2\varpi\right)\zeta^3-\left(J^4+6J^2\varpi\right)\zeta^2-\left(4J^4+114J^2\varpi+720J^2\right)\zeta+30J^2+360\varpi^2}{\left(J^2+12\varpi\right)\left(J^2+15\varpi\right)}\right) \\ \Lambda_4 = \dfrac{\zeta(\zeta+1)(\zeta-1)}{4J}\left(\dfrac{\left(J^6+6J^4\varpi-72J^2\varpi^2\right)\zeta^2+\left(J^6+15J^4\varpi\right)\zeta+\left(-6J^4\varpi+48J^2\varpi^2+1440\varpi^3\right)}{\left(J^2+12\varpi\right)\left(J^2+15\varpi\right)}\right) \\ \Lambda_5 = (\zeta+1)(\zeta-1)\left(\dfrac{\varpi^2\zeta^2-J^2-12\varpi}{\left(J^2+12\varpi\right)}\right) \\ \Lambda_6 = \dfrac{\zeta(\zeta+1)(\zeta-1)}{J}\left(\dfrac{\left(J^4+3J^2\varpi\right)\zeta^2-J^4-27J^2\varpi-60\varpi^2}{\left(J^2+15\varpi\right)}\right) \end{cases} \quad \textbf{(II-30)}$$

and

$$\begin{cases}
\Gamma_1 = \zeta(\zeta+1)(\zeta-1)\dfrac{J}{4}\left(\dfrac{\left(15J^2+180\varpi\right)\zeta-8J^2-120\varpi}{\left(J^2+12\varpi\right)\left(J^2+15\varpi\right)}\right) \\
\Gamma_2 = \dfrac{\zeta(\zeta-1)}{4}\left(\dfrac{\left(5J^4+30J^2\varpi-360\varpi^2\right)\zeta^2+\left(J^4-30J^2\varpi-360\varpi^2\right)\zeta+\left(-2J^4-6J^2\varpi+360\varpi^2\right)}{\left(J^2+12\varpi\right)\left(J^2+15\varpi\right)}\right) \\
\Gamma_3 = -\zeta(\zeta+1)(\zeta-1)\dfrac{J}{4}\left(\dfrac{\left(15J^2+180\varpi\right)\zeta+8J^2+120\varpi}{\left(J^2+12\varpi\right)\left(J^2+15\varpi\right)}\right) \\
\Gamma_4 = \dfrac{\zeta(\zeta+1)}{4}\left(\dfrac{\left(5J^4+30J^2\varpi-360\varpi^2\right)\zeta^2-\left(J^4-30J^2\varpi-360\varpi^2\right)\zeta+\left(-2J^4-6J^2\varpi+360\varpi^2\right)}{\left(J^2+12\varpi\right)\left(J^2+15\varpi\right)}\right) \\
\Gamma_5 = 4J(\zeta+1)(\zeta-1)\left(\dfrac{\zeta}{\left(J^2+12\varpi\right)}\right) \\
\Gamma_6 = (\zeta+1)(\zeta-1)\left(\dfrac{\left(5J^2+15\varpi\right)\zeta^2-J^2-15\varpi}{\left(J^2+15\varpi\right)}\right)
\end{cases} \tag{II-31}$$

This concludes the formulation of the shape functions. The reader is referred to figures C-4a and figure C-4b where the shape functions are plotted as a function of an element length. The shape functions are coded in subroutine SHAPEF5.FOR, which is listed in Appendix II-7.

II-4 INTEGRATION OF THE LOCAL MASS AND STIFFNESS MATRICES.

The integral equations describing the local mass and stiffness matrices of the Timoshenko beam element were derived in section C.3.2.3. The shape functions for the Timoshenko beam element may be theoretically solved, however a numerical integration procedure was instituted. In particular the Gauss-Legendre numerical integration scheme.

Consider an integral of a function $g(\zeta)$, then according to the Gauss-Legendre integration scheme the integral may be evaluated using the formula

$$\int_{-1}^{+1} g(\zeta)d\zeta = \sum_{i=1}^{n} W_i g(\zeta_i) \tag{II-32}$$

where

W_i are the weighting coefficients,
ζ_i are the sampling points, and
n is the number of summations.

The order of the summation, n, must be suitably chosen. If $g(\zeta)$ is a polynomial of degree $(2n\text{-}1)$, then it will be exactly integrated by a suitable choice of n sampling points and n weighting coefficients. The shape functions are polynomial functions and hence the order of the summation can be calculated by inspection of the respective mass and stiffness integral equations. Tabulated in **Table II-1** are the respective sampling points and weighting coefficients for varying degrees of polynomials

Table II-1 Sampling points and weight coefficients for the Gauss-Legendre integration scheme.

n	ζ_i	W_i
1	0	2
2	$-\sqrt{1/3}\ ,\ \sqrt{1/3}$	1, 1
3	$-\sqrt{3/5}\ ,\ 0\ ,\ \sqrt{3/5}$	$5/9\ ,\ 8/9\ ,\ 5/9$
4	$-\sqrt{\dfrac{15+2\sqrt{30}}{35}}\ ,\ \sqrt{\dfrac{15-2\sqrt{30}}{35}}\ ,\ -\sqrt{\dfrac{15-2\sqrt{30}}{35}}\ ,\ -\sqrt{\dfrac{15+2\sqrt{30}}{35}}$	$\dfrac{49}{6\left(18+\sqrt{30}\right)}\ ,\ \dfrac{49}{6\left(18-\sqrt{30}\right)}\ ,\ \dfrac{49}{6\left(18-\sqrt{30}\right)}\ ,\ \dfrac{49}{6\left(18+\sqrt{30}\right)}$

The software implementation of the Gauss-Legendre integration scheme may be easily described by inspection of Figure II-2.

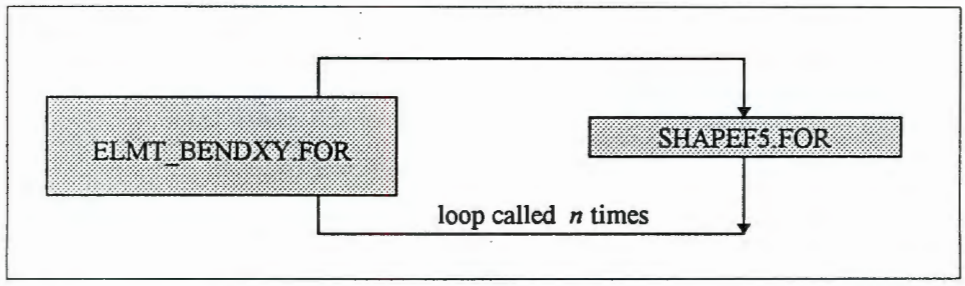

Figure II-2 Flow-diagram of the software implementation of the Gauss-Legendre integration scheme.

The routine ELMT_BENDXY.FOR calculates and assembles both the local mass and stiffness matrices. Thus coded in the routine are equations C-43 and C-40 respectively. The subroutine SHAPEF5.FOR is called *n* times from the ELMT_BENDXY.FOR routine. The subroutine evaluates the appropriate shape function at the passed value ζ_i

It should be appreciated that the identical procedure is followed for analysis in the *xz* plane. The software FORTRAN listing for both routines is given in Appendix II-7.

II-5 Assembly of the Global Mass and Stiffness Matrices.

The easiest way to describe the assembly process is by way of an example. Consider the assembly of the global matrices of a beam, composed of four three node elements. The nodes and elements of the structure are numbered as shown in Figure II-3.

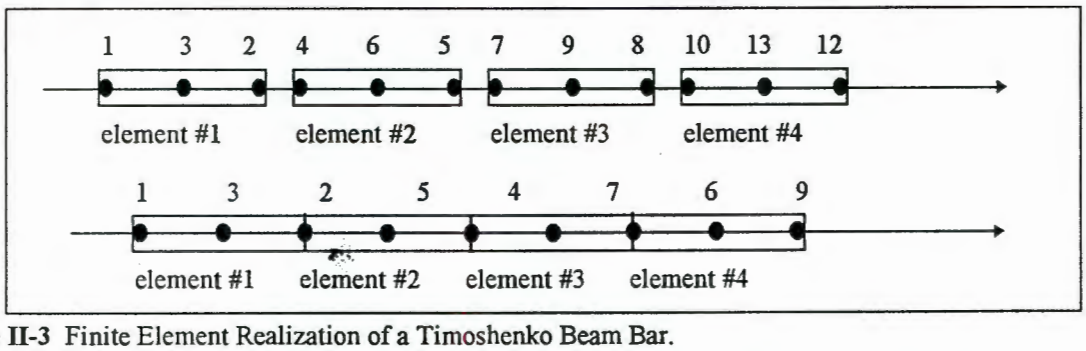

Figure II-3 Finite Element Realization of a Timoshenko Beam Bar.

It should be apparent from the upper diagram of figure II-3, that node 2 & 4, 5 & 7 and 8 & 10 are equivalent. Thus the node numbering of the upper figure may be revised as shown in the lower figure. The global mass and stiffness matrices describe the entire structure, as opposed to the local element mass and stiffness matrices, which merely describe the mass and stiffness of a single element within the structure. The resultant global mass and stiffness matrices form banded tridiagonal respective matrices.

The assembly of the global stiffness and mass matrices is accomplished in the main FORTRAN program, BENDXY.FOR. This program is listed in Appendix II-7.

II-6 The Eigen-Decomposition of $M^{-1} K$

In order to evaluate the natural undamped frequencies and mode shapes of the finite element model, it is necessary to solve the eigen-problem. The eigen-problem was derived in section C.4.1 as equation (C-49). The matrix product of $M^{-1} K$ is thus required, before the eigen-decomposition may proceed. Therefore this matrix product is initially discussed, before continuing the discussion.

II-6.1 Determination of the Matrix Product $M^{-1} K$.

Rather than performing the obvious operations of initially forming the inverse of M, followed by the matrix product, $M^{-1} K$, a more elegant approach was sought. The approach described does not solve for the mass inverse, but rather solves the invariant equation. The derivation follows.

Let $$M^{-1} K = \varpi \tag{II-33}$$

where M and K are square matrices of size [n x n]. Then by pre-multiplying by M, this equation can be re-written as

$$M\varpi = K \tag{II-34}$$

this is the identical form of the classical linear algebraic equation $Ax=B$. There exist a number of techniques to solve the matrix x or in this case ϖ . There is the Gauss-Jordan, LU decomposition, singular value decomposition or QR decomposition methods.

- The Gauss-Jordan elimination produces both the solution of the equations, ϖ, and the inverse of the mass matrix M. The Gauss-Jordan requires that the entire matrix K be stored and manipulated at the same time, and when the mass inverse is not desired, as is the case here, it is significantly slower than other methods. Thus the Gauss-Jordan elimination technique was not considered.
- The QR decomposition method involves about twice as many operations as LU decomposition, so was immediately discarded.
- The singular value decomposition technique is more suited to equations involving matrices which are singular or numerically close to singular. Thus this technique was also not implemented.

The LU decomposition was utilised to solve equation (II-34). The LU decomposition technique first decomposes the mass matrix M, as a product of two matrices,

$$M=L\,U \tag{II-35}$$

where L is the lower triangular and U is the upper triangular matrix.
Substitution equation (II-35) into (II-34)

$$(L\,U)\,\varpi = K \Leftrightarrow L\,(U\varpi) = K \tag{II-36}$$

by first solving for the vector y

$$L\,y = K' \tag{II-37}$$

$$U\varpi = y \tag{II-38}$$

Then equation (II-37) can be solved by forward substitution as given by equation (II-39),

$$y_1 = \frac{K_1'}{L_{11}}$$

$$y_i = \frac{K_i' - \sum_{j=1}^{i-1} L_{ij} y_j}{L_{ii}} \quad i = 2,3,\ldots\ldots n \tag{II-39}$$

$$\varpi_n = \frac{y_n}{U_{nn}}$$

$$\varpi_i = \frac{y_i - \sum_{j=i+1}^{n} U_{ij} \varpi_j}{U_{ii}} \quad i = (n-1),(n-2),\ldots\ldots 1 \tag{II-40}$$

where
K' refers to the stiffness matrix considered in column form.

while (II-38) can be solved by back-substitution as stated in (II-40). Thus equations (II-39) and (II-40) are repeated n times, for each of the respective columns.

This algorithm is implemented in subroutine INV_A_PRODUCT_B.FOR. The FORTRAN source listing is presented later in Appendix II-7. The subroutine INV_A_PRODUCT_B.FOR calls two other subroutines, LUDCMP.FOR .for which performs the LU decomposition of the mass matrix and LUBKSB.FOR which is called n times and performs the forward and back substitution described by equations (II-39) and (II-40). Both the LUDCMP.FOR and LUBKSB.FOR subroutines are customised versions of the code given by *Press et al. (1986).*

II-6.2 Eigen-Decomposition of the Matrix Product $M^{-1} K$

The eigen-decomposition is now considered. The form of the matrix product must be considered in the choice of an eigensolver. In general both the mass and stiffness matrices will be banded tridiagonal and real symmetric matrices. However, this in no way infers that the matrix product $M^{-1} K$ would have a similar form. In fact, ignoring special cases, the matrix $M^{-1} K$ is generally neither banded tridiagonal or symmetric.

The strategy of most modern eigensystem routines is to perform a sequence of similarity transformations on the matrix in order to diagonalise the matrix. The eigenvalues are then the diagonal terms and the columns are the eigenvectors. In this case only the eigenvalues are solved for in this manner, and hence it is sufficient to transform the matrix to a triangular form, with all elements below (or above) the diagonal zero. The eigenvalues are then given by the diagonal terms.

Computationally, it is more efficient to initially reduce the matrix to a tridiagonal form using a finite number of similarity transformations and then follow this with a factorisation method. In this dissertation the reduction to a upper Hessenberg matrix is performed followed by the implementation of the QR factorisation method. The QR algorithm iterates until the deviation of the matrix from the diagonal is negligibly small. The eigenvalues can then be extracted, being the diagonal terms.

II-6.2.1 The Reduction to upper Hessenberg form.

An upper Hessenberg form matrix has zeros everywhere below the diagonal except for the first subdiagonal row. This structure can be achieved by a sequence of orthogonal transformations, the Householders method. Each orthogonal transforms results in a complete row and column of zeros apart from the elements within the tridiagonal form. This is achieved without affecting the previous rows and columns and so only (n-2) transformations are required for a matrix of size (n x n).

An alternative procedure described by *Press et al (1986)* is however used, as the procedure is more efficient than the Householders method by a factor of two. The procedure described by *Press et al.* is analogous to Gaussian elimination with pivoting. This procedure is implemented as subroutine ELMHES.FOR, which is a modified version of the form given by *Press et al (1986)*

II-6.2.2 The QR Method.

Using the same notation of the preceding section, i.e. $M^{-1} K = \varpi$ .Then matrix ϖ can be expressed in the form

$$\varpi = Q R \qquad \text{(II-41)}$$

where
Q is an orthogonal matrix and R an upper tridiagonal matrix. If Q is used to apply an orthogonal similarity transformation then

$$Q^{T} \varpi Q = Q^{T} (Q R) Q = R Q \qquad \text{(II-42)}$$

since $Q^{T} Q = I$, form the orthogonal property.
The QR method, therefore, consists of carrying out the following sequence of operations

$$\varpi_r = Q_r R_r \qquad \text{and} \qquad R_r Q_r = \varpi_{r+1} \qquad \text{for} \qquad r=1,2,3.....n \qquad \text{(II-43)}$$

it can be shown that as $r \rightarrow \infty$, ϖ_{r+1} converges to a diagonal matrix.
The rate of convergence can be increased by using the method of shifting, as discussed by *Press et al (1986)*. The QR algorithm with shifting is implemented as subroutine HQR.FOR and once again is a slightly modified version of that given by *Press et al. (1986)*

II-6.2.3 Calculation of the Eigenvectors.

Generally the inverse iteration method is used to solve for the eigenvectors once the eigenvalues are defined, but as the eigenvectors will be real, a simpler strategy is employed.

$$\varpi U = \lambda U \tag{II-44}$$

The column eigenvector, U, corresponding to the eigenvalue, may be calculated directly from the solution of the eigenproblem. If the column eigenvector is considered as,

$$U = x + jy \tag{II-45}$$

corresponding to the eigenvalue

$$\lambda = \alpha + j\omega \tag{II-46}$$

where x, y, α and ω are all real. Then equation (II-44) may be rewritten as

$$\varpi(x + jy) = (\alpha + j\omega)(x + jy) \tag{II-47}$$

which may be separated into two equations, real and imaginary

$$\varpi x - \alpha x + \omega y = 0 \tag{II-48}$$

$$\varpi y - \alpha y - \omega x = 0 \tag{II-49}$$

However as the eigenvalues are only real valued, this implies that $\omega = 0$. As the eigenvalues are only real valued this implies that the eigenvectors are also only real valued, thus $y = 0$. Both equations (II-48) and (II-49) can be re-formulated as a single equation,

$$\varpi x - \alpha x = 0 \quad or \quad (\varpi - \alpha I)x = 0 \tag{II-50}$$

The form of equation (II-50) can not be solved directly, other than the trivial solution $x=0$. As the scaling of the eigenvectors are arbitrary, it is allowable to impose a constraint on a single element, of each eigenvector. Suppose that the real eigenvectors are scaled such that the first element, of x, is real and of magnitude unity, then the vector x may be partitioned into

$$x = \begin{bmatrix} 1 \\ x^* \end{bmatrix} \tag{II-51}$$

then equation (II-50) may be restated as

$$(\varpi_{k,k} - \alpha I)x^* = -\varpi_{k,1} \qquad for \quad k=2,3,....n \tag{II-52}$$

This equation is solved in the conventional fashion using the LU decomposition technique, for each of the n real eigenvalues. The computer implementation is in subroutine EIGENSandSCALE.FOR. The subroutine EIGENSandSCALE.FOR calls two other subroutines, LUDCMP.FOR and LUBKSB.FOR which performs the LU decomposition of equation (II-52). Both the LUDCMP.FOR and LUBKSB.FOR subroutines are customised versions of the code given by *Press et al. (1986).*

II-6.2.4 Scaling of Mode Shapes.

When general purpose eigenvalue and eigenvector routines are used, the eigenvectors may be normalised in a number of different ways. However, in order to satisfy $U^T MU=I$ so that the general response equations given as (II.3.1) apply, each eigenvector must be scaled appropriately. If U_{ri}, $r=1$ *to* n, are the elements of the j^{th} eigenvector as calculated by the eigen decomposition program, then the elements must be scaled by λ_j, such that

$$\lambda_i^2 \sum_{r=1}^{n}\sum_{s=1}^{n} M_{rs}U_{ri}U_{si} = 1, \qquad i = 1 \; to \; n \tag{II-53}$$

Hence the scaling factors are given by

$$\lambda_i = \frac{1}{\sqrt{\sum_{r=1}^{n}\sum_{s=1}^{n} M_{rs}U_{ri}U_{si}}}, \quad i = 1 \; to \; n \tag{II-54}$$

The computer implementation is in subroutine EIGENSandSCALE.FOR. The FORTRAN source listing of this routine is given in Appendix II-7.

II-7 FORTRAN SOURCE LISTINGS.

Figure II-4 shows a schematic representation of the finite element software algorithm. For analysis in the *xy* plane the main program is BENDXY.FOR and the local mass and stiffness matrices are evaluated by a routine ELMT_BENDXY.FOR. For analysis in the *xz* plane the main program is BENDXZ.FOR and the local mass and stiffness matrices are evaluated by the routine ELMT_BENDXZ.FOR. All other routines remain unchanged.

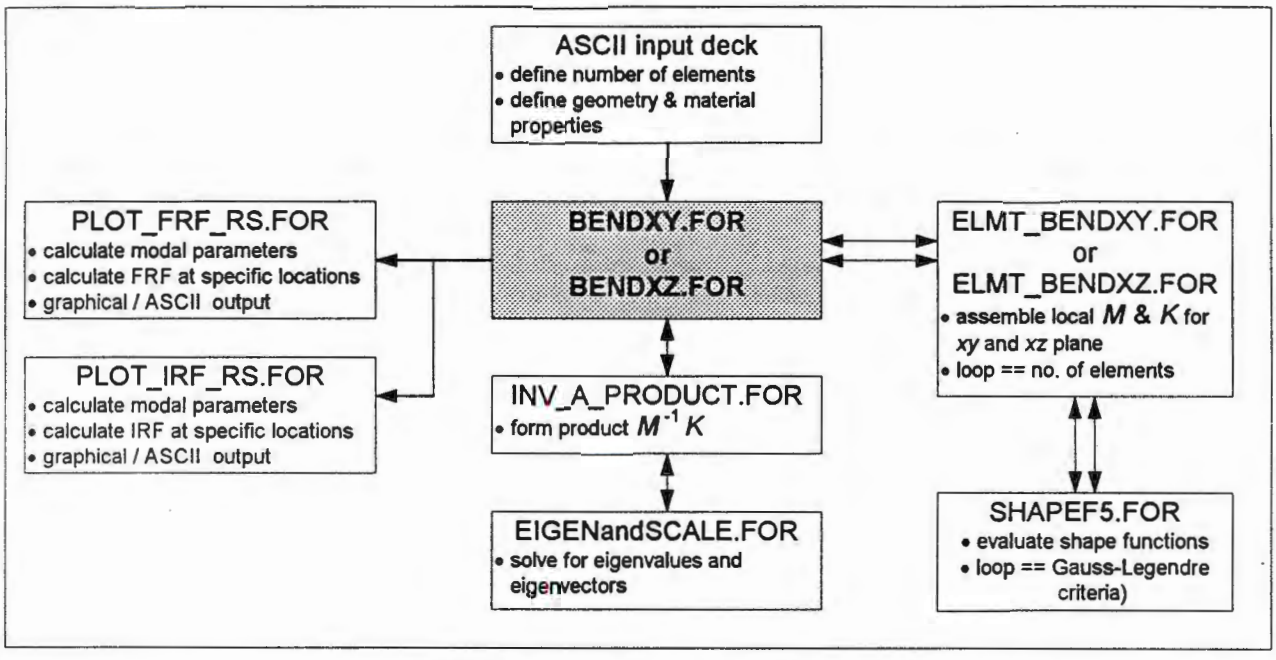

Figure II-4. Schematic algorithm of the Finite Element Software code, for analysis in the *xy* plane only. For analysis in the *xz* plane the local mass and stiffness matrices are evaluated by a routine ELMT_BENDXZ.FOR, all routines remain unchanged. The sequence follows a clockwise rotation.

Only those routines shown in Figure II-4 are listed, with the exception of PLOT_IRF_RS.FOR. Other routines such as LUDCMP.FOR, LUBKSB.FOR, ELMHES.FOR and HQR.FOR are not included as they are essentially customised versions of the code published by *Press et al. (1986).*

Appendix II -7

```
*MAIN PROGRAM - BENDXY.FOR
*-------------------------------------------------------------*
      double precision mass(:,:), stiff(:,:), A(:,:), U(:,:),wr(:),
     + MASS_xy(6,6), STIFF_xy(6,6), data(500)
      integer i, j, k,
     + bc_type, num_element, size,
     + ifree, ialloc,
     + choice, idummy, idummy_1
      integer vector(6)
     + /-11, -10, -7, -6, -5, -4/
      character*12 filein
      common/block_1/data
c.----------* read file, containing data, into common block *------
      open(unit=5, file='con')
      write(5,*) 'enter datafile name: '
      read(5,fmt=1000) filein
      open(unit=12, file=filein, status='old')
      read(unit=12, fmt=1010) bc_type              !1,2 or 3
      read(unit=12, fmt=1010) num_element
      do i=1, num_element
      read(12,*)
           do j=1, 2
            read(12,fmt=1030) (data(k+10*(i-1)), k=5*j-4,5*j)
           end do
      end do
      close(unit=12)
c.--------------* boundary condition *--------------------------
      if (bc_type.eq.1) then
           size=4*num_element+2  !dim[MASS,STIFF], free-free
           idummy=6
           idummy_1=0
      else if (bc_type.eq.2) then
           size=4*num_element+1  !dim[MASS,STIFF], fixed-free
           idummy=5
           idummy_1=1
      else
           size=4*num_element !dim[MASS,STIFF],clamp-free
           idummy=4
           idummy_1=2
      end if
c.dynamic allocate & initialise
      allocate(mass(size,size), stiff(size,size), A(size,size),
     +          stat=ialloc)
      if(ialloc.ne.0) print *, 'allocfail - mass,stiff,A'
      do i=1, size
      do j=1, size
            mass(i,j)=0.0
            stiff(i,j)=0.0
           end do
      end do
c.---------* form local element STIFF & MASS matrices *--------
      call elmt_bendxy(1, MASS_xy, STIFF_xy)      ! i=1
      do j=1, idummy
           do k=1, idummy
            mass(j,k)=MASS_xy(j+idummy_1,k+idummy_1)
            stiff(j,k)=STIFF_xy(j+idummy_1,k+idummy_1)
           end do
      end do
! idummy=6 free-free !idummy=5,fixed-free !idummy=4, clamped-
free
      do i=2,num_element
          call elmt_bendxy(i, MASS_xy, STIFF_xy)
          do j=1,6                          !row counter
               do k=1,6                     !col. counter
         mass(4*i+vector(j)+idummy,4*i+vector(k)+idummy)=
     +        mass(4*i+vector(j)+idummy,4*i+vector(k)+idummy)+
     +         MASS_xy(j,k)
               stiff(4*i+vector(j)+idummy,4*i+vector(k)+idummy)=
     +         stiff(4*i+vector(j)+idummy,4*i+vector(k)+idummy)+
     +         STIFF_xy(j,k)
               end do
      end do
      end do
 print *,'completed assembly, boundary conditions'
c.-------------------* eigensolver *-------------------------
      call inv_A_product_B(mass,stiff,A,size)
      deallocate(stiff,stat=ifree)
      if(ifree.ne.0) print *, 'deallocfail - stiff'
      allocate(U(size,size),wr(size), stat=ialloc)
      if(ialloc.ne.0) print *, 'allocfail - U, wr'
      call eigensANDscale(mass,A,size,wr,U)
      deallocate(mass,A,stat=ifree)
      if(ifree.ne.0) print *, 'deallocfail - mass,A'
     print *,'completed eigen-solution'
c.-----------------* rigid body motion removal *----------------
      if (bc_type.eq.1) then          !bendxy / bendzx fe model
           wr(1)=0.0
           wr(2)=0.0
      else if (bc_type.eq.2) then
           wr(1)=0.0
      end if
c.--------------------* plotting routines *-------------------
      choice=1
      do while (choice.ne.0)
           loop
                print *, '** BENDING XY-VIBRATION ANALYSIS **'
                print *, 'Enter choice'
                print *, '(0)   duck,'
                print *, '(1)   Impulse Response IRF_rs(t),'
                print *, '(2)   Freq Response    FRF_rs(w)'
                read(unit=5, fmt=1010) choice
                if (choice.gt.2) then
                     cycle
                else
                     exit
                end if
           end loop
           if (choice.eq.1) then
                call plot_IRF_rs(2, bc_type, U, wr, size)
           else if (choice.eq.2) then
                call plot_FRF_rs(2, bc_type, U, wr, size)
           end if
      end do
 1000 format(a12)
 1010 format(i5)
 1020 format(6f12.6)
 1030 format(5f12.6)
 1040 format(e10.6e2)
 1050 format(f12.6,4X,f12.6,4X,f12.6,4X,f12.6)
 1060
format(e12.6,1X,e12.6,1X,e12.6,1X,e12.6,1x,e12.6,1x,e12.6)
c.-----------------* closing deallocation *-------------------
      deallocate(U,wr,stat=ifree)
      if(ifree.ne.0) print *, 'deallocfail - U,wr'
      end

SUBROUTINE elmt_bendxy(elnum, MASS_xy, STIFF_xy)
     integer elnum,              !number of element
     & i,j,k,                    !do/enddo variables
     & q                         !dummy, vector_pointer
      real*8 p,                  !intemediate varaible
     & data(500),                !define common block
     & MASS_xy(6,6), STIFF_xy(6,6), !local mass & stiffness
     & vec(8)                    !
real*8 eta_s(6)
                &/-0.932469514203152,   -0.661209386466265,   -
0.238619186083197,
               &      0.238619186083197,      0.661209386466265,
0.932469514203152/
     real*8 weight(6)
                     &/0.171324492379179,     0.360761573048139,
0.467913934572691,
                    &     0.467913934572691,     0.360761573048139,
0.171324492379179/
     common/block_1/data
     q=10*(elnum-1)       !CHANGED!!!!!!!!!!!!!!!!!!!!!!!!!!!!!!!!
c.--------* initialise local mass & stiffness matrices *----------
     do i=1, 6
          do j=1, 6
               MASS_xy(i,j)=0.0
               STIFF_xy(i,j)=0.0
          end do
     end do
c.-----------------* perform integration, *--------------------
     do i=1, 6
     do j=i, 6
```

```
            do k=1, 6
            call shapef5(i,j,eta_s(k),data(1+q)/2.0,p,vec)
c.      MASS ELEMENT
     MASS_xy(i,j)=MASS_xy(i,j)+
    & (data(2+q)*data(5+q)*vec(1)*vec(2)*data(1+q)/2.0*
    & weight(k)) +
    & (data(2+q)*data(8+q)*vec(5)*vec(6)*data(1+q)/2.0*
    & weight(k))
c.      STIFFNESS MATRIX
     STIFF_xy(i,j)=STIFF_xy(i,j)+
& (data(3+q)*data(8+q)*vec(7)*vec(8)*2.0/data(1+q)*weight(k)) +
    &
        &  (data(10+q)*data(5+q)*data(4+q)*(vec(3)*2./data(1+q)-
vec(5))*
    & (vec(4)*2./data(1+q)-vec(6))*data(1+q)/2.0*weight(k))
            end do
            MASS_xy(j,i)=MASS_xy(i,j)
            STIFF_xy(j,i)=STIFF_xy(i,j)
        end do
     end do
     return
     end

SUBROUTINE shapef5(n, m, eta, Jac, p, vec)
.c.....
     integer choice, pass,     !dummy varnables
    &        n, m       !non-local variables, input
     real*8 eta, Jac, p     !non-local variables, input
     real*8 vec(8)
c.----------* shape functnons *----------
     choice=n
     do pass=0,1
        select case (choice)
        case (1)     !.....
     vec(1+pass)=0.25*eta*(eta-1.)/(Jac**2+12.*p)/(15.*p+Jac**2)*
    &   ((3.*Jac**4 + 36.*Jac**2*p)*eta**3 +
    &    (1.*Jac**4 +  6.*Jac**2*p)*eta**2 -
    &    (4.*Jac**4 +114.*Jac**2*p + 720.*p**2)*eta -
    &            ( 30.*Jac**2*p + 360.*p**2))
     vec(3+pass)=0.25/(Jac**2+12.*p)/(15.*p+Jac**2)*
    &     ((15.*Jac**4 + 180.*Jac**2*p)*eta**4 -
    &      ( 8.*Jac**4 + 120.*Jac**2*p)*eta**3 -
    &      (15.*Jac**4 + 360.*Jac**2*p + 2160.*p**2)*eta**2 -
    &      ( 8.*Jac**4 + 168.*Jac**2*p +  720.*p**2)*eta +
    &               ( 30.*Jac**2*p +  360.*p**2))
     vec(5+pass)=0.25*eta*(eta-1.)*(eta+1.)/(Jac**2+12.*p)/
    &                          (15.*p+Jac**2)*
    &     ((15.*Jac**2 + 180.*p)*eta -
    &      ( 8.*Jac**2 + 120.*p))*Jac
     vec(7+pass)=0.5*Jac/(Jac**2+12.*p)/(15.*p+Jac**2)*
    &     ((30.*Jac**2 + 360.*p)*eta**3 -
    &      (12.*Jac**2 + 180.*p)*eta**2-
    &      (15.*Jac**2 + 180.*p)*eta+
    &      ( 4.*Jac**2 +  60.*p))
        case (2)     !.....
     vec(1+pass)=0.25*eta*(eta-1.)*(eta+1.)/(Jac**2+12.*p)
    &                          /(15.*p+Jac**2)*
    & ((1.*Jac**6 +  6.*Jac**4*p - 72.*Jac**2*p**2)*eta**2 -
    &  (1.*Jac**6 + 15.*Jac**4*p)*eta -
    &           ( 6.*Jac**4*p - 48.*Jac**2*p**2-1440.*p**3))/Jac
     vec(3+pass)=0.25/(Jac**2+12.*p)/(15.*p+Jac**2)*
    &((5.*Jac**6 + 30.*Jac**4*p - 360.*Jac**2*p**2)*eta**4 -
    & (4.*Jac**6 + 60.*Jac**4*p)*eta**3 -
                &    (3.*Jac**6    +    36.*Jac**4*p-360.*Jac**2*p**2-
4320*p**3)*eta**2+
    & (2.*Jac**6 + 30.*Jac**4*p)*eta+
    & (          6.*Jac**4*p- 48.*Jac**2*p**2-1440*p**3))/Jac
     vec(5+pass)=0.25*eta*(eta-1.)/(Jac**2+12.*p)/(15.*p+Jac**2)*
    &   ((5.*Jac**4 + 30.*Jac**2*p - 360.*p**2)*eta**2 +
    &    (1.*Jac**4 - 30.*Jac**2*p - 360.*p**2)*eta -
    &    (2.*Jac**4 +  6.*Jac**2*p - 360.*p**2))
     vec(7+pass)=-0.5/(Jac**2+12.*p)/(15.*p+Jac**2)*
    &     ((-10.*Jac**4 - 60.*Jac**2*p + 720.*p**2)*eta**3 +
    &      ( 6.*Jac**4 + 90.*Jac**2*p)*eta**2+
    &      ( 3.*Jac**4 - 24.*Jac**2*p - 720.*p**2)*eta-
    &      ( 1.*Jac**4 +  3.*Jac**2*p - 180.*p**2))
        case (3)     !.....
     vec(1+pass)=-0.25*eta*(eta+1.)/(Jac**2+12.*p)/
    &                          (15.*p+Jac**2)*
    &     ((3.*Jac**4 + 36.*Jac**2*p)*eta**3 -
    &      (1.*Jac**4 +  6.*Jac**2*p)*eta**2 -
    &      (4.*Jac**4 +114.*Jac**2*p + 720.*p**2)*eta +
    &               ( 30.*Jac**2*p + 360.*p**2))
     vec(3+pass)=-0.25/(Jac**2+12.*p)/(15.*p+Jac**2)*
    &     ((15.*Jac**4 + 180.*Jac**2*p)*eta**4 +
    &      ( 8.*Jac**4 + 120.*Jac**2*p)*eta**3 -
    &      (15.*Jac**4 + 360.*Jac**2*p + 2160.*p**2)*eta**2 -
    &      ( 8.*Jac**4 + 168.*Jac**2*p +  720.*p**2)*eta +
    &               ( 30.*Jac**2*p +  360.*p**2))
     vec(5+pass)=-0.25*eta*(eta-1.)*(eta+1.)/(Jac**2+12.*p)/
    &                          (15.*p+Jac**2)*
    &     ((15.*Jac**2 + 180.*p)*eta +
    &      ( 8.*Jac**2 + 120.*p))*(Jac)
     vec(7+pass)=-0.5*Jac/(Jac**2+12.*p)/(15.*p+Jac**2)*
    &     ((30.*Jac**2 + 360.*p)*eta**3 +
    &      (12.*Jac**2 + 180.*p)*eta**2-
    &      (15.*Jac**2 + 180.*p)*eta-
    &      ( 4.*Jac**2 +  60.*p))
        case (4)     !.....
     vec(1+pass)=0.25*eta*(eta-1.)*(eta+1.)/(Jac**2+12.*p)/
    &                          (15.*p+Jac**2)*
    & ((1.*Jac**6 +  6.*Jac**4*p - 72.*Jac**2*p**2)*eta**2 +
    &  (1.*Jac**6 + 15.*Jac**4*p)*eta -
    &           ( 6.*Jac**4*p - 48.*Jac**2*p**2-1440.*p**3))/Jac
     vec(3+pass)=0.25/(Jac**2+12.*p)/(15.*p+Jac**2)*
    &((5.*Jac**6 + 30.*Jac**4*p - 360.*Jac**2*p**2)*eta**4 +
    & (4.*Jac**6 + 60.*Jac**4*p)*eta**3 -
                &    (3.*Jac**6    +    36.*Jac**4*p-360.*Jac**2*p**2-
4320*p**3)*eta**2-
    & (2.*Jac**6 + 30.*Jac**4*p)*eta+
    & (          6.*Jac**4*p- 48.*Jac**2*p**2-1440*p**3))/Jac
     vec(5+pass)=0.25*eta*(eta+1.)/(Jac**2+12.*p)/(15.*p+Jac**2)
*
    &   ((5.*Jac**4 + 30.*Jac**2*p - 360.*p**2)*eta**2 -
    &    (1.*Jac**4 - 30.*Jac**2*p - 360.*p**2)*eta -
    &    (2.*Jac**4 +  6.*Jac**2*p - 360.*p**2))
     vec(7+pass)=-0.5/(Jac**2+12.*p)/(15.*p+Jac**2)*
    &     ((-10.*Jac**4 - 60.*Jac**2*p + 720.*p**2)*eta**3 -
    &      ( 6.*Jac**4 + 90.*Jac**2*p)*eta**2+
    &      ( 3.*Jac**4 - 24.*Jac**2*p - 720.*p**2)*eta+
    &      ( 1.*Jac**4 +  3.*Jac**2*p - 180.*p**2))
        case (5)     !.....
     vec(1+pass)=(eta-1.)*(eta+1.)/(Jac**2+12.*p)*
    &   ((1.*Jac**2)*eta**2 -
    &    (1.*Jac**2 + 12.*p))
     vec(3+pass)=4.*eta/(Jac**2+12.*p)*
    &   ((1.*Jac**2)*eta**2 -
    &    (1.*Jac**2 + 6.*p))
     vec(5+pass)=4.*Jac*eta*(eta-1.)*(eta+1.)/(Jac**2+12.*p)
     vec(7+pass)=4.*Jac*(3.*eta**2-1.)/(Jac**2+12.*p)
        case (6)     !.....
     vec(1+pass)=eta*(eta-1.)*(eta+1.)/(15.*p+Jac**2)*
    &   ((1.*Jac**4 +  3.*Jac**2*p)*eta**2 -
    &    (1.*Jac**4 + 27.*Jac**2*p + 60.*p**2))/Jac
     vec(3+pass)=1./(15.*p+Jac**2)*
    &   ((5.*Jac**4 + 15.*Jac**2*p)*eta**4 -
    &    (6.*Jac**4 + 90.*Jac**2*p + 180.*p**2)*eta**2+
    &    (1.*Jac**4 + 27.*Jac**2*p +  60.*p**2))/Jac
     vec(5+pass)=(eta-1.)*(eta+1.)/(15.*p+Jac**2)*
    &   ((5.*Jac**2 + 15.*p)*eta**2 -
    &    (1.*Jac**2 + 15.*p))
     vec(7+pass)=4.*eta/(15.*p+Jac**2)*
    &   ((5.*Jac**2 + 15.*p)*eta**2 -
    &    (3.*Jac**2 + 15.*p))
     end select   !.....
     choice=m
     end do
     return
     end


SUBROUTINE inv_A_product_B(mat_A, mat_B, mat_C, n)
*    (inverse mat_A)*mat_B=mat_C
*    n    size of square matrices mat_A, mat_B & mat_C
     integer i, j, n, ifree, ialloc
     double precision
    + mat_A(n,n), mat_B(n,n), mat_C(n,n),     !adjustable array
    + dummy_vector_a(:),                      !allocate
    + dummy_vector_b(:),
    + dummy_array(:,:)
```

```
      real dummy_real
      allocate
(dummy_vector_a(n),dummy_vector_b(n),dummy_array(n,n),
     +        stat=ialloc)
      if(ialloc.ne.0) print *, 'allocfail - invMxK..dummys'
c.    copy mat_A, before going into ludcmp, as returns corrupted!
      do i=1,n
          do j=1,n
          dummy_array(i,j)=mat_A(i,j)
          end do
      end do
      call ludcmp(dummy_array,n,dummy_vector_a,dummy_real)
      do j=1, n
          do i=1, n
             dummy_vector_b(i)=mat_B(i,j)
          end do
          call
lubksb(dummy_array,n,dummy_vector_a,dummy_vector_b)
          do i=1, n
              mat_C(i,j)=dummy_vector_b(i)
          end do
      end do
      deallocate (dummy_vector_a,dummy_vector_b,dummy_array,
     +          stat=ifree)
      if(ifree.ne.0) print *, 'deallocfail - invMxK...dummys'
      return
      end
end


 SUBROUTINE eigensANDscale(mass,mat_A, n, wr, mat_U)
      integer i, j, k, l, n, ifree, ialloc
      double precision
     + mass(n,n), mat_A(n,n), mat_U(n,n),wr(n),    !adjustable array
     + dummy_array_A(:,:), dummy_array_B(:,:),
     + dummy_vector_A(:),
     + dummy_vector_B(:),
     + dummy_vector_C(:),
     + wi(:)                              !imag eigenvalues
      real dummy_real, delta
      allocate (
     + dummy_array_A(n,n), wi(n),
     + stat=ialloc)
      if (ialloc.ne.0) print *, 'allocfail, eig_scal.dummy_array_A'
c.-----------------------* solve eigenvalues *-----------------
      do i=1,n
          do j=1,n
          dummy_array_A(i,j)=mat_A(i,j)
          end do
      end do
      call balanc(dummy_array_A,n)
      call elmhes(dummy_array_A,n)
      call hqr(dummy_array_A,n, wr,wi)      !
      deallocate (dummy_array_A,stat=ifree)
      if (ifree.ne.0) print *, 'deallocfail, eig_scal.dummy_array_A'
      call sort2(n,wr,wi)                  ! sort eigenvalues
c. check that imag eigenvalues are ALL ZERO!!
      do i=2,n
          wi(1)=wi(1)+wi(i)
      end do
      if (wi(1).ne.0.0) then
          print *, 'ERROR mass or stiffness matrix non-symmetric,'
          print *, 'ERROR causing imag eigenvalues <> 0.0,'
          print *, 'ERROR program will terminate !'
          STOP 'program has successfully terminated'
      end if
      deallocate (wi, stat=ifree)
      if (ifree.ne.0) print *, 'deallocfail, eig_scal...wi'
c.-----------------------* solve eigenvectors *-----------------
      allocate (
     + dummy_array_B(n-1,n-1),
     + dummy_vector_A(n-1),dummy_vector_B(n-1),
     + stat=ialloc)
      if (ialloc.ne.0) print *, 'allocfail, dummy_vars'
      do i=1, n
          mat_U(1,i)=1.0              !assumption
              do j=2,n
                mat_U(j,i)=0.0        !initialise
              end do
              do j=2, n
                do k=2, n
                  if (j.eq.k) then
                  delta=1.
                  else                !kronecker delta
                     delta=0.0
                  end if
                dummy_array_B(j-1,k-1)=mat_A(j,k)-wr(i)*delta
                end do
                dummy_vector_A(j-1)=mat_A(j,1)*(-1.0)
              end do
      call                                ludcmp(dummy_array_B,(n-
1),dummy_vector_B,dummy_real)
      call                                lubksb(dummy_array_B,(n-
1),dummy_vector_B,dummy_vector_A)
          do l=1,(n-1)
              mat_U(l+1,i)=dummy_vector_A(l)
          end do
      end do
      deallocate (dummy_array_B,
     + dummy_vector_A, dummy_vector_B,stat=ifree)
      if (ifree.ne.0) print *, 'deallocfail,eig_scal. dummys'
c.-----------* scale eigenvector *-------------------------
      allocate (dummy_vector_C(n), stat=ialloc)
      if (ialloc.ne.0) print *, 'allocfail, eig_scal.dummy_vector_C'
      do k=1, n
          dummy_vector_C(k)=0.0      !initialise
      end do

      do k=1, n
          do i=1, n
              do j=1, n
              dummy_vector_C(k)=dummy_vector_C(k)+
     +                    mass(i,j)*mat_U(i,k)*mat_U(j,k)
              end do
          end do
      end do
      do l=1, n
          do k=1,n
            mat_U(k,l)=mat_U(k,l)/sqrt(dummy_vector_C(l))
          end do
      end do
      deallocate (
     + dummy_vector_C,stat=ifree)
      if (ifree.ne.0) print *, 'deallocfail, eig_scal.dummy_vector_C'
      return
      end
end


SUBROUTINE plot_FRF_rs(fe_type, bc_type, U, wr, dof)
      include 'graphapi.fi'
      include 'graph.fi'
      include 'pgapi.fi'
      include 'pg.fi'
      character*12 file_out      !file name for ASCII dump of results
      integer
     + fe_type,          !1 >> axial or torsion fe model
c                        2 >> bendxy or bendzx fe model
c                        3 >> composite fe model
     + bc_type,          !1 >> free-free boundary condition
c                        2 >> pin-free boundary condition
c                        3 >> clamped-free boundary condition
     + dof,              !dimension of array/vectors
     + num_samples,      !number of frequency samples
     + ifree, ialloc,    !allocation & dealloacation checks
     + r, s,             !r=impact node & s=response node
     + idummy, i, j,     !dummy variable & do-loop variables
     + choice            !

      real*4
     + alpha, beta,      !damp=alpha*mass+beta*stiff
     + eta(:),           !modal damping ratio
     + dfreq, freq_span, w(:), !freq step, freq span, freq/angvel
     + real_FRF_rs(:),   !real freq response function
     + imag_FRF_rs(:),   !imag freq response function
     + mag_FRF(:)        !magnitude of FRF

      double precision
     + U(dof,dof), !column wise eigenvectors
     + wr(dof),          !vector of eigenvalues
```

```
     + pi          !pi
      parameter (pi=3.14159265359)

      record/chartenv/env
      record/paletteentry/ pal( _PG_PALETTELEN )

c.--------* damping ratio, viscous damping - time domain *---------
      allocate (eta(dof),stat=ialloc)
      if (ialloc.ne.0) print *,'allocfail eta'
      remote block damping_block
          do i=1, dof
              eta(i)=0.0
          end do
          print *, 'VISCOUS DAMPING CHARACTERISTICS'
          print *, 'damp=alpha(MASS) + beta(STIFF), matrix'
          write(5,*) 'enter ALPHA & BETA values'
          read(5,fmt=1030) alpha
          read(5,fmt=1030) beta
          if ((fe_type.eq.1).AND.(bc_type.eq.1)) then
           print *,'axial/torsion, free-free..rigid-body motion'
           eta(1)=0.0
           idummy=2
          else if ((fe_type.eq.2).AND.(bc_type.eq.1)) then
           print *,'bendxy/bendzx, free-free..rigid-body motion'
           eta(1)=0.0
           eta(2)=0.0
           idummy=3
          else if ((fe_type.eq.2).AND.(bc_type.eq.2)) then
           print *,'bendxy/bendzx, pin-free..rigid-body motion'
           eta(1)=0.0
           idummy=2
          else if ((fe_type.eq.3).AND.(bc_type.eq.1)) then
           print*,'composite fe-model,free-free.rigid-body motion'
           do i=1, 6
              eta(i)=0.0
           end do
           idummy=7
          else if ((fe_type.eq.3).AND.(bc_type.eq.2)) then
           print*,'composite fe-model,pin-free.rigid-body motion'
          else
           idummy=1
          end if
          do i=idummy, dof
              eta(i)=(alpha+wr(i)*beta)/2./sqrt(wr(i))
          end do
      end block
1111  execute damping_block
      j=0
      do while (j.ne.dof)
          if (eta(j).gt.1.0) then
              print 5
              goto 1111
          else
              j=j+1
          end if
      end do
 5    format('damping ratio/mode > 1.0 ... re-enter')
c.-----------* frequency domain information *-----------------------
      print *, 'FREQUENCY DOMAIN INFORMATION'
      print *, 'enter FREQ_RESOLUTION and FREQ_SPAN ..(Hz)'
      read(5,fmt=1030) dfreq
      read(5,fmt=1030) freq_span
c.-----------------* Impulse response information *-----------------
      print *,'FREQUENCY RESPONSE FUNCTION'
      print *,'enter location of impulse (r) and response (s)'
      read(5,fmt=1000)  r
      read(5,fmt=1000)  s
c.-----------------* number of freq samples *----------------------
      num_samples=aint(freq_span/dfreq)      !freq samples
c.    print *, 'number of samples', num_samples
c.----------------* Calculation of FRF_rs(t) *--------------------
      allocate
(real_FRF_rs(num_samples),imag_FRF_rs(num_samples),
     +          w(num_samples),stat=ialloc)
      if (ialloc.ne.0) print *,'allocfail IRF_rs & t'
      do i=1, num_samples                    ! fill vector
          real_FRF_rs(i)=0.0
          imag_FRF_rs(i)=0.0
          w(i)=2.*pi*dfreq*i                 !convert freq >> rad/s
c.        do j=1, dof
          do j=idummy, dof
           real_FRF_rs(i)=real_FRF_rs(i)+
     +          U(r,j)*U(s,j)*(wr(j)-w(i)*w(i))/
     + ((wr(j)-w(i)**2)**2+(2.*eta(j)*sqrt(wr(j))*w(i))**2)
           imag_FRF_rs(i)=imag_FRF_rs(i)+
     +          U(r,j)*U(s,j)*(-2.*eta(j)*sqrt(wr(j))*w(i))/
     + ((wr(j)-w(i)**2)**2+(2.*eta(j)*sqrt(wr(j))*w(i))**2)
          end do
          w(i)=w(i)/2./pi                    !convert rad/s >> freq
      end do
c.-------------------* output routine *-----------------------------
      choice=1
      do while (choice.ne.0)
          loop
              call _clearscreen( _GCLEARSCREEN )
              print *, 'FREQUENCY RESPONSE FUNCTION'
              print *, '============================'
              print *, ' '
              print *, '( Note: rigid modes removed )'
              print *, ' '
              print *, '* Numerical Output of FRF_rs(t) *'
              print *, '       [1] Screen Dump or '
              print *, '       [2] ASCII file output'
              print *, ' '
              print *, '* Graphical Output of FRF_rs(t) *'
              print *, '       [3] real_FRF_rs(w) vs freq'
              print *, '       [4] imag_FRF_rs(w) vs freq'
              print *, '       [5] mag|FRF_rs(w)| vs freq'
          print *, '       [6] real_FRF_rs(w) vs imag_FRF_rs(w)'
              print *, ' '
              print *, '       [0] duck'
              read(5,fmt=1000) choice
              if (choice.gt.6) then
                  cycle
              else
                  exit
              end if
          end loop
       select case (choice)
       case(1)
              execute screen_dump
       case(2)
              execute ASCII_file
       case(3)
          execute graph_initialise
          env.maintitle.title='FRF <> real_FRF vs freq'//char(0)
          call      _pg_chartscatter(env,      w,      real_FRF_rs,
num_samples)
          pause
          call _setvideomode (_DEFAULTMODE)
       case(4)
          execute graph_initialise
          env.maintitle.title='FRF <> imag_FRF vs freq'//char(0)
          call      _pg_chartscatter(env,      w,      imag_FRF_rs,
num_samples)
          pause
          call _setvideomode (_DEFAULTMODE)
       case(5)
          allocate(mag_FRF(num_samples), stat=ialloc)
          if (ialloc.ne.0) print *,'allocfail mag_FRF'
          do i=1, num_samples

mag_FRF(i)=sqrt(real_FRF_rs(i)**2+imag_FRF_rs(i)**2)
          end do

          execute graph_initialise
          env.maintitle.title='FRF <> mag|FRF| vs freq'//char(0)
          call _pg_chartscatter(env, w, mag_FRF, num_samples)
          pause
          call _setvideomode (_DEFAULTMODE)
          deallocate(mag_FRF, stat=ifree)
          if (ifree.ne.0) print *,'deallocfail mag_FRF'
       case(6)
          execute graph_initialise
          env.maintitle.title='FRF <> Re(FRF) vs Im(FRF)'//char(0)
          call _pg_chartscatter(env, real_FRF_rs,
     +                    imag_FRF_rs, num_samples)
          pause
          call _setvideomode (_DEFAULTMODE)
       end select
```

```
      end do

      remote block screen_dump
          print *, 'Screen dump of FRF_rs(t) results'
          print *, '-------------------------------'
          do i=1, dof
              print 20, i
              print 30, sqrt(wr(i))/2./pi
              print 40, eta(i)
              print 50, (sqrt(wr(i))*sqrt(1.-eta(i)**2))/2./pi
              print 60
              write(5,fmt=1050) (U(j,i),j=1,dof)
              pause
          end do
          print *, 'frequency response function H_rs(w), '
          write(5,fmt=1010) r, s
          print *, 'freq (Hz)      Re(H_rs)     Imag(H_rs)'
          do i=1, num_samples
           write(5,fmt=1020) w(i), real_FRF_rs(i), imag_FRF_rs(i)
          end do
          pause
      end block

      remote block ASCII_file
          print *, 'ASCII file dump of FRF_rs(t) results'
          print *, '------------------------------------'
          print *, 'enter new file name for dump of results'
          read(5,'(a12)') file_out
          open(unit=11, file=file_out, status='new')
          do i=1, dof
           write(11,fmt=20) i
           write(11,fmt=30) sqrt(wr(i))/2./pi
           write(11,fmt=40) eta(i)
           write(11,fmt=50) (sqrt(wr(i))*sqrt(1.-eta(i)**2))/2/pi
           write(11,fmt=60)
           write(11,fmt=1050) (U(j,i),j=1,dof)
          end do
          write(11,*) 'impulse response function h_rs(t), '
          write(11,fmt=1010) r, s
          write(11,*) 'freq (Hz) Re(H_rs)     Imag(H_rs)'
          do i=1, num_samples
           write(11,fmt=1020) w(i), real_FRF_rs(i), imag_FRF_rs(i)
          end do
          close(unit=11)
      end block

      remote block graph_initialise
          call _setvideomode( _VRES16COLOR)
          call _pg_initchart()
          call _pg_defaultchart(env, _PG_SCATTERCHART,
     +                          _PG_POINTANDLINE)
          call _pg_getpalette(pal)
          pal(2).plotchar=0              !forces no point
          call _pg_setpalette(pal)
      end block

   20 format('mode number: 'i5)
   30 format('natural (undamped) resonant frequency (Hz): ',f12.4)
   40  format('damping ratio/mode                 : ',f12.6)
   50 format('damped resonant frequency (Hz):       : ',f12.4)
   60 format('corresponding eigenvector')
 1000 format(i5)
 1010 format(2i5)
 1020 format(f12.4,4X,e12.4e3,4X,e12.4e3)
 1030 format(f12.6)
 1040 format(4e16.8e2)
 1050 format(6f12.6)
c.----------* closing routines *---------------------
      deallocate(real_FRF_rs, imag_FRF_rs, eta, w, stat=ifree)
      if (ifree.ne.0) print *,'deallocfail FRF_rs & w'
      return
      end
```

Reference:

Press W.H., Flannery B.P., Teukolsky S.A. and Vetterling W.T. **Numerical Recipes in C,** Cambridge University Press, Cambridge 1986.

Appendix III

Experimental Details.

Appendix III-1. Specifications of Experimental Apparatus.

Specifications of the Force Transducer and Battery-Powered Power Supply.

PCB® PIEZOTRONICS

SPECIFICATIONS
Voltage Output
Force Transducer

Model No. 208B03

Revisions

DYNAMIC PERFORMANCE				
Range:	Compression	lb [kN]	500 [2,224]	
	Tension	lb [kN]	500 [2,224]	
Maximum Force:	Compression	lb [kN]	5000 [22,24]	
	Tension	lb [kN]	750 [3,336]	
Resolution		lb [kN]	0.01 [4,48 E-5]	
Sensitivity		mV/lb [mV/kN]	10 [2248,2]	
Resonant Frequency		kHz	70	[5]
Rise Time		µ sec	10	
Discharge Time Constant		sec	≥2000	[1]
Low Frequency Response (-5%)		Hz	0.0003	[3]
Amplitude Non-Linearity		% F.S.	1	[2]
Stiffness		lb/µin [kN/µm]	10 [1,75]	
ENVIRONMENTAL				
Temperature Range		°F [°C]	-65 to +250 [-54 to +121]	
Temperature Coefficient		%/°F [%/°C]	≤0.03 [≤0,054]	
Vibration		±g pk [±m/s² pk]	2000 [19 620]	[4]
Shock		±g pk [±m/s² pk]	10000 [98 100]	[4]
ELECTRICAL				
Full Scale Output		+ volt	5	[6]
Output Impedance		ohm	≤100	
Output Bias		+ volt	8 to 14	
Excitation:	Voltage	+ VDC	24 to 27	
	Constant Current	mA	2 to 20	
Polarity		compression	Positive	
MECHANICAL				
Dimensions		in [mm]	0.625 x 0.625 [15,88 x 15,88]	
Weight		oz [grams]	0.93 [26]	
Housing		material	Stainless Steel	
Connector		type	10-32 Coaxial Jack	
Connector Orientation		position	Side	
Mating Connector Required		type	10-32 Coaxial Plug	
Sealing		type	Epoxy	

PCB® PIEZOTRONICS

SPECIFICATIONS
Battery-Powered Signal Conditioning
For Use With ICP Sensors

Model No. 480E09

Revisions
-A- Rev # 5070
DM 5/27/04

Supply Voltage	+V	27	
Supply Current (thru internal current limiting diode)	mA	2 (±0.6)	
Current Avail to Drive Readout	mA	1	
Coupling Capacitor	µF	22	
DC Offset (maximum) (w/1M Ω load at "scope" output)	mV	±30	
Battery Life	hours	40, 12 (±10%)	[2] [3]
Battery (3 supplied) (Alkaline)	V	9, NEDA 1604A	[4]
Frequency Response (±5% voltage all gain)	Hz/kHz	0.15/100	[1]
Noise, Electrical, pk to pk: x1	mV	0.2	
x10	mV	2	
x100	mV	20	
Fault Monitor Meter (1 mA movement)	V/FS	27	
External Power, Input	V/mA	18-28/8	
Connectors: Input (transducer)	jack	BNC	
Output (scope)	jack	BNC	
External Power, Input	jack	1/8 Diameter Miniature	
Charge Connector	jack	#722 Switchcraft	
Size: H x W x D	inch	4.0 x 2.9 x 1.5	
	[mm]	[101.6 x 73.7 x 38.1]	
Weight (including batteries)	oz [grams]	[340.2]	

Calibration Data for the Force Transducer.

ICP CALIBRATION DATA

PCB PIEZOTRONICS

Model 208B03 | Cal Range 0 - 500 lbs. | Input TC > 2000 sec
S/N 12465 | Sens* 10.44 mV/lb | Rise Time 10 usec
Linearity* < 1.0 %FS | Nat'l Freq 70 kHz | By Chuck DiMaggio
* By comparison with reference standard per ISA S37.10. Zero Based best straight line. | Output Imp < 100 ohms | Date Aug 31, 1995

Calibration of instrumentation used to certify this sensor is traceable to NIST.

PCB Piezotronics' calibration procedure is in compliance with MIL-STD-45662A.

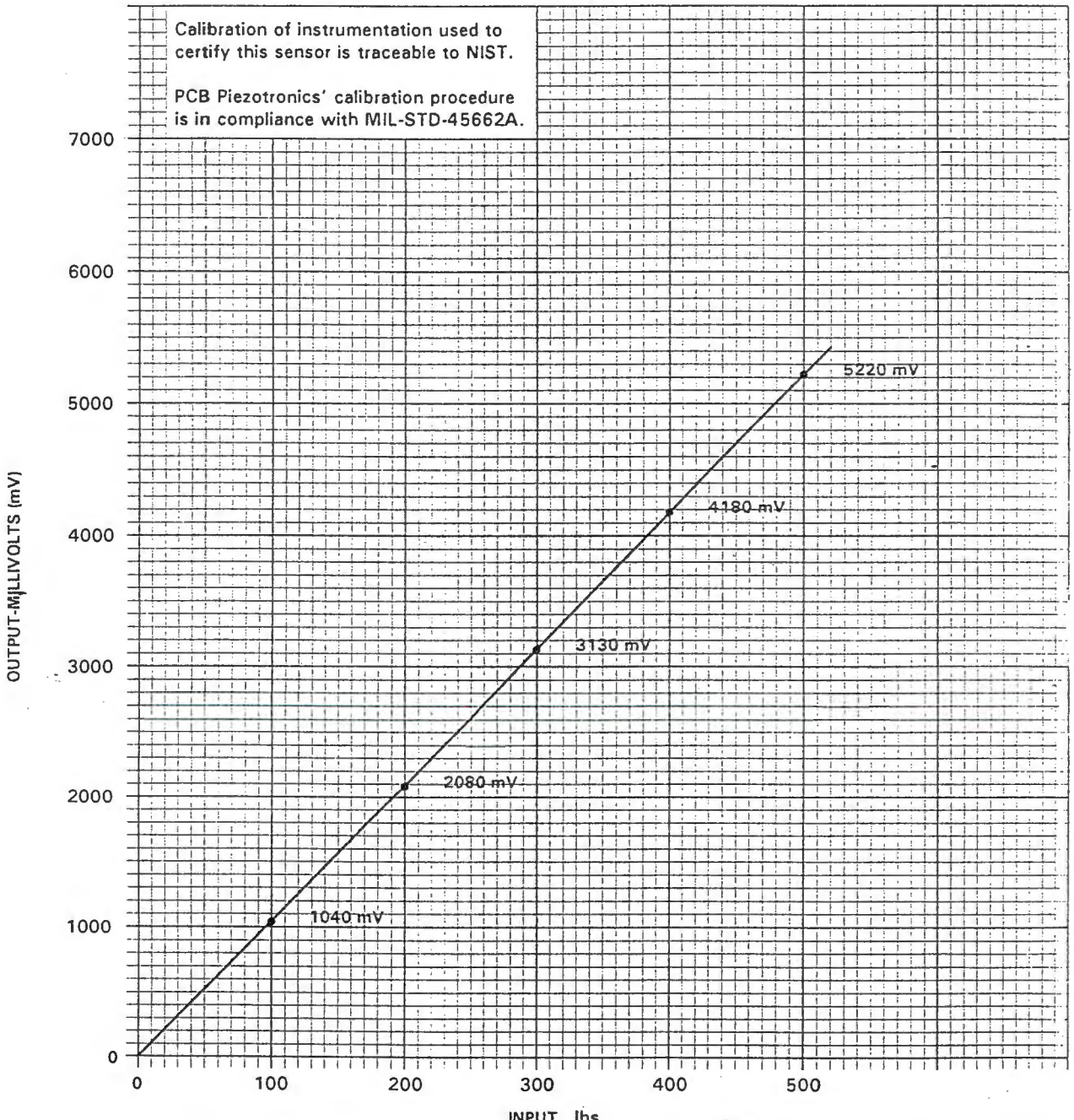

PCB PIEZOTRONICS, INC.
3425 Walden Avenue, Depew NY 14043
Tel:716-684-0001 TWX:710-263-1371

Customer _____
PO Number _____
Calibration Traceable to NIST thru project No. 6.6/156007

Specifications of the Response Accelerometer.

Models 732A & 736
High Sensitivity/High Frequency Accelerometer

Features:
- Wide dynamic range
- High sensitivity
- Compact construction to fit in tight spaces
- Wide frequency range
- Standardized sensitivity
- Hermetically sealed

Applications:
- Fans
- Bearings
- Rotating machinery
- Laboratory research
- Predictive maintenance

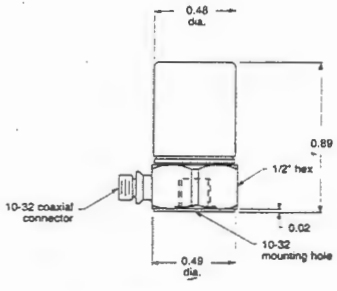

Models 732A & 736

SPECIFICATIONS		732A	736	UNITS
DYNAMIC				
Sensitivity, ±5 %, 25 °C		10	100	mV/g
Acceleration Range[1]		250	50	g peak
Amplitude Nonlinearity		1		%
Frequency Response:				
	±5 %	3 - 15,000	6 - 15,000	Hz
	±3 dB	1 - 25,000	2 - 25,000	Hz
Resonance Frequency, mounted, nom.				kHz
Transverse Sensitivity, max.		5		% of axial
Temperature Response		see graph		
ELECTRICAL				
Power Requirement, voltage source		18 - 30		VDC
	current regulating diode[1,2]	2 - 10		mA
Electrical Noise, equiv. g, nom.:				
Broadband, 2.5 Hz to 25 kHz		2000	150	µg
Spectral	10 Hz	100	10	µg/√Hz
	100 Hz	30	2	µg/√Hz
	1,000 Hz	10	1	µg/√Hz
	10,000 Hz	5	0.8	µg/√Hz
Output Impedance, max.		100	150	Ω
Bias Output Voltage, nom.		10		VDC
Grounding		case grounded		
ENVIRONMENTAL				
Temperature Range		-50 to 120		°C
Vibration Limit		500		g peak
Shock Limit		5000		g peak
Electromagnetic Sensitivity, equiv. g.		100		µg/gauss
Base Strain Sensitivity		0.005		g/µstrain
PHYSICAL				
Weight		15		grams
Case Material		stainless steel		
Mounting		10-32 tapped hole		
Output Connector		10-32 coaxial		
Cabling: Mating Connector		Microdot 10-32 (R1)		
Standard Cable		J93, coaxial, Teflon jacket, 30 pF/ft		

NOTES: [1] Signal distortion can occur when measuring high vibration levels, especially with long cables. A 24-30 VDC powering source is recommended for minimizing distortion. Current regulating diode must be at least 2 mA plus 1 mA per 1000 pF of cable capacitance.
[2] A maximum current of 6 mA is recommended for operating temperatures in excess of 100 °C.

OPTIONS: Customer specified sensitivity, filtering, top connector (BNC), PVC jacketed cable.

ACCESSORIES SUPPLIED: SF1 mounting stud, R12-J93-10 cable assembly.

ACCESSORIES AVAILABLE: Power supplies, amplifiers, signal conditioners, cementing studs, magnetic mounting bases, isolating studs.

TYPICAL TEMPERATURE RESPONSE

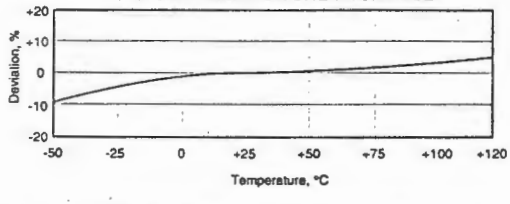

TYPICAL FREQUENCY RESPONSE

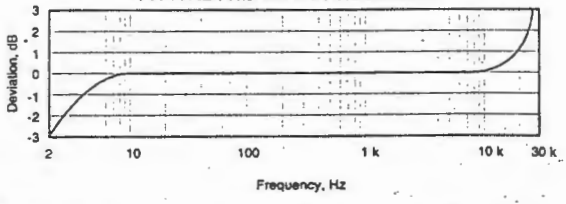

Due to continued research and product development, Wilcoxon Research reserves the right to amend this specification without notice.

Wilcoxon Research, 2096 Gaither Road, Rockville, Maryland 20850 USA • 1-800-VIB-SENS or (301) 330-8811 • Fax: (301) 330-8873

Typical Accelerometer Calibration Results .

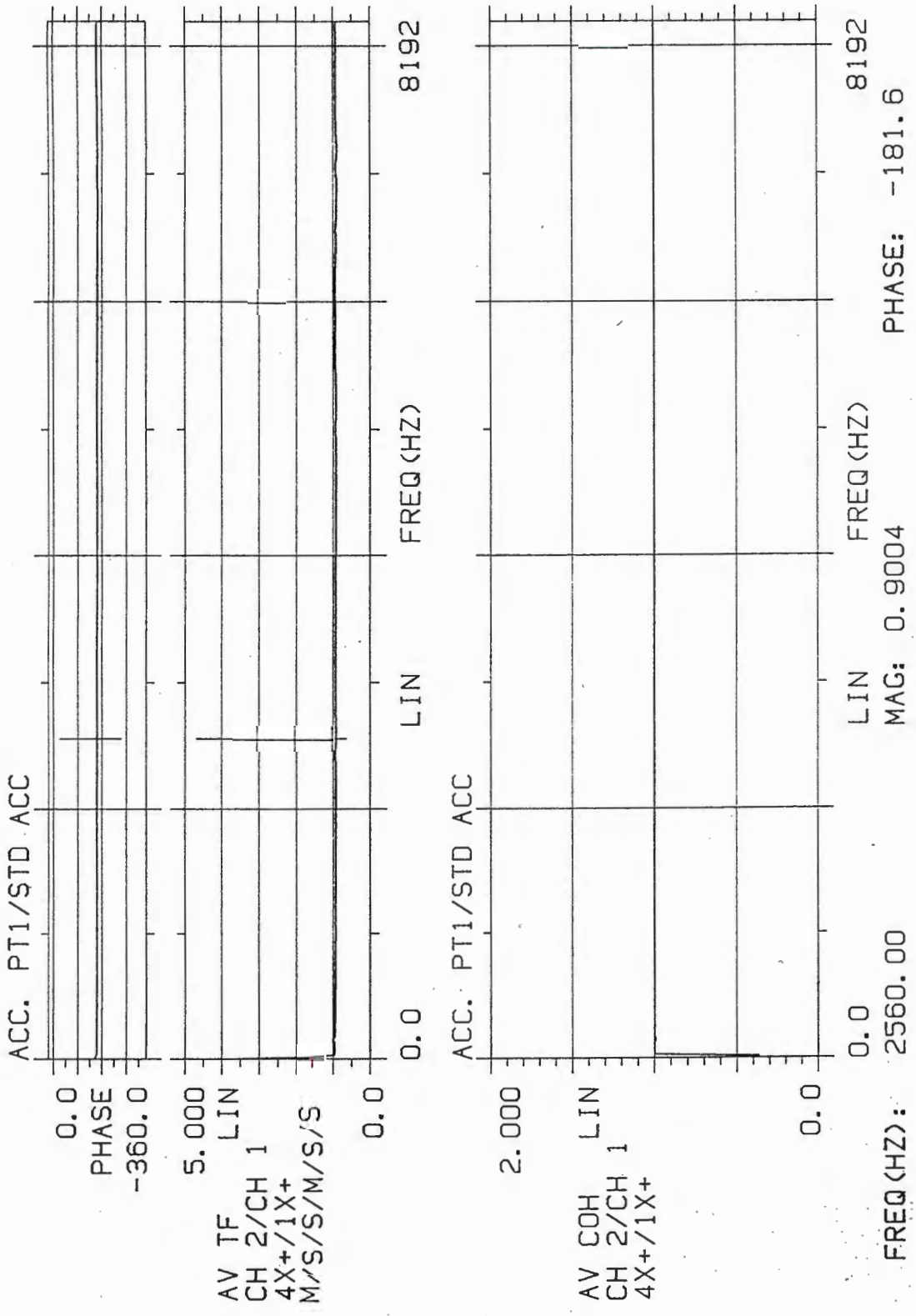

Specifications of the Referenced Accelerometer, used for Calibration.

Brüel & Kjær

CERTIFICATE of CALIBRATION

Absolute Calibration by Laser-Interference

(Estimated Error less than 0.5%)

Accelerometer Reference Normal Type 8305 S Serial No. ...1068945.....

**

Reference Sensitivity at 160 Hz and ...21... °C: ...1.250. pC/g

Frequency Response

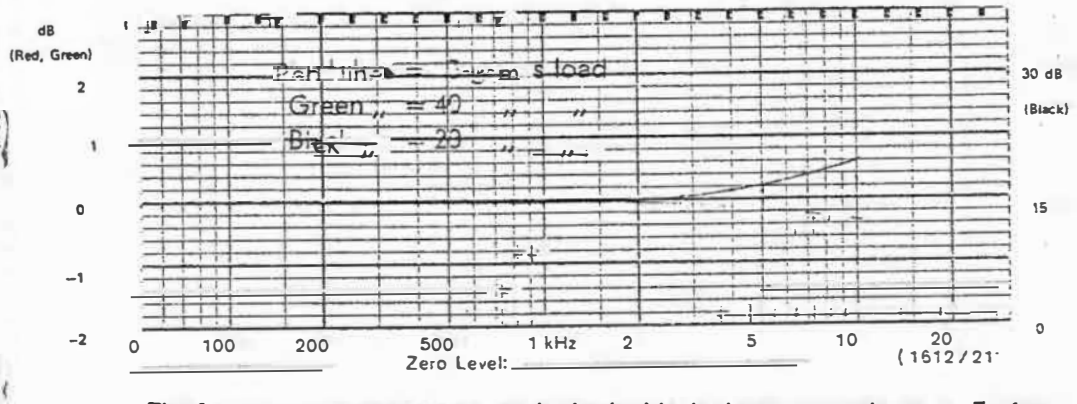

The frequency response curves are obtained with the base mounted on an Exciter and with a load applied to the top. The load acceleration is kept constant.

Maximum Transverse Sensitivity at 30 Hz ...1.5.. %

Accelerometer Capacitance .....74.6.. pF

Weight:.....39.7... grams

Polarity is negative on the center of the connector for an acceleration directed from the base into the body of the accelerometer.

Resistance minimum 10^{13} Ω at room temperature.

Environmental:
Humidity: Hermatically sealed.
(All welded and glass to metal diffusion seal)
Max. Temperature: 200°C or 392°F
Max. Shock Acceleration: 1000 g

- Magnetic Sensitivity: (50–400 Hz) < 0.1 g/kgauss
  Acoustic Sensitivity:
  Equivalent at 154 dB SPL < 0.03
- Base Strain Sensitivity: < 5×10^{-4} g/μstrain (in plane of the base)
- Temperature Transient Sensitivity:
  < 1 g/°C (Preamp. 2626 Low Lim. Freq.: 0.3 Hz)
  < 0.1 g/°C (Preamp. 2626 Low Lim. Freq.: 3 Hz)
  For further information see instruction book.
- Ref.: ANSI - S2. 11-1969

** This calibration is traceable to the National Bureau of Standards Washington D.C.

Physical:

Material: Stainless Steel
Mounting Thread: 10-32 UNF-2 B
Electrical Connector: Coaxial 10-32 UNF-2A thread

Individual Temperature Sensitivity Error in dB rel. the Reference Values.

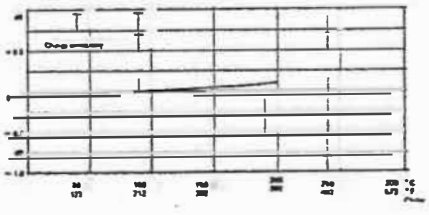

Nærum on ....28. juni... 19.83...

Approved Signature Removed

Signed Signature Removed

BC 0073

Appendix III-2.

Data Processing Software.

```
clear all;
num_samples=4096;N=4096;
num_channels=4;
A=zeros(num_channels, num_samples);
%
T_s=25.e-6;                    %sample time = 1/40 KHz
PSpec_pp=zeros(1,N); PSpec_qq=zeros(1,N);
PSpec_rr=zeros(1,N); PSpec_ss=zeros(1,N);
CSpec_qp=zeros(1,N); CSpec_rp=zeros(1,N);
CSpec_sp=zeros(1,N);
% col P==Channel#0==force transducer
% col Q==Channel#1==accel #1
% col R==Channel#2==accel #2
% col S==Channel#3==accel #3
%
w_0=2.*pi/(T_s*N);          % freq resolution (rad/s)
w=[(0:N/2),(-(N/2-1):-1)].*w_0; % freq. vector for matLAB fft
%.....................................................................
files=['m11xy01.mod';'m11xy02.mod';'m11xy03.mod';'m11xy04
.mod';

'm11xy05.mod';'m11xy06.mod';'m11xy07.mod';'m11xy08.mod';

'm11xy09.mod';'m11xy10.mod';'m11xy11.mod';'m11xy12.mod';

'm11xy13.mod';'m11xy14.mod';'m11xy15.mod';'m11xy16.mod';

'm11xy17.mod';'m11xy18.mod';'m11xy19.mod';'m11xy20.mod';

'm11xy21.mod';'m11xy22.mod';'m11xy23.mod';'m11xy24.mod';
    'm11xy25.mod';'m11xy26.mod';'m11xy27.mod'];
num=input('enter number ');
for i=1:num
        disp('reading, opened file'); files(i,1:11)
        file_name=files(i,1:11);
% open file
        fid=fopen(file_name,'r');
        A=fscanf(fid,'%f',[num_channels,num_samples]);
        status=fclose(fid);
% scaling
        A=A*1.21951;
        %initial op-amp
% unit conversion
        A(1,:)=A(1,:).*425.86920+1.62646; % convert
voltage >> newtons
        A(2,:)=A(2,:)*98.1;    % convert voltage >> m/s2
        A(3,:)=A(3,:)*98.1;    % convert voltage >> m/s2
        A(4,:)=A(4,:)*98.1;    % convert voltage >> m/s2
% resample at 5 times
        q_rs=interp(A(2,:),5);
        r_rs=interp(A(3,:),5);
        s_rs=interp(A(4,:),5);
% reform
        q_mod=[0,q_rs(5:5:num_samples*5-1)];
        r_mod=[0,r_rs(4:5:num_samples*5-1)];
        s_mod=[0,s_rs(3:5:num_samples*5-1)];
% fourier analysis
        P=fft(A(1,:),N);       % P==Channel 0 == input
        Q=fft(q_mod,N);        % Q==Channel 1 == accel#1
        R=fft(r_mod,N);        % R==Channel 2 == accel#2
        S=fft(s_mod,N);        % S==Channel 3 == accel#3
        PSpec_pp= PSpec_pp + P.*conj(P);       %power
spectrum of input
        PSpec_qq= PSpec_qq + Q.*conj(Q);       %power
spectrum of q
        PSpec_rr= PSpec_rr + R.*conj(R);       %power
spectrum of r
        PSpec_ss= PSpec_ss + S.*conj(S);       %power
spectrum of s
        CSpec_qp= CSpec_qp + Q.*conj(P);       %cross
spectrum of Q*conj(P)
        CSpec_rp= CSpec_rp + R.*conj(P);       %cross
spectrum of R*conj(P)
        CSpec_sp= CSpec_sp + S.*conj(P);       %cross
spectrum of S*conj(P)
end;
%---------------- ensemble averaging ----------------------
clear A q_rs q_mod r_rs r_mod s_rs s_mod P Q R S;
%
disp('Ensemble averaging')
PSpec_pp=PSpec_pp./num; PSpec_qq=PSpec_qq./num;
PSpec_rr=PSpec_rr./num; PSpec_ss=PSpec_ss./num;
CSpec_qp=CSpec_qp./num; CSpec_rp=CSpec_rp./num;
CSpec_sp=CSpec_sp./num;
%---------------- frequency transfer function ------------
disp('Calculating FRF & Coherence Functions')
H_pq=CSpec_qp./PSpec_pp;
Coh_pq=(abs(CSpec_qp)).^2./(PSpec_pp.*PSpec_qq);
H_pr=CSpec_rp./PSpec_pp;
Coh_pr=(abs(CSpec_rp)).^2./(PSpec_pp.*PSpec_rr);
H_ps=CSpec_sp./PSpec_pp;
Coh_ps=(abs(CSpec_sp)).^2./(PSpec_pp.*PSpec_ss);

clear Pspec_pp  Pspec_qq  Pspec_rr  PSpec_ss;
clear Cspec_qp  Cspec_rp CSpec_sp;
%
%---------------- impulse response function ---------------
disp('Calculating IRF')
h_pq=real(ifft(H_pq));  h_pr=real(ifft(H_pr));
h_ps=real(ifft(H_ps));
%%
disp('done - shut down')
disp('save workspace as....')
%end.
%%%%%%%%%% plotting routines %%%%%%%%%%%%
a=1; b=N/2;
figure(1);
subplot(3,1,1);
semilogy(w(a:b)./(2.*pi),20*log10(Coh_pq(a:b)));
 ylabel('mag|Coh_pq|(dB)');xlabel('freq. (Hz)');grid
 title('Magnitude of Coherence Function [P>>Q]... (20
averages xy data)')
subplot(3,1,2);
semilogy(w(a:b)./(2.*pi),20*log10(Coh_pr(a:b)));
 ylabel('mag|Coh_pr|(dB)');xlabel('freq. (Hz)');grid
 title('Magnitude of Coherence Function [P>>R]... (20
averages xy data)')
subplot(3,1,3);
semilogy(w(a:b)./(2.*pi),20*log10(Coh_ps(a:b)));
 ylabel('mag|Coh_ps|(dB)');xlabel('freq. (Hz)');grid
 title('Magnitude of Coherence Function [P>>S]... (20
averages xy data)')
 end
```

Appendix IV

Time Domain Identification.

Appendix IV .

The ERA was implemented in the visualization software MATLAB,

era_go.m

```
%%%%%%%%%%%%%%%%%%%%%%%%%%%%%%
%file era_go.m
%%%%%%%%%%%%%%%%%%%%%%%%%%%%%%
clear all; format compact;
%
m=1; disp ('enter number of "inputs" ... (m=1) ');
p=3; disp ('enter number of "outputs"... (p=3) ');
disp ('criteria 1) s & r >= (2*dof-1) ')
disp ('criteria 2) s > r ');
s=input ('input value of block cols for the Hankel matrix (s) ');
r=input ('input value of block rows for the Hankel matrix (r) ');
if s < r, break, end
%-------------------------------------------------------
disp ('..... load IRF data ');
%-------------------------------------------------------
disp ('discrete IRF files available..'); dir irf*.mat;
file=input('type name of discrete file (eg. str(irf_xz) ');
eval(['load ' file]);
h_pq=h_pq(1:s+r);                %minimise carried size
h_pr=h_pr(1:s+r);                %minimise carried size
h_ps=h_ps(1:s+r);                %minimise carried size
%
Dd_era=[h_pq(1);h_pr(1);h_ps(1)];
%
%-------------------------------------------------------
disp ('..... assemble Hankel Matrix ');
%-------------------------------------------------------
% Hankel_rs(k)=[Y(k+1) Y(k+2)  Y(k+3).... Y(k+s);
%               Y(k+2) Y(k+3)  Y(k+4).... Y(k+s+1);
%               Y(k+3) Y(k+4)  Y(k+5).... Y(k+s+2);
%                  .
%               Y(k+r) Y(k+r+1) Y(k+r+2)....Y(k+r+s)]
%
Han_rs_over=[h_pq(r:s);h_pr(r:s);h_ps(r:s)];
Han_rs_bot=[h_pq(s+1:r+s-1);h_pr(s+1:r+s1);...
h_ps(s+1:r+s-1)];
if s > r
 Han_rs_shift=[Han_rs_over(:,2:s-r+1),Han_rs_bot,...
          [h_pq(r+s);h_pr(r+s);h_ps(r+s)]];
else
 Han_rs_shift=[Han_rs_bot,...
                    [h_pq(r+s);h_pr(r+s);h_ps(r+s)]];
end
%%
disp ('starting Hankel assemble loop now...')
Han_rs_0=zeros(r*p,s*m);
for i=1:s
 j=1;
 for k=i:i+(r-1)
   Han_rs_0(j,i)=h_pq(k);
   Han_rs_0(j+1,i)=h_pr(k);
   Han_rs_0(j+2,i)=h_ps(k);
   j=j+p;                                  % assume p=3!!
 end
end
%visual output, Han_rs_0 Han_rs_shift
clear h_pq h_pr h_ps Han_rs_bot Han_rs_over;
%-------------------------------------------------------
disp ('..... Eigen Realization Algorithm ');
%-------------------------------------------------------
[P,D,Q]=svd(Han_rs_0);          % P*D*Q'=Han_rs_0
%-------------------------------------------------------
disp ('Normalised Singular Values, i.e. D/D(1)');
%-------------------------------------------------------
i=1:min(size(D));
singular_values=[i',diag(D)./D(1,1)]        %singular values
% plotting
figure(1); plot(i',diag(D)./D(1,1));
 title ('Normalised Singular Values, of SVD(Hankel matrix)');
 xlabel (' number of "dof"');
 ylabel ('singualar values -normailsed D/D(1)');
%-------------------------------------------------------
disp ('save workspace now, files available..'); dir *.mat;
%-------------------------------------------------------
file_save=input('type name of discrete file (eg. str(6x1allxz) ');
eval(['save ' file_save]);
%%now we're cooking !!!!!!!!!! %%%%%%%%%%%%%
num_singular=input('Number of significant values, to retain? (q)
');
%
D_r=D(1:num_singular,1:num_singular);  % D_r >> [q x q]
P_r=P(:,1:num_singular);         % P_r >> [(r)p x q]
Q_r=Q(:,1:num_singular);         % Q_r >> [(s)p x q]
clear P Q D;
%-------------------------------------------------------
% ** checking routines **
%-------------------------------------------------------
%disp ('CHECK #1  P_r*D_r*trn(Q_r) = Han_rs_0 ');
%P_r*D_r*Q_r';
%disp ('CHECK #2 (orthonormal cols) trn(P_r)*P_r = eye(q x q)
');
%diag(P_r'*P_r)
%disp ('CHECK #3 (orthonormal cols) trn(Q_r)*Q_r = eye(q x q)
');
%diag(Q_r'*Q_r)
%happy=input('continue (1/0) ');
%if happy < 1, break, end;
%=======================================
disp ('Realization formulation for Discrete State Space');
disp('**** calculate Ad_era ****');
%-----------------------
Ad_era=D_r^(-0.5)*P_r'*[Han_rs_0(p+1:r*p,:);Han_rs_shift]*...
                Q_r*D_r^(-0.5);
clear Han_rs_0 Han_rs_shift;
%
disp('**** calculate controlability & observability matrices');
%-------------------------------------------------------
Em=[eye(m)]; El=[eye(p)];
for i=2:(s), Em=[Em;zeros(m)]; end;
for i=2:(r), El=[El,zeros(p)]; end;
W_min=D_r^(0.5)*Q_r';
          V_min=P_r*D_r^(0.5);
%-----------------------
%disp ('CHECK #4 & #5                    ');
%disp (' trn(W_min)*W_min = trn(V_min)*V_min = D_r = D ');
%[diag(W_min *W_min'),diag(V_min'*V_min),diag(D_r),...
% diag(D(1:num_singular,1:num_singular))]
%happy=input('continue (1/0) ');
%if happy < 1, break, end;
%
disp('**** calculate Bd_era & Cd_era ****');
%-----------------------------------------
Bd_era=W_min*Em;              Cd_era=El*V_min;
disp('clearing off');
clear P_r Q_r D_r;
clear Em El V_min W_min;
%-----------------------------------------
% save workspace now
%-----------------------------------------
disp ('save workspace now, files available..'); dir disc*.mat;
file_save=input('type name of discrete file (eg. str(disc_50) ');
eval(['save ' file_save]);  end;
```

cbsi_xz.m

```
clc;clear all;format compact;
```

```
%%%%%%%%%%%%%%%%%%%%%%%%%%%%%'
disp('convert discrete to continuous, convert to displ measure ');
disp('% mass normalise, extract nat freq, moda damping etc
%');
%%%%%%%%%%%%%%%%%%%%%%%%%%%%'%%%
%-------------------------------------------------------
disp ('Discrete ERA files available..'); dir s*.mat;
%-------------------------------------------------------
file=input('type name of discrete file (eg. str(s8r2z48) ');
eval(['load ' file]);
%-------------------------------------------------------
disp('Convert to Continuous Time: method d2c
"zoh"+Dd_era=[0]');
%-------------------------------------------------------
[Ac_era,Bc_era]=d2c(Ad_era,Bd_era,T_s);
%%[hc_era,x]=impulse(Ac_era,Bc_era,Cd_era,zeros(p,m),1,tim
e);
Cc_era=Cd_era;      Dc_era=Dd_era;
%
clear Ad_era Bd_era Cd_era Dd_era;
%
%-------------------------------------------------------
disp('.....Convert y_accel >>> y_displ');
%-------------------------------------------------------
Cc_era_displ=Cc_era*inv(Ac_era)*inv(Ac_era);
%
%-------------------------------------------------------
disp('Perform eigen-decompostion & Transformation & Allow
checking!')
%-------------------------------------------------------
[phi,Ac_decouple]=eig(Ac_era);
%Ac_decouple=inv(phi)*Ac_era*phi;
Bc_decouple=inv(phi)*Bc_era;
Cc_decouple=Cc_era_displ*phi;
%Dc_decouple=Dc_era;
%%
for j=1:num_singular
   if imag(Ac_decouple(j,j))==0
            disp('rigid body motion');
   end
end
%-------------------------------------------------------%
omega=imag(diag(Ac_decouple));
sigma=real(diag(Ac_decouple));
choice=0;
while choice==0
 disp('possible damped frequencies available ');
 [(1:2:num_singular)',omega(1:2:num_singular)/2/pi,...
 (2:2:num_singular)',omega(2:2:num_singular)/2/pi]
 choice=input('is first column of sigma ALL positive? (0/1) ');
 if choice==0
  disp('enter correct sorting vector')
  sort_vector=input('sorting vector [1,2,3....] ');
  sort_vector
  omega=omega(sort_vector);
  sigma=sigma(sort_vector);
  Bc_decouple=Bc_decouple(sort_vector,:);
  Cc_decouple=Cc_decouple(:,sort_vector);
 end
end
%-------------------------------------------------------
b=Bc_decouple(2:2:num_singular,1); %m=1 no change !!
c=Cc_decouple(:,2:2:num_singular);%%do not change !!
sigma=sigma(1:2:num_singular);      %%do not change !!
omega=omega(1:2:num_singular);   %%do not change !!
%-------------------------------------------------------
choice=input('check sigma & omega definitions (0/1) ');
if choice==1
[diag(Ac_decouple((1:2:num_singular),(1:2:num_singular)))],...
[diag(Ac_decouple((2:2:num_singular),(2:2:num_singular)))],
... [sigma,omega]]
  choice=input('happy? (0/1) ');
  if choice==0, break; end;
end
%%
%clear Ac_decouple Bc_decouple Cc_decouple;
%-------------------------------------------------------
disp('displacement measured and hence normalised...')
%-------------------------------------------------------
row=input('row of collocated data ');
d=zeros(1,num_singular/2);
j=1; k=1;
%
while k < (num_singular/2+1)
% [k,j]
 ratio=imag(b(k,1))/real(b(k,1));
 sq_d_displ=2*real(b(k,1))/...
          ((ratio*sigma(k)-omega(k))*imag(c(row,k))-...
           (sigma(k)+ratio*omega(k))*real(c(row,k)));
 if sq_d_displ > 0
            d=sqrt(sq_d_displ);
            Bc_cbsi2(j)=2*real(b(k))/d;
            for i=1:p
              Cc_cbsi1(i,j)=d*...
            ((ratio*sigma(k)-omega(k))*imag(c(i,k))-...
            (sigma(k)+ratio*omega(k))*real(c(i,k)));
        Cc_cbsi2(i,j)=d*(real(c(i,k))-ratio*imag(c(i,k)));
            end
            w_nat(j)=sqrt(sigma(k)^2+omega(k)^2);
            two_eta_wn(j)=2*abs(sigma(k));
            eta(j)=-sigma(k)/w_nat(j);
            w_damp(j)=omega(k);
            j=j+1;
 else
%           disp('negative sq_d_displ');
 end
 k=k+1;
end
retain=j-1;
%-------------------------------------------------------
disp(' form Continuous State Space Matrices ')
%-------------------------------------------------------
%dummy1=zeros(retain,retain);dummy2=eye(retain,retain);
%Ac_cbsi=[dummy1,dummy2];
%for j=1:retain
% dummy1(j,j)=(-w_nat(j)^2);
% dummy2(j,j)=-two_eta_wn(j);
%end
%Ac_cbsi=[Ac_cbsi;dummy1,dummy2];
%Bc_cbsi=[zeros(retain,1);Bc_cbsi2'];
disp('Cc_cbsi2 matrix should be zero, replaced by zero matrix');
[Cc_cbsi2]
Cc_cbsi=[Cc_cbsi1,zeros(p,retain)];%high freq influence
%-------------------------------------------------------
disp('%%%%%.... OUTPUT .....%%%%%')
%-------------------------------------------------------
disp('{real(Bc_cbsi2)}   {real(Cc_cbsi1)}      {freq_n} {2eta.w_n}
{freq_damp}')
[real(Bc_cbsi2)',        real(Cc_cbsi1)',        w_nat'*1.e-4/2/pi,
two_eta_wn'*1.e-4,...
 w_damp'*(1.e-4)/2/pi]
disp('NOTE freq_n, two_eta_wn & freq_damp are multiplied by
1.e-4')
clear b c d count sq_d_displ;
%-------------------------------------------------------
disp ('Save CBSI results as..'); dir cbsi*.mat;
%-------------------------------------------------------
file=input('type name of cbsi file (eg. str(cbsiz72) ');
end



%%%%%%%%%%%%%%%%%%%%%%%%%%%%%%%%
function cbsi_frf(w_nat, two_eta_wn, C1 ,order)
%function cbsi_frf(w_nat, two_eta_wn, C1 ,order)
% order [1,2,3,4...] order of w_nat
%%%%%%%%%%%%%%%%%%%%%%%%%%%%%%%%
load frf_20xz;
%-------------------------------------------------------
C1=C1(:,order);      w_nat=w_nat(order);
          two_eta_wn=two_eta_wn(order);
B=zeros(length(order),1);
diag_omega=eye(length(order));
diag_two_eta_wn=eye(length(order));
```

```
for j=1:length(order)
 diag_omega(j,j)=-(w_nat(j))^2;
 diag_two_eta_wn(j,j)=-two_eta_wn(j);
 B=[B;   C1(3,j)];
end
A=[zeros(length(order),length(order)),eye(length(order));
   diag_omega,diag_two_eta_wn];
C=C1(:,1:j)*[diag_omega,diag_two_eta_wn];
%%
[MAG,PHASE]=bode(A,B,C,[0;0;0],1,w(1:1024));
[th_Hpq,R]=cart2pol(real(H_pq(1:1024)),imag(H_pq(1:1024)));
[th_Hpr,R]=cart2pol(real(H_pr(1:1024)),imag(H_pr(1:1024)));
[th_Hps,R]=cart2pol(real(H_ps(1:1024)),imag(H_ps(1:1024)));
clear R;
%%
[h_cbsi,x]=impulse(A,B,C,[0;0;0],1,T_s*(1:N));
%-------------------------------------------------------
% plotting frequency response functions
%-------------------------------------------------------
my_axis1=[0,10000,-60,60];
figure(1)
subplot(2,1,1);
plot(w(1:1024)/2/pi,th_Hpq,...
    w(1:1024)/2/pi,PHASE(:,1)*pi/180,'r')
 ylabel('phase (rad)');
 title('Comparison of Cont. vs Experimental FRFs');
subplot(2,1,2);
plot(w(1:1024)/2/pi,20*log10(abs(H_pq(1:1024))),...
    w(1:1024)/2/pi,20*log10(MAG(:,1)),'r')
 xlabel('freq.(Hz)'); ylabel('magnitude H_pq & MAG(1) (dB)');
 axis(my_axis1);
%
figure(2);
subplot(2,1,1);
plot(w(1:1024)/2/pi,th_Hpr,...
    w(1:1024)/2/pi,(PHASE(:,2)*pi/180),'r')
 ylabel('phase (rad)');
 title('Comparison of Cont. vs Experimental FRFs');
subplot(2,1,2)
plot(w(1:1024)/2/pi,20*log10(abs(H_pr(1:1024))),...
    w(1:1024)/2/pi,20*log10(MAG(:,2)),'r')
 xlabel('freq.(Hz)'); ylabel('magnitude H_pr & MAG(2) (dB)');
 axis(my_axis1);
%
figure(3)
subplot(2,1,1);
plot(w(1:1024)/2/pi,th_Hps,...
    w(1:1024)/2/pi,unwrap(PHASE(:,3)*pi/180),'r')
 ylabel('phase (rad)');
 title('Comparison of Cont. vs Experimental FRFs');
subplot(2,1,2)
plot(w(1:1024)/2/pi,20*log10(abs(H_ps(1:1024))),...
    w(1:1024)/2/pi,20*log10(MAG(:,3)),'r')
 xlabel('freq.(Hz)'); ylabel('magnitude H_ps & MAG(3) (dB)');
 axis(my_axis1);
%%%%%%%%%%%%%%%
load irf_20xz;
figure(4)
subplot(2,1,1);plot(T_s*(1:1024),h_pq(1:1024))
 title('Comparison of Cont. vs Experimental IRFs');
 ylabel('h_pq(k)')
subplot(2,1,2);plot(T_s*(1:1024),h_cbsi(1:1024,1),'r')
 ylabel('IRF cbsi_1 '); xlabel('time (sec)');
%
figure(5)
subplot(2,1,1);plot(T_s*(1:1024),h_pr(1:1024))
 title('Comparison of Cont. vs Experimental IRFs');
 ylabel('h_pr(k)')
subplot(2,1,2);plot(T_s*(1:1024),h_cbsi(1:1024,2),'r')
 ylabel('IRF cbsi_2 '); xlabel('time (sec)');
%
figure(6)
subplot(2,1,1);plot(T_s*(1:1024),h_ps(1:1024))
 title('Comparison of Cont. vs Experimental IRFs');
 ylabel('h_ps(k)')
subplot(2,1,2);plot(T_s*(1:1024),h_cbsi(1:1024,3),'r')
 ylabel('IRF cbsi_3 '); xlabel('time (sec)');
%
figure(7)
subplot(2,1,1);
%plot(w(1:1024)/2/pi,th_Hps,...
%    w(1:1024)/2/pi,unwrap(PHASE(:,3)*pi/180),'r')
% ylabel('phase (rad)');
% title('Comparison of Cont. vs Experimental FRFs');
plot(w(1:1024)/2/pi,20*log10(imag(H_ps(1:1024))),...
    w(1:1024)/2/pi,20*log10(sin(th_Hps).*MAG(:,3)'),'r')
axis(my_axis1);
subplot(2,1,2)
plot(w(1:1024)/2/pi,20*log10(real(H_ps(1:1024))),...
    w(1:1024)/2/pi,20*log10(cos(th_Hps).*MAG(:,3)'),'b')
 xlabel('freq.(Hz)'); ylabel('real H_ps & sin(O)*MAG(3) (dB)');
axis(my_axis1);


function
[M_hat_cms,D_hat_cms,K_hat_cms]=cms(p,lamda,delta,p
hi_m)
%
%          p          >> number of measured outputs
%          lamda      >> undamped diag(w_nat^2)
%          delta      >> modal damping diag(2 x eta x w_n)
%          phi_m      >> mass normalised measured
eigenvectors
% NB lamda, delta & phi_m must correspond!!
% NB lamda ordered
%          M_hat_cms >> cms of mass matrix, etc.
%-------------------------------------------------------%
K_bar=inv(phi_m*inv(lamda)*phi_m');
          % non rigid modes!!
M_bar=K_bar*phi_m*lamda^(-2)*phi_m'*K_bar;
D_bar=K_bar*phi_m*inv(lamda)*delta*inv(lamda)*phi_m'*K_bar;

d_lamda=lamda-phi_m'*K_bar*phi_m
[P,D_svd,Q]=svd(d_lamda)
%check rank
[rank(lamda)-rank(phi_m'*K_bar*phi_m),rank(d_lamda)]
diag(D_svd)
num_singular=input('input number of significant singular  ')
%
%therefore take only non-singular values
P_p=[P(:,1:num_singular)];
phi_a=[phi_m;P_p'];

stiff_36=inv(phi_a*inv(lamda)*phi_a');      %[K_bar,0; 0 K_res]
mass_36=inv(phi_a*phi_a');                  %[M_bar,0; 0 M_res]
damp_36=inv(phi_a*inv(delta)*phi_a');       %[D_bar,0; 0 D_res]

[row,col]=size(K_bar);
K_res=stiff_36(1+row:size(stiff_36),1+col:size(stiff_36));
M_res=mass_36(1+row:size(stiff_36),1+col:size(stiff_36));

[U_eta,lamda_eta]=eig(inv(M_res)*K_res);
[U_eta]=scale_M(M_res,U_eta);
          %scale eigenvectors
% check
%[U_eta'*M_res*U_eta];
%[U_eta'*K_res*U_eta,lamda_eta];
%-------------------------------------------------------%
%K_hat=[K_bar,zeros(size(K_bar),size(lamda_eta));
%       zeros(size(lamda_eta),size(K_bar)),lamda_eta];

U_a=[eye(size(K_bar)),zeros(size(K_bar),size(U_eta));
    zeros(size(U_eta),size(K_bar)),U_eta'];
U_b=[eye(size(K_bar)),zeros(size(K_bar),size(U_eta));
    zeros(size(U_eta),size(K_bar)),U_eta];

K_hat_cms=U_a*stiff_36*U_b;
M_hat_cms=U_a*mass_36*U_b;
D_hat_cms=U_a*damp_36*U_b;
%------------------------------- end
```